JOURNAL OF TELECOMMUNICATIONS AND INFORMATION TECHNOLOGY

3/2017



(*Contents Continued on Back Cover*)

ISSN 1509-4553 on-line: ISSN 1899-8852




Circulation: 300 copies Sowa – Druk na życzenie, www.sowadruk.pl, tel. 22 431-81-40

Ministry of Science and Higher Education
Republic of Poland

Improvement of language quality; Assigning DOIs; Subscription to the plagiarism detection system – tasks financed under 556/P-DUN/2017 agreement from the budget of the Ministry of Science and Higher Education under the science dissemination fund.

JOURNAL OF TELECOMMUNICATIONS AND INFORMATION TECHNOLOGY

# *Foreword to the Special Issue*

We are very pleased to present the Special Issue "Recent Progress in Electromagnetic Theory and its Applications", an outcome of the COST (European Cooperation in Science and Technology) Action TU1208 "Civil engineering applications of Ground Penetrating Radar". The Special Issue comprises two parts: Part I includes eight papers on Ground Penetrating Radar (GPR) technology, methodology and applications; Part II contains six papers dealing with other applications of electromagnetic fields. Overall, the papers are authored by scientists from nineteen institutes in nine countries (Armenia, France, Germany, India, Ireland, Italy, Poland, Russia, and United Kingdom).

## Part I

*GPR overview*

GPR is a non-destructive testing technique that uses low-power electromagnetic waves to produce high-resolution images of the subsurface and structures. A GPR instrument emits a wide-band electromagnetic signal and detects echoes coming from the environment, caused by discontinuities of electric and magnetic properties. By exploiting signal processing and imaging methods, the echoes recorded by the radar can be transformed into three-dimensional images, which enable seeing into structures that are opaque to the human eye.

GPR started being used in the 1970s for ice surveys in Antarctica and, through the decades, has gained broad acceptance internationally. Nowadays, it is successfully employed for a great variety of tasks. In civil engineering, GPR is used for the inspection of transport infrastructures (roads, highways, airport runways, railways, bridges, tunnels), to detect and locate voids, cavities and buried services (pipes, cables), for the monitoring of retaining walls, embankments and dams, for the investigation of buildings and foundations, to map soil layers, measure bedrock depth, and identify faults and fracture zones in rock (for geotechnical and geological studies, or foundation design) and more. In archaeology and cultural-heritage management, GPR is employed to discover and map buried archaeological artefacts, to inspect ancient buildings, bridges, columns and statues, to investigate frescoes, mosaics and decorations, and to study the internal conditions of several other objects of historical value. GPR is also used for the inspection of natural structures of historical, geological, biological

or landscape conservation value, such as trunks and roots of veteran trees, glaciers, caverns, fossil beds, sand dunes, and more. Furthermore, GPR is extensively applied in agriculture, for the investigation of the bottom of lakes and coastal regions, for planetary explorations, as an auxiliary tool in autonomous transport systems, and more.

At present, GPR systems typically operate in the 10 MHz – 10 GHz range. Generally, there is a direct relationship between the frequency of the electromagnetic waves emitted by the radar and the resolution that can be obtained. Conversely, there is an inverse relationship between frequency and penetration depth. Hence, high frequencies are used to detect small, shallow targets and low frequencies are used to detect larger, deeper targets. The antennas have dimensions comparable to the wavelengths of the signals. Therefore, the size of a GPR instrument is basically defined by the frequency range of operation. Some systems use two or more antennas operating simultaneously over different frequency ranges. To couple the electromagnetic energy into the investigated structure, the antennas can operate in close proximity (ground-coupled antennas), else at a limited distance above the structure (air-coupled antennas).

A GPR can be monostatic, bistatic, or multistatic – as all radar systems. In monostatic systems, a single antenna is used for transmitting and receiving electromagnetic signals (currently, this type of GPR can be considered as obsolete and is seldom used). A bistatic system uses two separate antennas for transmitting and receiving, which are often housed in a single module. Antennas in independent modules represent an interesting technological solution that allows placing the transmitter and receiver on the two opposite sides of the investigated structure, thus halving propagation and attenuation losses. Multistatic systems are composed by multiple spatially diverse monostatic or bistatic radar components, usually with a shared area of coverage. At the present time, commercial multistatic GPR systems are implemented as multiple bistatic systems and their main advantage is that they enable faster data collection by increasing the extension of the investigated area per time unit. Furthermore, they make it easier for the operator to produce three-dimensional images.

There are two main types of GPR: impulse and step-frequency systems. Impulse systems are the most widely used, they operate in the time domain and emit a series of short electromagnetic pulses (normally, of 1–10 ns duration). Step-frequency systems are less common, although they are less expensive. They operate in the frequency domain and emit a series of harmonic waves, which frequency is progressively incremented across a broad spectrum in a step-wise fashion. By exploiting the inverse Fourier transform (from frequency to time-domain), a step-frequency GPR provides results equivalent to those measured by an impulse GPR. The step frequency approach is possible because the investigated scenario is regarded as a time-invariant system and the received signal is a linear function of the transmitted one. Impulse systems are typically more sensitive to radio frequency interference and may require an averaging of measurements to improve the signal-to-noise ratio. Step-frequency systems can process a higher energy without increasing the maximum level of the signal. The thermal noise at their receiver is lower, therefore the signal to noise ratio is higher. Another advantage of step-frequency systems is the ability to skip frequencies that could interfere with broadcast stations. A drawback of step-frequency systems is that attention must be paid to the aliasing problem, due to the sampling of the harmonic answer. This is resolved by using a frequency step small enough, which slows down the collection of data.

### *Data interpretation and visualization*

To enable analysis and interpretation of results, GPR data are normally plotted as a two-dimensional map, showing the amplitude of the field measured by the receiver as a function of time and position (B-scan or profile). Time can be replaced by depth when the propagation velocity in the subsurface or structure is known. Looking at single traces (A-scan, amplitude of the field measured by the receiver as a function of time in a specific position) is also useful, in most applications. When several parallel profiles are acquired, a three-dimensional matrix of field amplitudes is available (C-scan) and three-dimensional images of the investigated scenario can be produced. From a C-scan it is possible and straightforward to obtain horizontal slices of data, i.e. plan views of field amplitudes at designated depths, which are very useful in most applications.

In some cases, raw GPR data are examined and interpreted. More often, signal processing algorithms are applied to the data, as required by the specific application and situation. The steps and algorithms may vary according to each survey, and normally involve filtering to remove unwanted noise, gain adjustment to balance signal strengths, migration to remove diffraction effects, corrections for variations in surface topographic elevation, and improvement of graphic display by using suitable color palettes. For complex scenarios and/or for analyzing and interpreting reflections coming from deep layers, more advanced procedures are used.

After the processing, GPR results are interpreted by recognizing reflection and diffraction patterns on the radargrams and by determining their position. Discrete buried objects with circular cross-section typically appear as hyperbolic reflections in the raw data, with hyperbola prongs projected downwards like an inverted V shape. Subsurface layers appear as continuous reflectors on the radargrams. More in general, reflection and diffraction patterns in the raw GPR profiles may have different shapes, which do not resemble the true shape or orientation of the scatterers. Various factors, including the innate design of the survey equipment and the complexity of electromagnetic propagation in the scenario, can disguise complex structures recorded on GPR profiles. For simple scenarios, such as regular structures hosting widely spaced targets, reflection patterns can be adequately interpreted by trained operators. For complex scenarios, such as natural subsoil with stones and rocks, ancient bridges, or any structures hosting closely spaced targets, it may be convenient to aid the interpretation by using an electromagnetic simulator or by applying to the radargrams suitable imaging and inversion algorithms.

### *The COST scientific programme*

A significant contribution to the GPR technique has been given by the COST Action TU1208 "Civil engineering applications of Ground Penetrating Radar".

COST is the longest-running European framework supporting cooperation among scientists and researchers across Europe and beyond. Founded in 1971, it is currently integrated in the Horizon 2020 programme. It contributes to reducing fragmentation in European research investment, building the European Research Area (ERA) and opening it to worldwide cooperation. It also aims at constituting a "bridge" towards the scientific communities of emerging countries, increasing the mobility of researchers across Europe and fostering the establishment of excellence in key scientific domains. Gender balance, support to early-career investigators and inclusiveness are strategic priorities of the COST programme.

COST does not fund research itself, but provides support for activities carried out within Actions: these are bottom-up science and technology networks, centered around nationally funded research projects, with a four-year (or, exceptionally, slightly longer) duration and a minimum participation of five countries. The Actions are active through a range of networking tools, such as meetings, workshops, conferences, training schools, short-term scientific missions and dissemination activities. They are open to researchers and experts from universities, public and private research institutions, nongovernmental organizations, industry and small and medium-sized enterprises. By creating open spaces where people and ideas can grow, COST fosters the birth of new ideas and unlocks the full potential of science.

For more information about COST, please visit www.cost.eu.

### *The Action TU1208*

The Action TU1208 started in April 2013 and is coming to an end in October 2017. It involves more than 300 experts from 150 partner institutes in 28 COST countries (Austria, Belgium, Croatia, Czech Republic, Denmark, Estonia, Finland, France, former Yugoslav Republic of Macedonia, Germany, Greece, Ireland, Italy, Latvia, Malta, the Netherlands, Norway, Poland, Portugal, Romania, Serbia, Slovakia, Slovenia, Spain, Sweden, Switzerland, Turkey, and the United Kingdom), a COST cooperating state (Israel), 6 COST near neighbor countries (Albania, Armenia, Egypt, Jordan, Russia, Ukraine) and 6 COST international partner countries (Australia, Colombia, Hong Kong, The Philippines, Rwanda, the United States). University researchers, software developers, civil and electronic engineers, archaeologists, geophysics experts, non-destructive testing equipment designers and manufacturers, end-users from private companies and public agencies have participated in the Action.

The scientific structure of Action TU1208 includes four Working Groups (WGs), which research activities cover all areas of the GPR technology, methodology, and applications.

- WG 1 focuses on the development of novel GPR instrumentation. Within this WG, novel equipment has been designed, realized and tested. Moreover, new tests have been proposed for checking the performance and stability of GPR systems.
- WG2 focuses on the use of GPR in civil engineering. This WG has developed guidelines for GPR inspection of flexible pavements, utility detection in urban areas, and evaluation of concrete structures. Recommendations for a safe use of GPR have been produced. Among the most interesting outcomes of WG2, it is worth mentioning a catalogue of European test sites where GPR equipment and procedures can be verified and tested. Additionally, WG2 has developed a wide series of investigations and case studies where GPR has been successfully used in a plethora of different civil-engineering works.
- WG3 studies electromagnetic forward and inverse methods for the solution of near-field scattering problems by buried structures, imaging techniques and data processing algorithms. This WG has released free software for the electromagnetic modeling of GPR scenarios and for the processing of GPR data. A database of radargrams has been composed and organized, openly available for researchers who can use the proposed datasets to test and validate their electromagnetic forward- and inverse-scattering techniques, imaging and signal-processing methods.
- WG4 deals with the applications of GPR outside from the civil engineering area and with the combined use of GPR and complementary non-destructive testing methods. The most interesting output of this WG is a wide series of case studies showing how GPR can be applied in different fields, both in well-established and emerging applications. Special attention has been paid to the use of GPR for the management of our cultural heritage.

It is worth reporting that all WGs have been active in training activities (16 Training Schools were organized in four years) and produced an open-access educational package for teaching GPR in the university.

For more information about TU1208, please visit www.GPRadar.eu.

### *The issue contents*

In the opening paper of the Special Issue, entitled *Improving the GPR Detectability Using a Novel Loop Bowtie Antenna*, the Authors K. K. Ajith and Amitabha Bhattacharya compare the performance of a traditional resistive-capacitive (RC) loaded bowtie against a novel loop loaded bowtie. The bandwidth, gain and radiation patterns of both antennas are measured in the free-space and results are compared with simulations performed by using commercial software implementing the finite-integration technique. GPR profiles are acquired in various scenarios, with brass and iron pipes buried in the soil, or dry bamboo, and over reinforced concrete. GPR images produced by the loop-loaded antenna are better than those of the RC loaded bowtie, for all the considered targets. The Authors indicate that the loop loading technique may be employed in existing antennas also, to enhance their radiation properties.

The Authors of the paper entitled *Analytical Investigation on a New Approach for Achieving Deep Penetration in a Lossy Medium: The Lossy Prism*, Fabrizio Frezza, Patrizio Simeoni, and Nicola Tedeschi, investigate an innovative use of a lossy prism to generate an inhomogeneous wave. The proposed prism allows achieving a deeper microwave penetration in a lossy medium than a leaky-wave antenna.

In *Multiple-ring Circular Array for Ground-Penetrating Radar Applications: Basic Ideas and Preliminary Results*, Roberto Vescovo and Lara Pajewski study the possibility of using a multiple-ring circular array as a GPR antenna array. The theory behind the idea is described and preliminary results are presented. The proposed configuration allows achieving a wide frequency band with a low dynamic range ratio. Moreover, the synthesis of the array can be easily performed at a single frequency within the range of interest.

The Special Issue continues with the paper *Enhancement of Air-ground Matching by Means of a Chirped Multilayer Structure: Electromagnetic Modeling with the Method of Single Expression*, by Hovik Baghdasaryan, Tamara Knyazyan, Tamara Hovhannisyan, Marian Marciniak, and Lara Pajewski. In this contribution, a non-uniform multilayer structure contacted with the ground is designed, which reduces the back-reflection of electromagnetic waves towards the transmitting antenna and allows a deeper penetration into the ground. The structure is modeled by using the method of single expression, an analytical-numerical technique ideated and developed by Hovik Baghdasaryan.

The Authors of the paper *Advanced Inversion Techniques for Ground Penetrating Radar*, Alessandro Fedeli, Matteo Pastorino, and Andrea Randazzo, provide a short and useful overview of advanced inversion techniques for GPR. They address nonlinear and linear inverse scattering methods, qualitative approaches and sampling, and pre-processing methods. The need for initiatives dedicated to the validation of GPR inversion approaches is pointed out by the Authors, as well.

*SPOT-GPR: A Freeware Tool for Target Detection and Localization in GPR Data Developed within the COST Action TU1208*, is authored by Simone Meschino and Lara Pajewski. This paper presents and describes SPOT-GPR (release 1.0), free software implementing an innovative Sub-Array Processing method for the analysis of GPR data with the main purposes of detecting and localizing targets. The approach implemented in SPOT-GPR exploits the matched-filter technique, which has never been used before in the GPR field. The software is written in Matlab and it comes with a graphical user interface. Two examples of applications are provided in the paper, where SPOT-GPR is successfully employed for detecting and locating reinforcing elements in concrete cells. The obtained results are compared with those of a standard hyperbola-fitting approach, which is commonly used for the processing of GPR data when circular-section cylindrical targets are present, and SPOT-GPR demonstrates a good functioning.

The Author of the paper *Development of Data Processing Tools for the Analysis of Radargrams in Utility Detection Using Ground Penetrating Radar*, Florence Sagnard, reports on advanced processing techniques that can be used to extract quantitative information from radargrams recorded over pipes and strips with lateral dimension less than around ten centimeters, in a noisy background, in case of a low image quality, and with overlapping between signatures. The Author proposes a procedure suitable for small object detection and he enriches the model by exploiting the polarization diversity. The Author recommends including further advanced algorithms in the procedure, such as space-frequency time-reversal matrices and wavelet transform, to account for hyperbola misshapedness.

Part I of the Special Issue is concluded with the paper entitled *Search for Chelyabinsk Meteorite Fragments in Chebarkul Lake Bottom (GPR and Magnetic Data)*, authored by Vladimir Buzin, Dmitry Edemsky, Sergey Gudoshnikov, Vladimir Kopeikin, Pavel Morozov, Alexey Popov, Igor Prokopovich, Vladimir Skomarovsky, Nikolay Melnik, Andrey Berkut, Sergey Merkulov, Pavel Vorovsky, and Leonid Bogolyubov. The Authors have employed GPR in their search in Chelabinsk. They provide a detailed description of GPR use in lake water conditions and discuss the limits of its applicability in such an environment. An impressive technical and photographic documentation enclosed in the paper makes you feel as you are actually participating in the Chelabinsk surveys.

## Part II

### *Other applications of electromagnetic fields*

Part II of the Special Issue is opened with two papers on antenna arrays for free-space applications. The first contribution is entitled *Multi-Objective Evolutionary Optimization of Aperiodic Symmetrical Linear Arrays*, authored by Francesco Napoli, Lara Pajewski, Roberto Vescovo, and Marian Marciniak. In this paper, a multi-objective approach is used for the design of aperiodic linear arrays of antennas. The adopted procedure is based on a standard Matlab implementation of the Controlled Elitist Non-Dominated Sorting Genetic Algorithm-II and broadside symmetrical arrays of isotropic radiators are considered, with both uniform and non-uniform excitations. The work focuses on whether, and in which design conditions, aperiodic solutions obtained by the adopted standard multi-objective evolutionary procedure

can approximate, or outperform, the Pareto-optimal front for the uniform-spacing case computable by the Dolph-Chebyshev method.

In the paper *Reconfigurable Antenna Arrays with Phase-only Control in the Presence of Near-field Nulls*, by Giulia Buttazzoni and Roberto Vescovo, the Authors present a novel effective iterative algorithm for the power synthesis of reconfigurable antenna arrays. This approach allows designing antenna arrays of arbitrary geometry with phase-only control, simultaneously reducing the near-field amplitude in a region close to the antenna. The near-field reduction is obtained by imposing that the field vanishes at a prescribed number of suitably located points. Strong field reductions are obtained without increasing the dimensions of the problem, thus keeping low the required computational time.

Part II of the Special Issue continues with two contributions on grating structures.

The paper entitled *The Optimum-efficiency Beam Multiplier for an Arbitrary Number of Output Beams and Power Distribution*, by Fabrizio Frezza, Marian Marciniak, and Lara Pajewski, focuses on the problem of splitting a beam into a set of equi-intense output beams, or in beams that respect a given power distribution. The diffraction efficiency of a beam multiplier is the fraction of the incident beam power that is converted into the power of the desired output beams: the maximization of this parameter is a fundamental target in designing beam multipliers. The Authors consider beam splitters constituted by periodic diffractive elements and prove that an optimum-efficiency beam multiplier with an arbitrary number of diffraction orders exists. They derive its phase transmittance in an analytic form, by exploiting methods from the calculus of variation. Numerical examples are presented and commented on.

In the paper *Influence of Chirped DBR Reflector on the Absorption Efficiency of Multi-nanolayer Photovoltaic Structures: Wavelength-scale Analysis by the Method of Single Expression*, by Hovik Baghdasaryan, Tamara Knyazyan, Tamara Hovhannisyan, Gurgen Mardoyan, Marian Marciniak, and Trevor Benson, a novel solution to the topical problem of enhancing the efficiency of photovoltaic elements is proposed. In particular, the Authors investigate the use of a non-uniform multilayer reflector placed under the p-i-n semiconductor junction. The electromagnetic modeling of light interaction with the photovoltaic structure is performed by using the method of single expression, where no division on counter-propagating waves is exploited.

The following two papers of Part II are concerned with photonic and electromagnetic band-gap materials.

In *A Photonic-Crystal Selective Filter*, authored by Lara Pajewski and Giuseppe Schettini, a highly selective filter is designed, working at 1.55 $\mu$m and having a 3-dB bandwidth smaller than 0.4 nm, as is required in Dense Wavelength Division Multiplexed systems. Different solutions are proposed, where photonic crystals made of rectangular- or circular-section dielectric rods are used, or else photonic crystals with holes drilled in a dielectric bulk. The required polarization and frequency selective properties are achieved by introducing a defect in the periodic structure. The device is studied by means of the Fourier Modal Method. Practical guidelines about advantages and limits of the investigated solutions are given.

In *Experimental Analysis of a Directive Antenna with a 3D-EBG Superstrate*, by Lara Pajewski, Fabrizio Frezza, Marian Marciniak, Emanuele Piuzzi, and Giorgia V. Rossi, electromagnetic band-gap (EBG) resonator antennas are studied. A woodpile is used to enhance the gain of a patch antenna. The compound radiating system is thoroughly characterized in the 8–12 GHz frequency range, in a shielded anechoic chamber, by using a vector network analyzer. The return loss, gain, and radiation patterns in the E- and H-planes are measured, for the patch antenna covered with the woodpile. The EBG superstrate is positioned at different suitable distances from the antenna and its orientation is varied. A gain enhancement of about 10 dB is achieved. The paper is concluded with a series of promising ideas for future work.

## Acknowledgments

We are warmly grateful to the team of specialists who reviewed the papers of this Special Issue. Their constructive comments and corrections were essential for the success and quality of this initiative. In particular, we thank Giulia Buttazzoni, Simone Meschino,

Robert Minasian, Santo Prontera, Silvestar Sesnic, Patrizio Simeoni, Sławomir Sujecki, Alessio Ventura, and Roberto Vescovo. We wish to thank all the Authors of the papers, for deciding to present the results of their studies in this Special Issue. We are truly grateful to the Editorial Office of the *Journal of Telecommunications and Information Technology*, for offering us the opportunity to organize this Special Issue. Special thanks to Ewa Kapuściarek, for the outstanding support in all the stages of this editorial venture and efficient handling of the editorial process, and to Robert Magdziak, for the careful editing of the papers. Finally, we are immensely grateful to COST for funding and supporting the COST Action TU1208.

Lara Pajewski
Hovik Baghdasaryan
Marian Marciniak
*The Guest Editors*

Paper

# Improving the GPR Detectability Using a Novel Loop Bowtie Antenna

K. K. Ajith[1,2] and Amitabha Bhattacharya[1]

[1] *Department of Electronics & Electrical Comm. Eng., Indian Institute of Technology Kharagpur, India*
[2] *Department of ETC, International Institute of Information Technology Bhubaneswar, India*

https://doi.org/10.26636/jtit.2017.120917

**Abstract—The Ground Penetrating Radar (GPR) technique finds immense applications in civil engineering today, as the most suitable approach for non-destructive testing of pavements, highways, concrete structures, and more. The major challenge in carrying out a GPR evaluation is that the properties of the probed medium are usually unknown. The permittivity and conductivity of the medium may vary from those of air to water. The electromagnetic waves also have a frequency dependent attenuation. The ability of GPR to detect signals reflected and scattered by the targets largely depends upon the antenna performance. This paper studies a novel 11:1 wideband loop bowtie antenna with very good radiation properties in the entire operating bandwidth. Synthetic and experimental results are presented for the return loss and gain of the antenna. Furthermore, experimental results are presented for the radiation patterns in the E- and H-plane. We also used the antenna to measure B-scans over two different pipes, a bamboo, and a reinforced concrete structure. All results obtained with the proposed antenna have been compared with results obtained by using a RC loaded antenna. It has been found that the loop bowtie antenna has excellent detection capability and produces less clutter. The loop loading technique can be applied to existing antennas for improved GPR imaging. This will improve the detectability of GPR by improving the target return signal.**

***Keywords—antenna, Ground Penetrating Radar, imaging, UHF, UWB.***

## 1. Introduction

Ground Penetrating Radar (GPR) is used in civil engineering for non-destructive testing (NDT) of pavements, roads, bridges, tunnels, and more [1]. It can also be used for rebar detection in concrete [2]. More recent and advanced applications include detecting corrosion of rebar due to contamination by water and salt [3]. Moreover, GPR is a powerful technique in archeological surveys for mapping buried artifacts [4]. In the defense sector, GPR is extensively used for landmine detection [5]. The main objective of GPR is to image subsurface targets or layers for a qualitative analysis. The produced data can also be used for a quantitative study of electromagnetic properties of the medium and targets.

The depth at which a GPR can probe, depends upon the electromagnetic properties of the soil. Depending upon the wetness condition and other composition of the soil, the permittivity and conductivity can vary in a wide range [6].

In a GPR system, the signals hitting the target and reflecting to the antenna undergoes a frequency dependent attenuation owing to the electrical conductivity of the medium. This is in addition to the loss, which is proportional to the square of the distance. The reflected amplitude is further determined by the electric permittivity of the medium and the target. The reflected amplitude is too small if the permittivity contrast of target and the medium is small. A deep probing requires a low frequency signal, that penetrates without much attenuation. For high-resolution imaging, a large bandwidth is required. Obtaining ultra-wide bandwidth at sub-gigahertz frequencies is a challenging task for GPR antenna designers. High frequency signals are highly attenuated as skin depth is inversely proportional to the square root of frequency. So, most GPRs are designed for sub-gigahertz frequencies. But, the bandwidth has to be large enough to get a high-resolution image of the target. A moderate gain is also desired to meet the link budget requirements. Size of the antenna is also an important factor as the GPR system has to be portable.

Bowtie antennas are most widely used in GPR due to wide impedance matching and radiation properties [1]. These antennas are mostly useful only in a 4:1 bandwidth. Beyond that, there is a reduction in boresight gain. Many GPR systems use resistive loaded bowtie antennas to reduce the size and for increased bandwidth, thus sacrificing the gain and efficiency. This is a major drawback. Bowtie antennas can be loaded with lumped resistors to attenuate the current at the antenna end to suppress the reflections. This will result in a large bandwidth and good pulse radiating ability. Another approach is to provide a continuous loading profile that increases towards the antenna end, which is found to be very good for pulse radiation. Many designs of resistive loaded bowtie antennas are available in the literature [7]–[9].

In this paper, we examine the detection capabilities of RC loaded bowtie and a novel loop loaded bowtie in an experimental GPR setup. RC loaded bowtie antenna having

a 10:1 bandwidth (0.3–3 GHz) had been designed by the authors [10]. The loop-loaded bowtie antennas has been recently designed by the authors [11]. The antenna has a 11:1 impedance bandwidth (0.5–5.5 GHz) without applying any kind of resistive loading. It has a very good gain and efficiency in the entire band. A stable radiation pattern has been obtained throughout the band. The measured results are interesting. Loading the bowtie antenna with a loop is an excellent way to confine the near field of the emitter.

A brief description of the considered antennas is given in Section 2. Simulated and measured parameters are presented and discussed in Section 3. Experimental results of GPR survey are given in Section 4. Section 5 concludes the work.

## 2. Description of the Antennas

Two types of antennas are considered and compared in this paper. The first is a RC loaded bowtie and the second one is a loop loaded bowtie. The design and optimization of these antennas were carried out by using a commercial electromagnetic simulation software CST Microwave Studio.

### *2.1. RC Loaded Bowtie Antenna*

The RC loaded bowtie antenna is designed for the 300 MHz – 3 GHz frequency range, as described in [10]. It is constituted by two half-ellipses. Periodic slots are cut on the antenna arms, which act as capacitive loading. A graphite sheet of 1 mm thickness is placed over each arm to provide a resistive loading. The combined resistive-capacitive loading enhances the bandwidth while maintaining the compact size $30 \times 23$ cm. The antenna is fed using a vertical microstrip to parallel stripline transition. The dimensions with reference to Fig. 1 are: $W = 220$ mm, $L = 286$ mm, $g = 1.5$ mm on FR4 substrate (relative permittivity 4.4) of dimensions $300 \times 230$ mm and thickness 1.5 mm (Fig. 3a).

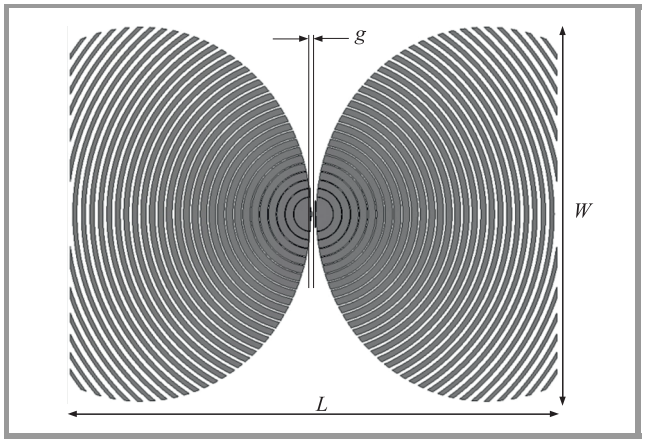


***Fig. 1.*** Geometry of RC bowtie antenna.

### *2.2. Loop Loaded Bowtie Antenna*

The geometry of the loop loaded bowtie antenna is depicted in Fig. 2. This antenna does not require any kind of dissipative loading. Each bowtie arm is etched on either side of the substrate. One of the arm is fed with a simple microstrip feed, while the other arm on the opposite side acts as ground plane. The overall size of the antenna is $23 \times 23$ cm. The dimensions with reference to Fig. 2 are: $W = 230$ mm, $L_b = 172$ mm, $R = 196$ mm, $g = 1.5$ mm. FR4 glass epoxy substrate (relative permittivity 4.4) with thickness 1.6 mm has been chosen for the design (Fig. 3b).

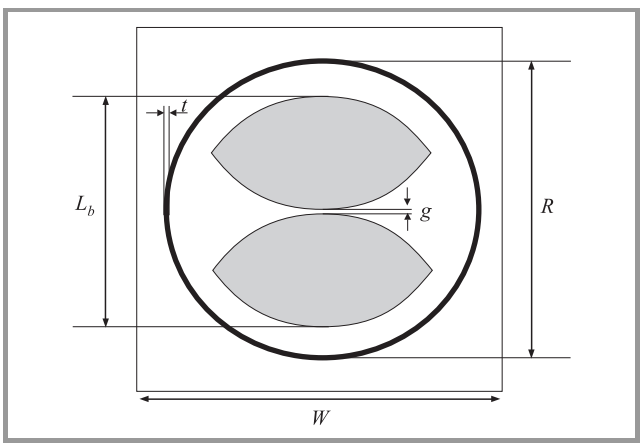


***Fig. 2.*** Geometry of loop bowtie antenna.

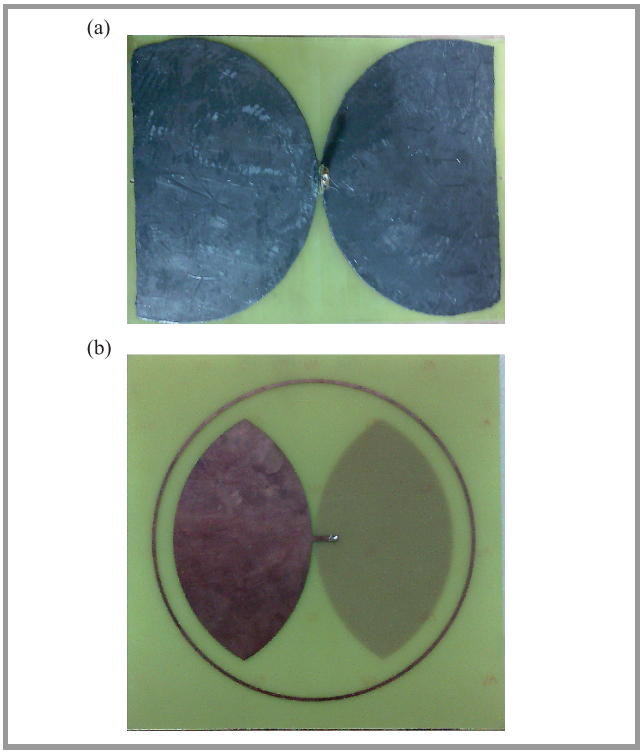


***Fig. 3.*** RC bowtie antenna (a) and loop bowtie antenna (b).

# 3. Simulation and Measurement of Antenna Parameters

Simulations were carried out by using the time-domain solver, based on the Finite Integration Technique (FIT), implemented in CST Microwave Studio. The meshing parameters were properly chosen, to represent correctly the smallest features of the antenna geometry. In particular, we applied the following rules of thumb: the largest mesh cells must be at least $\frac{\lambda}{10}$ at the highest frequency of simulation. The lower mesh limit must be appropriate for the modeling of the smallest dimensions of the geometry. The vacuum bounding box surrounding the antenna must be at a distance of $\frac{\lambda}{4}$ at the lowest frequency of interest.

### *3.1. Bandwidth*

Figure 4 shows the simulated and measured magnitude of the $S_{11}$ parameter for the RC bowtie. The graph indicates a 10 dB return loss in the frequency range 0.3–3 GHz, for a good impedance match with a 50 Ω feed. The bandwidth is 2.7 GHz. Figure 5 shows the magnitude of the $S_{11}$ parameter for the loop bowtie. The impedance bandwidth, as can be observed from the figure, is centered on 3 GHz and in the 0.5–5.5 GHz interval. This corresponds to a 11:1 bandwidth.

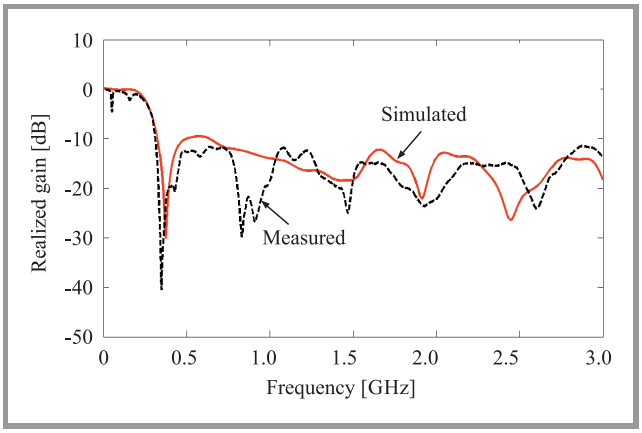


***Fig. 4.*** Measured $|S_{11}|$ vs. frequency of RC bowtie.

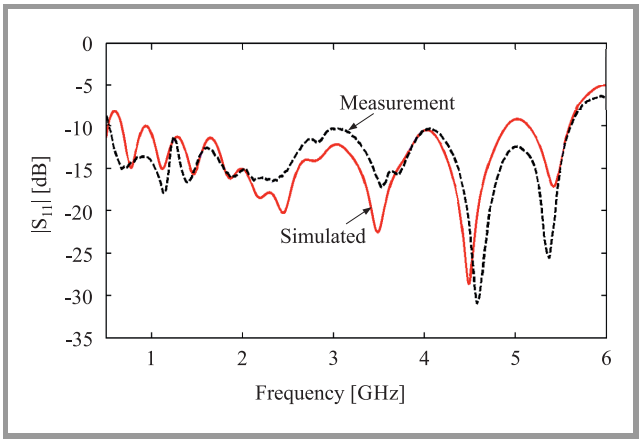


***Fig. 5.*** Measured $|S_{11}|$ vs. frequency of loop bowtie.

### *3.2. Realized Gain*

The realized gain was measured by exploiting a method based on Friis transmission formula and by using two identical antennas as outlined in [12]. The measured gain of the two antennas is plotted in Fig. 6. The gain of the RC loaded bowtie decreases considerably after 1.25 GHz. This is a drawback of the bowtie antenna – the forward gain drastically reduces after a two-octave bandwidth. The loop bowtie has a positive gain in the entire bandwidth, around an average value of 3.13 dBi. The reflected fields from the ring around the bowtie reach the center with the same phase and this significantly improves the forward gain throughout the operating frequency band. The peak gain is also higher compared to the RC bowtie.

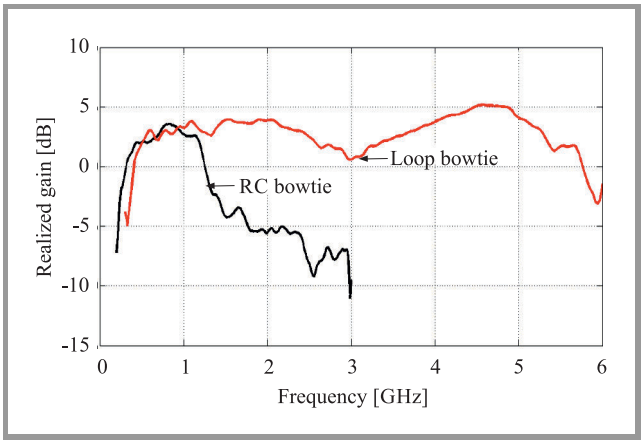


***Fig. 6.*** Realized gain vs. frequency.

The characteristics of the two antennas are summarized in Table 1.

Table 1
Summary of antenna characteristics

| Antenna type | Bandwidth | Peak gain | Average gain |
|---|---|---|---|
| RC loaded bowtie | 0.3–3 GHz | 3.6 dBi | –2.8 dBi |
| Loop bowtie | 0.5–5.5 GHz | 5.2 dBi | 3.13 dBi |

### *3.3. Radiation Pattern*

Radiation pattern measurements were carried out in outdoor environment. The measured radiation patterns of the RC bowtie antenna, in the E and H planes, at two representative frequencies (1 and 2.5 GHz) are shown in Fig. 7. The pattern is close to a "figure of 8" in the E-plane and omni-directional in the H-plane, at lower frequencies. One can observe the sharp null in the boresight at 2.5 GHz. The measured radiation patterns of the loop bowtie at the designated frequencies are presented in Fig. 8. Boresight radiation has been significantly improved at 2.5 GHz, due to the loop.

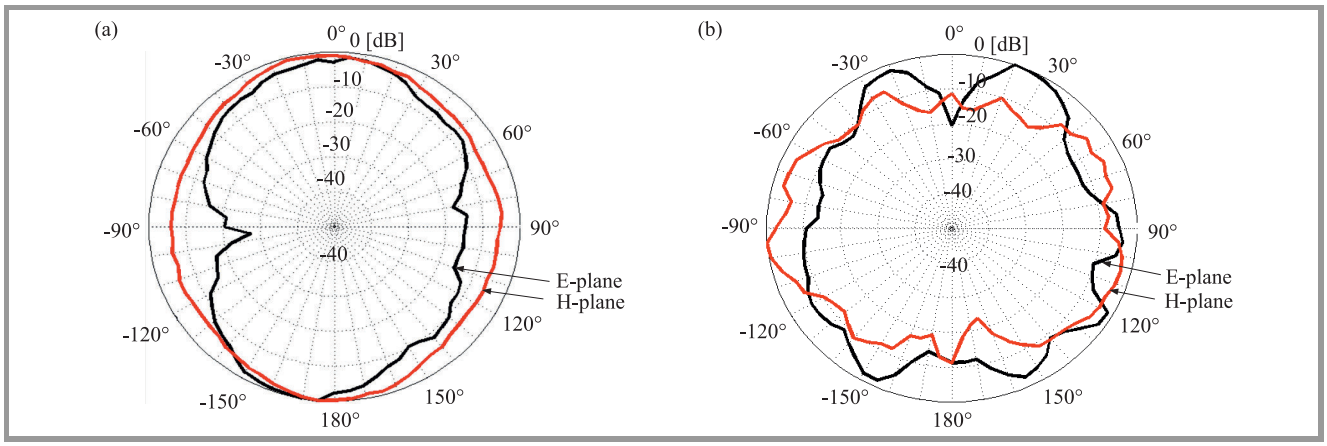


*Fig. 7.* E-plane and H-plane radiation pattern of RC bowtie at: (a) 1 GHz and (b) 2.5 GHz.

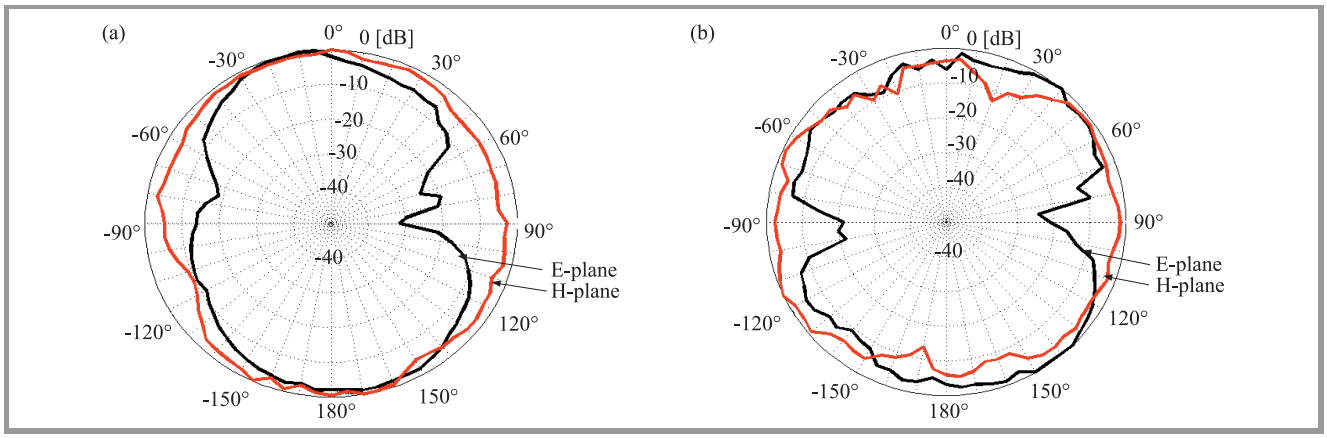


*Fig. 8.* E-plane and H-plane radiation pattern of loop bowtie at: (a) 1 GHz and (b) 2.5 GHz.

## 4. Results of GPR Experiments

Our experimental GPR comprises a portable Vector Network Analyzer (VNA) and a single antenna for transmission and reception of signals. The antenna is used without any reflector. The photograph of the setup is shown in Fig. 9. The transmitting/receiving antenna is connected to port 1 of the VNA. The frequency is swept from 300 MHz to 3 GHz, in steps of 4.5 MHz. Complex reflection coefficient data are acquired at a spatial interval of 2 cm, along a horizontal line. Each instance of measurement is called one A-scan. Inverse Fourier transform of the collected frequency domain data gives the time domain data. Ensemble of A-scans along a line gives the B-scan image of the target. The clutter in the image is removed by a simple averaging procedure, as outlined in [13].

To compare the performance of the antennas, GPR surveys were carried out to detect four types of targets:

1. a brass pipe of diameter 2.54 cm,
2. a galvanized iron pipe of diameter 5.08 cm,
3. a dry bamboo of diameter 7 cm and,
4. reinforcement bars inside concrete.

The depth of the target is about 40 cm from the antenna in the first three cases. In the fourth experiment, the depth of


*Fig. 9.* Photograph of the experimental GPR.

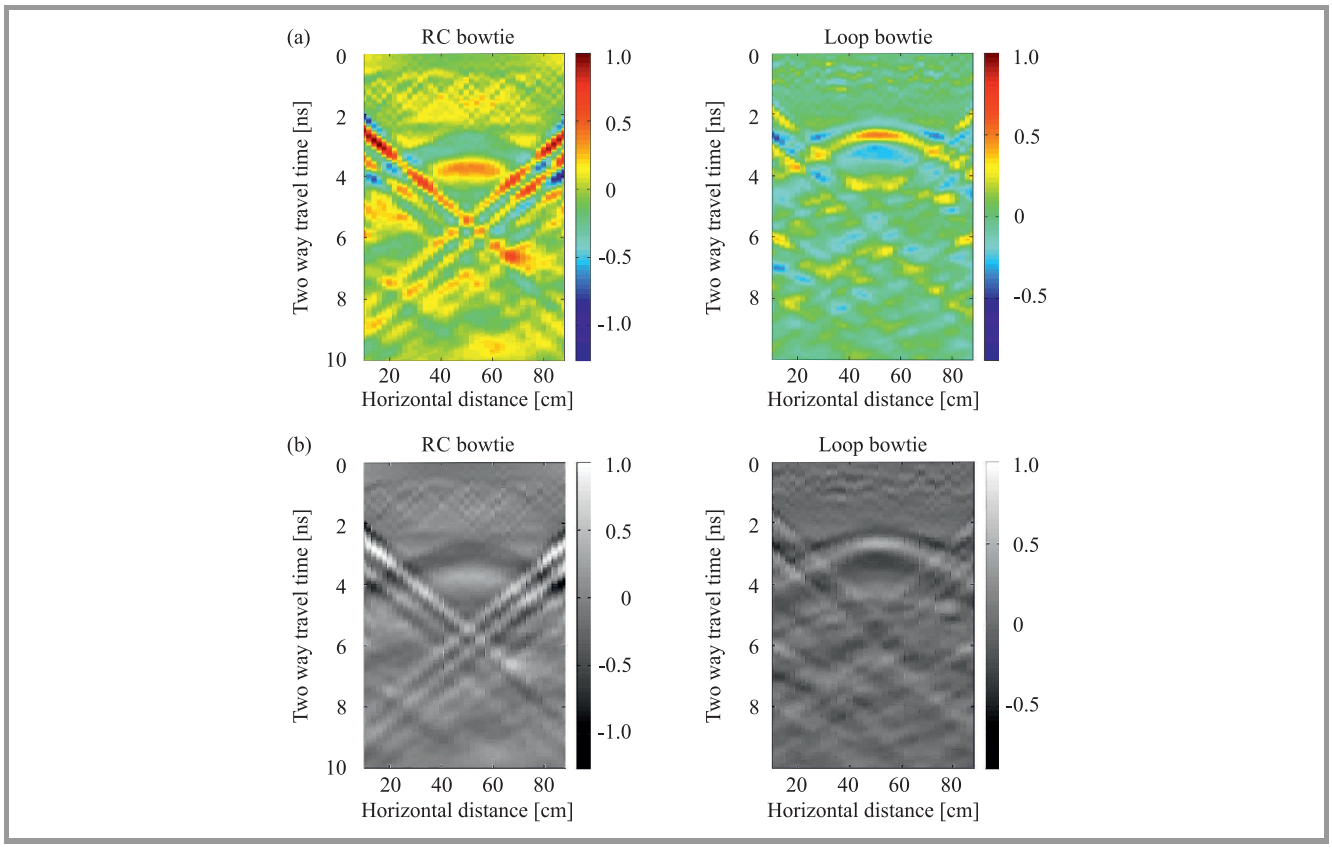


***Fig. 10.*** Color (a) and gray scale GPR images of brass pipe (b). (See color pictures online at www.nit.eu/publications/journal-jtit)

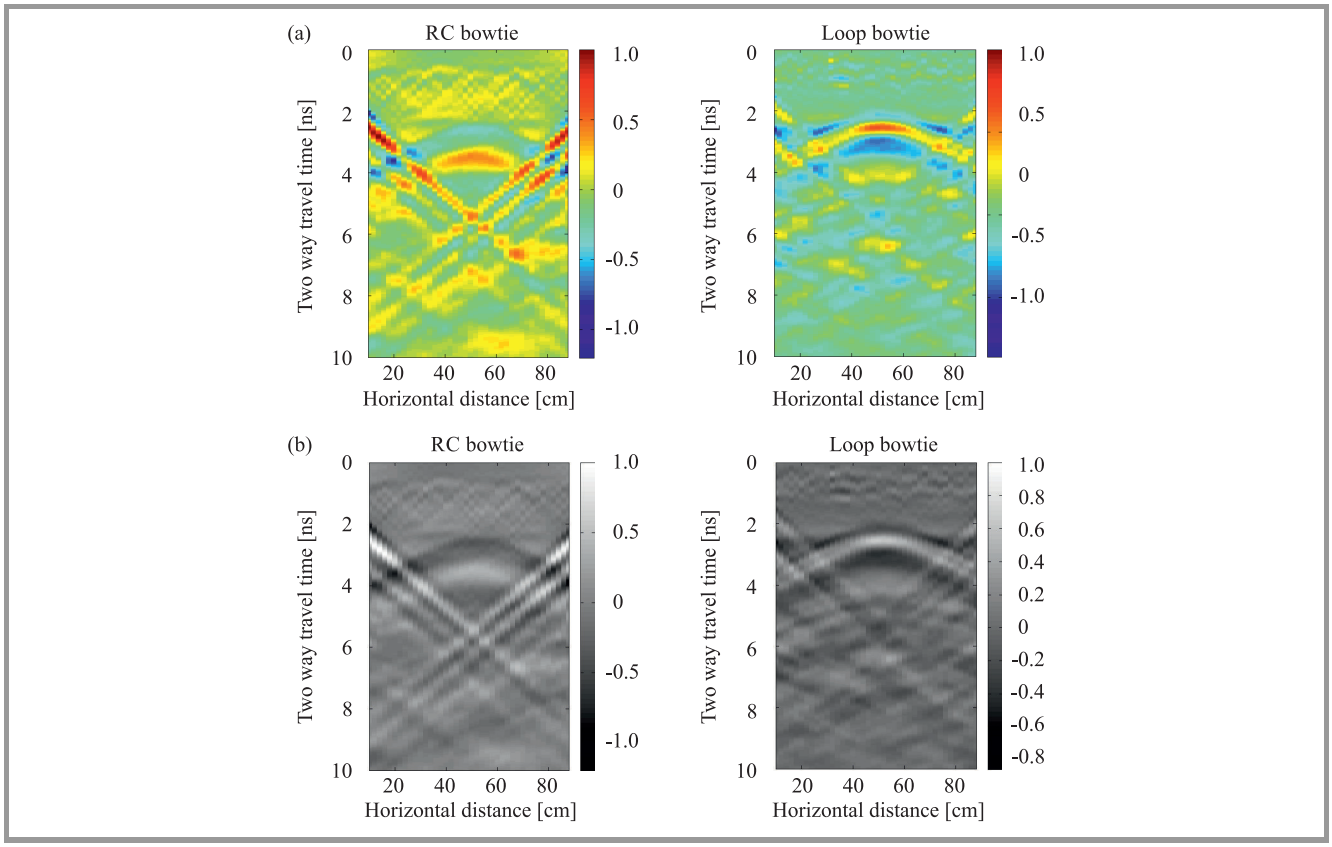


***Fig. 11.*** Color (a) and gray scale GPR images of galvanized iron pipe (b).

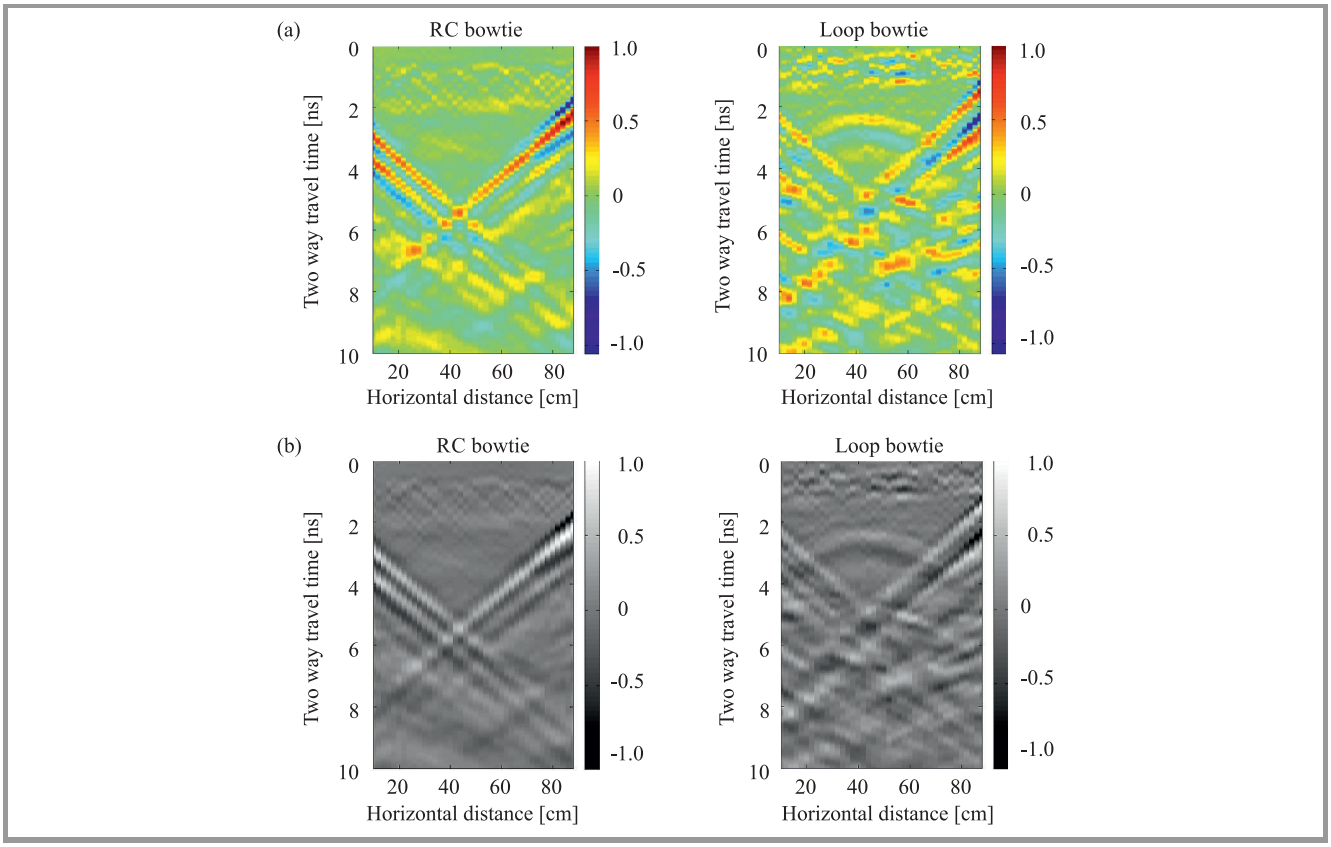


*Fig. 12.* Color (a) and gray scale GPR images of dry bamboo (b).

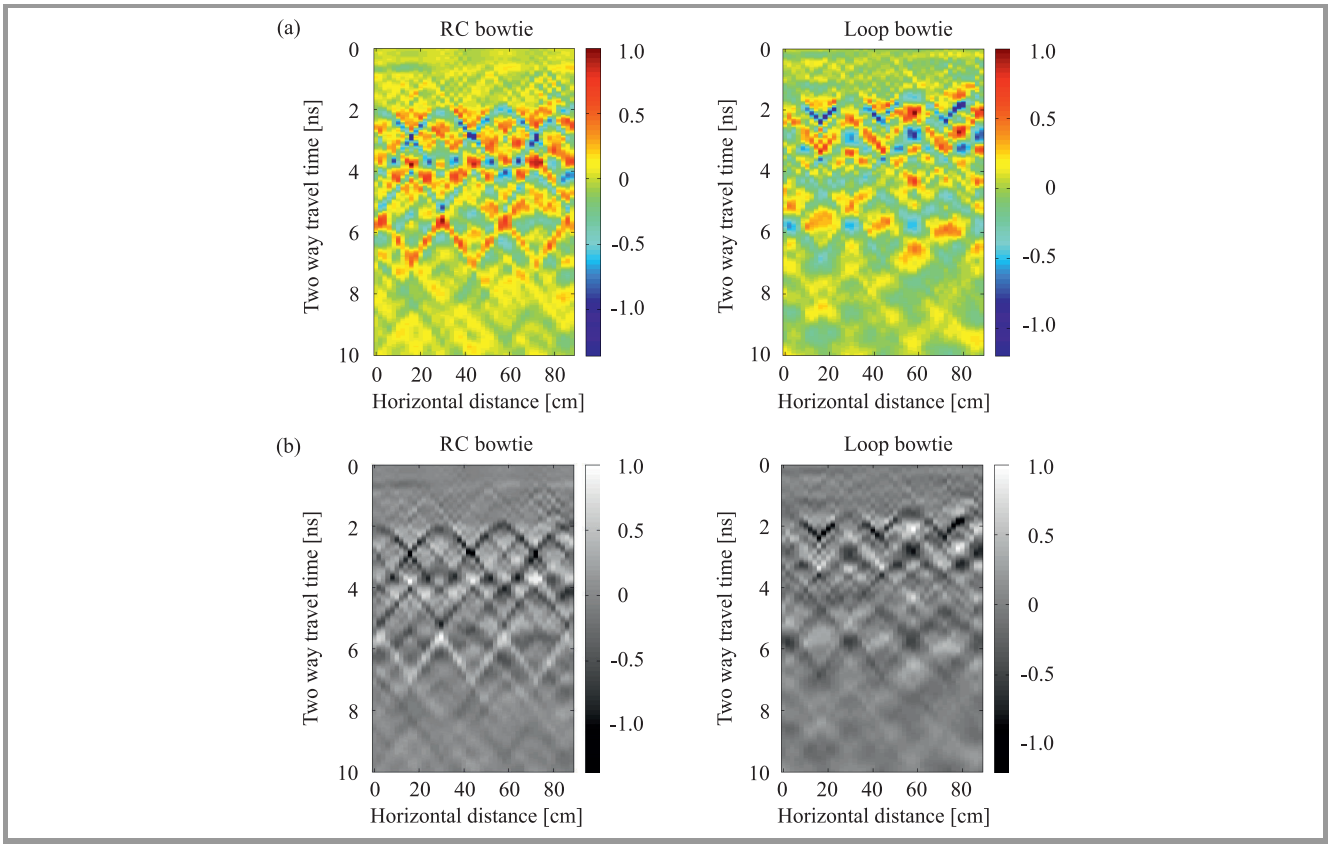


*Fig. 13.* Color (a) and gray scale GPR images of reinforcement bars in concrete (b).

the rebar and the distance between the bars are not known to us. Due to the fact that the bowtie antenna is linearly polarized, the antenna axis is aligned with the target to maximize the return signal.

Let us start with results obtained in the first experiment, i.e. when the target was a brass pipe. Figure 10 shows the GPR images in color and gray scale. The target is located at the apex of the hyperbola, about 50 cm on the horizontal axis. It can be seen that the image produced by the loop bowtie is sharper and more clutter free, compared to that produced by the RC bowtie.

In the second experiment, the target was a galvanized iron pipe of diameter 5.08 cm. Figure 11 shows the detected image of the pipe. In this case, too, a better image is obtained with the loop bowtie compared to the RC bowtie.

In the third experiment, the target was a dry bamboo. The GPR images are shown in Fig. 12. In the previous cases, the targets were metallic, hence reflections from the targets were high. But, in this case, there is a dielectric target and the dielectric contrast between the target and the surrounding medium is smaller. So, the reflections from the target are rather weak. From the figure, it is observed that RC bowtie could not produce an image of the target. Even in this case, the image produced by loop bowtie has been exemplary. So, a potential application of the loop bowtie antenna may be in detection of non-metallic landmines.

In the fourth experiment, a GPR survey of concrete roof was conducted in order to detect the rebar inside. The image obtained is shown in Fig. 13. The reinforcement bars separated by a distance of about 25 cm are visible in the image. In the case of the RC bowtie, there are multiple hyperbolas below the actual location of rebar. With the loop bowtie, those clutters are not much visible in the image.

## 5. Conclusion

The performance of two types of antennas for GPR: a RC loaded bowtie and a novel loop bowtie, has been experimentally studied and compared. GPR images produced by the loop loaded antenna turned out to be better than those produced by the RC loaded bowtie, for all the test targets considered. The loop loading technique can be employed in existing antennas also, to enhance the radiation properties. The results presented in this paper emphasize the role of efficient antennas for improved GPR detection capability. This also signifies the importance of more research required to design efficient ultra-wideband antennas at sub-gigaherz frequencies, for GPR and similar applications.

## Acknowledgements

We thank the Guest Editors Lara Pajewski, Hovik Baghdasaryan and Marian Marciniak for inviting us to participate in the JTIT Special Issue “Recent Progress in Electromagnetic Theory and its Applications”, organized by the COST Action TU1208 “Civil engineering applications of Ground Penetrating Radar”.

## References

[1] A. Benedetto and L. Pajewski, Eds., *Civil Engineering Applications of Ground Penetrating Radar*. Book Series: “Springer Transactions in Civil and Environmental Engineering”. Springer International Publishing Switzerland, 2015.

[2] C. W. Chang, C. H. Lin, and H. S. Lien, “Measurement radius of reinforcing steel bar in concrete using digital image GPR”, *Constr. and Build. Mater.*, vol. 23, no. 2, pp. 1057–1063, 2009.

[3] S. Hong, W. W.-L. Lai, G. Wilsch, R. Helmerich, R. Helmerich, T. Günther, and H. Wiggenhauser, “Periodic mapping of reinforcement corrosion in intrusive chloride contaminated concrete with GPR”, *Constr. and Build. Mater.*, vol. 66, pp. 671–684, 2014.

[4] C. J. Vaughan, “Ground Penetrating Radar surveys used in archaeological investigations”, *Geophys.*, vol. 51, no. 3, pp. 595–604, 1986.

[5] T. Montoya and G. Smith, “Land mine detection using a groundpenetrating radar based on resistively loaded Vee dipoles”, *IEEE Trans. on Antenn. and Propag.*, vol. 47, no. 12, pp. 1795–1806, 1999.

[6] H. M. Jol, *Ground Penetrating Radar Theory and Applications*. Elsevier Science, 2008.

[7] A. Lestari, A. Yarovoy, and L. Ligthart, “RC-loaded bow-tie antenna for improved pulse radiation”, *IEEE Trans. on Antenn. and Propag.*, vol. 52, no. 10, pp. 2555–2563, 2004.

[8] A. A. Lestari, A. G. Yarovoy, and L. P. Ligthart, “Adaptive wire bow-tie antenna for GPR applications”, *IEEE Trans. on Antenn. and Propag.*, vol. 53, no. 5, pp. 1745–1754, 2005.

[9] A. A. Lestari, E. Bharata, A. B. Suksmono, A. Kurniawan, A. G. Yarovoy, and L. P. Ligthart, “A modified bow-tie antenna for improved pulse radiation”, *IEEE Trans. on Antenn. and Propag.*, vol. 58, no. 7, pp. 2184–2192, 2010.

[10] K. K. Ajith and A. Bhattacharya, “Printed compact lens antenna for UHF band applications”, *Progress in Electromag. Res. C*, vol. 62, pp. 11–22, 2016.

[11] K. K. Ajith and A. Bhattacharya, “Improving the detectability and imaging capability of ground penetrating radar using novel antenna concepts”, in *EGU General Assembly Conference Abstracts*, ser. EGU General Assembly Conference Abstracts, vol. 19, Apr. 2017, p. 7562.

[12] C. A. Balanis, *Antenna Theory: Analysis and Design*. Hoboken, NJ: Wiley, 2005.

[13] D. J. Daniels, Ed., *Ground Penetrating Radar*. The Institution of Engineering and Technology, Michael Faraday House, Six HillsWay, Stevenage SG1 2AY, UK: IET, Jan 2004.

**K. K. Ajith** received his B.Tech. degree from Kannur University and M.Tech. degree from Cochin University of Science and Technology in 2006 and 2009 respectively. He worked as Assistant Engineer (Electrical) at Kerala State Electricity Board from Nov. 2009 to Dec 2011. Since 2011, he is pursuing Ph.D. at Indian Institute of Technology Kharagpur. He is working as an Assistant Professor at department of ETC, IIIT Bhubaneswar since Dec. 2016. His areas of interests are: printed antennas, metamaterials and GPR.

E-mail: ajithkkoroth@gmail.com
Department of ETC
International Institute of Information Technology
Bhubaneswar
751003, India

**Amitabha Bhattacharya** received the B.Tech., M.E. and Ph.D. degrees in Electronics and Electrical Communication Engineering from I.I.T. Kharagpur, Jadavpur University, Calcutta, and I.I.T. Kharagpur, in- 1986, 1994, and 1998, respec–tively. Since July 2007, he has been with the I.I.T Kharagpur, where he is now an Associate Professor of Electronics and Electrical Communication Engineering. His present research interest is in the field of microwave imaging, GPR systems analysis and EM propagation.

E-mail: amitabha@ece.iitkgp.ernet.in
Department of E & ECE
Indian Institute of Technology Kharagpur
721302, India

Paper

# Analytical Investigation on a New Approach for Achieving Deep Penetration in a Lossy Medium: The Lossy Prism

Fabrizio Frezza[1], Patrizio Simeoni[2], and Nicola Tedeschi[1]

[1] *Department of Information Engineering, Electronics and Telecommunications, Sapienza University of Rome, Rome, Italy*
[2] *Transport Infrastructure Ireland (TII), Dublin, Ireland*

https://doi.org/10.26636/jtit.2017.119917

**Abstract—Recent studies highlighted deep-penetration properties of inhomogeneous waves at the interface between a lossless and a lossy medium. Such waves can be generated by means of radiating structures known as Leaky-Wave Antennas (LWAs). Here, a different approach is proposed based on the use of a lossy prism capable to generate an inhomogeneous wave when illuminated by a homogeneous wave. The lossy prism is conceived and designed thinking of Ground-Penetrating Radar (GPR). The results achieved by the lossy prism will be compared with those obtained by means of a previously designed LWA that was created with the identical objective. The approach of this paper is purely theoretical, and it aims at providing basic ideas and preliminary results useful for an innovative LWA design.**

***Keywords—deep-penetration, Ground Penetrating Radar, leaky-wave antennas.***

## 1. Introduction

The penetration depth is a very important parameter in many fields of applied electromagnetism, and particularly in Ground Penetrating Radar (GPR) applications where highly lossy media are often encountered. A typical technique to increase penetration employed in GPR surveys is the reduction of the operating frequency: this implies lower resolution [1]. An alternative approach, where applicable, requires the employment of ground-coupled antennas [2]. Those antennas increase the coupling with the soil avoiding the first reflection at the interface between air and soil and potentially reducing the speed of a survey. Ground-coupled antennas do not resolve the issue of sub-soil lossy materials.

In this paper we propose a particular configuration of a structure, named lossy prism, as an alternative technique for increasing the penetration. The lossy prism is a two-dimensional structure with two non-parallel, planar and infinite interfaces proposed in [3] that allows the generation of inhomogeneous waves. The lossy prism, designed here, radiates an inhomogeneous wave in air to meet the deep-penetration theory requirements. The proposed structure is therefore a preliminary input for the development of an air-coupled antenna, which increases the penetration depth without the need of reducing the operating frequency. The deep-penetration condition was first defined in [4] for a plane wave incoming from a lossless medium and impinging on a separation surface with a lossy medium. This condition occurs when the attenuation vector of the transmitted wave in the lossy medium is parallel to the separation surface between lossless and lossy media. Mandatory requirements for the deep-penetration condition are: inhomogeneous incident wave incoming from a lossless medium, oblique incidence, and an amplitude of the incident phase vector (or attenuation vector) greater than or equal to a given minimum value.

The article is divided into three main sections. In Section 1 a literature background on the deep-penetration effect is illustrated. Section 2 describes the lossy prism design proposed here and illustrates its potential in terms of penetration increase. Finally, conclusions are given in Section 3.

## 2. Overview on Previous Research Activities

### *2.1. Deep-penetration Condition and Large Penetration*

In a lossless medium two plane-wave solutions are possible: a conventional homogeneous wave, with a real wave vector $\underline{k}$, and an inhomogeneous wave, where the wave vector $\underline{k}$ is complex and can be expressed as a superposition of two real vectors, the phase vector $\underline{\beta}$ and the attenuation vector $\underline{\alpha}$; those vectors must be orthogonal to each other [5].

Let us take an inhomogeneous wave incoming from a lossless medium, said medium 1, and impinging on a lossy medium said medium 2, as illustrated in Fig. 1. The wave vector of the incident wave is $\underline{k}_1 = \underline{\beta}_1 - j\underline{\alpha}_1$ and the wave vector of the transmitted wave is $\underline{k}_2 = \underline{\beta}_2 - j\underline{\alpha}_2$. Let us now define with $\xi_1$ the angle that the phase vector of the incident wave $\underline{\beta}_1$ forms with the normal to the interface between air and lossy medium. The theory developed in [4], [6] demonstrates that, when $\xi_1$ is smaller than or equal to 45° it is

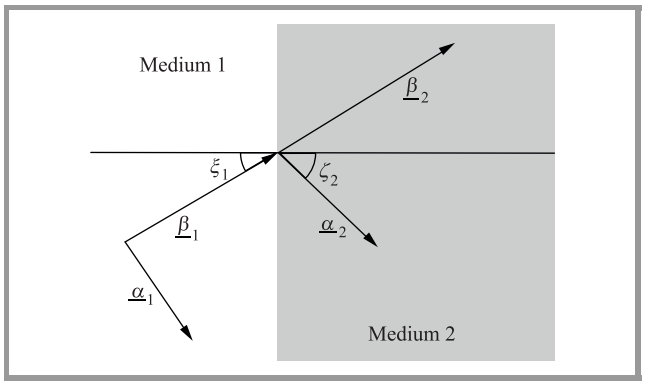


***Fig. 1.*** Deep-penetration problem definition: inhomogeneous plane wave incoming from a lossless medium (medium 1) and impinging on the infinite and planar separation surface with a lossy medium (medium 2).

possible to find a critical value $\beta_{1c}$ for the amplitude of $\underline{\beta}_1$ such that the angle $\zeta_2$ formed by $\underline{\alpha}_2$ with the normal to the separation surface is 90° (deep-penetration condition), this happens for a critical incident angle $\xi_1 = \xi_{1c}$. For a given $\beta_{1c}$, the smaller the angle $\xi_1 < \xi_{1c}$, the worse the penetration. The deep-penetration condition can be met for smaller angles by increasing the amplitude of $\underline{\beta}_1$ (and consequently of $\underline{\alpha}_1$), anyway this condition can never be satisfied for normal incidence. Even when deep-penetration condition cannot be met, large penetration through inhomogeneous waves is always possible, because, if a homogeneous wave impinges on a separation surface with a lossy medium, the attenuation vector of the transmitted wave is necessarily orthogonal to the separation surface ($\zeta_2 = 0$). However, if the incident wave is inhomogeneous, the attenuation vector cannot be orthogonal because there is a tangential component to the interface with the lossy medium that has to be necessarily conserved ($\zeta_2 > 0$). This is due to the well-known conservation of the tangential component of the electromagnetic field at a planar boundary between two media [5].

### *2.2. Large EM Penetration Employing Leaky-wave Antennas*

Possible physical solutions for inhomogeneous waves at infinite planar boundaries between lossless and lossy media are represented by lateral waves, surface waves and leaky waves. The last ones represent the only suitable solutions for deep penetration because they can effectively radiate in the lossy medium [7]. Leaky waves can be artificially generated by structures called leaky-wave antennas (LWAs) [8].

The large penetration achievable employing LWAs is a subject well known in the literature. In [9], [10] researchers designed LWA applicators, which guaranteed large penetration, and in [11], a wave was generated by means of a periodical, bi-dimensional, LWA structure operating at microwave frequencies (X band) to prove that the existence of an attenuation vector of the incident wave leads to large penetration also in practical applications.

In [11], the antenna proposed in [12] was designed on CST software to radiate at broadside, and to impinge on a lossy medium represented by a prism having one face parallel to the antenna aperture.

The amplitude of the electric field in the lossy medium was then compared against the E field transmitted into the same medium by a customary horn antenna.

The results of this preliminary investigation were interesting. The antenna presented a slightly larger penetration than the one produced by the horn antenna, but the deep-penetration condition could not be achieved because of the normal incidence. Moreover, even increasing the incidence angle, the deep-penetration condition could not be met. This is mainly due to the very low amplitude of the attenuation vector for the antenna chosen [12].

An alternative antenna design was proposed in [13] to allow the deep-penetration condition. The designed antenna was based on uniform and mono-dimensional LWAs, in particular, a microstrip LWA [14] derived from the Menzel antenna [15] was considered and designed using the method proposed in [16]. The antenna, originally designed by Menzel, had its maximum beam angle at 41°, with $\beta_{1n} = \frac{\beta_1}{k_0} = 1.0025$ and $\alpha_{1n} = \frac{\alpha_1}{k_0} = 0.0528$: such a value was considered very high, in comparison with values often used in LWA design, by Oliner and Lee in [14], but this value was not sufficient for deep-penetration. Therefore in [13] the design of the antenna was optimised for deep penetration, obtaining $\beta_{1n} = 1.0028$ at a maximum radiation angle of 45°. This value, according to Eqs. (12)–(13) of [4] allowed the deep-penetration condition on a medium with conductivity $\sigma_2 = 0.05$ S/m.

While we cannot exclude the possibility of realizing a conventional LWA [8], [17] that may provide even higher amplitudes of attenuation and phase vectors, the design proposed in [13] shows evident limits in the deep penetration achievable by means of a uniform LWA. Therefore, we propose a different, innovative approach that promises better results.

## 3. The Lossy Prism

Historically, to the best of our knowledge, leaky waves artificially generated were exclusively produced by means of leaky-wave antennas, but recent papers tried to exploit the inhomogeneous-wave generation that can be obtained by irradiating a two-dimensional lossy dielectric structure with a homogeneous wave. Such a two-dimensional structure was first called in [3] lossy prism, and presents two non-parallel, planar and infinite interfaces (see Fig. 2).

In [18], the prism was illuminated by a finite beam treated in the optical approximation in order to neglect the interaction with the wedge of the prism. Moreover, the impact of the first reflection was considered, and it was pointed out that while multiple reflections could be neglected for the lossy nature of the prism, at least the first reflection should be taken into account.

In the approximation that assumes the beam width negligible in comparison with the prism dimensions, which is the situation illustrated in [18], it is possible to find geometrical requirements that allow the avoidance of multiple reflections like the ones experienced in such a paper.

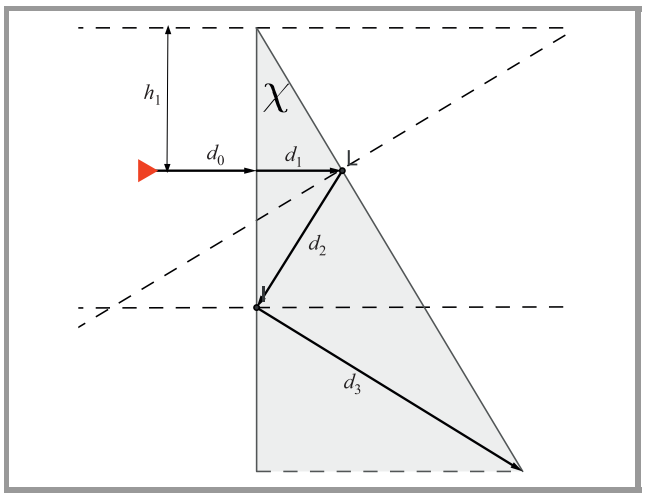


***Fig. 2.*** Lossy prism: paths followed by direct and reflected waves when $\chi < 90^\circ$ is the angle formed by the prism wedge.

In the case of normal incidence of the homogeneous wave upon the vertical side, the transmitted wave is always normal to the separation surface [5]. With reference to Fig. 2, where $d_1$ is the path followed by the direct-transmitted wave from the first to the second interface, and $d_2$ is the path followed by the first reflection, it comes out from simple trigonometrical relations [18]:

$$d_1 = h_1 \tan\chi\,, \tag{1}$$

$$d_2 = \frac{d_1}{\cos 2\chi}\,, \tag{2}$$

where $h_1$ indicates the distance between the wedge of the prism and the center of the incident beam.

When the amplitude of the wedge angle $\chi$ is greater than or equal to $45^\circ$, $d_2$ never returns back to the illuminated edge, but, if $\chi < 45^\circ$, this happens. Therefore also a second reflection, indicated with $d_3$ in Fig. 2, appears. Such a wave may reflect back to the oblique interface if the angle $\chi$ is smaller than $30^\circ$. The length of $d_3$ can easily be computed by observing the triangle formed by $d_2$ and $d_3$:

$$d_3 = d_2 \frac{\cos\chi}{\cos 3\chi} = \frac{[h_1 + d_1 \tan(2\chi)]\sin\chi}{\cos 3\chi}\,. \tag{3}$$

In Fig. 3 the normalized quantities $\frac{d_1}{h_1}$, $\frac{d_2}{h_1}$, and $\frac{d_3}{h_1}$ are plotted as a function of $\chi$ for $\chi \in ]0.25^\circ[$ and it is clear that the larger the angle $\chi$, the bigger the distance where the reflected rays will impinge on the prism edges.

An angle $\chi \geq 45^\circ$ must be chosen in order to avoid reflections. Anyway, the larger the angle $\chi$, the higher is $\frac{d_1}{h_1}$, therefore also the attenuation introduced on the illuminating beam increases when $\chi$ increases. The prism must be

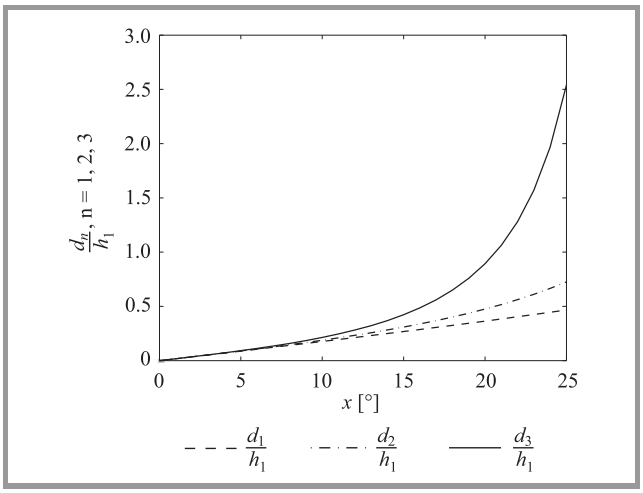


***Fig. 3.*** Lossy prism: normalized direct wave path ($\frac{d_1}{h_1}$), normalized first-reflection path ($\frac{d_2}{h_1}$), and normalized second-reflection path ($\frac{d_3}{h_1}$) for $\chi \in [0.25^\circ]$.

built using a low-loss medium. But, if the beam is narrow enough, it is possible to accept angles even smaller than $30^\circ$. In this case the second reflection can be neglected, but the first one, which is directed toward the illuminator, remains critical (see Fig. 3), and to avoid it the beam illuminating the lossy prism must impinge obliquely on the first prism face.

The angle $\chi$ is not the only parameter that allows to control reflections. In numerical simulations reflections can be neglected choosing suitable values for the medium characteristics of the lossy prism. A similar approach was taken in [11], [13], where unitary values for both permittivity and permeability of the lossy medium were chosen, and the conductivity $\sigma$ was assumed sufficiently low ($\sigma = 0.05$ S/m). This kind of medium adaptation is useful in numerical simulations, because it allows to isolate the transmission problem from the reflection problem, but such an approach may result in strong restrictions on the prototyping and manufacturing processes of the lossy prism.

In this study, we will impinge obliquely on the lossy prism and we will also choose a value for the $\chi$ angle that will allow to neglect internal reflections. The amplitudes of phase and attenuation vectors achievable employing this structure will then be compared against the corresponding values that can be obtained employing conventional LWAs. We know that, to obtain deep penetration, the amplitude of the attenuation vector needs to be greater than a minimum value [4], but LWAs are usually designed to produce efficient beams with a negligible amplitude of the attenuation vector ($\alpha_1 << k_0$ [8], [17]), this makes the design of a deeply penetrating antenna by means of commonly used LWAs very challenging, while the structure proposed here shows better results.

The first consideration that needs to be exposed when comparing the lossy prism and the LWA is that in the former losses are present in the material, while in the latter losses are mainly due to radiation (LWAs do not require a lossy

medium), and only a small quantity of energy is really dissipated (usually through a matched load posed at the end of the antenna).

In the following, we will neglect the effects of the prism wedge, this corresponds to assume that the lossy prism is larger than the antenna aperture. In the former assumption, also the hypothesis of infinite length for the lossy prism holds.

Equations (12)–(13) of [4] provide requirements in terms of amplitude of both phase vector and incident angle of an inhomogeneous wave incoming from a lossless medium to guarantee deep penetration on a lossy medium with given electromagnetic characteristics. An antenna designed for the deep-penetration condition needs to be able to radiate an inhomogeneous wave in a lossless medium, for instance a vacuum (air), such that the mentioned equations are satisfied. As a consequence, the structure proposed in this paper is designed to radiate in a vacuum. The amplitude of the phase vector generated by this structure is compared against the one obtained in [13] (that was also designed to radiate in a vacuum). A higher value of the phase vector, for a given incidence angle, implies higher penetration.

In the first part of this article the evaluation of the amplitude of phase and attenuation vectors shown in Fig. 4 will be studied considering exclusively the direct wave, while effects due to reflections will be analyzed at the end of this paper, in particular it will be shown that, in the proposed configuration, reflections can be neglected.

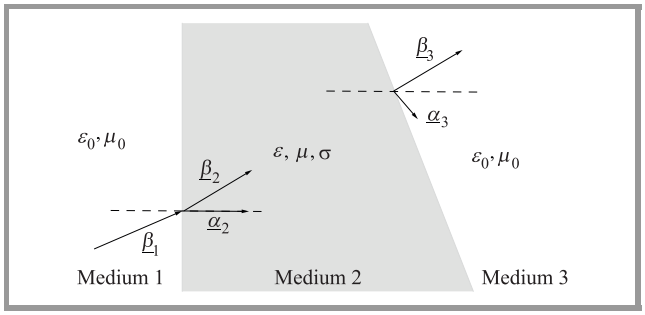


***Fig. 4.*** Propagation in a stratified medium, in which medium 1 and medium 3 are vacuum and the inner medium (medium 2) is a lossy medium; the two interfaces are not parallel, planar and infinite.

The lossy prism structure work principle is the conservation of the tangential component. Let us consider a stratified medium as illustrated in Fig. 4, in which medium 1 and medium 3 are vacuum and medium 2 is a lossy region. The permittivity and permeability of the surrounding-vacuum region are indicated respectively with $\varepsilon_0$ and $\mu_0$. The complex permittivity of the lossy prism is indicated as:

$$\varepsilon_{c2} = \varepsilon_2 - j\sigma_2/\omega = \varepsilon_0\varepsilon_{r2} - \frac{j\sigma_2}{\omega},$$

where $\sigma_2$ is the conductivity, $\omega$ the angular frequency, $\varepsilon_0$ the vacuum permittivity, and $\varepsilon_{r2}$ the relative permittivity. The permeability of medium 2 is $\mu_2 = \mu_0\mu_{r2}$, where $\mu_0$ is the vacuum permeability and $\mu_{r2}$ is the relative permeability.

Let us take a homogeneous wave incoming from medium 1 and impinging on an infinite planar interface with medium 2, with an incident angle $\xi_1$. The incident wave, characterized by a phase vector $\underline{\beta}_1 = \underline{k}$ produces a transmitted wave in the medium 2 that must have attenuation vector $\underline{\alpha}_2$ that forms an angle $\zeta_2' = 0$ with the normal to the separation surface, because there is no tangential component of the incident wave that can be conserved. The transmitted wave is also characterized by a phase vector $\underline{\beta}_2$. The angle $\xi_2'$ that this wave vector forms with the normal to the separation surface depends on the media involved and on $\xi_1$ (for angles definition see Fig. 5).

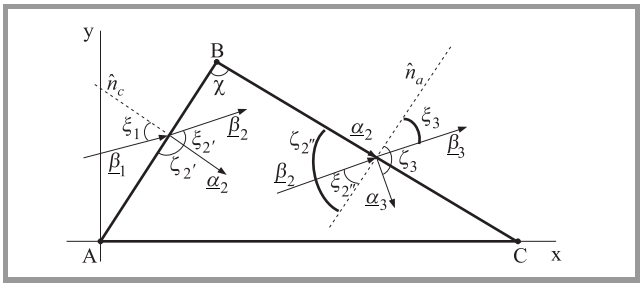


***Fig. 5.*** Propagation in a prism in which $\chi = 90°$: the wedge is shown here only to give evidence of the structure, anyway it is considered far from the source in the real scenario, $\overline{BC}$ and $\overline{AB}$ are assumed of infinite length (or sufficiently larger than the antenna aperture).

Let us now define with $k_{1t}$ the amplitude of the tangential component to the first interface with the prism of the incident wave vector $\underline{k}_1$. We can then evaluate the amplitudes of phase and attenuation vectors inside the prism employing Eqs. (13) and (14) of [19], that we report here:

$$\beta_2 = \sqrt{\frac{|k_{1t}|^2 + \mathrm{Re}(k_2^2) + |k_{1t}^2 - k_2^2|}{2}}, \tag{4}$$

$$\alpha_2 = \sqrt{\frac{|k_{1t}|^2 - \mathrm{Re}(k_2^2) + |k_{1t}^2 - k_2^2|}{2}}. \tag{5}$$

So, now there is a need to evaluate an expression of phase and attenuation vectors for the wave transmitted in the lossless medium 3.

Let us imagine that the inhomogeneous wave, described by Eqs. (4)–(5), reaches the other side of the lossy prism impinging on the separation surface with medium 3, which is assumed again a vacuum. This time, assuming that the separation interface is not parallel to the one between medium 1 and medium 2, the incident angle of $\underline{\beta}_2$ must be $\xi_2'' \neq \xi_2'$ and also the incident angle of $\underline{\alpha}_2$ needs to be $\zeta_2'' \neq 0$. Then a tangential component of the attenuation vector must exist at the interface and it needs to be conserved. As a result, the transmitted wave in the vacuum is, this time, inhomogeneous, and characterized by a phase vector $\underline{\beta}_3$ and an attenuation vector $\underline{\alpha}_3$ that form an angle $\theta_3 = 90°$, i.e.

called $\xi_3$ and $\zeta_3$ the angles that phase and attenuation vectors form with the normal to the separation surface, it needs to be $\xi_3 \pm 90^\circ = \zeta_3$.

Medium 3 does not introduce any losses, therefore the maximum value of the attenuation vector is obtained when $\underline{\alpha}_2$ is fully conserved. This happens when $\chi = 90^\circ$.

If the two faces of the lossy prism are parallel, then the incident wave in Medium 1 and the transmitted wave in medium 3 are both homogeneous. Therefore the attenuation vector $\underline{\alpha}_2$ created by the introduction of lossy medium 2, does not imply the existence of an attenuation vector $\underline{\alpha}_3$ in medium 3, and the wave produced in medium 3 is homogeneous. On the opposite, if the two faces form an angle of 90°, then $\underline{\alpha}_2$, being normal to the first face, needs to be parallel to the second one: therefore it is fully conserved. This is the case in which we fully exploit the $\underline{\alpha}_2$ vector generated in medium 2, and therefore this is the most interesting case for deep-penetration studies: the lossy prism needs to be modeled as in Fig. 5.

In Fig. 5, the wedge is drawn for clarity, but in a possible near-field simulation carried to verify the effect, the radiating aperture should not see the wedge, so that wedge effects can be avoided.

Let us apply the generalized Snell law:

$$\begin{cases} \beta_1 \sin\xi_1 = \beta_2 \sin\xi_2' \\ \beta_2 \sin\xi_2'' = \beta_3 \sin\xi_3 \\ \alpha_2 \sin\zeta_2'' = \alpha_3 \sin\zeta_3 \end{cases} . \tag{6}$$

From the conservation of the tangential component, and from $\chi = 90^\circ$, it follows:

$$\begin{cases} \zeta_2' = 0 \\ \zeta_2'' = 90^\circ \\ \xi_2'' = 90^\circ - \xi_2' \\ \zeta_3 + \xi_3 = 90^\circ \end{cases} . \tag{7}$$

Substituting the values of Eqs. (7) in Eqs. (6), we find:

$$\begin{cases} \beta_1 \sin\xi_1 = \beta_2 \sin\xi_2' \\ \beta_2 \cos\xi_2' = \beta_3 \sin\xi_3 \\ \alpha_2 = \alpha_3 \cos\xi_3 \end{cases} . \tag{8}$$

Applying the dispersion relation to the media of interest [5]:

$$\begin{cases} \beta_1^2 = k_0^2 = \omega^2 \varepsilon_0 \mu_0 \\ \beta_3^2 - \alpha_3^2 = \omega^2 \varepsilon_0 \mu_0 \\ \beta_2^2 - \alpha_2^2 = \omega^2 \mu_2 \varepsilon_2 \\ \beta_2 \alpha_2 \cos\xi_2' = \dfrac{\omega \mu \sigma_2}{2} \end{cases} . \tag{9}$$

Now, we can put the second and the third of Eqs. (8) in the fourth of (9), obtaining:

$$\beta_3 \alpha_3 \sin(2\xi_3) = \omega \mu_2 \sigma_2 \ . \tag{10}$$

The above equation allows to evaluate the amplitude of the $\xi_3$ angle, the expression of which was already found in Eq. (12) of [4]. The amplitude of $\xi_3$ is reported here for completeness:

$$\xi_3 = \frac{1}{2} \arcsin \frac{\omega \mu_2 \sigma_2}{\alpha_3 \beta_3} . \tag{11}$$

Putting the second of Eqs. (9) in Eq. (10), instead, values of $\beta_3$ and $\alpha_3$ can be found as a function of $\xi_3$ and the conductivity of the medium 2. For $\beta_3$ it is:

$$\frac{\beta_3}{k_0} = \frac{1}{\sqrt{2}} \sqrt{1 + \sqrt{1 + \left[ \frac{2\sigma_2}{\omega \varepsilon_0 \sin(2\xi_3)} \right]^2}} , \tag{12}$$

having assumed $\mu_2 = \mu_0$ (non-magnetic medium). These equations are the complementary of Eqs. (12)–(13) presented in [4]. In that paper the incidence from lossless to lossy media was presented, here the opposite.

The value for $\frac{\alpha_3}{k_0}$ simply follows from the second of Eqs. (9):

$$\frac{\alpha_3}{k_0} = \frac{1}{\sqrt{2}} \sqrt{\sqrt{1 + \left[ \frac{2\sigma_2}{\omega \varepsilon_0 \sin(2\xi_3)} \right]^2} - 1} . \tag{13}$$

The inhomogeneous wave generated in medium 3 has larger $\beta_3$ and $\alpha_3$ values for higher $\sigma_2$ values. Therefore, in principle, if there is enough power provided to the lossy prism, it is sufficient to increase the $\sigma_2$ value to obtain the wished $\beta_3$ amplitude.

In particular, we can compare the results obtained through this lossy prism configuration against the antenna presented in [13]. The minimum value of $\beta$ that allows deep-penetration effect is found by imposing $\sin(2\xi_3) = 1$, i.e. $\xi_3 = 45^\circ$. In this condition, putting $\sigma_2 = 0.008$ S/m at a frequency of 12 GHz we obtain $\beta_{3n} = \frac{\beta_3}{k_0} \geq 1.00282$. Larger values can be obtained either increasing the angle $\xi_3$ (by means of suitably impinging with the angle $\xi_1$), or increasing the conductivity of the lossy prism.

The small amplitude of $\sigma_2$ obtained is sufficient to guarantee a larger phase vector amplitude than the one obtained with the microstrip leaky-wave antenna optimized for deep-penetration in [13].

Finally, the angle $\xi_1$ can be analytically determined as a function only of the quantities in the medium 3. Squaring the first and the second of Eqs. (8) and summing them together yields:

$$\beta_1^2 \sin^2\xi_1 + \beta_3^2 \sin^2\xi_3 = \beta_2^2 ,$$

but $\beta_1^2 = k_0^2$ and $\beta_2^2 = \omega^2 \mu_2 \varepsilon_2 + \alpha_3^2 \cos^2\xi_3$, so, in the case in which medium 3 is non magnetic:

$$\xi_1 = \arcsin \sqrt{\varepsilon_{r2} + \beta_{3n}^2 \cos(2\xi_3) - \cos^2\xi_3} . \tag{14}$$

having introduced the normalized quantity $\beta_{3n}$ defined as $\beta_{3n} = \frac{\beta_3}{k_3} = \frac{\beta_3}{k_0}$.

For the illustrated scenario, where $\xi_3 = 45^\circ$ is wished, it is:

$$\xi_1 = \arcsin \sqrt{\varepsilon_{r2} - 0.5} . \tag{15}$$

The above condition is valid for every $\varepsilon_{r2}$ such that $0.5 \leq \varepsilon_{r2} \leq 1.5$. In particular, if $\varepsilon_{r2} = 1$, the incident angle is $\xi_1 = 45^\circ$ as it should be expected due to the continuity of the dielectric constant in this scenario.

In Fig. 6 it is illustrated how the radiation angle is dependent on the normalized amplitude of the attenuation vector $\beta_{3n} \in [1.1, 1.8]$ when $\varepsilon_{r2} = 1$. The curve $\xi_3 = \xi_3(\xi_1)$ tends to a constant value when $\beta_{3n}$ increases (in the case considered, for which $\varepsilon_{r2} = 1$, this value corresponds to 45°).

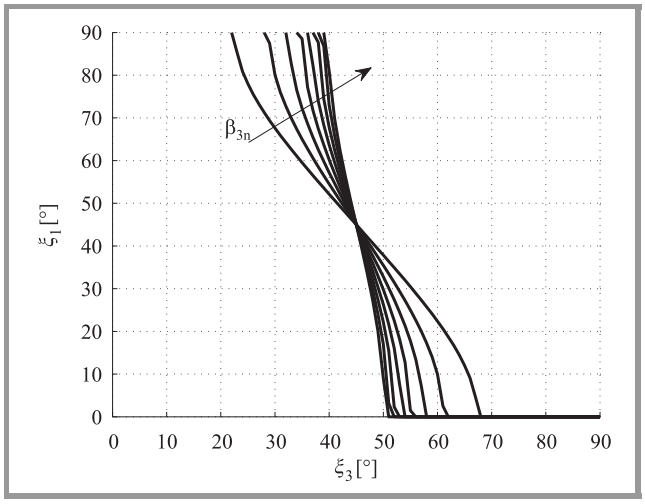


***Fig. 6.*** Curves described by $\xi_3$ when $\xi_1$ varies from 0 to 90° and $\beta_{3n} \in [1.1; 1.8]$, being $\varepsilon_{r2} = 1$.

The condition $0.5 \leq \varepsilon_{r2} \leq 1.5$ can be satisfied properly choosing the material. We can conclude therefore that $\xi_3 = 45^\circ$ does not represent an issue, and can always be found. This condition represents, according to [4], the incident angle that guarantees maximum penetration in a lossy medium, therefore we can pose a lossy medium parallel to the separation surface between medium 2 and medium 3 and expect maximum-penetration condition, reproducing the configuration that we proposed through the microstrip leaky-wave antenna in [13]. This setup represents, in fact, the easiest scenario for experimenting the deep penetration through numerical simulations.

For some GPR applications, the condition $\xi_3 = 0$ is required. This requirement does not allow the deep-penetration condition, but, employing inhomogeneous waves, a larger penetration is still achieved. Imposing $\xi_3 = 0$ in Eq. (14), the following is obtained:

$$\begin{aligned} \xi_1 &= \arcsin\sqrt{\varepsilon_{r2} + \beta_{3n}^2 - 1} \\ &= \arcsin\sqrt{\varepsilon_{r2} + \alpha_{3n}^2}\,. \end{aligned} \tag{16}$$

From Eq. (16), we can see that the $\xi_1$ angle is real only for materials such that $-(1-\alpha_{3n}^2) \leq \varepsilon_{r2} \leq 1-\alpha_{3n}^2$, and achievable at the microwave frequencies through metamaterials because they can expose relative permittivities either negative or smaller than 1 [20]. Note that $\xi_3 \approx 0$ can also be guaranteed by $\varepsilon_{r2} = 1$, if $\alpha_{2n}$ is small enough.

It is worth mentioning that the former equation is valid only as a limit, and therefore $\xi_3 = 0$ does not strictly represent a valid solution for Eqs. (12)–(14) because such condition would come from a multiplication by zero in Eqs. (8) and (10). $\xi_3 = 0$ can be studied, instead, imposing $\alpha_3 = \alpha_2$ (for the conservation of the tangential component). From the second of Eqs. (8), it follows $\xi_2'' = 0$, and therefore, $\xi_2' = 90^\circ$, which is possible when $\xi_1$ is the critical angle for total reflection. Therefore such a wave does not penetrate the prism.

In Fig. 7, different curves are shown for $\varepsilon_{r2} \in [0.2,\ 2]$ and $\beta_{3n} = 1.2$. In particular, we can see that the smaller is $\varepsilon_{r2}$, the closer $\xi_3$ is to broadside radiation (note that $\xi_3 = 0$ for broadside radiation while $\xi_3 = 90^\circ$ for a generated surface wave).

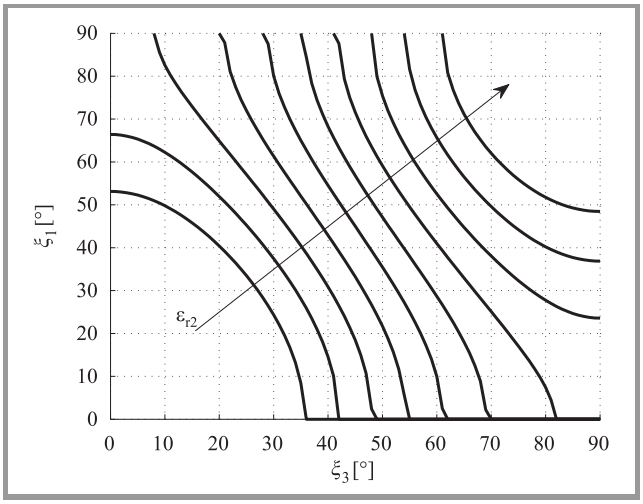


***Fig. 7.*** Curves described by $\xi_3$ when $\xi_1$ varies from 0 to 90° and $\varepsilon_{r2} \in [0.2,\ 2]$, being $\beta_{3n} = 1.2$.

Let us finally study the effects of the reflections produced at the interface between medium 2 and medium 3: the incident angle at such interface is $\xi_2'' = 90^\circ - \xi_2'$; consequently, because of Snell law, the reflected angle is equal, again, to $90^\circ - \xi_2'$. It follows that the angle formed by the incident and reflected waves is $\theta = 180^\circ - 2\xi_2'$. The reflected wave hits again the interface between media 1 and 2 only when $\theta + \xi_2' < 90^\circ$, therefore $180^\circ - \xi_2' < 90^\circ$, i.e. $\xi_2' > 90^\circ$. Hence, it is possible to confirm that with this configuration the reflected wave does not return back to the illuminated interface. Moreover, in the assumption of infinite edges, the reflected wave never hits the edge $\overline{AC}$ of Fig. 5, so the edge $\overline{AB}$ of Fig. 5 experiences only the presence of the direct wave. In normal scenarios, the edges $\overline{BC}$ and $\overline{AB}$ will need to be chosen long enough to avoid that the reflection occurring on $\overline{AC}$ would reach the $\overline{AB}$ and $\overline{BC}$ edges, again.

In the entire paper, we analyzed the prism from the point of view of the generated field. We optimized the prism structure to have negligible internal reflections, and to reduce the amplitude of multiple lobes of the radiated field. Doing so, we always neglected the wave eventually reflected by

the edge directly illuminated by the source. In applicative scenarios this first reflection cannot be neglected because it causes additional dispersion of power and, possibly, noise on the receiver, if this is in the path of the reflected wave. The noise in the receiver is avoided for $\xi_1 > 0$ if the receiver is small enough. The operative condition $\varepsilon_{r2} < \frac{4}{3}$ was found, and it was also highlighted that a value of conductivity $\sigma_2$ of few mS/m is sufficient to guarantee higher penetration than the one obtained through a conventional LWA. The choice of a lossy prism medium such that $\varepsilon_{r2} = 1$, and $\sigma_2$ of few thousands of S/m, can allow to neglect the reflection from the first side of the prism independently of the size of the transmitter and the incident angle $\xi_1$.

## 4. Conclusions

An innovative approach, based on the use of a lossy prism for increasing the penetration of electromagnetic waves in lossy media, was presented. This approach promises to guarantee deeper penetration than the one achievable through conventional leaky-wave antennas. In particular, the amplitudes of phase and attenuation vectors can be controlled not only operating on the angle of the prism, but also on its conductivity. This allows to obtain good penetration conditions even for values close to the normal incidence (note, anyway, that the attenuation vector in the lossy medium to be penetrated will hardly be parallel to the separation surface in this case).

In this preliminary study, a finite beam behaving as a plane wave was assumed as excitation, while a realistic feeding or guiding structure should be considered.

The lossy prism also produces losses, the effects of which may conflict with the deep-penetration property of the generated wave.

## Acknowledgement

The authors are deeply indebted to the GPR COST Action TU1208 and its network activities that made this study possible.

## References

[1] D. J. Daniels, *Ground Penetrating Radar*. Wiley, 2005.

[2] E. Eide, P. A. Våland, and J. Sala, "Ground-coupled antenna array for step-frequency GPR", in *15th Int. Conf. on Ground Penetrating Radar GPR 2014*, Brussels, Belgium, 2014, pp. 756–761.

[3] N. Tedeschi and F. Frezza, "An analysis of the inhomogeneous wave interaction with plane interfaces", in *General Assembly and Scient. Symp. URSI GASS 2014*, Beijing, China, 2014, pp. 109–112.

[4] F. Frezza and N. Tedeschi, "Deeply penetrating waves in lossy media", *Optics Lett.*, vol. 37, pp. 2616–2618, 2012.

[5] F. Frezza, *A Primer on Electromagnetic Fields*. Springer, 2015.

[6] F. Frezza and N. Tedeschi, "On the electromagnetic power transmission between two lossy media: discussion", *J. of the Opt. Soc. of America A*, vol. 29, no. 11, pp. 2281–2288, 2012.

[7] F. Frezza and N. Tedeschi, "Electromagnetic inhomogeneous waves at planar boundaries: tutorial", *J. of the Opt. Soc. of America A*, vol. 32, no. 8, pp. 1485–1501, 2015.

[8] A. A. Oliner and D. R. Jackson, "Leaky-Wave Antennas", in *Antenna Engineering Handbook*, 4th ed., J. Volakis, Ed. McGraw Hill Professional, 2007.

[9] L. Taylor, "Penetrating electromagnetic wave applicators", *IEEE Trans. on Antenn. and Propag.*, vol. 32, no. 10, pp. 1138–1141, 1984.

[10] G. d'Ambrosio and M. D. Migliore, "The grounded dielectric layer fed by a current line as a planar microwave applicator", *IEEE Trans. on Antenn. and Propag.*, vol. 42, no. 11, pp. 1467–1475, 1994.

[11] F. Frezza, S. Leo, F. Mangini, N. Tedeschi, and P. Simeoni, "Deep penetration in lossy media through non uniform electromagnetic waves", in *Proceedings of the Third Action's General Meeting*, L. Pajewski, A. Benedetto, A. Alani, and S. Lambot, Eds. London, UK: Aracne, March 2015; Rome, Italy: Aracne, May 2015.

[12] T. Zhao, D. R. Jackson, J. T. Williams, H. Y. D. Yang, and A. A. Oliner, "2-D periodic leaky-wave antennas – part I: metal patch design", *IEEE Trans. on Antenn. and Propag.*, vol. 53, pp. 3505–3514, 2005.

[13] P. Baccarelli, F. Frezza, P. Simeoni, and N. Tedeschi, "Inhomogeneous wave penetration in lossy media", in *Proc. Int. Symp. on Electromag. Theory EMTS 2016*, Espoo, Finland, 2016, pp. 797–799.

[14] A. A. Oliner and K. S. Lee, "Microstrip leaky wave strip antennas", in *Proc. of IEEE Int. Symp. on Antenn. and Propag. Soc.*, Philadelphia, PA, USA, 1986, pp. 443–446.

[15] W. Menzel, "A new travelling-wave antenna in microstrip", in *Proc. 8th Eur. Microwave Conf.*, Paris, France, 1978, pp. 302–306.

[16] P. Baccarelli, C. Di Nallo, S. Paulotto, and D. R. Jackson, "A full-wave numerical approach for modal analysis of 1D periodic microstrip structures", *IEEE Trans. on Microwave Theory and Techniq.*, vol. 54, pp. 1350–1362, 2006.

[17] D. R. Jackson and A. A. Oliner, "Leaky-wave antennas", in *Modern Antenna Handbook*, C. A. Balanis, Ed. New York: Wiley, 2008, pp. 325–367.

[18] N. Tedeschi, V. Pascale, F. Pelorossi, and F. Frezza, "Generation of inhomogeneous electromagnetic waves by a lossy prism", in *Proc. Int. Symp. on Electromag. Theory EMTS 2016*, Espoo, Finland, 2016, pp. 838–841.

[19] J. E. Roy, "New results for the effective propagation constants of nonuniform plane waves at the planar interface of two lossy media", *IEEE Trans. on Antenn. and Propag.*, vol. 51, pp. 1206–1215, 2003.

[20] C. Caloz and T. Itoh, *Electromagnetic Metamaterials: Transmission Line Theory and Microwave Applications*. Wiley, 2005.

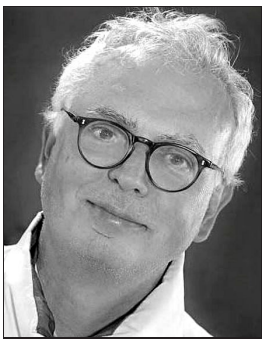

**Fabrizio Frezza** received the "Laurea" degree (cum laude) in Electronics Engineering and the Ph.D. degree in Applied Electromagnetics and Electrophysical Sciences from La Sapienza University of Rome, Italy, in 1986 and 1991, respectively. He joined the Department of Electronics, Sapienza University of Rome, in 1986, where he was a Researcher from 1990 to 1998, a Temporary Professor of Electromagnetic Fields from 1994 to 1998, and an Associate Professor from 1998 to 2004. He has been a Full Professor of Electromagnetic Fields with Sapienza

University of Rome since 2005. His current research interests include guiding structures, antennas and resonators for microwaves and millimeter waves, numerical methods, scattering, optical propagation, plasma heating, anisotropic media, artificial materials, and metamaterials.

E-mail: fabrizio.frezza@uniroma1.it
Department of Information Engineering, Electronics and Telecommunications
La Sapienza University of Rome
via Eudossiana 18
00184 Rome, Italy

**Patrizio Simeoni** received both the "Laurea" (degree) in Electronic Engineering and the Ph.D. in Mathematical Models for Engineering, Electromagnetics and Nanosciences from La Sapienza University of Rome, Italy. He worked as embedded, software and system engineer in both military and commercial environments from 2002. As a software engineer he developed firmware on both DSPs and Controllers, Device Drivers and user-level applications. As a system engineer he designed solutions for telecommunication and transport projects. His main research topic in electromagnetism is the study of electrotromagnetic wave penetration in lossy media. From 2012, he is employed in the National Transport Authority, Ireland, as senior technical engineer in the Integrated Ticketing System project.

E-mail: patrizio.simeoni@nationaltransport.ie
Transport Infrastructure Ireland (TII)
Parkgate Business Centre
Parkgate Street
Dublin 8, D08 DK10, Ireland

**Nicola Tedeschi** received the M.Sc. degree in Electronic Engineering and the Ph.D. degree from La Sapienza University of Rome, Rome, Italy, in 2009 and 2013, respectively. Currently, he is a Postdoctoral Fellow with La Sapienza University of Rome. He has been a visiting student with the Department of Radio Science and Engineering, Aalto University, Espoo, Finland, in 2012. His research interests include electromagnetic scattering by objects near interfaces, propagation of inhomogeneous waves in dissipative media, and the characterization of dispersive properties of natural and artificial materials.

E-mail: nicola.tedeschi@uniroma1.it
Department of Information Engineering, Electronics and Telecommunications
La Sapienza University of Rome
via Eudossiana 18
00184 Rome, Italy

Paper

# Multiple-ring Circular Array for Ground-Penetrating Radar Applications: Basic Ideas and Preliminary Results

Roberto Vescovo[1] and Lara Pajewski[2]

[1] *Department of Engineering and Architecture, University of Trieste, Trieste, Italy*
[2] *Department of Information Engineering, Electronics and Telecommunications, Sapienza University of Rome, Rome, Italy*

https://doi.org/10.26636/jtit.2017.120217

**Abstract—In this paper, the possibility of using a multiple-ring circular array as an antenna array for Ground-Penetrating Radar systems is investigated. The theory behind the proposed idea is presented. The preliminary numerical results that are obtained suggest that the proposed configuration is promising. It allows achieving a wide frequency band and low dynamic range ratio of excitations, thus simplifying the feeding network. Further interesting requirements may be satisfied by exploiting a combination of deterministic and stochastic synthesis techniques to design the array.**

***Keywords—antenna array, ultra-wideband, Ground-Penetrating Radar.***

## 1. Introduction

Antennas are a critical hardware component of a radar system, dictating its performance in terms of capability to detect targets. Nevertheless, most research efforts in the Ground-Penetrating Radar (GPR) field are focused on the applications of the technique and on the development of modeling, inversion and data-processing approaches [1], [2]. Only a limited number of studies deal with technological issues related to the design of novel systems [3]–[7], including the synthesis, optimization and characterization of new antennas [8], [9]. Even fewer are the research projects where innovative antenna arrays are developed [10].

Requirements that GPR antennas have to satisfy are somehow unique and very different than in conventional radar antennas, as GPR antennas operate in a strongly demanding environment, in close proximity to or at a limited distance from the natural or manmade investigated structure [11]. The same applies to GPR antenna arrays.

The first requirement is an ultra-wide frequency band: the radar has to transmit and receive short-duration time-domain waveforms, in the order of a few nanoseconds, the time-duration of the emitted pulses being a trade-off between the desired radar resolution and penetration depth. Additionally, GPR antennas shall have a linear phase characteristic over the whole operational frequency range, as well as predictable polarization and gain. Due to the fact that a subsurface imaging system is essentially a short-range radar, the coupling between transmitting and receiving antennas has to be low and short in time. Moreover, GPR antennas shall have quick ring-down characteristics, in order to prevent masking of targets and guarantee a good resolution. The radiation pattern shall ensure minimal interference with unwanted objects, usually present in the complex operational environment. To this aim, antennas have to provide high directivity and concentrate the electromagnetic energy into a narrow solid angle. As GPR antennas work very close to the matter or even in contact with it, changes in electrical properties of the matter should not affect strongly the antenna performance, so that a wide applicability of the radar system can be achieved. Furthermore, antennas should provide stable performance at different elevation levels. For an efficient coupling of electromagnetic waves into the ground/investigated structure, good impedance matching is necessary at the antenna/matter interface. Another important requirement regards the weight and size of the antennas: for ease of utilization and to allow a wide applicability, GPR antennas shall be light and compact.

Array of antennas can be used in GPR systems to enable a faster data collection by increasing the extension of investigated area per time unit. This can be a significant advantage in archaeological prospection, road and bridge inspection, mine detection, as well as in several other civil engineering and geoscience applications where the collection of data requires the execution of a large number of profiles. Moreover, antenna arrays allow collecting multi-offset measurements simultaneously, thereby providing additional information for a more effective imaging and characterization of the scenario under test.

Two approaches are possible to GPR array design. The simplest and most common is to conceive the array as a multi-channel radar system composed of single-channel radars. Much more can be achieved, if array-design techniques are employed to synthesize the whole system. This second approach is just starting in the GPR field and is definitely promising, as it gives the possibility to fully exploit the potentiality of arrays: they can provide a high directivity by using simple elements and the capability of a steerable beam, as in smart antennas.

Another important issue, to be considered when using multi-antenna GPR systems on irregular surfaces, is that the position of array elements has to be recorded during the surveys, by using high-precision positioning systems [12].

In this paper, which resumes and further extends the contribution presented in [13], we investigate the possibility of using a multiple-ring circular array as an antenna array for GPR systems. This configuration seems promising for achieving a wide frequency band and low dynamic range ratio of excitations, thus simplifying the feeding network. Further interesting requirements might be satisfied by exploiting a combination of deterministic and stochastic synthesis techniques to design the array.

## 2. Theory of Multiple-ring Circular Array

The concept of pattern multiplication is well known. If all antennas of an array are identical and have the same physical orientation, then the radiation (or reception) pattern of the array is given by the radiation pattern of the single antenna element multiplied by the array factor. With reference to Fig. 1, the array factor $F$ is a function of the direction of observation, specified by the unit vector $\hat{\mathbf{r}}$. It also depends on the positions of the N antennas in the array, $\mathbf{r}_\mathrm{n}$, and on the complex weights used to feed them, $a_n$ ($\mathrm{n} = 1, \ldots, \mathrm{N}$):

$$F = \sum_{\mathrm{n}=1}^{\mathrm{N}} a_\mathrm{n} \mathrm{e}^{jk\mathbf{r}_\mathrm{n}\cdot\hat{\mathbf{r}}} \tag{1}$$

where $k = \frac{2\pi}{\lambda}$ is the wave number, being $\lambda$ the wavelength.

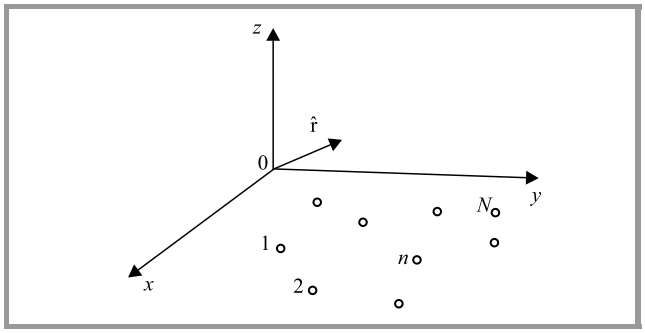


***Fig. 1.*** Antenna array of $N$ elements in arbitrary positions.

By tailoring the geometry and feeding network of an array, its performance may be optimized to achieve desirable properties. For instance, the array pattern can be steered (i.e., the direction of maximum radiation or reception can be changed) by modifying the weights.

In a GPR antenna array, the single element will be an ultra-wideband antenna (see Fig. 2). It is desirable that the overall radiation pattern of the array be "independent" of the frequency, not only the radiation pattern of the single antenna. Therefore, the array factor has to be "independent" of the frequency as well. A possible solution is a multiple

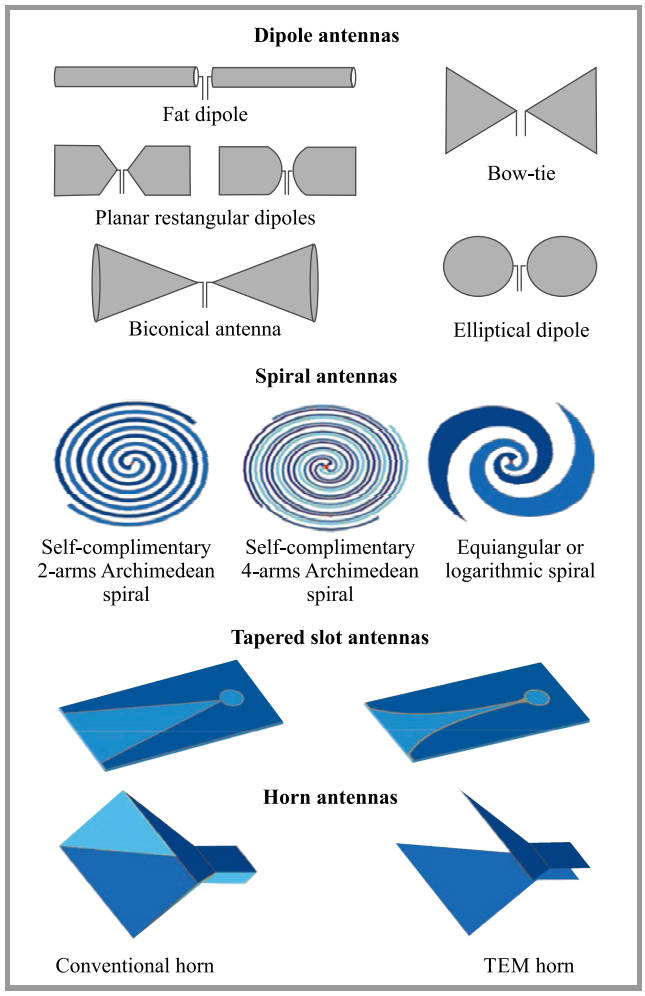


***Fig. 2.*** Most frequently used GPR antennas.

ring circular array, schematized in Fig. 3. This is constituted by M concentric rings of radii $R_\mathrm{m}$, where each ring includes $L_\mathrm{m}$ equispaced antennas ($m = 1, \ldots, \mathrm{M}$). The total number of antennas is:

$$\mathrm{N} = \sum_{m=1}^{\mathrm{M}} L_\mathrm{m} \,. \tag{2}$$

In a customary spherical coordinate system ($r$, $\theta$, $\phi$) with origin in the center of the radiating rings, the array factor of radiating rings with a continuous excitation $a_\mathrm{m}$ (being $a_\mathrm{m}$ the excitation density on the $m$-th ring) has the following expression:

$$F = \sum_{\mathrm{m}=1}^{\mathrm{M}} a_\mathrm{m} R_\mathrm{m} \int_0^{2\pi} \mathrm{e}^{jR_\mathrm{m} k \sin\theta \cos\phi'} \mathrm{d}\phi' \,. \tag{3}$$

Recalling the integral properties of the Bessel functions, it results:

$$F = 2\pi \sum_{\mathrm{m}=1}^{\mathrm{M}} a_\mathrm{m} R_\mathrm{m} J_0(R_\mathrm{m} k \sin\theta) \,. \tag{4}$$

In the structure that we are considering, instead, the excitation is discrete. The $\ell$-th element on the ring m ($\ell = 1, \ldots, L_\mathrm{m}$) is located at the angular position

$$\phi_{\ell\mathrm{m}} = \frac{2\pi(\ell - 1)}{L_\mathrm{m}} + \delta_m \,,$$

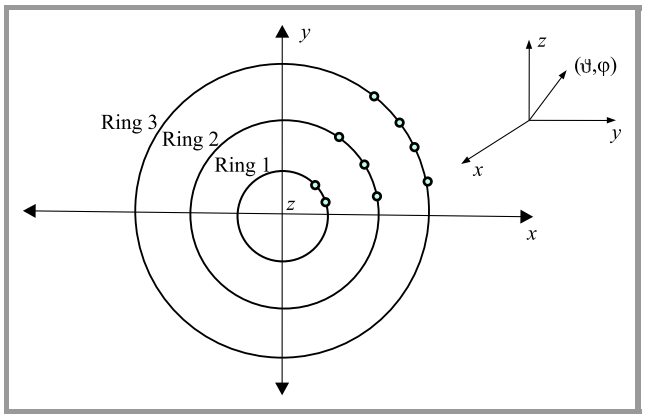


***Fig. 3.*** Multiple ring circular array.

where $\delta_{\mathrm{m}}$ is the angular position of the first element. Let us call $a_{\ell \mathrm{m}}$ the excitation of the $\ell$-th element on the ring m and let us also assume that uniform excitation is adopted in each ring, i.e.:

$$a_{\ell \mathrm{m}} = \frac{2\pi R_{\mathrm{m}} a_{\mathrm{m}}}{L_{\mathrm{m}}} \quad \forall \ell \,.$$

Then, by using Eq. (1) and after some manipulations, the array factor is given by:

$$F = \sum_{\mathrm{m}=1}^{\mathrm{M}} \frac{2\pi R_{\mathrm{m}}}{L_{\mathrm{m}}} a_{\mathrm{m}} \sum_{\ell=1}^{L_{\mathrm{m}}} \mathrm{e}^{jR_{\mathrm{m}} k \sin\theta \cos(\phi - \phi_{\ell \mathrm{m}})} \,. \tag{5}$$

Such array factor is weakly affected by a change of the frequency, as will be illustrated in Section 3 via a numerical example.

## 3. Results

In this Section, we present a simple example of array-factor synthesis for the multiple-ring circular array. The aim of this example is to illustrate the frequency-dispersion properties of the array factor. In the example, we set $\delta_{\mathrm{m}} = 0$. As a desired pattern, we choose $F_d(u) = |\mathrm{sinc}(\mathrm{c}_1 \mathrm{u})|^{\mathrm{c}_2}$, where $u = k \sin\theta$, and $c_1$, $c_2$ are given real numbers. This pattern has a maximum in $\theta = 0$. By exploiting Eq. (4), we want to find the coefficients $a_{\mathrm{m}}$ that minimize the squared distance:

$$\rho^2 = \left\| F_d(u) - 2\pi \sum_{\mathrm{m}=1}^{M} a_{\mathrm{m}} R_{\mathrm{m}} J_0(R_{\mathrm{m}} u) \right\|^2 , \tag{6}$$

where $\|f\| = \int_0^{2\pi} |f(\gamma)|^2 \mathrm{d}\gamma$. By manipulating (6) and setting

$$\frac{\partial \rho}{\partial a_{\mathrm{p}}} = 0 , \quad \mathrm{p} = 1, \ldots, \mathrm{M} ,$$

we obtain a system of M linear equations in the M (real) unknowns $a_{\mathrm{m}}$:

$$\sum_{\mathrm{m}=1}^{\mathrm{M}} T_{\mathrm{pm}} a_{\mathrm{m}} = U_{\mathrm{p}} \quad (\mathrm{p} = 1, \ldots, \mathrm{M}) , \tag{7}$$

where $T_{\mathrm{pm}} = 2\pi R_{\mathrm{m}} < J_0(R_{\mathrm{m}} u), J_0(R_{\mathrm{p}} u) >$ and $U_{\mathrm{p}} = < F_d, J_0(R_{\mathrm{p}} u) >$, being $< f_1, f_2 > = \int_0^{2\pi} f_1(\gamma) f_2(\gamma) \mathrm{d}\gamma$ a scalar product between the real functions $f_1$ and $f_2$. The system (7) can be solved by standard techniques and the solutions $a_{\mathrm{m}}$ minimize $\rho^2$ in Eq. (6).

The same coefficients $a_{\mathrm{m}}$ can be used in (5) as well, to calculate the array factor of the array with $L_{\mathrm{m}}$ elements on the m-th ring.

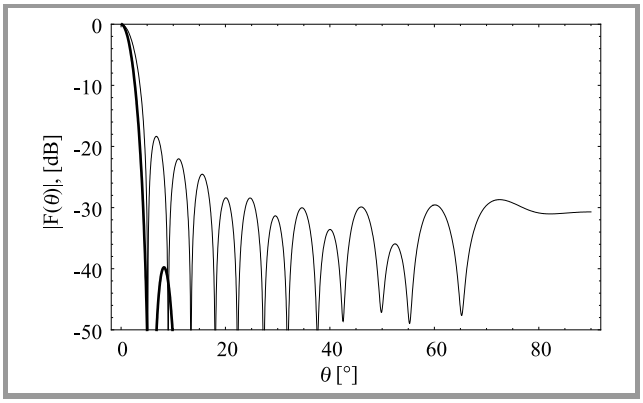


***Fig. 4.*** Desired (thick line) and synthesized (thin line) patterns for the multiple-ring circular array with M = 8 rings described in the text, when $\phi = 0$ and at the nominal frequency $f_0$.

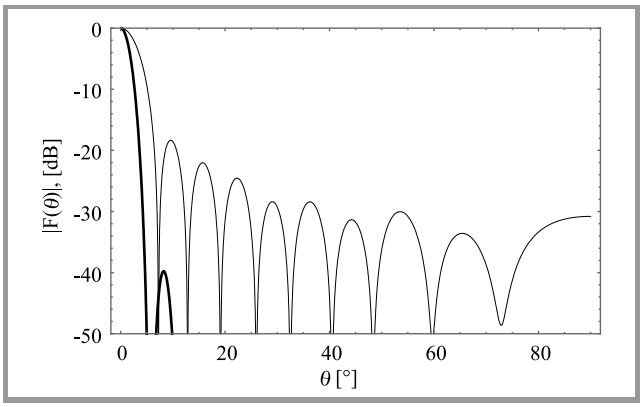


***Fig. 5.*** Same as in Fig. 4, when the frequency is $f_1 = 0.707 f_0$.

In Fig. 4, the desired and synthesized patterns are plotted as a function of $\theta$ when $\phi = 0$, for a multiple-ring circular array with M= 8 rings. Different cuts of the radiation pattern give similar results. The number of elements and radius of the m-th ring are: $L_{\mathrm{m}} = 5\mathrm{m}$, $R_{\mathrm{m}} = 0.8\mathrm{m}\lambda$ $(\mathrm{m} = 1, \ldots, \mathrm{M})$. Moreover, $c_1 = 5$ and $c_2 = 3$. The dynamic range ratio, which is the ratio between the maximum and minimum excitation amplitudes of the array elements, is $DRR = 1.375$. Note that a limited dynamic range ratio allows the practical realization of noncomplex feeding networks, where the number of power dividers may be kept low or the design of the feeding lines may be simplified.

Now, for the same geometry and keeping the same excitations, we modify the frequency and study how a change of frequency affects the radiation pattern.

In Fig. 5, the same as in Fig. 4 is shown, when the frequency is $f_1 = \frac{f_0}{\sqrt{2}} = 0.707 f_0$. In Fig. 6, the same as in Fig. 4 is shown, when the frequency is $f_2 = 1.1 f_0$. Finally,

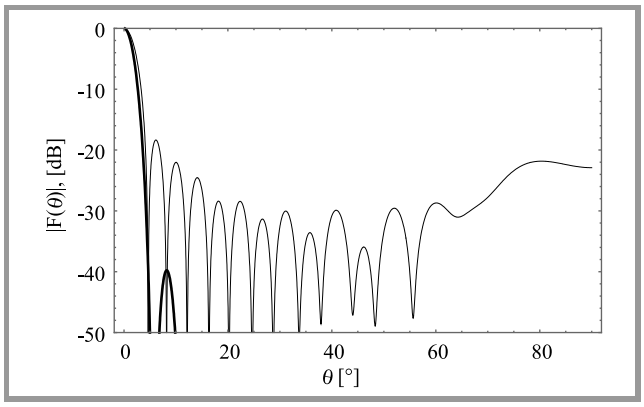


***Fig. 6.*** Same as in Fig. 4, when the frequency is $f_2 = 1.1 f_0$.

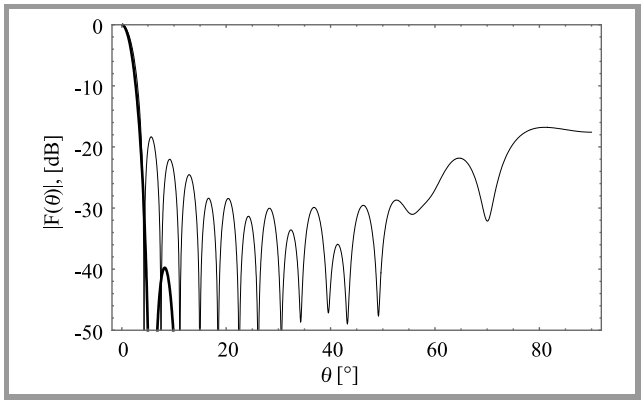


***Fig. 7.*** Same as in Fig. 4, when the frequency is $f_3 = 1.5 f_0$.

in Fig. 7, the same as in Fig. 4 is shown, when the frequency is $f_3 = 1.5 f_0$. Note that, in the latter case, $f_3 - f_0 = 0.5 f_0$. It is apparent that the radiation properties of the array are not significantly affected by the frequency change.

# 4. Conclusions and Future Work

Usually, a multi-antenna Ground-Penetrating Radar (GPR) is simply conceived as a multi-channel radar system composed of single-channel independent systems. Much more can be achieved, if array-design techniques are employed to synthesize the overall set of antennas. Such approach is slowly starting in the GPR field and is definitely promising, as it gives the possibility to fully exploit the potentiality of arrays.

In this paper, we have suggested and investigated the multiple circular-ring array, as a possible solution for a GPR antenna array. The preliminary results that we have obtained show that our idea is promising. The proposed structure yields the possibility of a wide frequency band with a low dynamic range ratio. Moreover, the synthesis can be easily performed at a single frequency within the range of interest.

The natural continuation of this work is the design of a realistic GPR array and the testing of its performance in a realistic scenario.

For the design of the GPR array, two deterministic methods may be used, i.e. the techniques presented in [14] and [15]. The former is based on an alternate projections approach and requires a given array geometry. The latter allows an optimization of the radii of the circular rings. The method determines the array geometry starting from a dense grid of fictitious elements and reducing their number iteratively. This allows to optimize the array geometry and to meet constraints on the copolar and crosspolar patterns, on the dynamic range ratio, on the near field properties and on the pattern reconfigurability.

For testing the array performance in a realistic scenario, the open-source electromagnetic simulator gprMax [16] may be employed, implementing the Finite-Difference Time-Domain method.

# Acknowledgements

This work is a contribution to COST (European CO-operation in Science and Technology, www.cost.eu) Action TU1208 “Civil engineering applications of Ground Penetrating Radar” (www.GPRadar.eu). The authors thank COST for funding and supporting the Action TU1208.

# References

[1] A. Benedetto and L. Pajewski, Eds., *Civil Engineering Applications of Ground Penetrating Radar*, Book Series: *Springer Transactions in Civil and Environmental Engineering*. Springer, 2015 (doi: 10.1007/978-3-319-04813-0).

[2] R. Persico, *Introduction to Ground Penetrating Radar: Inverse Scattering and Data Processing*. Wiley-IEEE Press, 2014.

[3] F. Tosti, S. Adabi, L. Pajewski, G. Schettini, and A. Benedetto, “Large-scale analysis of dielectric and mechanical properties of pavement using GPR and LFWD”, in *Proc. 15th Int. Conf. on Ground Penetrat. Radar GPR 2014*, Brussels, Belgium, 2014, pp. 868–873 (doi: 10.1109/ICGPR.2014.6970551).

[4] E. Huuskonen-Snicker, P. Eskelinen, T. Pellinen, and M.-K. Olkkonen, “A new microwave asphalt radar rover for thin surface civil engineering applications”, *Frequenz J. of RF-Engin. and Telecommun.*, vol. 69, no. 7–8, pp. 377–381, 2015 (doi: 10.1515/freq-2015-0034).

[5] R. Persico and G. Leucci, “Interference mitigation achieved with a reconfigurable stepped-frequency GPR system”, *Remote Sensing*, vol. 8, no. 11, Article no. 926, 2016 (doi: 10.3390/rs8110926).

[6] V. Ferrara, F. Troiani, F. Frezza, F. Mangini, L. Pajewski, P. Simeoni, and N. Tedeschi, “Design and realization of a cheap Ground Penetrating Radar prototype @ 2.45 GHz”, in *Proc. 10th IEEE Eur. Conf. on Antenn. and Propag. EuCAP 2016*, Davos, Switzerland, 2016, pp. 1–4 (doi: 10.1109/EuCAP.2016.7482008).

[7] L. Pajewski, R. Persico, S. Chicarella, V. Ferrara, F. Frezza, and F. Troiani, “Ground Penetrating Radar prototypes developed in COST Action TU1208”, in *Proc. 24th Int. Conf. on Software, Telecommun. and Comp. Netw. SoftCOM 2016*, Split, Croatia, 2016, pp. 1–5.

[8] C. Warren, A. Giannopoulos, N. Diamanti, and P. Annan, “An extension module to embed commercially sensitive antenna models in gprMax”, in *Proc. 8th Int. Worksh. on Adv. Ground Penetrat. Radar IWAGPR 2015*, Florence, Italy, 2015, pp. 1–3 (doi: 10.1109/IWAGPR.2015.7292623).

[9] C. Warren and A. Giannopoulos, “Experimental and modeled performance of a ground penetrating radar antenna in lossy dielectrics”, *IEEE J. of Selec. Topics in Appl. Earth Observ. and Remote Sensing (JSTARS)*, vol. 9, no. 1, pp. 29–36, 2016 (doi: 10.1109/JSTARS.2015.2430933).

[10] E. Eide, P. A. Våland, and J. Sala, "Ground-coupled antenna array for step-frequency GPR", in *Proc. 15th Int. Conf. on Ground Penetra. Radar GPR 2014*, Brussels, Belgium, 2014, pp. 756–761 (doi: 10.1109/ICGPR.2014.6970527).

[11] L. Pajewski, F. Tosti, and W. Kusayanagi, "Antennas for GPR Systems", in *Civil Engineering Applications of Ground Penetrating Radar*, Book Series: *Springer Transactions in Civil and Environmental Engineering*, A. Benedetto and L. Pajewski, Eds. Springer, 2015, pp. 41–67 (doi: 10.1007/978-3-319-04813-0_2).

[12] S. Chicarella, V. Ferrara, F. Frezza, A. D'Alvano, and L. Pajewski, "Improvement of GPR tracking by using inertial and GPS combined data", in *Proc. 24th Int. Conf. on Software, Telecommun. and Comp. Netw. SoftCOM 2016)*, Split, Croatia, 2016, pp. 1–5 (doi: 10.1109/SOFTCOM.2016.7772148).

[13] R. Vescovo, L. Pajewski, and F. Tosti, "State-of-the-art and trends of Ground-Penetrating Radar antenna arrays", Geophysical Research Abstracts, European Geosciences Union (EGU) General Assembly 2016, article ID EGU2016-18097, 2016, Vienna, Austria.

[14] G. Buttazzoni and R. Vescovo, "An efficient and versatile technique for the synthesis of 3D copolar and crosspolar patterns of phase-only reconfigurable conformal arrays with DRR and near-field control", *IEEE Trans. on Antenn. and Propag.*, vol. 62, no. 4, part 1, pp. 1640–1651, 2014.

[15] B. Fuchs, "Synthesis of sparse arrays with focused or shaped beampattern via sequential convex optimizations", IEEE Trans. on Antenn. and Propag., vol. 60, no. 7, pp. 3499–3503, 2012.

[16] C. Warren, A. Giannopoulos, and I. Giannakis, "gprMax: Open source software to simulate electromagnetic wave propagation for Ground Penetrating Radar", Comp. Phys. Commun., vol. 209, pp. 163–170 (doi: 10.1016/j.cpc.2016.08.020).

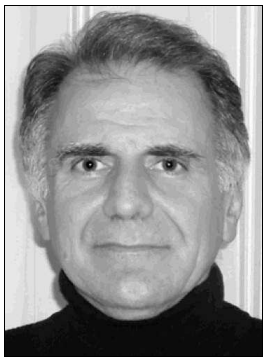

**Roberto Vescovo** received the Laurea degree (summa cum laude) in Electronic Engineering from the University of Trieste, Italy (1982), and the Ph.D. in Electronics and Information Engineering from the University of Padova, Italy (1987). He served as an Assistant Professor at the Department of Engineering and Architecture, University of Trieste, where he is currently an Associate Professor of electromagnetic fields. His main research interests are the synthesis of antenna arrays, the electromagnetic scattering, the electromagnetic theory and numerical methods, and the study of interactions between electromagnetic fields and relativistic electrons.

E-mail: vescovo@units.it
Department of Engineering and Architecture
University of Trieste
via A. Valerio 10
34127 Trieste, Italy

**Lara Pajewski** is a Professor of electromagnetic fields in the Department of Information Engineering, Electronics and Telecommunications of Sapienza University of Rome, Italy. She is an electronic engineer with a Ph.D. in applied electromagnetics and electrophysics sciences earned in Sapienza University. Since 2013, she is chairing the COST Action TU1208 "Civil engineering applications of Ground Penetrating Radar". Her current research interests include Ground Penetrating Radar (GPR) technology, methodology and applications, integration of GPR with complementary non-destructive testing methods, electromagnetic modeling of complex scenarios, antenna design and characterization, measurement of electromagnetic pollution and evaluation of its impact.

E-mail: lara.pajewski@uniroma1.it
Department of Information Engineering, Electronics and Telecommunications
Sapienza University of Rome
via Eudossiana 18
00184 Rome, Italy

Paper

# Enhancement of Air-ground Matching by Means of a Chirped Multilayer Structure: Electromagnetic Modeling with the Method of Single Expression

Hovik Baghdasaryan[1], Tamara Knyazyan[1], Tamara Hovhannisyan[1], Marian Marciniak[2], and Lara Pajewski[3]

[1] *National Polytechnic University of Armenia, Yerevan, Armenia*
[2] *National Institute of Telecommunications, Warsaw, Poland*
[3] *Sapienza University of Rome, Department of Information Engineering, Electronics and Telecommunications, Rome, Italy*

https://doi.org/10.26636/jtit.2017.121117

**Abstract—The enhancement of air-ground electromagnetic matching by means of a chirped multilayer structure is investigated. The modeling and simulation of the considered structure are performed by using the method of single expression (MSE), which is a convenient and accurate tool for wavelength-scale simulations of multilayers comprising lossy, amplifying or nonlinear (Kerr-type) materials. Numerical results show that a suitable chirped multilayer structure can reduce the reflection from the ground. Different values of the number of layers and of the layer thicknesses are considered. The distributions of the electric field components and the power flow density within the modelled structures are calculated.**

***Keywords—chirped multilayer structure, ground matching, method of single expression.***

## 1. Introduction

Ground Penetrating Radar (GPR) is an electromagnetic technique currently in use for detection and imaging of buried objects, with resolution ranging from centimeters to few meters depending on the operation wavelength of the radar antenna [1]–[6]. The principles of GPR for detecting buried objects are well known, indeed GPR uses the same fundamental physical principles as conventional radars. GPR is a technique typically operating at frequencies included within the 10 MHz to 5 GHz range. The chosen frequency band depends on measurement purposes and properties of the investigated media. Target objects can be buried pipes, cables and reinforcing elements, caverns, flaws and cracks, as well as ground water and moisture, and more [6]–[11]. Nowadays, GPR is widely applied in archaeological investigations and for cultural heritage management, planetary exploration, forensics, civil, hydrogeological, geophysical and geotechnical engineering [6]–[11].

GPR detects the electromagnetic field backscattered by the targets and generates an image of it, which is interpreted after proper signal processing. The GPR transmitter emits electromagnetic waves towards the ground or structure under test. When the waves encounter a buried object or a boundary between materials having different permittivity and conductivity values, they are reflected, refracted and scattered back to the radar. A receiving antenna catches the returned signal, which is analyzed and recorded. Depth and shape of the objects are calculated from the travel time and amplitude of the reflected signals, along an acquisition profile.

The signal attenuation and penetration depth at the desired operating frequency are the main factors influencing the functionality and resolution of a GPR device [2]–[6]. Resolution of GPR primarily is a function of the radar frequency and the permittivity of the detected medium. High resolution can be reached at the cost of penetration depth, because the attenuation of electromagnetic waves in common ground materials, as well as in materials utilized in manmade structures, is rather high and increases with frequency. At a lower frequency, GPR can sample deeper, but the resolution is lower. A higher frequency range gives a narrower pulse, yielding a higher time or depth resolution. On the other hand, attenuation increases with frequency. Therefore, a high frequency signal cannot propagate far and the depth of detection becomes shallower [12], [13]. To give a practical example, for applications requiring high resolution and a penetration depth down to approximately 60 cm, such as assessment of concrete structures, a frequency spectrum centered over 1 GHz is normally used. For applications requiring penetration from tens of centimeters to hundreds of meters, frequencies between 12.5 MHz to 500 MHz are used.

Antennas are essential components of GPR systems, which transmit and receive electromagnetic waves. Various types of antennas can be used: dipole, bowtie and horn antennas are the most common. Several systems use two separate antennas for transmitting and receiving, although they can

be packaged together. Some commercial systems employ shielded antennas to avoid reflections from objects in the air. The antenna gain is very important for efficiently emitting and receiving the electromagnetic energy. Antennas with a high gain improve the signal/noise ratio. A lower operating frequency requires larger antennas. Small antennas make the system compact, but they have a low gain at lower frequencies [12], [13].

Though the GPR technique is mature enough, some problems are still waiting for their solution [6]. One of them is to achieve a better matching of the electromagnetic waves emitted by the GPR with the ground, which would increase the signal penetration depth, minimize back reflections at the air-ground interface and enhance the signal/noise ratio at the receiving end. Different antenna configurations and antenna-medium interactions have been studied in the literature, mostly by using the finite-difference time-domain (FDTD) method or the method of moments [14]–[16].

In this paper, the possibility to enhance air-ground electromagnetic matching by means of a suitable chirped multilayer structure is studied. The wavelength-scale electromagnetic modeling and simulation of a chirped multilayer structure over a dielectric half-space, illuminated by a monochromatic plane wave, is performed by using the method of single expression (MSE) [17]–[22] (Section 2). The behavior of different structures is analyzed, to find advantageous configurations for matching enhancement (Section 3). Preliminary results were presented in [22]. Further studies are necessary, to consider more realistic sources and ultra-wideband radiation.

## 2. Electromagnetic-modeling Method

The method of single expression (MSE) allows to accurately analyze wavelength-scale multilayer structures comprising lossy, amplifying or nonlinear (Kerr-type) dielectric, semiconductor or metallic materials [17]–[22]. In this Section, the backbone of the MSE for normal wave incidence on a multilayer structure is resumed.

From Maxwell's equations in the one-dimensional case, the Helmholtz equation can be obtained, for the linearly polarized complex electric field component $\dot{E}_x(z)$:

$$\frac{d^2\dot{E}_x(z)}{dz^2} + k_0^2\dot{\varepsilon}(z)\dot{E}_x(z) = 0\,, \tag{1}$$

where $k_0 = \frac{\omega}{c}$ is the free space propagation constant and $\dot{\varepsilon}(z) = \varepsilon'(z) + j\varepsilon''(z)$ is the complex permittivity of a medium.

The essence of the MSE is the use of a general solution of the Helmholtz equation, having the following single expression:

$$\dot{E}_x(z) = U(z)\cdot \mathrm{e}^{-jS(z)}\,, \tag{2}$$

instead of the traditional solution expressed as a sum of counter-propagating waves. In (2), $U(z)$ and $S(z)$ are real quantities describing the electric field amplitude and phase, respectively. Time dependence $\mathrm{e}^{j\omega t}$ is assumed, but suppressed in the formulas. The expression (2) can describe all the possible electric field amplitude distributions in a medium, corresponding to propagating, standing and evanescent waves. This gives advantages in the investigation of the interaction of electromagnetic waves with longitudinally non-uniform linear media and with intensity dependent non-linear media.

By introducing (2) in (1), the Helmholtz equation can be rewritten as a set of first-order differential equations:

$$\begin{cases} \dfrac{dU(z)}{d(k_0z)} = Y(z) \\ \dfrac{dY(z)}{d(k_0z)} = \dfrac{P^2(z)}{U^3(z)} - \varepsilon'(z)\cdot U(z) \\ \dfrac{dP(z)}{d(k_0z)} = \varepsilon''(z)\cdot U^2(z) \end{cases}, \tag{3}$$

where $Y(z)$ is the spatial derivative of $U(z)$ and $P(z)$ is a quantity that is proportional to the power flow density (Poynting vector) in a medium, i.e. $P(z) = U^2(z)\frac{dS(z)}{d(k_0z)}$. The sign of $\varepsilon'(z)$ can assume either positive or negative values, describing relevant electromagnetic features of dielectric materials or plasma, respectively. The sign of $\varepsilon''(z)$ indicates loss or gain in a medium.

The set of equations in (3) can be integrated numerically starting from the non-illuminated side of a multilayer structure, where only one outgoing traveling wave is supposed to be present. The initial values for the integration can be obtained from the boundary conditions of electrodynamics at the non-illuminated side of the structure ($z = L$), i.e., $U(L) = E_{tr}$, $Y(L) = 0$, and $P(L) = \sqrt{\varepsilon_r}E_{tr}^2$, where $E_{tr}$ and $\varepsilon_r$ are the amplitude of the transmitted wave and the permittivity of the medium beyond the multilayer structure at $z > L$, respectively. Numerical integration of (3) continues step by step towards the illuminated side of the structure, taking into account the actual value of the permittivity for the given coordinates at each step of integration. In the process of integration, any variable in (3) can be calculated and recorded, so that it is possible to obtain full information regarding the distribution of the electric field amplitude in the space, as well as the distribution of its derivative and power flow density.

At the interfaces between different material of the multilayer structure, the ordinary boundary conditions of electrodynamics bring to the continuity of $U(z)$, $Y(z)$ and $P(z)$. From the boundary conditions of electrodynamics at the illuminated side of the structure ($z = 0$), the amplitude of the incident wave $E_{inc}$:

$$E_{inc} = \left| \frac{U^2(0)\cdot\sqrt{\varepsilon_l} + P(0) + jU(0)\cdot Y(0)}{2U(0)\cdot\sqrt{\varepsilon_l}} \right|, \tag{4}$$

and the power reflection coefficient $R$:

$$R = \left|\frac{E_{ref}}{E_{inc}}\right|^2 = \left| \frac{U^2(0)\cdot\sqrt{\varepsilon_l} - P(0) - jU(0)\cdot Y(0)}{U^2(0)\cdot\sqrt{\varepsilon_l} + P(0) + jU(0)\cdot Y(0)} \right|^2, \tag{5}$$

are restored at the end of the calculation. Here, $U(0)$ is the amplitude of the electromagnetic wave, $Y(0)$ is its derivative and $P(0)$ the power flow density at the illuminated

interface of the structure $z = 0$, $E_{ref}$ is the amplitude of the reflected wave, and finally $\varepsilon_l$ is the permittivity of the medium in front of the structure, for $z < 0$.
The power transmission coefficient $T = \frac{E_{tr}^2\sqrt{\varepsilon_r}}{E_{inc}^2\sqrt{\varepsilon_l}}$ is defined as the ratio of transmitted power to the incident one.

## 3. Numerical Results

The geometry of the modeled and simulated structure is represented in Fig. 1.

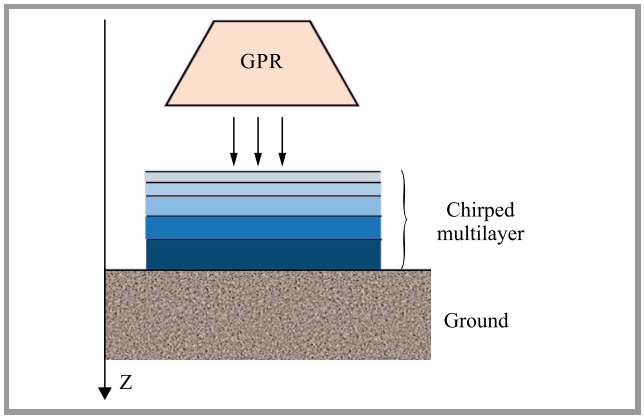


***Fig. 1.*** Plane wave interaction with the ground through a chirped multilayer structure.

Normal incidence of a plane wave with wavelength $\lambda_0 =$ 10 cm on a ground of complex permittivity $\dot{\varepsilon}_{gr} = \varepsilon'_{gr} + j\varepsilon''_{gr} = 10 - j0.3$ [23] is considered. A chirped multilayer structure is positioned above the ground. It consists of two alternating dielectric slabs of low $\varepsilon'_{low} = 2.25$ and high $\varepsilon'_{high} = 6.0$ permittivity creating bilayers of increasing thickness towards the ground. A numerical analysis and optimization carried out by using the MSE revealed that bilayers should have the following normalized thicknesses (NT): $NT_i = 0.3471;\ 0.4471;\ 0.5471$, where $NT_i = \frac{L_i}{\lambda}$ ($i = 1, 2, 3$ is a number of bilayers) starting from the illuminated side, being $\lambda = \frac{\lambda_0}{\sqrt{\varepsilon}}$ the wavelength in the slab with $\varepsilon = \varepsilon'_{low}$ and $\varepsilon = \varepsilon'_{high}$ permittivity, respectively.
Results for two particular structures are presented in the following. The permittivity profile of such structures is plotted in Fig. 2. For the first structure (Fig. 2a):

$NT_1 = 0.3471$ ($\varepsilon'_{high}$ and $\varepsilon'_{low}$),

$NT_2 = 0.4471$ ($\varepsilon'_{high}$ and $\varepsilon'_{low}$),

$NT_3 = 0.5471$ ($\varepsilon'_{high}$ and $\varepsilon'_{low}$).

The material with low permittivity $\varepsilon'_{low}$ is adjacent to the ground.
For the second structure (Fig. 2b):

$NT_1 = 0.3471$ ($\varepsilon'_{low}$ and $\varepsilon'_{high}$),

$NT_2 = 0.4471$ ($\varepsilon'_{low}$ and $\varepsilon'_{high}$),

$NT_3 = 0.5471$ ($\varepsilon'_{low}$ and $\varepsilon'_{high}$).

The material with high permittivity $\varepsilon'_{high}$ is adjacent to the ground.

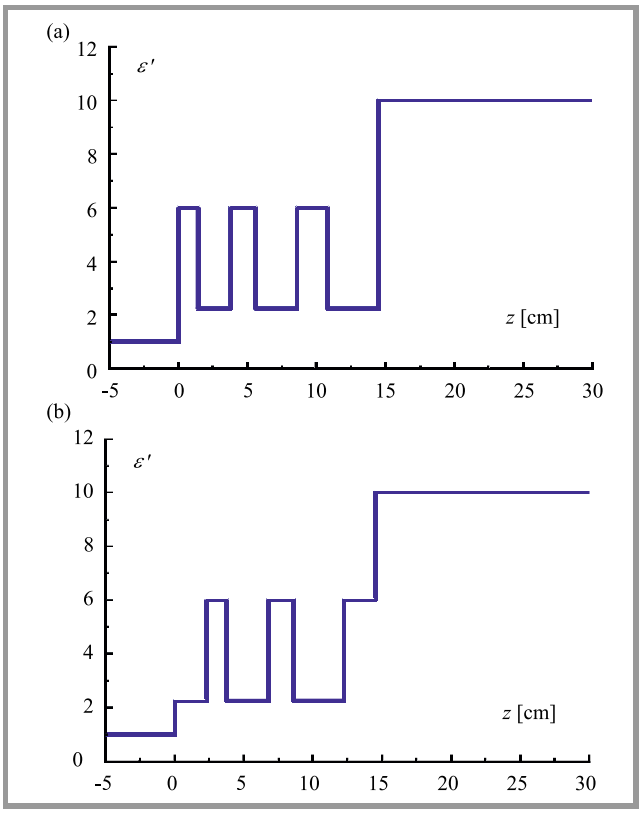


***Fig. 2.*** Permittivity profiles of two chirped multilayer structures positioned on the ground. Wave incidence from the left side of the graphs is considered.

The reflectance $R$ from the structures air-multilayer-ground or air-ground interface is defined as $R = \frac{P_{ref}}{P_{inc}}$ – see Eq. (5), where $P_{inc}$ is a power flow density (Poynting vector) of the electromagnetic wave impinging on the multilayer structure, and $P_{inc}$ is a power flow density (Poynting vector) of the electromagnetic wave reflected from the structure.
In the absence of a chirped multilayer structure the reflectance $R_{gr}$ from the ground is defined as:

$$R = \left| \frac{\sqrt{\varepsilon_l} - \sqrt{|\dot{\varepsilon}_{gr}|}}{\sqrt{\varepsilon_l} + \sqrt{|\dot{\varepsilon}_{gr}|}} \right|^2, \tag{6}$$

which is a reflectance from the air-ground interface, the so-called Fresnel reflection coefficient. For the considered case, in the absence of the chirped multilayer structure, the reflectance $R_{gr}$ from the air-ground interface equals to $R_{gr} \approx 0.27$. This value has been calculated by using the MSE and the formula in Eq. (6).
The structure in Fig. 2b, where the layer of high permittivity is contacted with the ground, permits to attain air-ground matching with overall reflectance of $R \approx 0.0019$ while the structure in Fig. 2a indicated reflectance $R \approx 0.25$ that is close to relevant value of reflectance $R_{gr} \approx 0.27$ for the air-ground interface (without multilayer structure). Thus, an enhancement of air-ground matching is obtained for the structure where the slab of $\varepsilon'_{high}$ is contacted with the ground (Fig. 2b).

In Fig. 3 the reflectance spectra of the air-ground and air-multilayer-ground for the two types of chirped multilayer structures are presented for the wavelength range of $\lambda_0 = (9.5 \div 10.5)$ cm.

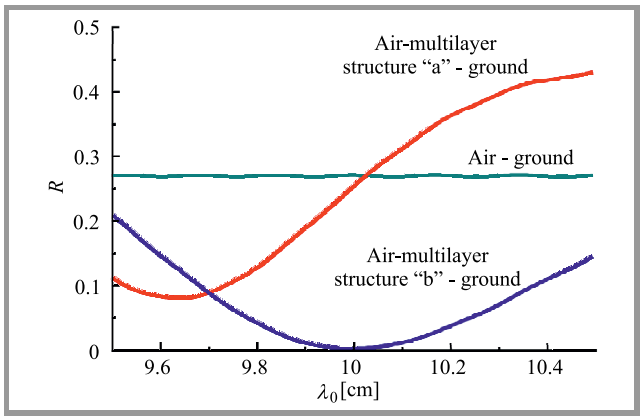


***Fig. 3.*** Reflectance spectra of the air-ground and air-multilayer-ground for two types of chirped multilayer structures. (See color pictures online at www.nit.eu/publications/journal-jtit)

The chirped multilayer structure with a layer of high permittivity contacted with the ground, i.e. the structure “b” in Fig. 2 has the lowest reflectance in the whole wavelength range as compared with the structure “a” in Fig. 2 and air-ground case. The lowest value of the reflectance $R \approx 0.0019$ of the structure “b” is observed at the wavelength $\lambda_0 = 10$ cm.

Thus, for better air-ground matching a chirped multilayer structure with a layer of high permittivity contacted with the ground (with reflectance of $R \approx 0.0019$) at the wavelength of 10 cm should be chosen (structure “b”, Fig. 2b). Low reflectance permits deeper penetration of electromagnetic waves in the ground as it will be seen from the physics of difference of operation of two chirped multilayer structures, as well as of the air-ground interface in the absence of the multilayer structure.

In the absence of the multilayer structure, partially-standing wave amplitude of electric field is formed at the air-ground interface at $z < 0$, which indicates essential reflectance from the interface (Fig. 4). Exponentially decreasing electric field amplitude due to the loss in the ground is observed.

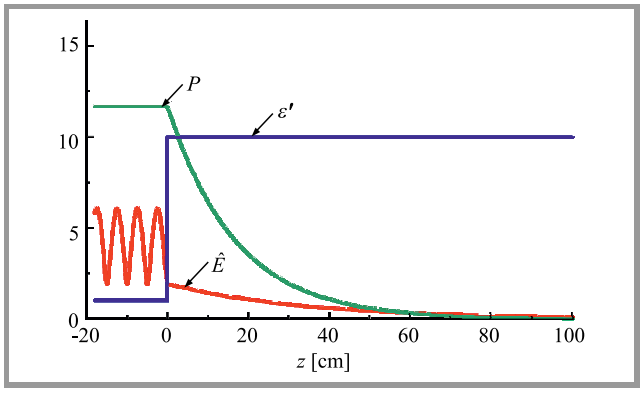


***Fig. 4.*** Permittivity profile, distributions of electric field amplitude $\hat{E}$ and Poynting vector $P$ within the air and the ground. The amplitude of incident wave (from the left at $z < 0$) is $E_{inc} = 4$ a.u., $\lambda_0 = 10$ cm, $R_{gr} \approx 0.27$.

For $z < 0$, the resultant Poynting vector $P$ is $P = P_{inc} - P_{ref} = P_{inc}(1 - R_{gr})$. The Poynting vector $P$ is a constant value in the air and exponentially decreases in the ground. Consequently, because of the reflection from the air-ground interface and small resultant value of $P \approx 11.68$, the penetration depth into the ground is limited.

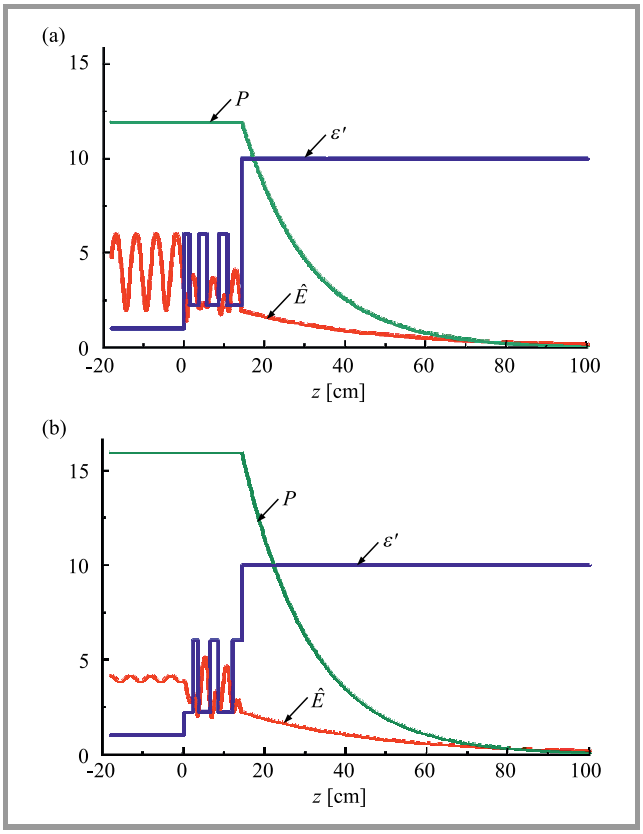


***Fig. 5.*** Permittivity profile, distribution of electric field amplitude $\hat{E}$ and Poynting vector $P$ within and outside of the chirped multilayer structures. The amplitude of incident wave (from the left at $z < 0$) in both cases is the same $E_{inc} = 4$ a.u. at $\lambda_0 = 10$ cm, $R \approx 0.25$ for the structure “a” and $R \approx 0.0019$ for the structure “b”.

The distributions of the electric field amplitude $\hat{E}$ and of the Poynting vector $P$ strongly depend on the alternation of layers in the chirped multilayer structure. The relevant distributions of electric field amplitude and Poynting vector within and outside the structures are presented in Fig. 5. Due to the absence of losses in the chirped multilayer structures, the Poynting vector $P$ is constant in them and the electric field amplitude $\hat{E}$ has an oscillating behavior following the permittivity profiles of multilayer structures. A partially-standing wave amplitude of the electric field is formed in front of the structure in Fig. 5a, indicating higher reflectance $R$ and $P \approx 11.93$. An almost traveling wave pattern is created in front of the structure in Fig. 5b, indicating lower reflectance $R$ and $P \approx 15.97$. The power flow penetrating into the ground increases of approximately 1.34 times, which causes a deeper penetration.

## 4. Conclusions

A wavelength-scale electromagnetic analysis by means of the method of single expression (MSE) permitted to find chirped multilayer structures providing enhancement of air-ground matching, when the electromagnetic source is a monochromatic plane wave. The number and thicknesses of the layers can be optimized to minimize back reflection towards the electromagnetic source. The use of non-uniform (chirped) multilayers can enlarge the reflectance spectrum if compared to the standard quarter-wavelength multilayers. Interesting results have been found for a structure consisting of three bilayers of high and low permittivity, where the highest value of the permittivity does not exceed the permittivity of the ground. Bilayers have increasing thickness towards the ground and a better matching is achieved when the layer closer to the ground has the high permittivity.

The reflectance spectra and the distributions of electric field amplitude and Poynting vector within and outside the structures have been calculated. This allowed finding the favorable structures.

Mainly, the novelty of this work is in the application of a non-traditional method, the MSE, to the analysis of multilayers; the methods permits an easy calculation of the field amplitude and Poynting vector spatial distributions inside and outside the multilayer and in the presence of lossy media. Further studies are necessary, to design structures providing good results when illuminated by a pulsed electromagnetic wave.

## Acknowledgement

This work originated from a Short-Term Scientific Mission funded by the COST Action TU1208 "Civil Engineering Applications of Ground Penetrating Radar", no. STSM-TU1208-010816-080185. The authors are thankful to the members of the COST Action TU1208 for fruitful discussions.

## References

[1] L. B. Conyers and D. Goodman, *Ground Penetrating Radar: An Introduction for Archaeologists*. London and New Delhi: AltaMira Press, Walnut Creek, 1997.

[2] D. J. Daniels, Ed., *Ground Penetrating Radar*, 2nd ed. London: The Institution of Engineering and Technology, 2004.

[3] H. M. Jol, *Ground Penetrating Radar: Theory and Applications.* Elsevier, 2009.

[4] D. J. Daniels, "GPR Design Challenges, COST Action TU1208, in *Proc. The 1st Action's Gen. Meet. of the COST Action TU1208*, Rome, Italy, 2013.

[5] R. Persico, *Introduction to Ground Penetrating Radar*. Wiley-IEEE Press, 2014.

[6] A. Benedetto and L. Pajewski, *Civil Engineering Applications of Ground Penetrating Radar*. Springer, 2015.

[7] F. Finck, "Introduction of a ground penetrating radar system for investigations on concrete structures", *Otto-Graf-Journal*, vol. 14, pp. 35–44, 2003.

[8] R. J. Yelf, "Application of Ground Penetrating Radar to civil and geotechnical engineering", *Electromag. Phenom.*, vol. 7, no. 18, pp. 102–117, 2007.

[9] D. Goodman and S. Piro, *GPR Remote Sensing in Archaeology.* Berlin Heidelberg: Springer, 2013.

[10] L. Pajewski and A. Benedetto, Eds., *Civil Engineering Applications of Ground Penetrating Radar*, Proceedings of COST Action TU1208: First General Meeting, Rome, Italy, 2013.

[11] L. Pajewski and X. Derobert, Eds., *Proceedings of COST Action TU1208: Civil Engineering Applications of Ground Penetrating Radar*, 2014 Working Group Progress Meeting, Nantes, France, 2014.

[12] K. Takahashi, J. Igel, H. Preetz, and S. Kuroda, "Basics and application of Ground-Penetrating Radar as a tool for monitoring irrigation process", in *Problems, Perspectives and Challenges of Agricultural Water Management*, M. Kumar, Ed. InTech, 2012, pp. 155–180.

[13] A. P. Annan, *Ground Penetrating Radar Principles, Procedures Applications*. Sensors & Software Inc., 2003.

[14] Z.-Q. Zhu, L.-X. Peng, G.-Y. Lu, and S.-W. Mi, "Borehole-GPR numerical simulation of full wave field based on convolutional perfect matched layer boundary", *J. Cent. South Univ.*, vol. 20, no. 3, pp. 764–769, 2013 (doi: 10.1007/s11771-013-1546-3).

[15] S. Lambot, F. André, E. Slob, and H. Vereecken, "Effect of antenna-medium coupling in the analysis of ground-penetrating radar data", *Near Surface Geophys.*, vol. 10, pp. 631–639, 2012.

[16] W. Kang *et al.*, "A Study of antenna configuration for bistatic Ground-Penetrating Radar", in *Proc. of the 16th Int. Conf. of Ground Penetrating Radar (GPR)*, Hong Kong, China, 2016.

[17] H. V. Baghdasaryan, "Method of backward calculation", in *Photonic Devices for Telecommunications: How to Model and Measure*, G. Guekos, Ed. Springer, 1999, pp. 56–65.

[18] H. V. Baghdasaryan and T. M. Knyazyan, "Problem of plane EM wave self-action in multilayer structure: An exact solution", *Optical and Quant. Electron.*, vol. 31, pp. 105–1072, 1999.

[19] H. V. Baghdasaryan and T. M. Knyazyan, "Modelling of strongly nonlinear sinusoidal Bragg gratings by the Method of Single Expression", *Optical and Quant. Electron.*, vol. 32, no. 6-8, pp. 869–883, 2000.

[20] H. V. Baghdasaryan and T. M. Knyazyan, "Method of single expression – an exact solution for wavelength scale 1D photonic structures' computer modeling", *Proceedings of SPIE*, vol. 5260, pp. 141–148, 2003.

[21] H. V. Baghdasaryan, *Basics of the Method of Single Expression: New Approach for Solving Boundary Problems in Classical Electrodynamics*. Yerevan: Chartaraget, 2013.

[22] H. V. Baghdasaryan, T. M. Knyazyan, T. T. Hovhannisyan, M. Marciniak, and L. Pajewski, "Numerical modelling of GPR ground-matching enhancement by a chirped multilayer structure – output of cooperation within COST Action TU1208", EGU General Assembly 2016, Geophysical Research Abstracts, vol. 18, EGU2016-18507, 2016.

[23] Y.-Y. Li, K. Zhao, J.-H. Ren, Y.-L. Ding, and L.-L. Wu, "Analysis of the dielectric constant of Saline-Alkali soils and the effect on radar backscattering coefficient: A Case Study of Soda Alkaline Saline Soils in Western Jilin Province Using RADARSAT-2 Data", *The Scient. World J.*, vol. 2014, Article ID 563015, 2014.

**Hovik V. Baghdasaryan** graduated in Radiophysics from the Yerevan State University in Yerevan, Armenia, in 1971. He received the Ph.D. degree in Physics and Mathematics from the Institute of Radiophysics and Electronics of the Academy of Sciences of Armenia, in 1980. From 1976 to 1982, he was with the Institute of Ra-

diophysics and Electronics of the Academy of Sciences of Armenia as a Junior Research Scientist. From 1983 to 1994, he was with the Research Institute "Lazerayin Tekhnika", Yerevan, Armenia as a Senior Research Scientist. From 1995 to 2016, he was an Associate Professor of Faculty of Radioengineering and Communication Systems at the State Engineering University of Armenia (now National Polytechnic University of Armenia), Yerevan, Armenia. From 2016 he is a Professor at the same Faculty. He is also a Head of Fiber Optics Communication Laboratory of the same university, where his scientific efforts have included work on developing a new non-traditional method of boundary problems solution, called Method of Single Expression (MSE). His main research interests include theory of electromagnetic wave interaction with nonlinear and laser-active media, wave propagation through multilayer and modulated structures, semiconductor and dye laser systems simulation, plasmonics, integrated optoelectronics, fiber optics communication and communication technology. He is a member of OSA. Since 1995 he has been involved in European programmes under different COST Actions. He is a member of the COST Actions TU 1208, MP1403 and MP1401. He is a scientific committee member of International Conference on Transparent Optical Networks (ICTON). He has contributed to a number of national and international conferences and published more than 125 papers in scientific journals and conference proceedings.

E-mail: hovik@seua.am; hovik_b@yahoo.com
National Polytechnic University of Armenia
105 Terian St
0009 Yerevan, Armenia

**Tamara M. Knyazyan** graduated in Radio-engineering from the Yerevan Polytechnic Institute in Yerevan, Armenia, in 1988. She received the M.Sc. degree in communication means from the State Engineering University of Armenia (now National Polytechnic University of Armenia) in Yerevan, Armenia in 1995, and the Ph.D. degree in Radiophysics from the Yerevan State University in Yerevan, Armenia, in 2000. Her postgraduate research dealt with computer modelling of narrowband nonlinear optical filters for DWDM systems by using the Method of Single Expression (MSE). Since 1995, she has been with the Fiber Optics Communication Laboratory at National Polytechnic University of Armenia, as a Research Scientist, where she is involved in the research works on computer modeling of passive and active multilayer and modulated photonic structures. She joined the Faculty of Radioengineering and Communication Systems at National Polytechnic University of Armenia in 1998 as a Senior Lecturer. From 2005 she is an Associate Professor at the same Faculty. From 2010 to 2015 she was a Head of Chair of Communication Systems at the same Faculty. Since 1995 she has been involved in European programmes under different COST Actions. She is a member of the COST Actions TU 1208, MP1403 and MP1401. Her main research interests include theoretical investigation of electromagnetic waves interaction with 1D multilayer and modulated photonic structures (including intensity dependent), photonics, plasmonics and modelling of fiber optics communication components. She has contributed to a number of national and international conferences and published more than 100 papers in scientific journals and conference proceedings.

E-mail: ktamara@seua.am; tamknyazyan@yahoo.com
National Polytechnic University of Armenia
105 Terian St
0009 Yerevan, Armenia

**Tamara T. Hovhannisyan** graduated in Chemistry from the Yerevan State University, Armenia, in 1976. From 1976 till 1998 she was with ReaKhRom IREA Armenia, as a Scientific Researcher. Since 1998 she has been with Fiber Optics Communication Laboratory at the National Polytechnic University of Armenia as a Research Scientist. Her scientific interests are directed to the numerical analysis of electromagnetic waves interaction with different wavelength-scale multilayer and modulated structures. She has contributed to a number of national and international conferences and published more than 20 papers in scientific journals and conference proceedings. She is member of the COST Actions TU 1208, MP1403 and MP1401.

E-mail: tomi_mark@yahoo.com
National Polytechnic University of Armenia
105 Terian St
0009 Yerevan, Armenia

**Marian Marciniak** graduated in Solid State Physics from Marie Curie-Skłodowska University in Lublin, Poland, in 1977. He holds a Ph.D. degree in Optoelectronics (1989), and a Doctor of Sciences (Habilitation) degree in Physics/ Optics (1997). He is a Professor at the National Institute of Telecommunications, Warsaw, Poland. He has authored over 400 publications, including a number of invited conference presentations. He serves as a Honorary International Advisor to the George Green Institute for Electromagnetics Research, University of

Nottingham, UK. He is the leading organizer of the International Conferences on Transparent Optical Networks ICTON series since 1999. He serves, together with Prof. Trevor Benson and Prof. Yaping Zhang, as The Editor-in-Chief of Optical and Quantum Electronics journal. He served as the Chairman of COST Action MP0702 "Towards Functional Sub-Wavelength Photonic Structures" (2008–2012). He is a Management Committee Member and the Short-Term Scientific Mission Manager of COST Action TU1208 "Civil Engineering Applications of Ground Penetrating Radar".

E-mail: M.Marciniak@itl.waw.pl;
marian.marciniak@ieee.org
National Institute of Telecommunications
1 Szachowa St
04-894 Warsaw, Poland

**Lara Pajewski** – for biography, see this issue, p. 29.

Paper

# Advanced Inversion Techniques for Ground Penetrating Radar

Alessandro Fedeli, Matteo Pastorino, and Andrea Randazzo

*Department of Electrical, Electronic, Telecommunications Engineering, and Naval Architecture (DITEN), University of Genoa, Genova, Italy*

https://doi.org/10.26636/jtit.2017.119717

**Abstract—Ground Penetrating Radar (GPR) systems are nowadays standard inspection tools in several application areas, such as subsurface prospecting, civil engineering and cultural heritage monitoring. Usually, the raw output of GPR is provided as a B-scan, which has to be further processed in order to extract the needed information about the inspected scene. In this framework, inverse-scattering-based approaches are gaining an ever-increasing interest, thanks to their capabilities of directly providing images of the physical and dielectric properties of the investigated areas. In this paper, some advances in the development of such inversion techniques in the GPR field are revised and discussed.**

***Keywords—electromagnetic scattering, Ground Penetrating Radar, inverse problems.***

## 1. Introduction

Ground Penetrating Radar (GPR) imaging has attracted a lot of interest in the last years. Nowadays, GPR systems are used in a great variety of research and application areas, including civil engineering [1]–[3], archaeological and geophysical prospecting [4], and cultural heritage monitoring [5]. Besides these classical areas, novel applications, such as through-wall imaging [6], contaminant detection [7], [8], tunnel and underground facility detection [9], and planet exploration [10], are attracting an ever-increasing attention.

In order to obtain accurate GPR images, it is necessary to carefully design the different parts of the system, ranging from the acquisition hardware to the signal processing algorithms needed to interpret the data. Moreover, there are usually several requirements, such as portability of the imaging systems, ultra-wide-band behavior, and limited coupling between transmitting and receiving antennas, which must be suitably considered in the GPR design and realization.

Concerning the data interpretation, there is also the need for performing some preparatory steps. In fact, usually scattered field extraction procedures must be employed in order to isolate the scattering contribution in the measured electromagnetic field data and to suppress the effects of clutter [11]. Moreover, it is needed to obtain a satisfactory estimate of the dielectric properties of the background medium [12] and to develop appropriate forward scattering models [13], [14]. Antennas also represent key elements in the development of effective imaging systems. In fact, since they are located in close proximity with the ground (or more generally, with the host medium) accurate antenna characterizations are needed [15], [16].

Although GPR is now a standard inspection tool, there are still open issues that must be faced in order to further enhance the imaging capabilities. In particular, GPRs usually provide the output images in the form of B-scans, i.e. two-dimensional representations of the amplitude of the acquired scattered field data versus position and time. Such images can be quite difficult to interpret, especially when dealing with complex embedding media. Significant improvements can be obtained by reformulating the image formation process as an electromagnetic inverse scattering problem, where the main parameters describing the inspected scene are retrieved by inverting a proper model describing the scattering phenomena.

Several research groups around the world follow this point of view and very interesting numerical and experimental results have been already reported in the scientific literature. In this paper, some recent advances concerning the development of inverse scattering procedures for GPR imaging are revised and discussed.

## 2. GPR Imaging as an Inverse Problem

Subsurface imaging requires to solve an electromagnetic inverse scattering problem [17], i.e. starting from measurements of the scattered electric field collected in a proper measurement domain (e.g. a line over the air-ground interface), the aim is to retrieve some parameters describing the buried targets. Such parameters can be the full distributions of the dielectric properties or some features able to describe the target (e.g. its shape and position). As it is well known, such kind of problems turns out to be non-linear [18] and ill-posed [19]. Consequently, special care is required in the development of effective solving strategies.

### *2.1. Quantitative Electromagnetic Inversion*

In the scientific literature, several methods have been proposed for tackling this task, not only in the field of subsurface imaging [20]–[24]. When a quantitative reconstruc-

tion is needed, e.g. when the aim is to retrieve the whole dielectric distribution of the inspected region, the full non-linear problem must be taken into account. In this case, the imaging problem is usually recast as an optimization problem. Newton-like iterative methods [25]–[27] and gradient based solution procedures [28]–[30] are often used in this case. However, such approaches suffer from local minima problems [31], and thus are quite sensitive to the availability of a suitable starting guess. Stochastic minimization schemes have also been largely used [32]–[34]. These methods are in principle able to overcome the problem of local minima, but their numerical complexity is often higher than the one of deterministic approaches.

The imaging problem can be simplified by using linearized scattering models, e.g. by exploiting Born or Rytov approximations [17] in the case of penetrable scatterers and the Kirchhoff one for metallic objects. It is worth noting that the class of scatterers for which linear models effectively work is limited, and consequently, they usually do not allow a quantitative reconstruction. Anyway, such approaches are able to detect, localize and provide rough information about the scatterers' shape [35]. Moreover, linear estimations can be used to provide a starting point for non-linear quantitative approaches. In all cases, ill-posedness still remains an issue and consequently there is a need to employ some regularization scheme able to increase the stability versus noise [19].

### *2.2. Other GPR Imaging Techniques*

In the framework of GPR imaging, migration algorithms are still being used for obtaining qualitative reconstructions of the inspected scene. Although such approaches have been initially developed in the framework of seismic imaging starting from qualitative concepts, they can be derived from approximated linear scattering models [36]. Some of the main approaches belonging to such class are back-propagation [37], time-reversal [38], and omega-kappa algorithms [39].

Beside the previous approaches, other qualitative methods, aimed at directly retrieving only a limited set of information about the embedded scatterers (e.g. their positions and external supports), have also been proposed. The linear sampling [40], the factorization, and the MUltiple SIgnal Classification (MUSIC) methods [41] belong to this class of inversion algorithms.

## 3. Recent Advancements in the Development of Inversion Techniques for GPR Imaging

In the last few years, several research activities have been performed in order to increase the imaging capabilities of GPR systems. In particular, beside the development of novel inverse-scattering schemes, also methods for background removal and clutter rejection, soil models and medium estimation procedures, and GPR antenna modeling as well as deconvolution techniques have been proposed. Moreover, efficient approaches for solving the forward scattering problem by buried structures have also been developed.

### *3.1. Nonlinear Inverse Scattering Methods*

Concerning the development of novel inverse-scattering schemes, several different approaches that extend and combine various methods previously mentioned have been discussed and evaluated in the scientific literature. Iterative multi-scale strategies have been proposed in [42]–[45], allowing an efficient usage of the limited amount of available information. In such techniques, the inspected area is iteratively reconstructed at different scales and at each scale specific inversion methods are used to obtain a quantitative reconstruction of the dielectric properties. Compressive sensing techniques have also been successfully applied in the field of GPR imaging [46]–[48]. In such approaches, the imaging problem is recast as a minimization in $L^1$ functional spaces. Consequently, sparse solutions (with respect to a properly selected basis) are obtained. Non-linear inversion algorithms performing a regularization in $L^p$ Banach spaces (with $p$ greater than 1) have also been recently proposed in [49], [50]. Such methods have been found to be very effective in reconstructing small targets and in reducing over smoothing and background artifacts with respect to standard inversion in the Hilbert space ($p = 2$).

### *3.2. Linear Inverse Scattering Techniques*

Linear strategies have been considered, too. For example, in [51] a tomographic approach based on a truncated singular value decomposition (TSVD) inversion procedure has been compared to common procedures creating three-dimensional images by interpolating two-dimensional reconstructions. The problem of imaging buried targets from airborne gathered scattered field data has also been addressed in in [52] by using linear techniques.

### *3.3. Qualitative Approaches and Sampling Methods*

Concerning the use of qualitative techniques, subspace-based approaches [53] and sampling methods [54] have been found to be quite effective. It is worth noting that sampling techniques able to provide quantitative reconstructions have also been recently developed [55], [56]. Approaches devoted to the localization and shaping of targets have also been reported. As an example, a technique belonging to this class has been presented in [57]–[59]. The positions of buried targets are detected by estimating the scattered field directions of arrival through subarrays processing followed by a statistical filtering and a triangularization technique.

Real-time detection of multiple buried scatterers has also been attained by using learning based techniques such as Support Vector Machines (SVM) [60].

### *3.4. Preprocessing Methods*

Several novel algorithmic solutions have also been proposed for the preprocessing stage needed to successfully apply inverse scattering methods. Concerning the background removal and surface clutter mitigation problem, several strategies have been proposed in the past. Although average trace subtraction is often used for its simplicity, more effective approaches could enhance the reconstruction quality. As an example, in [61] a time-gating entropy based method is presented, which is able to provide better reconstructions than standard methods.

### *3.5. Soil Properties Estimation*

The development of soil models and medium estimation procedures is also of great interest. In fact, such information is always required for correctly defining the electromagnetic models used in the inversion procedures. For example, in [62] an efficient algorithm for the computation of the time domain reflection coefficient in the transverse magnetic (TM) case has been developed in order to better characterize the surface reflections. In [63], [64] subspace methods and learning-based strategies have been used for the estimation of time delays, permittivity and roughness parameters within pavement structures. Estimation of specific soil parameters (e.g., moisture and clay content) have also been addressed in [65]. Moreover, in [12], [66], [67] inversion approaches have been employed for determining ground water contents in hydrological applications.

### *3.6. Inclusion of Advanced Antenna Models*

Because of the complexity of the inverse problem which has to be solved in GPR imaging, reconstruction procedures can be significantly improved including detailed models of the involved antennas [68], [69]. These models can in principle allow to avoid the introduction of strong simplifying approximations, which clearly degrade the inversion results. The combination of far-field antenna models with a tomographic linear inverse scattering method (under the Born approximation) has been proposed in [70]. More recently, near-field models have been developed and included in inversion techniques [16], [71], [72].

### *3.7. Validation of GPR Inversion Approaches*

In the development of inverse scattering methods, the validation of results is crucial. Frequently, inversion techniques are tested using synthetic data, and sometimes with experimental measurements (where experimental facilities are available). However, it is difficult to compare different approaches without a common benchmark. In this respect, it is worth noting that in the framework of the COST Action TU1208 "Civil Engineering Applications of Ground Penetrating Radar" an open database of radargrams is available [73]. This database, which contains both synthetic and experimental data (e.g., radargrams of concrete cells, roads, trees, columns, bridges, and so on) can be exploited by researchers for testing and comparing the performance of GPR inversion techniques. A contribution to this initiative has also been represented by the GPR imaging challenge organized within the IWAGPR 2017 conference [74], where a simulated three-dimensional realistic landmine detection environment has been proposed.

## 4. Conclusions

In this paper, a brief overview about advanced inversion techniques for GPR has been presented. GPR imaging can be seen as an inverse scattering problem, in which the dielectric properties of the buried targets have to be estimated starting from measurements of the electromagnetic field. With respect to free space configurations, the problem is more challenging. Therefore, the estimation of the soil properties and the use of advanced antenna models act important roles. Of course, several kinds of solution techniques can be adopted. In particular, both quantitative (linear and nonlinear) and qualitative approaches have been considered, discussing some of the recent research trends.

## Acknowledgements

This work benefited from the networking activities within the EU funded COST Action TU1208, "Civil Engineering Applications of Ground Penetrating Radar".

## References

[1] A. Benedetto and L. Pajewski, *Civil engineering applications of ground penetrating radar*. Springer, 2015.

[2] J. Hugenschmidt and A. Kalogeropoulos, "The inspection of retaining walls using GPR", *J. of Appl. Geophys.*, vol. 67, no. 4, pp. 335–344, 2009.

[3] A. Randazzo and C. Estatico, "A regularisation scheme for electromagnetic inverse problems: application to crack detection in civil structures", *Nondestruc. Testing and Evaluation*, vol. 27, no. 3, pp. 189–197, 2012.

[4] L. B. Conyers, *Ground-penetrating radar for archaeology*. Rowman Altamira, 2004.

[5] N. Masini, R. Persico, and E. Rizzo, "Some examples of GPR prospecting for monitoring of the monumental heritage", *J. of Geophys. and Engin.*, vol. 7, no. 2, p. 190–199, 2010.

[6] E. J. Baranoski, "Through-wall imaging: Historical perspective and future directions", *J. of the Franklin Institute*, vol. 345, no. 6, pp. 556–569, 2008.

[7] M. J. Bevan, A. L. Endres, D. L. Rudolph, and G. Parkin, "The non-invasive characterization of pumping-induced dewatering using ground penetrating radar", *J. of Hydrol.*, vol. 281, no. 1-2, pp. 55–69, 2003.

[8] J. L. Porsani, W. M. Filho, V. R. Elis, F. Shimeles, J. C. Dourado, and H. P. Moura, "The use of GPR and VES in delineating a contamination plume in a landfill site: a case study in SE Brazil", *J. of Appl. Geophys.*, vol. 55, no. 3-4, pp. 199–209, 2004.

[9] L. Lo Monte, D. Erricolo, F. Soldovieri, and M. C. Wicks, "Radio frequency tomography for tunnel detection", *IEEE Trans. on Geosci. and Remote Sensing*, vol. 48, no. 3, pp. 1128–1137, 2010.

[10] T. R. Watters *et al.*, "MARSIS radar sounder evidence of buried basins in the northern lowlands of Mars", *Nature*, vol. 444, no. 7121, pp. 905–908, 2006.

[11] O. Lopera, N. Milisavljević, and S. Lambot, "Clutter reduction in GPR measurements for detecting shallow buried landmines: a Colombian case study", *Near Surface Geophys.*, vol. 5, no. 9, pp. 57–64, 2007.

[12] J. Minet, S. Lambot, E. C. Slob, and M. Vanclooster, "Soil surfaces water content estimation by full-waveform GPR signal inversion in the presence of thin layers", *IEEE Trans. on Geosci. and Remote Sensing*, vol. 48, no. 3, pp. 1138–1150, 2010.

[13] F. Frezza, L. Pajewski, C. Ponti, G. Schettini, and N. Tedeschi, "Cylindrical-wave approach for electromagnetic scattering by subsurface metallic targets in a lossy medium", *J. of Appl. Geophys.*, vol. 97, pp. 55–59, 2013.

[14] I. Giannakis, A. Giannopoulos, and C. Warren, "A realistic FDTD numerical modeling framework of ground penetrating radar for landmine detection", *IEEE J. of Selec. Topics in Appl. Earth Observ. and Remote Sensing*, vol. 9, no. 1, pp. 37–51, 2016 (doi: 10.1109/JSTARS.2015.2468597).

[15] N. Diamanti and A. P. Annan, "Characterizing the energy distribution around GPR antennas", *J. of Appl. Geophys.*, vol. 99, pp. 83–90, 2013.

[16] A. Tran, C. Warren, F. André, A. Giannopoulos, and S. Lambot, "Numerical evaluation of a full-wave antenna model for near-field applications", *Near Surface Geophys.*, vol. 11, no. 2, pp. 155–165, 2013.

[17] M. Pastorino, *Microwave Imaging.* Hoboken: Wiley, 2010.

[18] W. C. Chew, *Waves and Fields in Inhomogenous Media*. Wiley, 1999.

[19] M. Bertero and P. Boccacci, *Introduction to inverse problems in imaging.* Bristol, UK: IOP Publishing, 1998.

[20] C. Dourthe, C. Pichot, J. Y. Dauvignac, and J. Cariou, "Inversion algorithm and measurement system for microwave tomography of buried object", *Radio Science*, vol. 35, no. 5, pp. 1097–1108, 2000.

[21] M. Benedetti, M. Donelli, A. Martini, M. Pastorino, A. Rosani, and A. Massa, "An innovative microwave-imaging technique for nondestructive evaluation: Applications to civil structures monitoring and biological bodies inspection", *IEEE Trans. on Instrument. and Measur.*, vol. 55, no. 6, pp. 1878–1884, 2006.

[22] M. A. Ali and M. Moghaddam, "3D nonlinear super-resolution microwave inversion technique using time-domain data", *IEEE Trans. on Antenn. and Propag.*, vol. 58, no. 7, pp. 2327–2336, 2010.

[23] G. A. Meles, J. Van der Kruk, S. A. Greenhalgh, J. R. Ernst, H. Maurer, and A. G. Green, "A new vector waveform inversion algorithm for simultaneous updating of conductivity and permittivity parameters from combination crosshole/borehole-to-surface GPR data", *IEEE Trans. on Geosc. and Remote Sensing*, vol. 48, no. 9, pp. 3391–3407, 2010.

[24] C. Patriarca, S. Lambot, M. R. Mahmoudzadeh, J. Minet, and E. Slob, "Reconstruction of sub-wavelength fractures and physical properties of masonry media using full-waveform inversion of proximal penetrating radar", *J. of Appl. Geophys.*, vol. 74, no. 1, pp. 26–37, 2011.

[25] T. J. Cui, W. C. Chew, A. A. Aydiner, and S. Chen, "Inverse scattering of two-dimensional dielectric objects buried in a lossy earth using the distorted Born iterative method", *IEEE Trans. on Geosci. and Remote Sensing*, vol. 39, no. 2, pp. 339–346, 2001.

[26] C. Estatico, M. Pastorino, and A. Randazzo, "A novel microwave imaging approach based on regularization in Lp Banach spaces", *IEEE Trans. on Antenn. and Propag.*, vol. 60, no. 7, pp. 3373–3381, 2012.

[27] C. Estatico, M. Pastorino, and A. Randazzo, "An inexact-Newton method for short-range microwave imaging within the second-order Born approximation", *IEEE Trans. on Geosci. and Remote Sensing*, vol. 43, no. 11, pp. 2593–2605, 2005.

[28] H. Harada, D. J. N. Wall, T. Takenaka, and M. Tanaka, "Conjugate gradient method applied to inverse scattering problem", *IEEE Trans. on Antenn. and Propag.*, vol. 43, no. 8, pp. 784–792, 1995.

[29] T. Isernia, V. Pascazio, and R. Pierri, "A nonlinear estimation method in tomographic imaging", *IEEE Trans. on Geosci. and Remote Sensing*, vol. 35, no. 4, pp. 910–923, 1997.

[30] P. M. van den Berg and A. Abubakar, "Contrast source inversion method: state of art", *Progress in Electromag. Res.*, vol. 34, pp. 189–218, 2001.

[31] T. Isernia, V. Pascazio, and R. Pierri, "On the local minima in a tomographic imaging technique", *IEEE Trans. on Geosci. and Remote Sensing*, vol. 39, no. 7, pp. 1596–1607, 2001.

[32] Y. Rahmat-Samii and E. Michielssen, Eds., *Electromagnetic Optimization by Genetic Algorithms*, 1st ed. New York, NY: Wiley, 1999.

[33] M. Pastorino, "Stochastic optimization methods applied to microwave imaging: a review", *IEEE Trans. on Antenn. and Propag.*, vol. 55, no. 3, pp. 538–548, 2007.

[34] A. Randazzo, "Swarm optimization methods in microwave imaging", *International Journal of Microwave Science and Technology*, vol. 2012, Article ID 491713, 2012.

[35] M. Slaney, A. C. Kak, and L. E. Larsen, "Limitations of imaging with first-order diffraction tomography", *IEEE Trans. on Microw. Theory and Techniq.*, vol. 32, no. 8, pp. 860–874, 1984.

[36] F. Soldovieri and R. Solimene, "Ground penetrating radar subsurface imaging of buried objects", in *Radar Technology*, G. Kouemou, Ed. InTech, 2010.

[37] T. B. Hansen and P. M. Johansen, "Inversion scheme for ground penetrating radar that takes into account the planar air-soil interface", *IEEE Trans. on Geosci. and Remote Sensing*, vol. 38, no. 1, pp. 496–506, 2000.

[38] M. Fink, "Time reversal of ultrasonic fields. I. Basic principles", *IEEE Trans. on Ultrasonics, Ferroelec., and Frequen. Control*, vol. 39, no. 5, pp. 555–566, 1992.

[39] C. Cafforio, C. Prati, and F. Rocca, "SAR data focusing using seismic migration techniques", *IEEE Trans. on Aerospace and Elec. Syst.*, vol. 27, no. 2, pp. 194–207, 1991.

[40] D. Colton, K. Giebermann, and P. Monk, "A regularized sampling method for solving three-dimensional inverse scattering problems", *SIAM J. on Scient. Comput.*, vol. 21, no. 6, pp. 2316–2330, 2000.

[41] E. A. Marengo, F. K. Gruber, and F. Simonetti, "Time-reversal MUSIC imaging of extended targets", *IEEE Trans. on Image Process.*, vol. 16, no. 8, pp. 1967–1984, 2007.

[42] M. Salucci, L. Poli, N. Anselmi, and A. Massa, "Multifrequency particle swarm optimization for enhanced multiresolution GPR microwave imaging", *IEEE Trans. on Geosci. and Remote Sensing*, vol. 55, no. 3, pp. 1305–1317, 2017.

[43] M. Salucci, L. Poli, and A. Massa, "Advanced multi-frequency GPR data processing for non-linear deterministic imaging", *Signal Process.*, vol. 132, pp. 306–318, 2017.

[44] M. Salucci, G. Oliveri, and A. Massa, "GPR prospecting through an inverse-scattering frequency-hopping multifocusing approach", *IEEE Trans. on Geosci. and Remote Sensing*, vol. 53, no. 12, pp. 6573–6592, 2015.

[45] M. Salucci, G. Oliveri, A. Randazzo, M. Pastorino, and A. Massa, "Electromagnetic subsurface prospecting by a fully nonlinear multifocusing inexact Newton method", *J. of the Opt. Soc. of America A*, vol. 31, no. 12, pp. 2618–2629, 2014.

[46] L. Poli, G. Oliveri, P. P. Ding, T. Moriyama, and A. Massa, "Multifrequency Bayesian compressive sensing methods for microwave imaging", *J. of the Opt. Soc. of America A*, vol. 31, no. 11, pp. 2415–2428, 2014.

[47] A. Massa, P. Rocca, and G. Oliveri, "Compressive sensing in electromagnetics - a review", *IEEE Antenn. and Propag.n Mag.*, vol. 57, no. 1, pp. 224–238, 2015.

[48] M. Ambrosanio and V. Pascazio, "A compressive-sensing-based approach for the detection and characterization of buried objects", *IEEE J. of Selec.Topics in Appl. Earth Observ. and Remote Sensing*, vol. 8, no. 7, pp. 3386–3395, 2015.

[49] C. Estatico, A. Fedeli, M. Pastorino, and A. Randazzo, "Buried object detection by means of a Lp Banach-space inversion procedure", *Radio Science*, vol. 50, no. 1, pp. 41–51, 2015.

[50] C. Estatico, A. Fedeli, M. Pastorino, and A. Randazzo, "A multifrequency inexact-Newton method in Lp Banach spaces for buried objects detection", *IEEE Trans. on Antenn. and Propag.*, vol. 63, no. 9, pp. 4198–4204, 2015.

[51] I. Catapano, A. Affinito, G. Gennarelli, F. d. Maio, A. Loperte, and F. Soldovieri, "Full three-dimensional imaging via ground penetrating radar: assessment in controlled conditions and on field for archaeological prospecting", *Appl. Phys. A*, vol. 115, no. 4, pp. 1415–1422, 2013.

[52] I. Catapano, L. Crocco, Y. Krellmann, G. Triltzsch, and F. Soldovieri, "Tomographic airborne ground penetrating radar imaging: Achievable spatial resolution and on-field assessment", *ISPRS J. of Photogramm. and Remote Sensing*, vol. 92, pp. 69–78, 2014.

[53] R. Solimene, G. Leone, and A. Dell'Aversano, "MUSIC algorithms for rebar detection", *J. of Geophys. and Engin.*, vol. 10, no. 6, p. 064006, 2013.

[54] I. Catapano, L. Crocco, and T. Isernia, "Improved sampling methods for shape reconstruction of 3-D buried targets", *IEEE Trans. on Geosci. and Remote Sensing*, vol. 46, no. 10, pp. 3265–3273, 2008.

[55] L. Di Donato, M. T. Bevacqua, L. Crocco, and T. Isernia, "Inverse scattering via virtual experiments and contrast source regularization", *IEEE Trans. on Antenn. and Propag.*, vol. 63, no. 4, pp. 1669–1677, 2015.

[56] L. Di Donato and L. Crocco, "Model-based quantitative cross-borehole GPR imaging via virtual experiments", *IEEE Trans. on Geosc. and Remote Sensing*, vol. 53, no. 8, pp. 4178–4185, 2015.

[57] A. Sahin and E. L. Miller, "Object detection using high resolution near-field array processing", *IEEE Trans. on Geosci. and Remote Sensing*, vol. 39, no. 1, pp. 136–141, 2001.

[58] S. Meschino, L. Pajewski, M. Pastorino, A. Randazzo, and G. Schettini, "Detection of subsurface metallic utilities by means of a SAP technique: Comparing MUSIC- and SVM-based approaches", *J. of Appl. Geophys.*, vol. 97, pp. 60–68, 2013.

[59] S. Meschino, L. Pajewski, and G. Schettini, "A SAP-DoA method for the localization of two buried objects", *Int. J. of Antenn. and Propag.*, vol. 2013, Article ID e702176, pp. 1–10, 2013 (doi: 10.1155/2013/702176).

[60] E. Bermani, A. Boni, S. Caorsi, and A. Massa, "An innovative real-time technique for buried object detection", *IEEE Trans. on Geosci. and Remote Sensing*, vol. 41, no. 4, pp. 927–931, 2003.

[61] R. Solimene, A. Cuccaro, A. Dell'Aversano, I. Catapano, and F. Soldovieri, "Background removal methods in GPR prospecting", in *Proc. Eur. Radar Conf. EuRAD 2013*, Nuremberg, Germany, 2013, pp. 85–88.

[62] S. Antonijevic and D. Poljak, "A novel time-domain reflection coefficient function: TM case", *IEEE Trans. on Electromag. Compatibil.*, vol. 55, no. 6, pp. 1147–1153, 2013.

[63] C. Le Bastard, Y. Wang, V. Baltazart, and X. Dérobert, "Time delay and permittivity estimation by ground-penetrating radar with support vector regression", *IEEE Geosci. and Remote Sensing Lett.*, vol. 11, no. 4, pp. 873–877, 2014.

[64] M. Sun, N. Pinel, C. L. Bastard, V. Baltazart, A. Ihamouten, and Y. Wang, "Time delay and surface roughness estimation by subspace algorithms for pavement survey by radar", in *7th Int. Worksh. on Adv. Ground Penetrating Radar IWAGPR 2013*, Nantes, France, 2013, pp. 1–6.

[65] A. Di Matteo, E. Pettinelli, and E. Slob, "Early-time GPR signal attributes to estimate soil dielectric permittivity: A theoretical study", *IEEE Trans. on Geosci. and Remote Sensing*, vol. 51, no. 3, pp. 1643–1654, 2013.

[66] N. Gueting, A. Klotzsche, J. van der Kruk, J. Vanderborght, H. Vereecken, and A. Englert, "Imaging and characterization of facies heterogeneity in an alluvial aquifer using GPR full-waveform inversion and cone penetration tests", *J. of Hydrology*, vol. 524, pp. 680–695, 2015.

[67] A. R. Mangel, S. M. J. Moysey, and J. van der Kruk, "Resolving precipitation induced water content profiles by inversion of dispersive GPR data: A numerical study", *J. of Hydrology*, vol. 525, pp. 496–505, 2015.

[68] S. Lambot, E. C. Slob, I. van den Bosch, B. Stockbroeckx, and M. Vanclooster, "Modeling of Ground-Penetrating Radar for accurate characterization of subsurface electric properties", *IEEE Trans. on Geosci. and Remote Sensing*, vol. 42, no. 11, pp. 2555–2568, 2004.

[69] F. André and S. Lambot, "Intrinsic modeling of near-field electromagnetic induction antennas for layered medium characterization. *IEEE Trans. on Geosci. and Remote Sensing*, vol. 52, no. 11, pp. 7457–7469, 2014.

[70] F. Soldovieri, O. Lopera, and S. Lambot, "Combination of advanced inversion techniques for an accurate target localization via GPR for demining applications", *IEEE Trans. on Geosci. and Remote Sensing*, vol. 49, no. 1, pp. 451–461, 2011.

[71] A. P. Tran, F. André, and S. Lambot, "Validation of near-field Ground-Penetrating Radar modeling using full-wave inversion for soil moisture estimation", *IEEE Trans. on Geosci. and Remote Sensing*, vol. 52, no. 9, pp. 5483–5497, 2014.

[72] A. De Coster, A. P. Tran, and S. Lambot, "Fundamental analyses on layered media reconstruction using GPR and full-wave inversion in near-field conditions", *IEEE Trans. on Geosci. and Remote Sensing*, vol. 54, no. 9, pp. 5143–5158, 2016.

[73] L. Pajewski, "The open database of experimental and synthetic GPR radargrams", COST Action TU1208, 2016 [Online]. Available: http://gpradar.eu/onewebmedia/TU1208%20TS%20Split%20-%20Pajewski%20-%20Database%20of%20radargrams.pdf

[74] "GPR imaging challenge", 9th Int. Worksh. on Advanced Ground Penetrating Radar IWAGPR 2017, Edinburgh, Scotland, 2017 [Online]. Available: https://github.com/gprMax/iwagpr2017-model

**Alessandro Fedeli** received the B.Sc. and the M.Sc. in Electronic Engineering from the University of Genoa (Italy) in 2011 and 2013, respectively. In 2017 he received the Ph.D. degree in Science and Technology for Electronic and Telecommunications Engineering from the same University. His research activity is mainly focused on microwave imaging and computational methods for the solution of forward and inverse electromagnetic scattering problems. He is interested in biomedical imaging applications and advanced processing techniques for Ground Penetrating Radar (GPR) systems. He is WG Member of the COST Action TU1208 "Civil Engineering Applications of Ground Penetrating Radar", and Member of the IEEE Antennas and Propagation Society.

E-mail: alessandro.fedeli@edu.unige.it
Department of Electrical, Electronic, Telecommunications Engineering, and Naval Architecture
University of Genoa
Via Opera Pia, 11A
I-16145 Genova, Italy

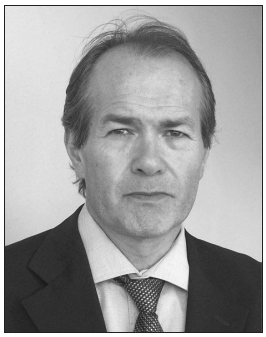

**Matteo Pastorino** is a Full Professor of electromagnetic fields at the Polytechnic School of the University of Genoa, where he has been the past Director of the Department of Biophysical and Electronic Engineering (DIBE, 2008–2011) and the past Director of the Department of Electrical, Electronic, Telecommunications Engineering and Naval Architecture (DITEN, 2011–2013). At present, he is a Fellow of the IEEE, the Chair of the National URSI Commission B (Fields and Waves), the responsible for the local section of the National Society of Electromagnetics (SIEM), and the chair of the local section of the Interuniversity Center for the Interaction between Electromagnetic Fields and Biosystems (ICEmB). He has coauthored about 450 papers in international journals and conference proceedings in the field of applied electromagnetics. Prof. Pastorino is an Associate Editor of the *IEEE Antennas and Propagation Magazine* and of the *IEEE Transactions on Instrumentation and Measurement*.

E-mail: matteo.pastorino@unige.it
Department of Electrical, Electronic, Telecommunications Engineering, and Naval Architecture
University of Genoa
Via Opera Pia, 11A
I-16145 Genova, Italy

**Andrea Randazzo** received the laurea degree in Telecommunication Engineering from the University of Genoa, Genoa, Italy, in 2001 and the Ph.D. degree in Information and Communication Technologies from the same university in 2006. Currently, he is an Associate Professor at the Department of Electrical, Electronic, Telecommunications Engineering, and Naval Architecture of the University of Genoa. His primary research interests are in the field of electromagnetic scattering (both direct and inverse), smart antennas, and numerical methods for microwave nondestructive evaluations and imaging.

E-mail: andrea.randazzo@unige.it
Department of Electrical, Electronic, Telecommunications Engineering, and Naval Architecture
University of Genoa
Via Opera Pia, 11A
I-16145 Genova, Italy

Paper

# SPOT-GPR: A Freeware Tool for Target Detection and Localization in GPR Data Developed within the COST Action TU1208

Simone Meschino[1] and Lara Pajewski[2]

[1] *Airbus Defence and Space, Friedrichshafen, Germany*
[2] *Department of Information Engineering, Electronics and Telecommunications, Sapienza University of Rome, Rome, Italy*

https://doi.org/10.26636/jtit.2017.121017

**Abstract—SPOT-GPR (release 1.0) is a new freeware tool implementing an innovative Sub-Array Processing method, for the analysis of Ground-Penetrating Radar (GPR) data with the main purposes of detecting and localizing targets. The software is implemented in Matlab, it has a graphical user interface and a short manual. This work is the outcome of a series of three Short-Term Scientific Missions (STSMs) funded by European COoperation in Science and Technology (COST) and carried out in the framework of the COST Action TU1208 "Civil Engineering Applications of Ground Penetrating Radar" (www.GPRadar.eu). The input of the software is a GPR radargram (B-scan). The radargram is partitioned in sub-radargrams, composed of a few traces (A-scans) each. The multi-frequency information enclosed in each trace is exploited and a set of dominant Directions of Arrival (DoA) of the electromagnetic field is calculated for each sub-radargram. The estimated angles are triangulated, obtaining a pattern of crossings that are condensed around target locations. Such pattern is filtered, in order to remove a noisy background of unwanted crossings, and is then processed by applying a statistical procedure. Finally, the targets are detected and their positions are predicted. For DoA estimation, the MUltiple SIgnal Classification (MUSIC) algorithm is employed, in combination with the matched filter technique. To the best of our knowledge, this is the first time the matched filter technique is used for the processing of GPR data. The software has been tested on GPR synthetic radargrams, calculated by using the finite-difference time-domain simulator gprMax, with very good results.**

***Keywords—Direction-of-Arrival algorithms, Ground-Penetrating Radar, matched filter technique, MUltiple SIgnal Classification (MUSIC), Sub-Array Processing.***

## 1. Introduction

The identification of cables, pipes, conduits and other utilities buried in the soil or embedded in walls, as well as the localization of reinforced elements in concrete structures, are important tasks in civil engineering and have been extensively studied in the last years. The most commonly used non-destructive testing methods exploit electromagnetic waves – a Ground-Penetrating Radar (GPR) [1], [2] illuminates the area of interest by using a transmitting antenna or a set of sources. The echo is collected by a receiving antenna or a set of sensors, then, the recorded radargrams are processed, in order to extract information about the scenario and localize the sought objects [3]–[6].

SPOT-GPR stands for "Sub-array Processing Open Tool for GPR applications" and is a novel freeware tool that can be used for detecting (spotting) targets in a GPR radargram and for estimating their positions. The tool implements an innovative sub-array processing method, based on the use of smart-antenna and radar techniques. It has a Graphical User Interface (GUI) and a short manual, with examples. It was developed during three European COoperation in Science and Technology (COST) Short-Term Scientific Missions (STSMs), as a contribution to the COST Action TU1208 "Civil Engineering Applications of Ground Penetrating Radar" [7]. Those STSMs were carried out in May 2015 [8], [9], January 2016 [10]–[12], and December 2016 – January 2017 [13], [14].

In applications involving smart antennas and in the presence of several transmitters operating simultaneously, it is important for a receiving array to be able to estimate the Directions of Arrival (DoAs) of the incoming signals, in order to decipher how many emitters are present and predict their positions [15], [16]. A number of methods have been devised for DoA estimation: MUltiple SIgnal Classification (MUSIC) [17] and Estimation of Signal Parameters via Rotational Invariance Technique (ESPRIT) [18] are amongst the most popular ones. When a GPR is used to detect and localize targets in the ground or in a structure, the scenario is similar; hence, analogous techniques can be used for target detection and localization. The electromagnetic sources are the currents induced on the sought targets and DoA algorithms can be used for estimating where the electromagnetic field back-scattered by the targets comes from [19]–[22]. However, there are important differences between smart-antenna and GPR problems, which need to be considered and properly treated:

- In GPR scenarios, targets are embedded in a medium different than the one where the GPR antennas are operating: refraction effects occurring at the interface between the air and the host medium cannot be neglected.
- A GPR radargram (usually denominated B-scan), to be processed for predicting the number of targets and their positions, is a set of traces (A-scans) measured by an antenna in different spatial points. Each trace is a vector of electric-field amplitudes measured in a series of instants, within a suitable time window. After recording a trace in a given spatial point, the GPR is moved to the subsequent point, where a new trace is recorded. In smart-antennas applications, instead, the data to be processed are collected by different antennas, which perform their measurements simultaneously. Inasmuch a GPR scenario usually does not change while a radargram is recorded, this difference is not important. The radargram can be treated as if the A-scans were recorded by an array of identical antennas performing simultaneous measurements.
- DoA algorithms assume that the electromagnetic sources are in the far-field region of the receiving array, hence the wavefront illuminating the array can be considered as planar and the dominant angular directions of the impinging field can be estimated. In GPR applications, instead, targets can be present both in the far-field region and near to the antenna. In order to work with DoA algorithms in near-field conditions, we adopted a Sub-Array Processing (SAP) approach [19]: a B-scan is partitioned in sub-radargrams composed of few A-scans each, and the dominant DoA is predicted for each sub-radargram. This method allows to correctly estimate DoAs due to objects that are in the near field of the whole array, as long as they are in the far field of each sub-array. Then, all the estimated angles are triangulated and a set of crossings is obtained, with intersections condensed around object locations. This pattern is filtered, in order to remove the noisy background of unwanted crossings. Finally, the number of targets and their positions are estimated.
- DoA algorithms are conceived by considering a monochromatic or narrowband signal model. They are based on the assumption that the radar is dwelling for a long time on a standing target, gathering the energy in a narrow spectrum of frequencies. Even though this ideal model is adopted in many practical systems (e.g. pulse Doppler radar), the narrowband assumption is too limitative for the GPR case and would lead to a poor spatial localization capability. Moreover, it would impact on the possibility to detect multiple objects. GPR radargrams contain multi-frequency information about the surveyed scenario, which is definitely worth being exploited. Here resides the most innovative part of our method, which takes into account that the radar emits an ultra-wideband signal and exploits the information contained in the entire spectrum of the received signal. In particular, for target-depth estimation (which is more challenging, compared to the estimation of the horizontal position of the target), the matched filter technique is applied [23]. This technique is well known and widely used in other radar applications (such as pulse-doppler, frequency-modulated continuous-wave, and synthetic-aperture radar). However, it does not seem to be used for the processing of radargrams measured by pulsed GPR systems, yet. To the best of our knowledge, our work represents the first application of the matched filter technique for GPR signal processing purposes.

We tested the accuracy of our software tool on synthetic radargrams calculated by using the finite-difference time-domain simulator gprMax [24], with very good results [10], [13].

In Section 2, we provide more information about the approach that we developed and implemented. We also describe the merits and limits of the method.

In Section 3, two examples of application and numerical results are presented. In particular, we use SPOT-GPR for processing the synthetic radargrams obtained for two reference scenarios defined within the COST Action TU1208 [25] (concrete cells with reinforcing elements). We also considered modified versions of such scenarios, where we gradually varied the distances between the reinforcing elements. In this way, we could assess how the electromagnetic interactions between the targets influence the accuracy of our method. We compared the results of proposed method against the classical hyperbola estimation based on a Minimum Mean Square Error technique [26].

In Section 4, conclusions are drawn and plans for future work are outlined.

## 2. Data-processing Approach Implemented in SPOT-GPR 1.0

We developed and implemented a SAP-DoA method that allows detecting target reflections in a GPR radargram and estimating target positions. For the evaluation of horizontal ($x$) positions (i.e. the target positions along the acquired GPR profile), our method is based on a beamforming on-receive technique for cross-range localization [26]. For the evaluation of vertical ($y$) positions (i.e. the target burial depths), which is a more challenging task, proposed method is based on the classic matched-filter technique for range estimation [26]. In Fig. 1, a block diagram of the SAP-DoA method implemented in SPOT-GPR 1.0 is presented.

Our approach operates on the amplitudes of the back-scattered electric field. Hence, as a preliminary step, the radargram of the back-scattered field has to be obtained from the radargram under process where the amplitudes of the total electric field are recorded. The radargram of the

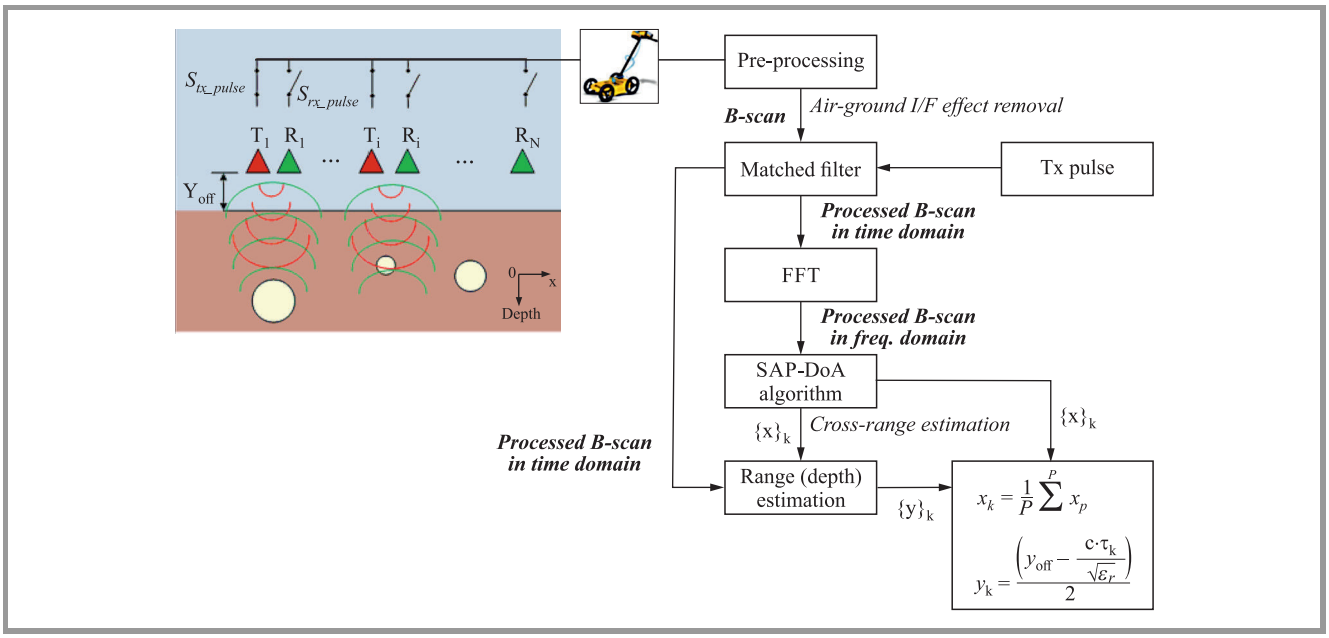


***Fig. 1.*** Block diagram of the signal processing technique implemented in SPOT-GPR 1.0.

back-scattered field can be easily obtained by subtracting a background radargram from the radargram under process. Under the assumption that all the involved media are linear. Let us suppose that the radargram under process includes N A-scans, measured by the GPR in N spatial points along a profile. Then, the background radargram includes N A-scans that would be measured by the GPR in the same spatial points, in the absence of the targets. If the radargram under process is synthetic, the background radargram can be easily produced by using the same electromagnetic simulator that was employed to calculate the radargram under process. If the radargram under process is experimental, an artificial background radargram can be built as follows: the user can select in the B-scan a few traces measured in an area where, for sure, no targets are present (such area has obviously to be far enough from the targets). Then, the selected traces can be averaged and the resulting average trace can be repeated N times.

As was mentioned in the introduction, our approach partitions the radargram of the back-scattered field in sub-radargrams, composed of few traces each. A DoA estimation algorithm is applied to every sub-radargram, for estimating the dominant angle of arrival of the backscattered field. In SPOT-GPR 1.0, the MUSIC algorithm [17] is implemented, which has been widely studied in the literature and is currently the most popular DoA method. Several other high-resolution DoA methods exist. We intend to implement them in the near future and carry out a comparison of their performance when embedded in our approach and applied to GPR scenarios.

By triangulating all the estimated angles, a pattern of intersections (crossings) is obtained. Such intersections are condensed around object locations. The pattern is filtered, in order to remove the noisy background of unwanted crossings [19], [20]. The number of targets and their cross-range (horizontal) positions are estimated by averaging clustered crossings.

DoA algorithms account for a narrowband signal model: they are based on the assumption that the radar is dwelling for a long time on a standing target, gathering the energy in a limited frequency spectrum. Despite this ideal model is used in many practical systems (e.g. pulse Doppler radar), the narrowband assumption is too limitative for the GPR case and would lead to a poor spatial resolution in the vertical direction (the estimation of the target burial depths is more critical than the estimation of their position along the acquisition profile) [8], [9]. Hence, for range estimation, proposed methods adopts the classical matched filter. This technique is widely used in many radar applications but, surprisingly, it does not seem to be used for the processing of GPR radargrams, yet. We carried out a series of tests and the benefits of having integrated this technique into our SAP-DoA approach are significant, in terms of accuracy [10]. Let us call $\{x\}_\mathrm{k}$ the set of horizontal coordinates of the intersections in the filtered crossing pattern (with k=1,...,K, being K the number of intersections in the filtered crossing pattern). For each $x_\mathrm{k} \in \{x\}_\mathrm{k}$, the nearest A-scan is cross-correlated in the time domain with the transmitted pulse. The time instant corresponding to the maximum of the correlated signal $\tau_{obj,\mathrm{k}}$ is used to extract the y-coordinate $y_\mathrm{k}$ for the k-th crossing. Finally, the position $(\hat{x}_{obj},\hat{y}_{obj})$ of each target is estimated by a simple coordinate averaging of all the $\{x,y\}_\mathrm{k}$ pairs located in an area selected by the user via the software GUI.

Let us now underline the main differences between the method implemented in SPOT-GPR, presented in this paper, and a SAP-DoA approach that we proposed and implemented a few years ago. In [19]–[22], the considered scenario was a dielectric lossless half-space hosting circular-section cylindrical targets. The electromagnetic source was

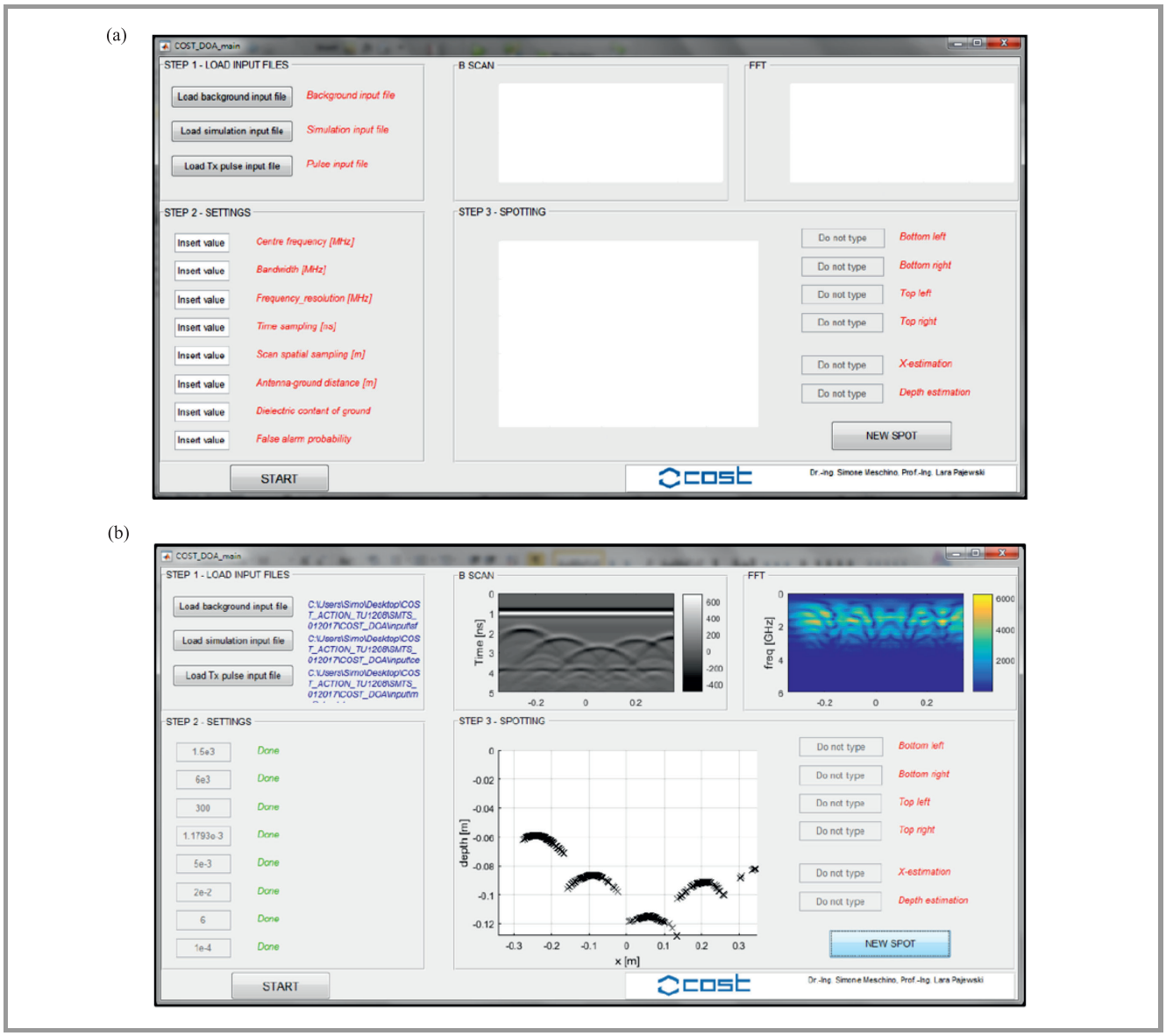


***Fig. 2.*** Layout of the GUI of SPOT-GPR 1.0: (a) screenshot of the input GUI, (b) screenshot of the output GUI.

a monochromatic plane-wave. Spectral-domain results, calculated at a fixed frequency by using the Cylindrical Wave Approach [27], [28], were used as input data for the SAP-DoA method. The old SAP-DoA, indeed, was conceived by considering a monochromatic-signal model. The localization results were satisfactory in the case of one circular-section cylinder and for moderate dielectric contrast between the air and the half-space hosting the target [19]–[21]. The performance of the approach degraded when two interacting cylinders were present, or when the relative permittivity of the soil was increased [22]. The method was not applicable in the presence of more than two cylinders (unless they were very far from each other), because it could not tackle with their electromagnetic interaction. Furthermore, the implemented codes needed a-priori information about the number of sought targets.

The method developed in the framework of the COST Action TU1208 and implemented in SPOT-GPR is more advanced and reliable. It is capable to deal with real GPR radargrams. No a-priori information about the number of targets is needed. Multiple interacting objects, of different size and shape, can be present in the scenario. The electromagnetic source is assumed to be an ultra-wideband signal. The software receives in input the time-domain response of the scenario, measured by the GPR receiving antenna, and is capable to exploit the multi-frequency information contained in it.

The main limitations of SPOT-GPR (release 1.0) are:

- a-priori information is needed concerning the relative permittivity of the medium hosting the targets,
- the method assumes that the medium hosting the target is the medium illuminated by the GPR antenna, i.e. the presence of different media can be taken into account, however they have to be beyond the medium

hosting the targets and not in between such medium and the antennas,

- a-priori information is needed concerning the time-shape of the pulse emitted by the GPR, for the application of the matched-filter technique,
- losses in the media are not taken into account.

We are keen to further develop our method in order to remove those limitations in the near future.
We would like to point out that, commonly, the processing of GPR data for target detection and localization consists in analyzing the hyperbolic reflections found in the radargram. When the electromagnetic pulse emitted by a GPR impinges on a circular-section target embedded in a host medium, the field is scattered and reflected by the target due to the discontinuity of permittivity. As is well known, when the GPR antenna is shifted along the surface between the air and the investigated subsoil/structure, the presence of a circular-section target translates into the recorded radargram as a hyperbola. However, if the target does not have a circular section, its signature in the radargram is not a hyperbola. Hence, the application of the classical hyperbola method for the estimation of its position gives inaccurate results or cannot be applied. Our SAP-DoA approach, instead, is applicable and successful also in the presence of arbitrary-section targets [10].
As mentioned in the introduction, SPOT-GPR 1.0 comes with a GUI. To give an idea, screenshots of the GUI are presented in Fig. 2.
When the software is launched, the graphical interface shown in Fig. 1a appears. This is divided into three main sections, corresponding to three steps to be done by the user in order to obtain the estimation of target positions, namely:

- Step 1 – Load input files: the user is required to select the relevant input files (containing the time shape of the pulse transmitted by the GPR and the data to be processed);
- Step 2 – Settings. The user is required to encode information about some GPR settings used during the measurement;
- Step 3 – Spotting. After the software is executed, the user will be able to interactively drag the mouse on the figure that will appear in the spotting area, in order to extract the estimated positions of the targets.

The GUI output is shown in Fig. 2 and includes the following items:

– a grey-scale map of the synthetic or experimental dataset under analysis (B-scan),

– a color map of the Fast Fourier Transform (FFT) of the compressed simulated/measured dataset,

– the spotting interactive panel, where the user can select an area by simply dragging a rectangular region with the mouse. The relevant estimation of the target positioned in the selected area is provided by the software in the dedicated box, on the right.

More details can be found in the software manual.

# 3. Examples

In this Section, we consider two reference scenarios proposed within the COST Action TU1208, namely the concrete Cells 1-1 and 1-2 designed and studied in [25].
Cell 1-1 hosts five perfectly-conducting (PEC) circular-section reinforcing bars, having different size and placed at different depths with respect to the air/concrete interface: see the sketch reported in Fig. 1a.
Cell 1-2 refers to a more complex scenario, including both conducting and dielectric objects: a PEC rebar, a polyvinyl chloride (PVC) tube filled with air, a PVC tube partially filled with a perfectly-conducting rebar and with air, and finally a steel pipe (see the sketch in Fig. 1b).
The size of both cells is $60 \times 18$ cm in the transverse plane, whereas the length of the cells (and of the reinforcing elements) is 100 cm. The cells are positioned on a compacted fill. Note that in both scenarios the targets are very close to each other: strong electromagnetic interactions take place and, although the geometry of the cells is rather simple, accurate target localization from GPR data is not a trivial task.
For each concrete cell, we simulated four additional configurations where we gradually increased the spacing between adjacent objects with a 5-cm step (as indicated on top of Figs. 1a and 1b).
For the original reference scenarios, synthetic radargrams were already available. They were calculated in [25] by using GprMax2D [29], a free electromagnetic simulator implementing the finite-difference time-domain technique. The new version of the simulator, gprMax [24], was not yet available at that time. For the enlarged versions of the cells, it was necessary to perform new simulations.
In all the simulations, the central frequency of the Ricker pulse emitted by the GPR was $f_c$ = 1.5 GHz. The transmitting antenna (a dipole) and the receiving antenna (not modeled) were at 2 cm from the air-concrete interface (Fig. 3). The distance between the antennas was 10 cm. Results were calculated on a time window of 5 ns, by moving the antennas along a line orthogonal to the axes of the scatterers. The distance between consecutive traces was 5 mm and the time sampling respected the Courant stability condition. The relative permittivity of concrete was $\varepsilon_{r,c} = 6$ and its conductivity was $\sigma_c$ = 0.01 S/m. The relative permittivity of the compacted fill was $\varepsilon_{r,cf}$ = 16 and its conductivity was $\sigma_{cf}$ = 0.005 S/m.
The input files for the original cells are reported in the following, in order to encourage interested Readers to consider the same cells for a possible testing of their inversion/imaging/processing approaches and a comparison with our results. The input files for the enlarged configurations can be easily derived.

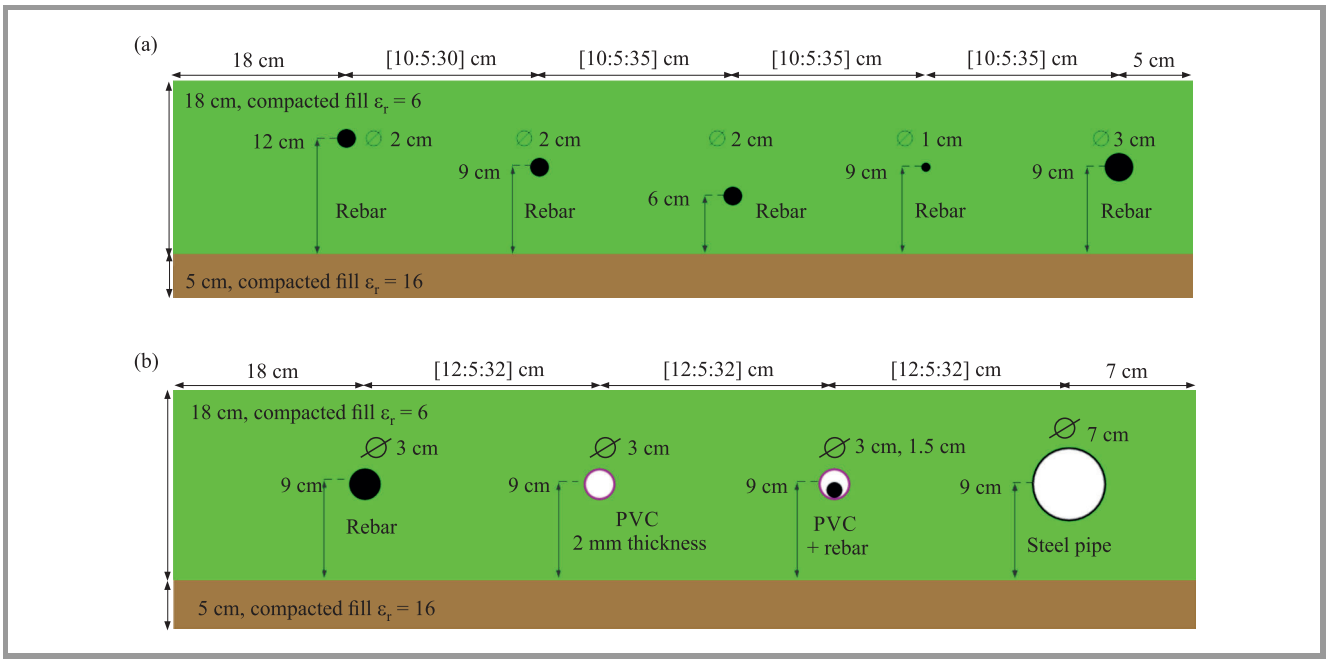


***Fig. 3.*** Test-case geometric model: (a) cell 1-1 – conductive rebars of different size, (b) cell 1-2 – conductive and dielectric objects of different size.

### cell_1-1

```
#medium:  6.0 0.0 0.0 0.01 1.0 0.0 concrete
#medium:  16.0 0.0 0.0 0.005 1.0 0.0 compacted_fill
---------------------------------------------------
#domain:  0.66 0.28
#dx_dy:  0.0005 0.0005
#time_window:  5e-9
#abc_type:  pml
#pml_layers:  10
---------------------------------------------------
#box:  0.0 0.0 0.66 0.05 compacted_fill
#box:  0.03 0.05 0.63 0.23 concrete
---------------------------------------------------
#cylinder:  0.18 0.17 0.01 pec
#cylinder:  0.28 0.14 0.01 pec
#cylinder:  0.38 0.11 0.01 pec
#cylinder:  0.48 0.14 0.005 pec
#cylinder:  0.58 0.14 0.015 pec
---------------------------------------------------
#line_source:  1.0 1500e6 ricker MyLineSource
---------------------------------------------------
#analysis:  100 cell_11_concrete.out b
#tx:  0.03 0.25 MyLineSource 0.0 5e-9
#rx:  0.13 0.25
#tx_steps:  0.005 0.0
#rx_steps:  0.005 0.0
#end_analysis:
---------------------------------------------------
#geometry_file:  cell_11_concrete.out.geo
#title:  Cell 1.1
#messages:  y
```

### cell_1-2

```
#medium:  6.0 0.0 0.0 0.01 1.0 0.0 concrete
#medium:  16.0 0.0 0.0 0.005 1.0 0.0 compacted_fill
#medium:  3.0 0.0 0.0 0.0 1.0 0.0 pvc
---------------------------------------------------
#domain:  0.66 0.28
#dx_dy:  0.0005 0.0005
#time_window:  5e-9
#abc_type:  pml
#pml_layers:  10
---------------------------------------------------
#box:  0.0 0.0 0.66 0.05 compacted_fill
#box:  0.03 0.05 0.63 0.23 concrete
---------------------------------------------------
#cylinder:  0.18 0.14 0.015 pec

#cylinder:  0.3 0.14 0.015 pvc
#cylinder:  0.3 0.14 0.013 free_space

#cylinder:  0.42 0.14 0.015 pvc
#cylinder:  0.42 0.14 0.013 free_space
#cylinder:  0.42 0.1345 0.0075 pec

#cylinder:  0.54 0.14 0.035 pec
#cylinder:  0.54 0.14 0.033 free_space
---------------------------------------------------
#line_source:  1.0 1500e6 ricker MyLineSource
---------------------------------------------------
#analysis:  100 cell_12_concrete.out b
#tx:  0.03 0.25 MyLineSource 0.0 5e-9
#rx:  0.13 0.25
#tx_steps:  0.005 0.0
#rx_steps:  0.005 0.0
#end_analysis:
---------------------------------------------------
#geometry_file:  cell_12_concrete.out.geo
#title:  Cell 1.2
#messages:  y
```

Table 1
Test scenario for Cell 1-1

| Cell 1-1 original | | | |
|---|---|---|---|
| **Object** | **Centre position [m]** | **Radius [m]** | **Material** |
| No. 1 | (0.18, 0.17) | 0.01 | PEC |
| No. 2 | (0.28, 0.14) | 0.01 | |
| No. 3 | (0.38, 0.11) | 0.01 | |
| No. 4 | (0.48, 0.14) | 0.005 | |
| No. 5 | (0.58, 0.14) | 0.015 | |
| **Size of the cell section:** $0.66 \times 0.28$ m$^2$ | | | |
| **No. of A-scans in the radargram:** 100 | | | |
| Cell 1-1 (a) | | | |
| **Object** | **Centre position [m]** | **Radius [m]** | **Material** |
| No. 1 | (0.18, 0.17) | 0.01 | PEC |
| No. 2 | (0.33, 0.14) | 0.01 | |
| No. 3 | (0.48, 0.11) | 0.01 | |
| No. 4 | (0.63, 0.14) | 0.005 | |
| No. 5 | (0.78, 0.14) | 0.015 | |
| **Size of the cell section:** $0.86 \times 0.28$ m$^2$ | | | |
| **No. of A-scans in the radargram:** 140 | | | |
| Cell 1-1 (b) | | | |
| **Object** | **Centre position [m]** | **Radius [m]** | **Material** |
| No. 1 | (0.18, 0.17) | 0.01 | PEC |
| No. 2 | (0.38, 0.14) | 0.01 | |
| No. 3 | (0.58, 0.11) | 0.01 | |
| No. 4 | (0.78, 0.14) | 0.005 | |
| No. 5 | (0.98, 0.14) | 0.015 | |
| **Size of the cell section:** $1.06 \times 0.28$ m$^2$ | | | |
| **No. of A-scans in the radargram:** 180 | | | |
| Cell 1-1 (c) | | | |
| **Object** | **Centre position [m]** | **Radius [m]** | **Material** |
| No. 1 | (0.18, 0.17) | 0.01 | PEC |
| No. 2 | (0.43, 0.14) | 0.01 | |
| No. 3 | (0.68, 0.11) | 0.01 | |
| No. 4 | (0.93, 0.14) | 0.005 | |
| No. 5 | (1.18, 0.14) | 0.015 | |
| **Size of the cell section:** $1.26 \times 0.28$ m$^2$ | | | |
| **No. of A-scans in the radargram:** 220 | | | |
| Cell 1-1 (d) | | | |
| **Object** | **Centre position [m]** | **Radius [m]** | **Material** |
| No. 1 | (0.18, 0.17) | 0.01 | PEC |
| No. 2 | (0.48, 0.14) | 0.01 | |
| No. 3 | (0.78, 0.11) | 0.01 | |
| No. 4 | (1.08, 0.14) | 0.005 | |
| No. 5 | (1.38, 0.14) | 0.015 | |
| **Size of the cell section:** $1.46 \times 0.28$ m$^2$ | | | |
| **No. of A-scans:** 260 | | | |
| General setup | | | |
| **Relative dielectric constant medium 1:** 6 (concrete) | | | |
| **Relative dielectric constant medium 2:** 16 (compact fill) | | | |
| **Trace spacing:** $5 \cdot 10^{-3}$ m | | | |
| **Time window:** $5 \cdot 10^{-9}$ s | | | |
| **Centre frequency:** 1500 MHz (Ricker pulse) | | | |

Table 2
Test scenario for Cell 1-2

| Cell 1-2 original | | | |
|---|---|---|---|
| **Object** | **Centre position [m]** | **Radius [m]** | **Material** |
| No. 1 | (0.18, 0.14) | 0.015 | PEC |
| No. 2 | (0.30, 0.14) | 0.015 | PVC |
| | (0.30, 0.14) | 0.013 | Free space |
| No. 3 | (0.42, 0.14) | 0.015 | PVC |
| | (0.42, 0.14) | 0.013 | Free space |
| | (0.42, 0.1345) | 0.0075 | PEC |
| No. 4 | (0.54, 0.14) | 0.035 | PEC |
| | (0.54, 0.14) | 0.033 | Free space |
| **Size of the cell section:** $0.66 \times 0.28$ m$^2$ | | | |
| **No. of A-scans in the radargram:** 100 | | | |
| Cell 1-2 (a) | | | |
| **Object** | **Centre position [m]** | **Radius [m]** | **Material** |
| No. 1 | (0.18, 0.14) | 0.015 | PEC |
| No. 2 | (0.35, 0.14) | 0.015 | PVC |
| | (0.35, 0.14) | 0.013 | Free space |
| No. 3 | (0.52, 0.14) | 0.015 | PVC |
| | (0.52, 0.14) | 0.013 | Free space |
| | (0.52, 0.1345) | 0.0075 | PEC |
| No. 4 | (0.69, 0.14) | 0.035 | PEC |
| | (0.69, 0.14) | 0.033 | Free space |
| **Size of the cell section:** $0.81 \times 0.28$ m$^2$ | | | |
| **No. of A-scans in the radargram:** 130 | | | |
| Cell 1-2 (b) | | | |
| **Object** | **Centre position [m]** | **Radius [m]** | **Material** |
| No. 1 | (0.18, 0.14) | 0.015 | PEC |
| No. 2 | (0.40, 0.14) | 0.015 | PVC |
| | (0.40, 0.14) | 0.013 | Free space |
| No. 3 | (0.62, 0.14) | 0.015 | PVC |
| | (0.62, 0.14) | 0.013 | Free space |
| | (0.62, 0.1345) | 0.0075 | PEC |
| No. 4 | (0.84, 0.14) | 0.035 | PEC |
| | (0.84, 0.14) | 0.033 | Free space |
| **Size of the cell section:** $0.96 \times 0.28$ m$^2$ | | | |
| **No. of A-scans in the radargram:** 160 | | | |
| Cell 1-2 (c) | | | |
| **Object** | **Centre position [m]** | **Radius [m]** | **Material** |
| No. 1 | (0.18, 0.14) | 0.015 | PEC |
| No. 2 | (0.45, 0.14) | 0.015 | PVC |
| | (0.45, 0.14) | 0.013 | Free space |
| No. 3 | (0.72, 0.14) | 0.015 | PVC |
| | (0.72, 0.14) | 0.013 | Free space |
| | (0.72, 0.1345) | 0.0075 | PEC |
| No. 4 | (0.99, 0.14) | 0.035 | PEC |
| | (0.99, 0.14) | 0.033 | Free space |
| **Size of the cell section:** $1.11 \times 0.28$ m$^2$ | | | |
| **No. of A-scans in the radargram:** 190 | | | |
| Cell 1-2 (d) | | | |
| **Object** | **Centre position [m]** | **Radius [m]** | **Material** |
| No. 1 | (0.18, 0.14) | 0.015 | PEC |
| No. 2 | (0.50, 0.14) | 0.015 | PVC |
| | (0.50, 0.14) | 0.013 | Free space |
| No. 3 | (0.82, 0.14) | 0.015 | PVC |
| | (0.82, 0.14) | 0.013 | Free space |
| | (0.82, 0.1345) | 0.0075 | PEC |
| No. 4 | (1.14, 0.14) | 0.035 | PEC |
| | (1.14, 0.14) | 0.033 | free space |
| **Size of the cell section:** $1.26 \times 0.28$ m$^2$ | | | |
| **No. of A-scans:** 220 | | | |
| General setup | | | |
| **Relative dielectric constant medium 1:** 6 (concrete) | | | |
| **Relative dielectric constant medium 2:** 16 (compact fill) | | | |
| **Trace spacing:** $5 \times 10^{-3}$ m | | | |
| **Time window:** $5 \times 10^{-9}$ s | | | |
| **Centre frequency:** 1500 MHz (Ricker pulse) | | | |

In Tables 1 and 2, the physical and geometrical properties of all the considered cells, as well as the simulation parameters, are resumed.

For each enlarged cell, the relevant synthetic B-scan is presented in Figs. 4 and 5. The B-scans of the original cells can be found in [25] and are not repeated here.

We processed all the simulated radargrams with SPOT-GPR, for detecting and localizing the targets. We compared the results obtained with our software with the results

obtained by using the traditional hyperbola-fitting method. In particular, for what concerns the latter method, we implemented a dedicated procedure, as follows.

The coordinates of each hyperbolic signature in a radargram do not perfectly lie on a hyperbola. For any point $(x_l, y_l)$ lying on the curve of maximum amplitude, the error with respect to the best fitting hyperbola can be defined as:

$$e^2 = \sum_{l=1}^{L} \left(1 - \frac{x_l^2}{a^2} - \frac{y_l^2}{b^2}\right), \tag{1}$$

being $a$ and $b$ the best-fitting-hyperbola semi major and semi minor axes, respectively.

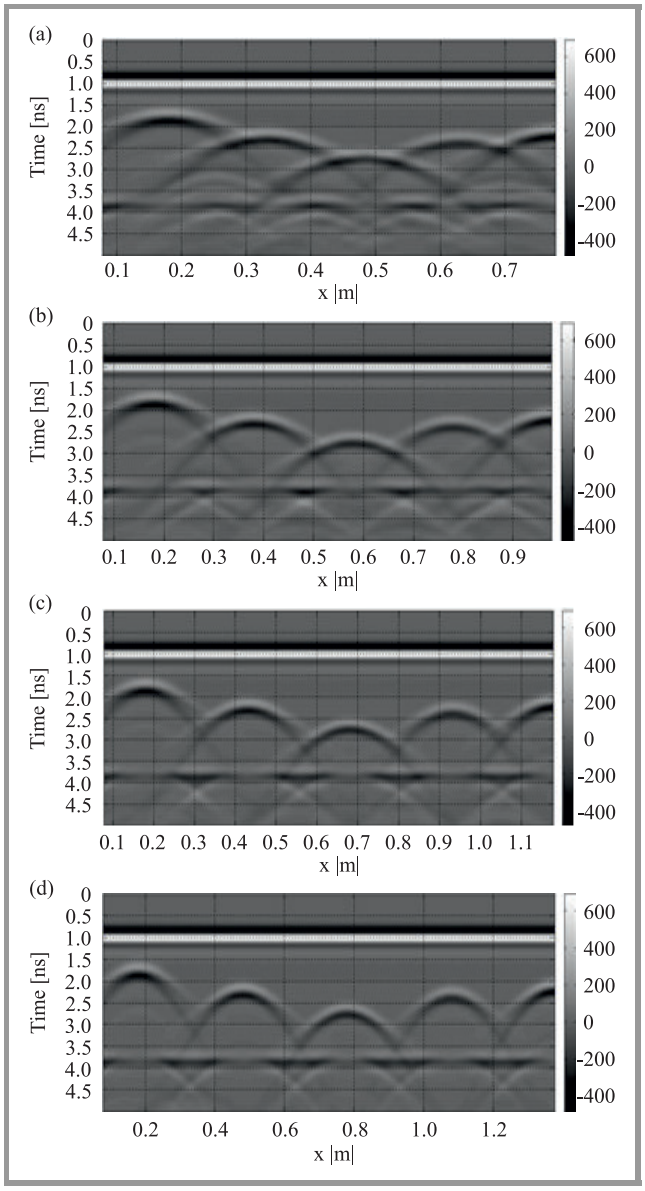


***Fig. 4.*** Radargrams for Cells 1-1 (a)–(d).

The error is therefore a function of the parameters $a$ and $b$, which have to be estimated by minimizing the square error $e^2$. The optimal values are obtainable by differen-

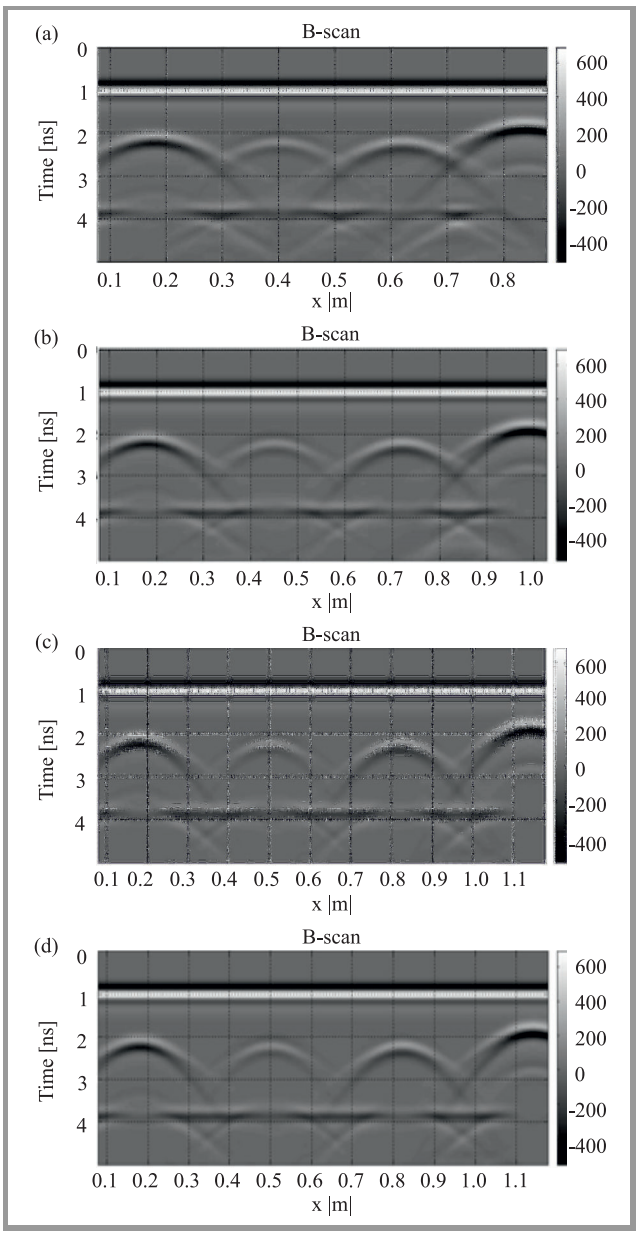


***Fig. 5.*** Radargrams for Cells 1-2 (a)–(d).

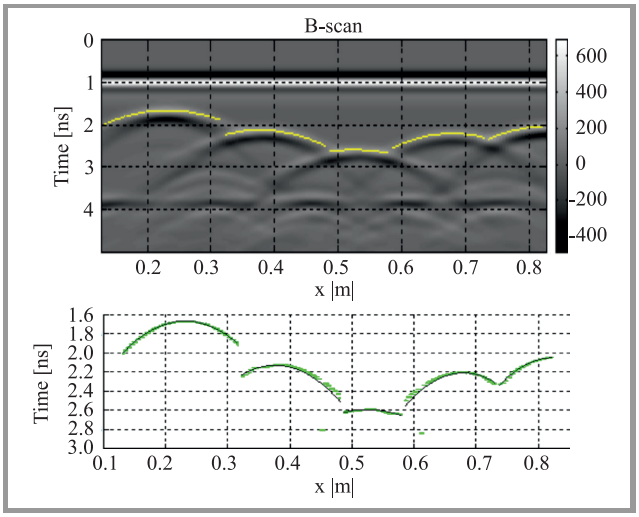


***Fig. 6.*** Hyperbolic data fitting on B-scan data – Cell 1-1 (a).

Table 3
Test scenario for Cell 1-1

| Cell 1-1 original | | | |
|---|---|---|---|
| **Object** | **Centre position [m]** | **Radius [m]** | **Material** |
| No. 1 | (0.18, 0.17) | 0.01 | PEC |
| No. 2 | (0.28, 0.14) | 0.01 | |
| No. 3 | (0.38, 0.11) | 0.01 | |
| No. 4 | (0.48, 0.14) | 0.005 | |
| No. 5 | (0.58, 0.14) | 0.015 | |
| **Size of the cell section:** $0.66 \times 0.28$ m$^2$ | | | |
| **No. of A-scans in the radargram:** 100 | | | |
| Cell 1-1 (a) | | | |
| **Object** | **Centre position [m]** | **Radius [m]** | **Material** |
| No. 1 | (0.18, 0.17) | 0.01 | PEC |
| No. 2 | (0.33, 0.14) | 0.01 | |
| No. 3 | (0.48, 0.11) | 0.01 | |
| No. 4 | (0.63, 0.14) | 0.005 | |
| No. 5 | (0.78, 0.14) | 0.015 | |
| **Size of the cell section:** $0.86 \times 0.28$ m$^2$ | | | |
| **No. of A-scans in the radargram:** 140 | | | |
| Cell 1-1 (b) | | | |
| **Object** | **Centre position [m]** | **Radius [m]** | **Material** |
| No. 1 | (0.18, 0.17) | 0.01 | PEC |
| No. 2 | (0.38, 0.14) | 0.01 | |
| No. 3 | (0.58, 0.11) | 0.01 | |
| No. 4 | (0.78, 0.14) | 0.005 | |
| No. 5 | (0.98, 0.14) | 0.015 | |
| **Size of the cell section:** $1.06 \times 0.28$ m$^2$ | | | |
| **No. of A-scans in the radargram:** 180 | | | |
| Cell 1-1 (c) | | | |
| **Object** | **Centre position [m]** | **Radius [m]** | **Material** |
| No. 1 | (0.18, 0.17) | 0.01 | PEC |
| No. 2 | (0.43, 0.14) | 0.01 | |
| No. 3 | (0.68, 0.11) | 0.01 | |
| No. 4 | (0.93, 0.14) | 0.005 | |
| No. 5 | (1.18, 0.14) | 0.015 | |
| **Size of the cell section:** $1.26 \times 0.28$ m$^2$ | | | |
| **No. of A-scans in the radargram:** 220 | | | |
| Cell 1-1 (d) | | | |
| **Object** | **Centre position [m]** | **Radius [m]** | **Material** |
| No. 1 | (0.18, 0.17) | 0.01 | PEC |
| No. 2 | (0.48, 0.14) | 0.01 | |
| No. 3 | (0.78, 0.11) | 0.01 | |
| No. 4 | (1.08, 0.14) | 0.005 | |
| No. 5 | (1.38, 0.14) | 0.015 | |
| **Size of the cell section:** $1.46 \times 0.28$ m$^2$ | | | |
| **No. of A-scans:** 260 | | | |
| General setup | | | |
| **Relative dielectric constant medium 1:** 6 (concrete) | | | |
| **Relative dielectric constant medium 2:** 16 (compact fill) | | | |
| **Trace spacing:** $5 \cdot 10^{-3}$ m | | | |
| **Time window:** $5 \cdot 10^{-9}$ s | | | |
| **Centre frequency:** 1500 MHz (Ricker pulse) | | | |

tiating $e^2$ with respect to $a$ and $b$ and by equating the differentials to zero:

$$\begin{cases} \dfrac{\partial e^2}{\partial a} = 0 \\ \dfrac{\partial e^2}{\partial b} = 0 \end{cases} . \tag{2}$$

The latter equation can be solved for $a$ and $b$ and the following expressions can be obtained [26]:

Table 4
Test scenario for Cell 1-2

| Cell 1-2 original | | | |
|---|---|---|---|
| **Object** | **Centre position [m]** | **Radius [m]** | **Material** |
| No. 1 | (0.18, 0.14) | 0.015 | PEC |
| No. 2 | (0.30, 0.14) | 0.015 | PVC |
| | (0.30, 0.14) | 0.013 | Free space |
| No. 3 | (0.42, 0.14) | 0.015 | PVC |
| | (0.42, 0.14) | 0.013 | Free space |
| | (0.42, 0.1345) | 0.0075 | PEC |
| No. 4 | (0.54, 0.14) | 0.035 | PEC |
| | (0.54, 0.14) | 0.033 | Free space |
| **Size of the cell section:** $0.66 \times 0.28$ m$^2$ | | | |
| **No. of A-scans in the radargram:** 100 | | | |
| Cell 1-2 (a) | | | |
| **Object** | **Centre position [m]** | **Radius [m]** | **Material** |
| No. 1 | (0.18, 0.14) | 0.015 | PEC |
| No. 2 | (0.35, 0.14) | 0.015 | PVC |
| | (0.35, 0.14) | 0.013 | Free space |
| No. 3 | (0.52, 0.14) | 0.015 | PVC |
| | (0.52, 0.14) | 0.013 | Free space |
| | (0.52, 0.1345) | 0.0075 | PEC |
| No. 4 | (0.69, 0.14) | 0.035 | PEC |
| | (0.69, 0.14) | 0.033 | Free space |
| **Size of the cell section:** $0.81 \times 0.28$ m$^2$ | | | |
| **No. of A-scans in the radargram:** 130 | | | |
| Cell 1-2 (b) | | | |
| **Object** | **Centre position [m]** | **Radius [m]** | **Material** |
| No. 1 | (0.18, 0.14) | 0.015 | PEC |
| No. 2 | (0.40, 0.14) | 0.015 | PVC |
| | (0.40, 0.14) | 0.013 | Free space |
| No. 3 | (0.62, 0.14) | 0.015 | PVC |
| | (0.62, 0.14) | 0.013 | Free space |
| | (0.62, 0.1345) | 0.0075 | PEC |
| No. 4 | (0.84, 0.14) | 0.035 | PEC |
| | (0.84, 0.14) | 0.033 | Free space |
| **Size of the cell section:** $0.96 \times 0.28$ m$^2$ | | | |
| **No. of A-scans in the radargram:** 160 | | | |
| Cell 1-2 (c) | | | |
| **Object** | **Centre position [m]** | **Radius [m]** | **Material** |
| No. 1 | (0.18, 0.14) | 0.015 | PEC |
| No. 2 | (0.45, 0.14) | 0.015 | PVC |
| | (0.45, 0.14) | 0.013 | Free space |
| No. 3 | (0.72, 0.14) | 0.015 | PVC |
| | (0.72, 0.14) | 0.013 | Free space |
| | (0.72, 0.1345) | 0.0075 | PEC |
| No. 4 | (0.99, 0.14) | 0.035 | PEC |
| | (0.99, 0.14) | 0.033 | Free space |
| **Size of the cell section:** $1.11 \times 0.28$ m$^2$ | | | |
| **No. of A-scans in the radargram:** 190 | | | |
| Cell 1-2 (d) | | | |
| **Object** | **Centre position [m]** | **Radius [m]** | **Material** |
| No. 1 | (0.18, 0.14) | 0.015 | PEC |
| No. 2 | (0.50, 0.14) | 0.015 | PVC |
| | (0.50, 0.14) | 0.013 | Free space |
| No. 3 | (0.82, 0.14) | 0.015 | PVC |
| | (0.82, 0.14) | 0.013 | Free space |
| | (0.82, 0.1345) | 0.0075 | PEC |
| No. 4 | (1.14, 0.14) | 0.035 | PEC |
| | (1.14, 0.14) | 0.033 | Free space |
| **Size of the cell section:** $1.26 \times 0.28$ m$^2$ | | | |
| **No. of A-scans:** 220 | | | |
| General setup | | | |
| **Relative dielectric constant medium 1:** 6 (concrete) | | | |
| **Relative dielectric constant medium 2:** 16 (compact fill) | | | |
| **Trace spacing:** $5 \cdot 10^{-3}$ m | | | |
| **Time window:** $5 \cdot 10^{-9}$ s | | | |
| **Centre frequency:** 1500 MHz (Ricker pulse) | | | |

$$a^2 = \frac{\sum_l x_i^4 \sum_l y_i^4 - \left(\sum_l x_i^2 y_i^2\right)^2}{\sum_l x_i^4 \sum_l y_i^2 - \left(\sum_l x_i^2 y_i^2\right) \sum_l x_i^2},$$
$$b^2 = \frac{\left(\sum_l x_i^2 \sum_l y_i^2\right) \sum_l x_i^4 - \left(\sum_l x_i^2 y_i^2\right)^2}{\left(\sum_l x_i^2 y_i^2\right) \sum_l y_i^2 - \sum_l x_i^2 \sum_l y_i^4}. \quad (3)$$

To provide a qualitative idea of the accuracy of such procedure, we present an example in Fig. 6.

The localization results for Cells 1-1 and 1-2 are presented in Tables 3 and 4, respectively. In particular, the position error is given for each target, for both the hyperbolic fitting method and the SAP-DOA technique. The position error is defined as the difference between the actual and estimated positions of the target. It can be noted that the hyperbolic fitting cross-range estimation is pretty close to the SAP-DoA method, whereas the range (depth) estimation of the SAP-DoA method differs from the hyperbolic fitting by less than 2 cm in the worst case. In some cases, the SAP-DoA method is more accurate than the hyperbolic fitting method.

In Fig. 7, the position error is plotted for all the targets of Cell 1-1 and for both localization methods, as a function of the horizontal distance between adjacent targets. Five points are present in each curve. The first point corresponds to the original cell and the subsequent four points correspond to the enlarged cells. In Fig. 8, the same as in Fig. 7 is reported, for Cell 1-2. The SAP-DoA depth-estimation seems to have a little offset in comparison with the hyperbolic fit, which is probably due to the presence of cavities in this case study.

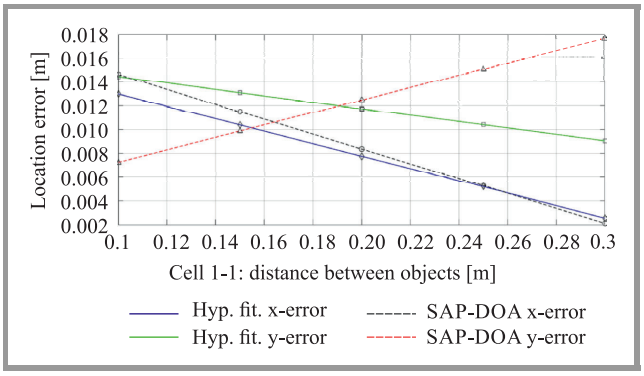


***Fig. 7.*** RMS estimation error vs object mutual distance (5 simulated cases) for Cell 1-1.

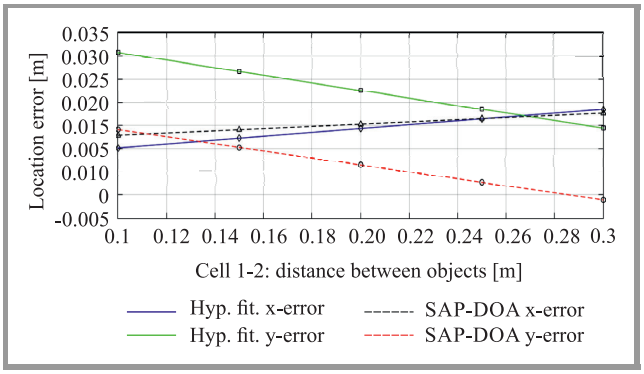


***Fig. 8.*** RMS estimation error vs object mutual distance (5 simulated cases) for Cell 1-2.

## 4. Conclusions

In this work, an innovative Sub-Array Processing (SAP) approach exploiting Direction of Arrival (DoA) algorithms was presented, for the processing of Ground-Penetrating Radar (GPR) data. The purpose of the method is to detect an unknown number of targets in the subsoil or in a structure, and estimate their positions. For the first time, the matched-filter technique was used in the GPR field, with very good results.

The proposed SAP-DoA approach was developed in the framework of the COST Action TU1208 activities and it was implemented in Matlab. A GUI was realized, too.

The resulting software tool has ben called SPOT-GPR and is freely distributed via the Action website, for academic and commercial use.

The accuracy of the developed tool was investigated by processing several synthetic radargrams, calculated by using the finite-difference time-domain simulator GprMax2D. In this paper we presented two examples. We considered two concrete cells, with embedded metallic and dielectric cylindrical targets. We simulated the cells varying the distance between the targets and processed all the obtained radargrams with SPOT-GPR and compared the obtained localization results with those of the standard hyperbola-fitting approach, which is commonly employed for the processing of GPR data when circular-section cylindrical targets are present. The SAP-DoA technique demonstrated a good functioning with respect to the hyperbolic approach. One of the advantages of our method is that it can be applied also in the presence of arbitrary-section targets, when the hyperbolic fitting method cannot be used.

Further tests will be carried out on synthetic radargrams obtained by including in the model a realistic representation of the transmitting and receiving antennas. Moreover, we will check how the presence of losses in the materials affects the accuracy of our approach.

Additional tests based on real measurements will be carried out. In particular, as a subsequent step, we plan to check the accuracy of SPOT-GPR against the TU1208 experimental dataset coming from measurements performed at the IFSTTAR Geophysical Test Site (Nantes, France) by using several different GPR systems and antennas.

We also plan to implement in our tool different DoA algorithms and compare their performance when applied to GPR scenarios (currently, the tool uses the well-known MUSIC) method.

## Acknowledgements

The tool presented in this paper was developed during three COST (European COoperation in Science and Technology) Short-Term Scientific Missions and is a contribution to the COST Action TU1208 "Civil engineering applications of Ground Penetrating Radar". The authors are grateful to COST for funding and supporting the Action TU1208.
This paper is included in the JTIT Special Issue "Recent Progress in Electromagnetic Theory and its Applications" organized by the COST Action TU1208.

## References

[1] A. Benedetto and L. Pajewski, Eds., *Civil Engineering Applications of Ground Penetrating Radar*. Book Series: "Springer Transactions in Civil and Environmental Engineering". Springer International Publishing Switzerland, 2015.

[2] R. Persico, *Introduction to Ground Penetrating Radar: Inverse Scattering and Data Processing.* Hoboken, NJ, USA Wiley, 2014.

[3] L. Mertens, R. Persico, L. Matera, and S. Lambot, "Automated detection of reflection hyperbolas in complex GPR images with no a priori knowledge on the medium", *IEEE Trans. of Geosci. and Remote Sensing*, vol. 54, no. 1, pp. 580–596, 2016 (doi: 10.1109/TGRS.2015.2462727).

[4] F. Sagnard, C. Norgeot, X. Derobert, V. Baltazart, E. Merliot, F. Derkx, and B. Lebental, "Utility detection and positioning on the urban site Sense-City using Ground-Penetrating Radar systems", *Measurement*, vol. 88, pp. 318–330, 2016 (doi: 10.1016/j.measurement.2016.03.044).

[5] A. Ristić, Ž. Bugarinović, M. Govedarica, L. Pajewski, and X. Derobert, "Verification of algorithm for point extraction from hyperbolic reflections in GPR data", in *Proc. 9th Int. Worksh. on Adv. Ground Penetrat. Radar IWAGPR 2017*, Nantes, France, 2017, pp. 1–5 (doi: 10.1109/IWAGPR.2017.7996109).

[6] A. Ristić, M. Vrtunski, M. Govedarica, L. Pajewski, and X. Derobert, "Automated data extraction from synthetic and real radargrams of district heating pipelines", in *Proc. 9th Int. Worksh. on Adv. Ground Penetrat. Radar IWAGPR 2017*, Nantes, France, 2017, pp. 1–5 (doi: 10.1109/IWAGPR.2017.7996046).

[7] L. Pajewski, A. Benedetto, X. Derobert, A. Giannopoulos, A. Loizos, G. Manacorda, M. Marciniak, C. Plati, G. Schettini, and I. Trinks, "Applications of Ground Penetrating Radar in civil engineering – COST Action TU1208", in *Proc. 7th Int. Worksh. on Adv. Ground Penetrat. Radar IWAGPR 2013*, Nantes, France, 2013, pp. 1–6 (doi: 0.1109/IWAGPR.2013.6601528).

[8] S. Meschino and L. Pajewski, "Application of a SAP-DoA Method to GPR data, for the Localisation of Scatterers in Concrete", in *Short Term Scientific Missions – Year 2*, COST Action TU1208, L. Pajewski, M. Marciniak, S. Lambot, Eds. Aracne Editrice, Rome, Italy, 2015 [Online]. Available: www.GPRadar.eu

[9] S. Meschino and L. Pajewski, "Application of a SAP-DoA method to GPR data for the location of reinforcing elements in concrete", in *Proc. IEEE 15th Mediterranean Microwave Symp MMS 2015*, Lecce, Italy, 2015, pp. 1–4 (doi: 10.1109/MMS.2015.7375408).

[10] S. Meschino and L. Pajewski, "A study of the accuracy of the SAP-DoA location technique applied to GPR data and comparison with the standard hyperbola approach", in *Short Term Scientific Missions – Year 3*. Aracne Editrice, Rome, Italy, 2017.

[11] L. Pajewski, A. Giannopoulos, S. Lambot, M. Marciniak, S. Meschino, N. Pinel, M. Sbartai, and C. Warren, "Short-term scientific missions on electromagnetic modelling and inversion techniques for ground penetrating radar – COST Action TU1208", in *Proc. 10th IEEE Eur. Conf. on Antennas and Propag. EuCAP 2016*, Davos, Switzerland, 2016 (doi: 10.1109/EuCAP.2016.7482011).

[12] S. Meschino, L. Pajewski, and M. Marciniak, "Development of SAP-DoA techniques for GPR data processing within COST Action TU1208", Geophysical Research Abstracts, European Geosciences Union (EGU) General Assembly 2016, 17-22 April 2016, Vienna, Austria, article ID EGU2016-12565.

[13] S. Meschino and L. Pajewski, "Finalization of a freeware data-processing tool implementing the SAP-DoA technique", in *Short Term Scientific Missions – Year 4*. Aracne Editrice, Rome, Italy, 2017.

[14] L. Pajewski, A. Giannopoulos, M. Marciniak, S. Meschino, A. Popov, I. Prokopovich, A. Ventura, and C. Warren, "Short-Term Scientific Missions on forward and inverse electromagnetic-scattering techniques for Ground Penetrating Radar", in *Proc. Int. Applied Comput. Electromag. Society Symp. ACES 2017*, Florence, Italy, 2017.

[15] B. Gross, *Smart Antennas for Wireless Communications*. New York, NY: McGraw-Hill, 2005.

[16] S. Chandran, *Advances in Direction-of-Arrival Estimation*. Norwood, MA: Artech House, 2005.

[17] R. Kumaresan and D. W. Tufts, "Estimating the angles of arrival of multiple plane waves", *IEEE Trans. on Aerosp. and Electron. Syst.*, vol. 19, no. 1, pp. 13–139, 1983.

[18] R. Roy and T. Kailath, "ESPRIT-estimation of signal parameters via rotational invariance techniques", *IEEE Trans. on Acoust., Speech, and Sig. Process*., vol. 37, no. 7, pp. 984–995, 1989.

[19] S. Meschino, L. Pajewski, and G. Schettini, "Use of a sub-array statistical approach for the detection of a buried object", *Near Surface Geophys.*, vol. 8, no. 5, pp. 365–375, 2010 (doi: 10.3997/1873-0604.2010031).

[20] S. Meschino, L. Pajewski, and G. Schettini, "A direction-of-arrival approach for the subsurface localization of a dielectric object", *J. of Appl. Geophys.*, vol. 85, pp. 68–79, 2012 (doi: 10.1016/j.jappgeo.2012.07.002).

[21] S. Meschino, L. Pajewski, M. Pastorino, A. Randazzo, and G. Schettini, "Detection of subsurface metallic utilities by means of a SAP technique: Comparing MUSIC- and SVM-based approaches", *J. of Applied Geophys*., vol. 97, pp. 60–68, 2013 (doi: 10.1016/j.jappgeo.2013.01.011).

[22] S. Meschino, L. Pajewski, and G. Schettini, "A SAP-DOA method for the localization of two buried objects", *Int. J. on Antenn. and Propag*., vol. 2013, Article ID 702176, 2013 (doi: 10.1155/2013/702176).

[23] C. E. Cook and M. Bernfeld, *Radar Signals: An Introduction to Theory and Application*, 1st ed. Artech House Radar Library, 1993.

[24] C. Warren, A. Giannopoulos, and I. Giannakis, "gprMax: Open source software to simulate electromagnetic wave propagation for Ground Penetrating Radar", *Computer Phys. Commun*., vol. 209, pp. 163–170, 2016 (doi: 10.1016/j.cpc.2016.08.020).

[25] L. Pajewski and A. Giannopoulos, "Electromagnetic modelling of Ground Penetrating Radar responses to complex targets", in *Short Term Scientific Missions and Training Schools – Year 1*, COST Action TU1208, L. Pajewski and M. Marciniak, Eds. Aracne Editrice, Rome, Italy [Online]. Available: www.GPRadar.eu

[26] Bello. Y. Idi and Md. N. Kamarudin, "Utility mapping with Ground Penetrating Radar: an innovative approach", *J. of American Sci.*, vol. 7, no. 1, pp. 644–649, 2011.

[27] M. Di Vico, F. Frezza, L. Pajewski, and G. Schettini, "Scattering by a finite set of perfectly conducting cylinders buried in a dielectric half-space: a spectral-domain solution", *IEEE Trans. on Antenn. and Propag.*, vol. 53, no. 2, pp. 719–727, 2005 (doi: 10.1109/TAP.2004.841315).

[28] M. Di Vico, F. Frezza, L. Pajewski, and G. Schettini, "Scattering by buried dielectric cylindrical structures", *Radio Science*, vol. 40, no. 6, RS6S18, 2005 (doi: 10.1029/2004RS003182).

[29] A. Giannopoulos, "Modelling ground penetrating radar by GprMax", *Construction and Build. Mater*., vol. 19, pp. 755–762, 2005.

**Simone Meschino** received the M.Sc. degree in Electrical Engineering from the Roma Tre University of Rome, Italy, in 2008. In 2010, he received the Italian engineering qualification and in 2011 the Ph.D. degree at the Roma Tre University of Rome on applied electromagnetics. In 2012 he joined the former Selex ES (nowadays Leonardo Finmeccanica) as radar system engineer then he moved to the former Astrium GmbH (now Airbus Defence and Space, Friedrichshafen, Germany) where he has been working since 2014. His research interests are mainly related to radar topics (including GPR and SAR), in particular sensor array processing, modeling and performance assessment.

E-mail: simone.meschino@gmail.com
Airbus Defence and Space GmbH
a Claude-Dornier-Straße
88090 Immenstaad am Bodensee
Germany

**Lara Pajewski** – for biography, see this issue, p. 29.

Paper

# Development of Data Processing Tools for the Analysis of Radargrams in Utility Detection Using Ground Penetrating Radar

Florence Sagnard

*Université Lille Nord de France, IFSTTAR, Villeneuve-d'Ascq, France*

https://doi.org/10.26636/jtit.2017.120717

**Abstract—The extraction of quantitative information from Ground Penetrating Radar (GPR) data sets (radargrams) to detect and map underground utility pipelines is a challenging task. This study proposes several algorithms included in the main stages of a data processing chain associated with radargrams. It comprises pre-processing, hyperbola enhancing, hyperbola detection and localization, and parameter extraction. Additional parameters related to the GPR system such as the frequency band and the polarization bring data sets additional information that need to be exploited. Presently, the algorithms have been applied step by step on synthetic and experimental data. The results help to guide future developments in signal processing for quantitative parameter estimation.**

***Keywords—buried pipes, dielectric characterization, GPR, ICA, PCA, polarization, template matching, ultra-wide band.***

## 1. Introduction

The rapid growth of buried utility networks of different types (i.e., fiber optics, telecommunication lines, electrical cables, water and gas pipes, district heating network) to fulfill services in the urban landscape need mapping of the underground to update urban cadastral databases, to contribute to space saving and a wise use of land resources when planning for new networks [1], [2]. Among non-destructive techniques, Ground Penetrating Radar (GPR) appears the most suitable device for locating and identifying objects made of a dielectric or conductive solid or hollow material buried within 1.5 m of the ground surface. A few international organizations promote recommendations to properly use GPR in utility engineering, such as the ASCE (CI/ASCE 38-02) and the ASTM (ASTM D6432-99) international (2011) in North America [3], [4], EuroGPR in Europe, and the CEI (306-08) in Italy [5]. Moreover, European COST (Cooperation in Science and Technology) Action TU1208 "Civil engineering applications of Ground Penetrating Radar" [6] promotes applied research and emits recommendations on GPR applied to civil engineering. One of its working groups is devoted to utility detection and mapping by GPR. In this work, ground-coupled radar systems have been employed because, compared to air-coupled systems, the energy transfer of electromagnetic (EM) waves in the sub-surface and the penetration depth is increased. The moving of the GPR system along a linear path gives a distance-time graph called radargram (also called B-scan, a set of traces or A-scans), contains diffraction hyperbolas associated with buried dielectric discontinuities due to the presence of circular-section objects that induce reflection with the emitted signal. It must be underlined that only small circular-section objects generate hyperbolas in radargrams. In the present work, the surveyed scenarios hosted long pipes compared to the GPR central wavelength, with a diameter shorter than 100 mm. The interpretation of hyperbolas, that represent the signatures of the objects, is a challenging task because several physical and geometrical parameters (i.e., soil heterogeneity and variations, soil absorption, antenna coupling, antenna-target coupling, target proximity) contribute to blur the information or mitigate contrasts. Consequently, several processing methods are developed in the literature because of the non-uniqueness of the solution, and they are generally adapted to a field situation because the EM problem is tedious.

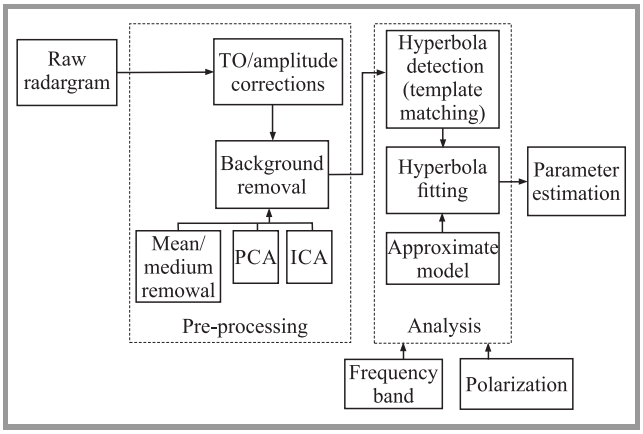


***Fig. 1.*** The several stages of the processing link for the quantitative analysis of a radargram associated with buried targets.

Thus, the data processing chain synthesized in Fig. 1 has been developed to particularly analyze theoretical and experimental data sets. The processing is made of two main

stages associated with pre-processing and analysis algorithms to extract quantitative information from the hyperbola signatures associated with detectable targets. The information is relative to the evaluation of the target location, depth, size and dielectric nature. Attention has been paid to clutter removal in the case of a shallow target depth and a low permittivity contrast between the target and the soil, and on hyperbola detection in the presence of multiple targets and a heterogeneous soil. Parameters such as the frequency band and polarization have been considered as they can bring more detailed information from radargrams with additional processing.

## 2. The Measurements

The acquisition of radargrams was achieved using several GPR systems operating at frequencies ranging from 300 MHz to 1.5 GHz either in the time domain (GSSI SIR 3000, UtilityScan DF) or in the frequency domain (a SFCW GPR conceived in our laboratory). The SFCW (Step Frequency Continuous Wave) GPR is a laboratory system and cannot make at present fast measurements such as commercial systems. The sampling distance step was around 5 mm using commercial GPRs, and defined to 40 mm using the laboratory system. The two types of GPR systems were used to make comparisons, and results are presented in this paper at 900 MHz.

The SIR 3000 was equipped with one of the three antenna pairs operating at the central frequencies 500, 900 MHz and 1600 MHz, and the UtilityScan DF worked with a double frequency antenna system at 300 MHz and 800 MHz that is supposed to collect data at the same sampling distance because the switching device is rapid enough during walking. Only the transverse magnetic (TM) polarization with respect to the pipe axes has been considered because these GPR systems only consider this polarization.

The SFCW GPR is made of a pair of shielded bowtie slot antennas (A4 sheet size designed on a single-sided FR4 substrate) has been used with a portable Anritsu MS 2026B Vector Network Analyzer (VNA) in the frequency band [0.05; 4 GHz] (1601 samples, intermediate frequency 500 Hz, 2 m coaxial N cables) [7]. A full two ports calibration was made that allows to measure the four $S_{ij}(f)$ coefficients.

Measurements in the frequency domain and in an Ultra-Wide Band (UWB) offer the advantages of selecting if needed a frequency band and shaping a Gaussian pulse associated with this frequency band, and using easily the polarization diversity. The complex transmission coefficient $\tilde{S}_{21}(f)$ measured at each scanning distance with a step of 40 mm is transformed in the time domain using an inverse Fourier transform to obtain a radargram. An apodization of each frequency curve has been made to smoothly extend the measured band from 4 to 9 GHz, and then perform the product with the spectrum of the excitation signal (the first derivative of the Gaussian function with duration 0.5 ns) used in Finite Difference Time Domain (FDTD) simulations. Two symmetric antenna configurations have been defined such as presented in Fig. 2 to consider two perpendicular polarizations: the end-fire configuration (or TM mode) with both antennas aligned along their larger dimension, and the broadside configuration or transverse electric mode (TE) with both antennas facing each other symmetrically along their larger dimension. The laboratory made SFCW GPR has been easily modeled as all the antenna characteristics and geometry are known.

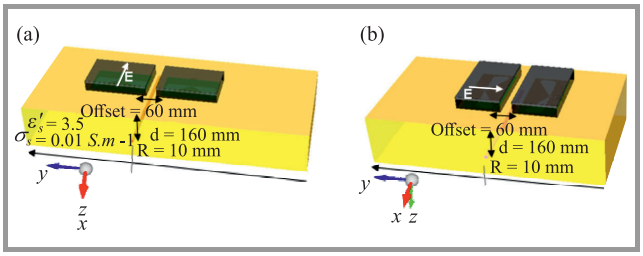


***Fig. 2.*** The two polarization configurations of the SFCW GPR: (a) TM polarization (end-fire), and (b) TE polarization (broadside).

The measurements have been performed in two different test sites:

- a large sandy box belonging to the public square Perichaux in Paris 15th district [8]. The sand was wet on the surface, and its permittivity has been estimated to a real permittivity $\varepsilon'_s$. A couple of canonical objects (pipe or blade) dielectric or conductive with lateral dimension less than 25 mm have been buried at a depth close to 160 mm. They have been separated by a distance around 750 mm;

- an utility zone built under the urban test bed SenseCity in Marne-La-Vallée (France) [9]. This zone is under the 10 m wide traffic circle with lawn at the center. The underground contains two series of 5 trenches parallel to each other with size $0.3 \times 4$ m and separated by an offset of 40 cm (Fig. 3). Each target has been positioned in the middle of a trench at a depth ranging from 14.5 to 64.5 cm from the 4.4 cm thick asphalt surface. The two series of trenches include dielectric or conductive pipes (diameter 63 mm) and dielectric or conductive blades (thickness between 1 and 3 cm). The pipes have been filled with air or water. The trenches were filled with a soil of fine elements (without gravels) commonly used in urban underground filling. The near sub-surface is made of four main layers corresponding to asphalt (layer 1), aggregate cement (layer 2), a natural soil (layer 3), and a quite wet natural soil (layer 4) located under a geotextile (a thin discontinuity). The real permittivities of the soil layers have been estimated as: asphalt (layer 1) $\varepsilon'_1 = 4.5$ (corresponding to a time propagation of 0.64 ns), aggregate cement (layer 2) $\varepsilon'_2 = 7.7$ (1.4 ns), natural soil $\varepsilon'_3 = 34$ (8.5 ns).

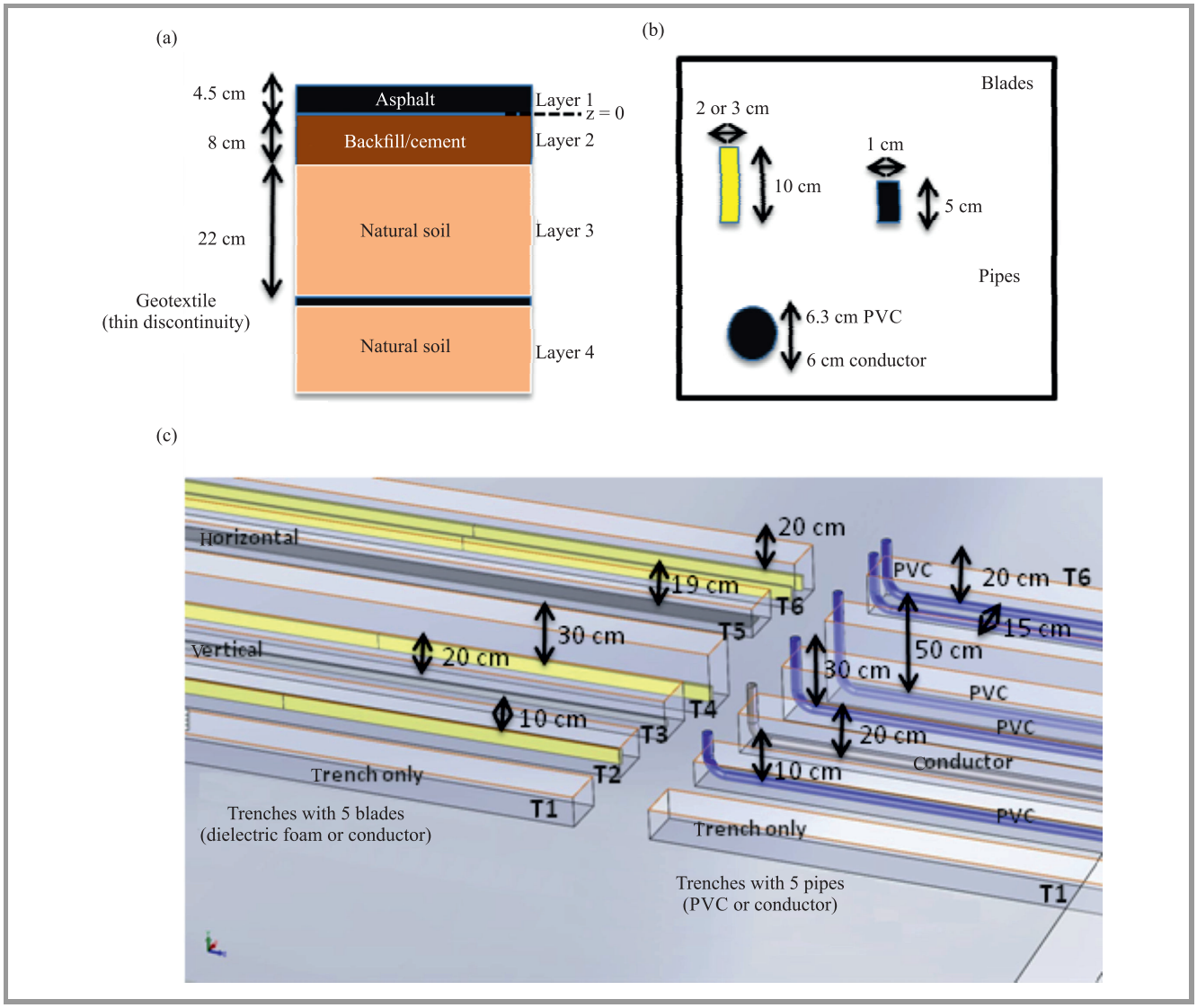


***Fig. 3.*** Structure of the sub-surface in Sense-City site: (a) the main multilayers of the soil, (b) geometries of the buried objects, (c) distribution of the buried pipes and strips.

## 3. Modeling

A 3D full-wave FDTD modeling using the commercial software EMPIRE has enabled to analyze EM phenomena as a function of parameters such as soil and pipe permittivity, pipe depth, and antenna polarization and make comparison with experimental results [8], [9]. The complete SFCW GPR made of a pair of shielded bowtie slot antennas (frequency band [0.46 ; 4] GHz) and designed on a FR4 substrate (real relative permittivity $\varepsilon' = 4.4$ and thickness $e = 1.6$ mm) has been modeled in the presence of a semi-infinite soil [7]. Each antenna is enclosed in a shielded conductive rectangular box filled with a three-layered absorbing foam with total dimensions $362 \times 23 \times 67.5$ mm. The offset between antennas in simulations and experiments has been fixed to 60 mm, and the elevation $h_s$ above the soil is $h_s = 40$ mm. The soil electrical parameters ($\varepsilon'_s$, $\sigma_s$) are assumed constant across the frequency range. The GPR system is moved linearly on the soil surface with a step $\Delta y = 40$ mm (see Fig. 2) to acquire a radargram. The excitation signal generally used in the simulations is the first derivative of the Gaussian function with a duration equal to 0.5 ns (99% of the total energy) and begins at 0.33 ns.

## 4. Pre-Processing

The pre-processing step aims to prepare radargrams before analyzing the hyperbola signatures of sub-surface targets to extract quantitative information. After time scaling and amplitude scaling (if needed), the main step consists of clutter removal to reduce the reflection component of the ground surface, direct waves between antennas, coupling between the antenna system, and a shallow target, as well as scattering induced by soil heterogeneities. The clutter often hides target signatures because its amplitude is far stronger and the arrival time is shorter. Several clut-

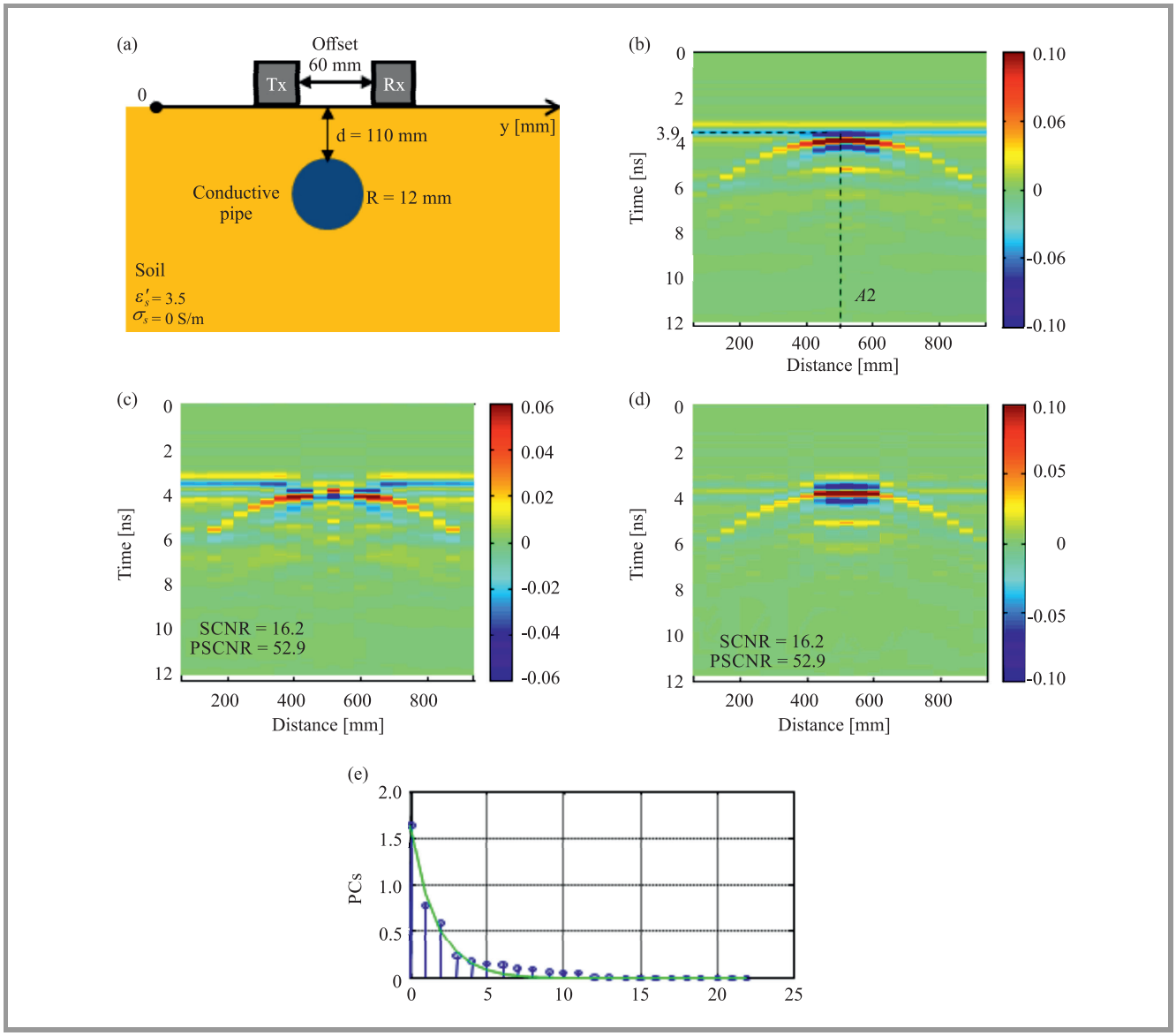


*Fig. 4.* Pre-processing applied on a synthetic radargram issued from FDTD simulations: (a) geometry of the soil structure including a buried conductive pipe probed by a pair of shielded bowtie slot antennas (TM polarization), (b) raw radargram, (c) radargram processed by PCA, (d) radargram processed by PCA modified, (e) distribution of the PCs. (See color pictures online at www.nit.eu/publications/journal-jtit)

ter reduction techniques were proposed in the literature and their development is an active research topic because the clutter is not uniform in a radargram, it is unsteady and it has different types [10].

The methods proposed appear initially suited to targets with small lateral dimension, overlapping hyperbola signatures, varying clutter along the scanning direction (a non-stationary signal), overlapped target and clutter signals in time and frequency [11]. The semi-automatic methods tested and compared are the mean or median subtraction [12], the Principal Component Analysis (PCA) that has been modified and the Independent Component Analysis (ICA) [13], [14]. Basically, PCA relies on the second order statistics to perform the correlation analysis, whereas ICA requires higher order statistics (4th moment). Both methods have the advantage of requiring limited prior information on the data set.

### *4.1. PCA*

The objective of PCA is to express the original data set in another domain by means of any appropriate linear transformation. PCA is a subspace projection method that is based on either on a Singular Value Decomposition (SVD) or an Eigenvalue Decomposition (EIG) to select relevant components in different subspace projections [13]. Each eigenvalue is related to a certain eigenvector (principal component), and the eigenvalues are ordered in the descending order. The main problem of this algorithm is how to choose the principal components where information is contained.

Every eigenvalue represents a specific amount of variance in measured data, and the objective is to obtain a new set of uncorrelated data.

From the initial data matrix $X(M \times N)$ (with $M$ amplitude signals A-scans and $N$ time samples; $M < N$) the first $k_1$ components associated with the clutter and the last $N-(k_2+1)$ components associated with noise are generally removed thus giving a new data set:

$$X_0 = \sum_{k_1+1}^{k_2} u_i s_i v_i^T , \tag{1}$$

where $u_i$ and $v_i$ are eigenvectors.

However, difficulties can be met when the clutter does not have the highest energy within the radargram in the case of a target that induces a strong Radar Cross Section (RCS) such as a conductive or a water filled target, or a high contrasted dielectric target with the surrounding soil [15]. Moreover, it appears difficult to select the index rank defined by $k_1$ and $k_2$ when there are multiple targets and reflections. Thus, we have proposed to modify PCA and apply the algorithm on a radargram with a reduced time scale (investigation depth) and a splitting of the scanning scale associated with a selected hyperbola signature into 3 parts. This splitting is based on an energy criterion that compares energy in the apex area and energy in the arms. This splitting allows to analyze separately the area close to the apex and relative to the two arms as they show distinct amplitude value and interaction with the clutter. It particularly concerns target response with high energy that is comparable to the clutter energy.

An illustration of the application of PCA and PCA modified is presented in the case of a conductive pipe with radius $R = 12$ mm (see Fig. 4a), buried at a depth d of 110 mm (that is, $\frac{3}{4}$ of the wavelength $\lambda_{soil}$ at 1 GHz) in a soil with real permittivity $\varepsilon' = 3.5(\frac{d}{\lambda_{soil}} \approx 1$ at 1 GHz), that has been probed by the pair of bowtie slot antennas used in the SFCW GPR (TM polarization). The data set have been obtained from FDTD simulations (see Fig. 4b) and, in this case, there is overlapping between clutter and hyperbola response. The arrival times of the clutter and the target are 3.4 and 3.9 ns, respectively. The PCs selected represents 90% of the energy, the first one is removed as it represents the clutter component (see Fig. 4e). The processing by conventional PCA depicts visually bad performance in reducing the coupling between antennas as part of the horizontal component of antenna coupling remains (see Fig. 4c). PCA modified preserves the target hyperbola shape (see Fig. 4d) but it does not eliminate completely the clutter over the apex, and a clutter remains in the time interval 3…4 ns.

### *4.2. ICA*

ICA has been recently proposed as an alternative to eigenvector decomposition in radar images as it has proved itself to be a very promising tool to better interpret non-Gaussian heterogeneous clutter. ICA that is based on higher order statistical moments, can recover statistical independent sources and the mixing mechanism without having any physical background of the latter [14], [15]. The ICA model associated with a data matrix $X$ that is assumed random is generated from a source matrix $S$ through a linear process:

$$X = SA , \tag{2}$$

where $X$ is the matrix used in the PCA algorithm, $S = (s_1, s_2, \ldots, s_{N2})$ is the $M \times N_2$ source matrix ($N_2 \leq N$), and $A$ is the $N_2 \times N$ mixing matrix.

ICA assumes that the components of the source matrix are statistically independent with respect to each other, that makes ICA more efficient in the separation process. Before processing with the calculations, $X$ is transposed ($X^T = A^T S^T$) and then ICA uses centering, whitening, and dimensionality reduction algorithms as pre-processing steps to simplify and reduce the complexity of the problem. The FastICA algorithm (fixed-point algorithm first proposed by Hyvärinen and Oja [15]) available in a Matlab package leads to the determination of two sub-solutions: 1) the estimation of the mixing matrix $A$, and 2) the estimation of the source signals $S$. To measure the non-Gaussianity (the independence) of the sources a non-linear and non-quadratic function, also called a contrast function, is used that helps to optimize the performance of the ICA algorithm.

In this work, negentropy has been used to measure the non-normality or the degree of unstructuredness of a ran-

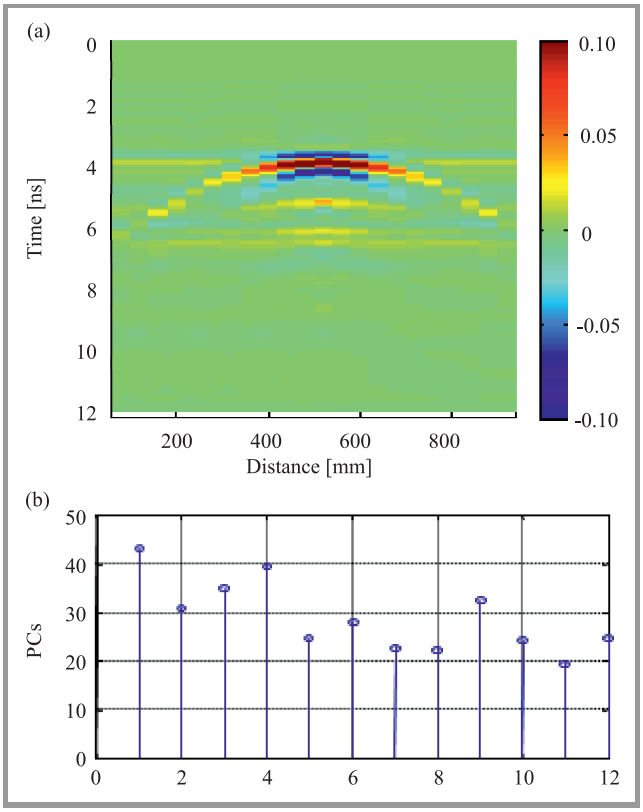


***Fig. 5.*** Pre-processing applied on the synthetic radargram of Fig. 4a using ICA: (a) radargram processed by ICA, (b) Kurtosis criterion applied on ICs.

dom vector. Negentropy is non-negative and has a high value for non-Gaussian variables. In practice, negentropy is difficult to calculate and must be approximated, a solution proposed by Hyvärinen [15]. An iteration based on the fast-fixed-point technique that uses random vectors as starting values, allows to estimate step by step the several independent components (ICs). Afterwards, the main difficulty relies on the selection of ICs which contain information. The Kurtosis criterion applied to the ICs has served to define a threshold beyond which the ICs selected contain information.

As an illustration, the previous synthetic radargram associated with a conductive pipe buried at 110 mm depth has been analyzed by the ICA algorithm. The results in Fig. 5a show that the clutter is better reduced by ICA than by PCA modified, as there is no artifact above the apex, however a weak horizontal clutter remains visible. The Kurtosis criterion applied on ICs are plotted in Fig. 5b.

### *4.3. Comparison Criteria between Processing Algorithms*

The visual comparison of the reconstructed images with reduced clutter provides a first qualitative assessment of the algorithms tested. Attention has to be paid to spatial coherency along the scanning direction in such a way that the visibility of a hyperbola must be strengthened as compared to that of the clutter. Thus, a few tools have been used to quantitatively compare the performance of the clutter reduction algorithms.

#### Signal to Clutter and Noise Ratio (SCNR)

The ratio is defined as the average energy of the reconstructed clutter-reduced image (represented by a matrix $F$ of real values $f_{i,j}$ with $i = 1,\ldots,M$ and $j = 1,\ldots,N$) with the average energy contained in the "noise" image (named $G$ with elements $g_{i,j}$ with $i = 1,\ldots,M$ and $j = 1,\ldots,N$), that is obtained by subtracting the raw image from the processed image such as [17]:

$$SCMR_{dB} = 10\log\frac{P_{\text{target}}}{P_{\text{clutter+noise}}} = 10\log\frac{\sum_{i=1,N}\sum_{j=1,M}|f_{i,j}|^2}{\sum_{i=1,N}\sum_{j=1,M}\left(|g_{i,j}-f_{i,j}|\right)^2}. \quad (3)$$

In practice, we don't have the opportunity to acquire an image without clutter and noise, that limits the interpretation of the SCNR.

#### Peak Signal to Noise and Clutter Ratio (PSCNR)

Another parameter is the PSCNR that uses presently the peak signal instead of its average energy such as [18]:

$$PSCNR_{dB} = 10\log\frac{NM\max(|f|)^2}{\sum_{i=1,N}\sum_{j=1,M}\left(|g_{i,j}-f_{i,j}|\right)^2}. \quad (4)$$

Again, this ratio has some limits.

#### Receiver Operating Characteristics (ROC) curves

ROC curves appear more appropriate to compare quantitatively clutter reduction algorithms. The ROC curve is simply a graph of detection versus false alarm probabilities parameterized by a threshold $S$ [19]. From a ROC curve ($1 \times 1$ square region), fundamental information extracted from metrics (in general area-under-roc-curve AUC) is derived. A ROC curve is calculated by comparing pixel to pixel two binary images, a reference image containing only the desired information and the image processed by an algorithm using a varying threshold $S$ in the amplitude range of the raw image. The reference image defined corresponds to a skeleton of the hyperbola response including the first positive and negative amplitudes. The threshold applied on the raw image serves to compute a binary image to make a comparison with the reference image.

As an illustration, these 3 parameters have been evaluated for the radargrams of Figs. 4c-d (PCA), and also Fig. 5a (ICA). The largest SCNR and PSCNR values belong to the median subtraction technique (14 and 72.9 respectively), and afterwards the better performances are attributed to PCA modified and ICA. The ROC curves visualized in Fig. 6 show that the curve associated with PCA is slightly below the one issued from the raw data. The curve associated with PCA modified appears higher than the one belonging to ICA.

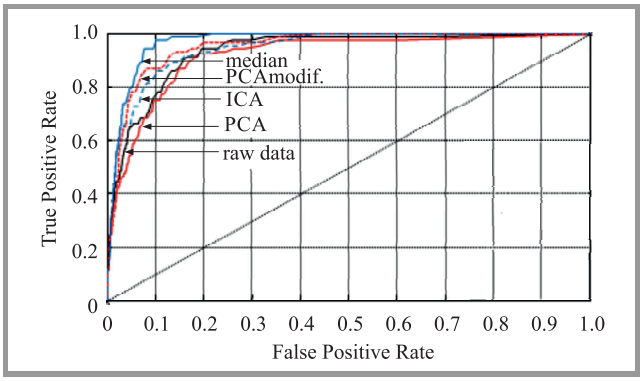


***Fig. 6.*** ROC curves associated with the different pre-processing algorithms (median subtraction, PCA, ICA) applied on the raw radargram of Fig. 4a.

As a conclusion, the median subtraction technique appears a robust method for clutter reduction but it has its limits in the case of the overlapping of clutter and hyperbola response. As a conclusion, the median subtraction technique appears a robust method for clutter reduction that has however its limits, in the case of overlapping between clutter and hyperbola response. The PCA algorithm shows better performance in the case of the relative pipe diameter $\frac{d}{\lambda_{soil}} \leq 0.7$ and when there exists partial overlapping between clutter and hyperbola. When the hyperbola response has a high amplitude, PCA modified improves the removing of the clutter The ICA algorithm shows better performance in the case $\frac{d}{\lambda_{soil}} \geq 1$ and without overlapping.

## 5. Hyperbola Detection and Fitting

In practice, the difficulties encountered in hyperbola detection in a radargram rely on the heterogeneity of the background and a weak contrast between the hyperbola and the background. Thus, we have proposed a semi-automatic detection algorithm based on template matching that doesn't require a training period [20]. It is applied after a preprocessing stage and is made of a series of steps:

- A template containing a typical hyperbola signature is built, that is issued from synthetic or experimental data. The template does not need to be fully similar to the responses to be detected. When the hyperbolas in the radargram cannot be detected by a single pattern, several patterns can be used in sequence. Each defined template includes a small portion of a hyperbola signature near the apex. It has to be scaled in time, distance and amplitude to the radargram that has to be analyzed.

- An amplitude distance map is calculated by translating on the radargram the predefined template at every possible positions. A mean amplitude distance is evaluated according to the $L_1$ norm.

  Assuming an observed image $G$ with elements $g_{i,j}$ or $g(i,j)$ and size $M \times N$, and a template image $T$ with elements $t_{i,j}$ or $t(i,j)$, both images with scaled amplitudes, we define the $L_1$ norm distance map $E$ between $g$ and $t$ by the following relation [18]:

$$E(m,n) = \sum_{i=1}^{M} \sum_{j=1}^{N} |t(i,j) - g(i-m, j-n)| . \qquad (5)$$

  The summation is evaluated at all pixels $(i,j)$ of the template $t$ that is translated to all possible positions $(m,n)$ along the observed image $g$. The position $(m,n)$ at which the smallest value $E(m,n)$ is obtained corresponds to the best match between the template $t$ and the corresponding sub-image in $g$.

- A threshold value increased progressively by the user allows to select a number of minima on the distance map that corresponds to a high level of similarly with the template.

- At the selected positions, the hyperbola points close to the apex that correspond to a maximum or a minimum amplitude have to be extracted. Because higher order reflections in a hyperbola pattern may produce a stronger amplitude as compared to the amplitude of the first reflection, an user interaction is necessary (semi-automatic) to select a hyperbola curve either on the upper or on the lower half zone of the central template position. Starting from the vertical symmetry axis of the template, close points belonging to the hyperbola curve on the left and on the right legs (usually 3 or 4 points) are extracted step-by-step. Because the number of curve points extracted is limited, a polynomial fitting of the second order was made to refine the estimate of the abscissa $y_0$ at the apex.

- The estimation of the several parameters describing the hyperbola curve such as $d, R, V$, the target depth and radius and the celerity in the soil, respectively (see Fig. 7) is obtained using a hyperbola fitting of the curve points to the classical analytical relation according to the LS criterion. Parameters SR and $y_0$, representing respectively the center-to-center distance between antennas and the horizontal coordinate of the object, are a priori known. The position of the radar referenced at the center of the system is located using coordinate $y_k$.

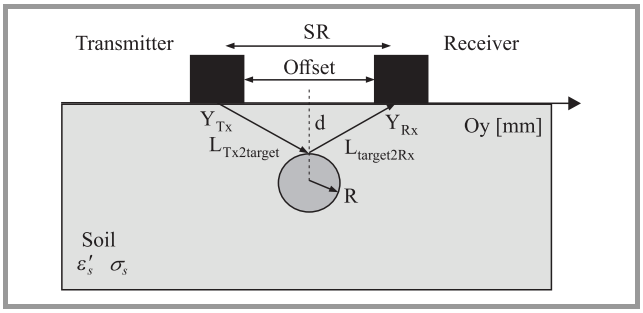


***Fig. 7.*** Cross-view of a pipe buried in a soil and parameters associated with the ray-path theory.

The equations associated with the travel-time write as follows [21]:

$$\begin{cases} y_T = y_k - \frac{SR}{2} \\ y_R = y_k + \frac{SR}{2} \end{cases} , \qquad (6)$$

$$\begin{cases} T_{Tx2target} = \left[ (y_0 - y_T)^2 + (d+R)^2 \right]^{\frac{1}{2}} - R \\ T_{target2Rx} = \left[ (y_0 - y_R)^2 + (d+R)^2 \right]^{\frac{1}{2}} - R \end{cases} , \qquad (7)$$

where $T_{Tx2target}$ and $T_{target2Rx}$ represents the ray paths between the transmitter or the receiver to the buried object. The velocity $v$ of the medium depends on the real relative permittivity $\varepsilon'_s$ such as:

$$v = \frac{c}{\sqrt{\varepsilon'_s}} ; \quad (\varepsilon''_s \ll \varepsilon'_s) . \qquad (8)$$

The generalized hyperbola equation $(y_k, t_k)$ including the antenna offset is expressed by:

$$t_k = \frac{T_{Tx2target} + T_{target2Rx}}{v} . \qquad (9)$$

Thus, $(y_0, t_0)$ represents the position in coordinate and time of the maximum of the hyperbola. It must be underlined that the hyperbola depends on five parameters $(SR, y_0, d, R, v)$. In general, the pipe radius cannot be properly estimated, as it appears smaller than the radiating aperture of one antenna (on the order of the first Fresnel zone in the soil). The minimum of the sum of squares of the

distances between theoretical $y_{k,theo}$ and measured $y_{k,meas}$ data has been solved using the Gauss-Newton method as follows:

$$F = \sum_{k=1}^{K} \left( y_{k,theo} - y_{k,meas} \right)^2 . \tag{10}$$

Some constraints relative to the parameter ranges have been added in the algorithm to better drive the solution.
The Hessian matrix in 2D and particularly its eigenvalues can be used to characterize the uncertainties on the estimated parameters $(d, v)$.

### 5.1. Application to Experimental Data

In the sandy box of the public square Perichaux, Paris 15th, the dielectric permittivity of the soil at this moment was estimated to 3.5 from common mid-point (CMP) measurements. Two targets, a 25 mm diameter dielectric pipe filled with air and a thin horizontal 10 mm width (2 mm thick) conductive strip were buried at the depths estimated to 160 and 170 mm respectively such as presented in Fig. 8a. Both objects are separated by a 750 mm distance. The scanning by the SFCW GPR has been performed in both end-fire and broadside polarizations (see Figs. 2a-b).
A synthetic template was computed from 3D FDTD simulations (software Empire) considering the detailed bowtie

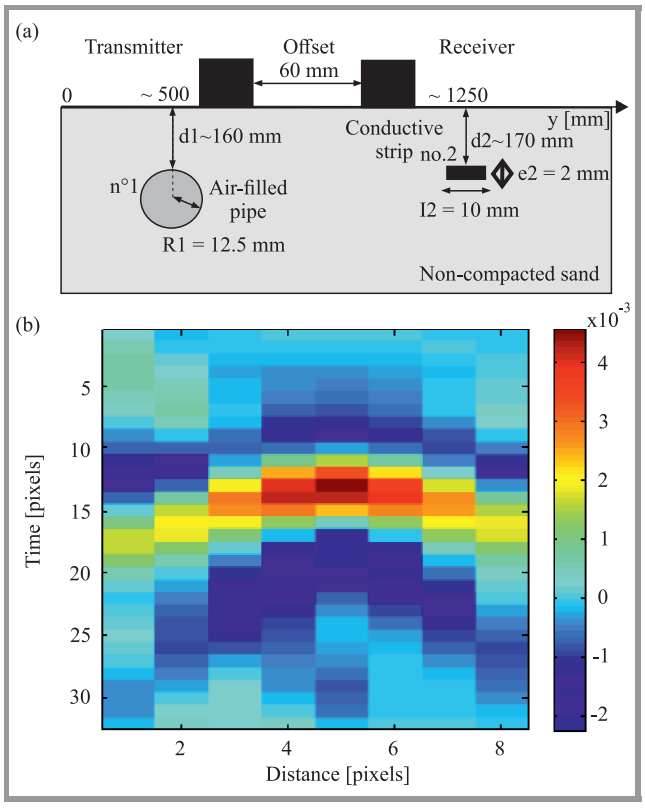


***Fig. 8.*** Geometry of the sandy box with two buried objects, an air-filled pipe and a horizontal conductive strip (a), synthetic template issued from FDTD simulations involving a pair of bowtie slot antennas (end-fire configuration) moved on a soil ($\varepsilon_s' = 3.5$, $\sigma_s = 0.01$ Sm$^{-1}$, $h_s = 10$ mm) with a buried conductive pipe ($R = 12.5$ mm) (b).

slot antenna geometry (Section 3) and 32 mm radius conductive pipe buried in a soil with a real relative permittivity $\varepsilon' = 3.5$ ($\sigma = 10^{-2}$ Sm$^{-1}$). The end-fire configuration has been considered. In this template visualized in Fig. 8b, it was wise to define a compact hyperbola signature with reduced multiple reflections to further detect different hyperbolas in a radargram in both polarizations. The template was scaled in time and amplitude to match the experimental time step $\Delta t = 5.56 \cdot 10^{-2}$ ns (step distance 40 mm used in the experiments), and the amplitude range of the experimental radargrams. Signed amplitudes have been used here to not deteriorate the image quality.

The template matching algorithm proposed has been performed on experimental radargrams considering the two orthogonal polarizations after application of the median subtraction technique. Results are presented for the geometry relative to Fig. 8a, and the time range has been defined to 5 ns. That leads to the L1 norm distance maps (also absolute distance maps) visualized in Figs. 9a and 9c. The position $(m, n)$ at which the smallest value $E(m, n)$ is obtained corresponds to the best match between the template t and the corresponding sub-image in $g$. A threshold value allows to select a limited number of local minima corresponding to distances less than the threshold where the template is well matched with enough amplitude (visualized by "+" signs on the radargrams). The maximum threshold values leading to the detection of the most significant hyperbolas are 0.162 and 0.195 in the broadside and end-fire configurations, respectively (see Figs. 9b and 9d). Higher values give additional detections (false alarms) that don't correspond to buried objects but to background heterogeneities. In the end-fire polarization, the distance map cannot permit to detect the air-filled pipe.

The results of the parameter evaluation from the least-square (LS) fitting of each hyperbola detected are collected in Tables 1 and 2. In general, the positions $y_0$ of the objects appear correctly evaluated. Concerning the real permittivity value of the soil, the broadside configuration gives higher estimates as compared to the end-fire configuration, and consequently the target depths appear more important.

Table 1
Parameter estimation in the broadside configuration for the experimental B-scan of Fig. 9b (max. is associated with the detection of the positive amplitude)

| Object | $d$ [mm] | $R$ [mm] | $\varepsilon'$ | $T_0$ [ns] | $y_0$ [mm] | *fval* |
|---|---|---|---|---|---|---|
| Pipe no. 1 (max) | 200 | 60 | 3.6 | 3.08 | 458.9 | $2.68 \cdot 10^{-2}$ |
| Pipe no. 1 (true values) | ~160 | 12.5 | 3.5–4 | | ~500 | |
| Strip no. 2 (max.) | 200 | 60 | 3.47 | 2.99 | 1232 | $2.23 \cdot 10^{-2}$ |
| Strip no. 2 (true values) | ~170 | 5 | 3.5–4 | | ~1200 | |

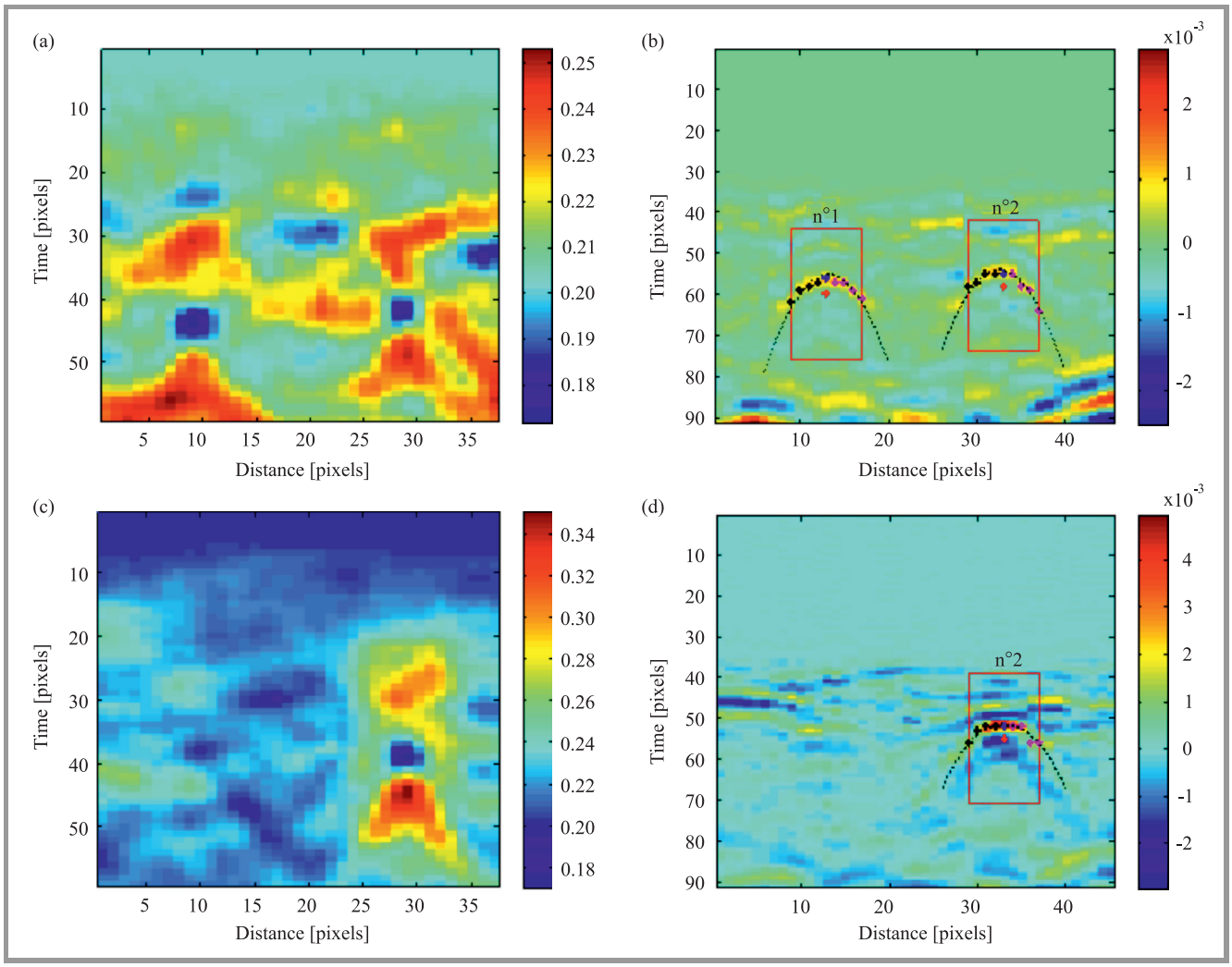


***Fig. 9.*** Analysis of experimental radargrams (in pixels, time range 5 ns) associated with an air-filled pipe and a horizontal conductive strip using the template matching algorithm: (a, b) in the broadside and (c, d) end-fire configurations; (a, c) time-distance maps, (b, d) positions of the image template in the original B-scans and hyperbola fitting.

Table 2
Parameter estimation in the end-fire configuration for the experimental B-scan of Fig. 9d

| Object | $d$ [mm] | $R$ [mm] | $\varepsilon'$ | $T_0$ [ns] | $y_0$ [mm] | *fval* |
|---|---|---|---|---|---|---|
| Strip no. 2 (max.) | 165.6 | 25.5 | 2.65 | 2.82 | 1250 | $1.85 \cdot 10^{-2}$ |

From Table 3 that collects eigenvalues of the Hessian matrix at the estimates of the depth and the velocity $(d, v)$, we remark that the depths of the pipe and the strip have been both estimated to 200 mm, and more important than those a priori known (see Fig. 8a). In the case of a soil having weak permittivity variations, an additional step would be to find an optimum permittivity value issued from the several estimates. We remark that the objective function *fval* associated with the LS fitting is presently higher for experimental data than for synthetic data of the order of $10^{-2}$, because the image quality appears lower.

To detect the air-filled pipe in Fig. 9d, joint information from radargrams issued from the parallel and end-fire configurations (polarization diversity) could be used. Thus, the mean distance map was calculated from the individual distance maps in the broadside and end-fire configurations (see Figs. 9a and 9c) leading to the result visualized

Table 3
Eigenvalues of the Hessian matrix at the estimates of the depth $d$ and velocity $v$ from hyperbola fitting in both polarizations

| Configuration | Eigenvalues for $(d; v)$ |
|---|---|
| Parallel | |
| Pipe no. 1 | $(4.1 \cdot 10^{-5};\ 2.1 \cdot 10^{-2})$ |
| Strip no. 2 | $(4.2 \cdot 10^{-5};\ 1.9 \cdot 10^{-2})$ |
| End-fire | |
| Strip no. 2 | $(4.0 \cdot 10^{-5};\ 9.6 \cdot 10^{-3})$ |

in Fig. 10a. A weak threshold (0.18) situated between the previous ones (0.162 and 0.195) associated with both polarizations (see Fig. 10b), has allowed here to detect both hyperbolas without false alarms in the end-fire configuration, that was not possible when this polarization was only considered. Further insight into the solutions of the parameters estimated in the fitting has been gained by calculating the Hessian matrix $H$ at the stationary point to evaluate its nature using its eigenvalues.

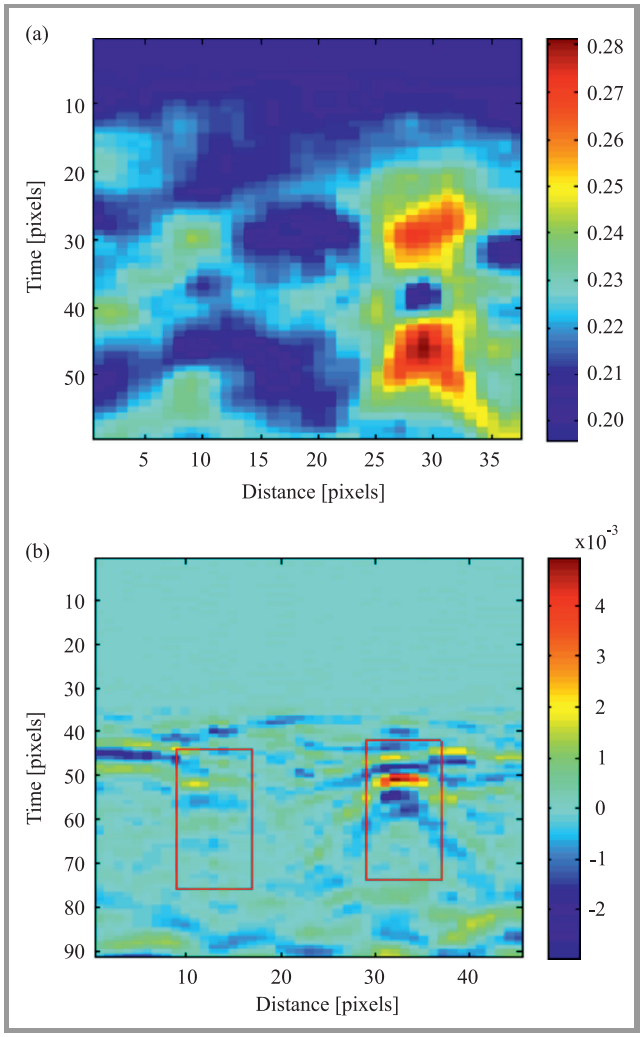


***Fig. 10.*** Mean distance map in the parallel and end-fire configurations associated with an air-filled pipe and a horizontal conductive strip (Fig. 8a) (a) and positions of the image template in the experimental B-scan in the end-fire configuration (b).

The rate of convergence and sensitivity to round-off errors is given by the condition number of matrix H, that is the ratio of its largest to its smallest eigenvalues. In the present examples, fixing the pipe radius that cannot be evaluated properly has led to a decrease of the condition number. The eigenvalues associated with the several fittings in both polarizations are collected in Table 3. In general, the condition number is high, that means that correlation may exist between the two parameters and thus the convergence of the estimation algorithm appears slow.

# 6. Polarization Diversity

As a target can depolarize the incident field, thus giving a scattering response depending and the orientation of the antennas relative to the target, it is worth to exploit the polarization to characterize the target, and its orientation, particularly in the case of a long target such as a cylinder.

## *6.1. Analytical Modeling*

The influence of the dielectric characteristics of a canonical target such as a cylinder (index $d$) illuminated by a electromagnetic (EM) polarized plane wave is described by the scattering theory [16], [23]. The backscattered fields depend strongly on the orientation of the cylinder relative to the antennas, its dielectric properties, and the radius of the cylinder compared to the wavelength $\lambda_0$ in the surrounding medium (index 0). The medium is usually air, but can be a dielectric material such as considered here. The scattering properties of a long cylinder has been described by the Bessel and Hankel functions. The scattering width (SW) is the equivalent area proportional to the apparent size of the target (in the far-field zone) that scatters the field relative to the incident power in each direction $\phi$. Four expressions associated with SW consider both TE and TM polarizations and the case of a dielectric or a conductive cylinder as follows [23]:

**TE polarization**

Conductive cylinder:

$$SW = \frac{2\lambda_0}{\pi}\left|\sum_{n=0}^{+\infty}\varepsilon_n \frac{J_n'(\beta_0 R)}{H^{(2)'}(\beta_0 R)}\cos(n\phi)\right|^2 \tag{11}$$

Dielectric cylinder:

$$SW = \frac{2\lambda_0}{\pi}\left|\sum_{n=0}^{+\infty}\varepsilon_n \times \right.$$

$$\left. \times \frac{\eta_d J_n'(\beta_d R)J_n(\beta_0 R) - \eta_0 J_n'(\beta_0 R)J_n(\beta_d R)}{\eta_0 J_n(\beta_d R)H_n^{(2)'}(\beta_0 R) - \eta_d J_n'(\beta_d R)H_n^{(2)}(\beta_0 R)}\right| \tag{12}$$

**TM polarization**

Conductive cylinder:

$$SW = \frac{2\lambda_0}{\pi}\left|\sum_{n=0}^{+\infty}\varepsilon_n \frac{J_n(\beta_0 R)}{H^{(2)}(\beta_0 R)}\cos(n\phi)\right|^2 \tag{13}$$

Dielectric cylinder

$$SW = \frac{2\lambda_0}{\pi}\left|\sum_{n=0}^{+\infty}\varepsilon_n \times \right.$$

$$\left. \times \frac{\eta_0 J_n'(\beta_d R)J_n(\beta_0 R) - \eta_d J_n'(\beta_0 R)J_n(\beta_d R)}{\eta_d J_n(\beta_d R)H_n^{(2)'}(\beta_0 R) - \eta_0 J_n'(\beta_d R)H_n^{(2)}(\beta_0 R)}\right| \tag{14}$$

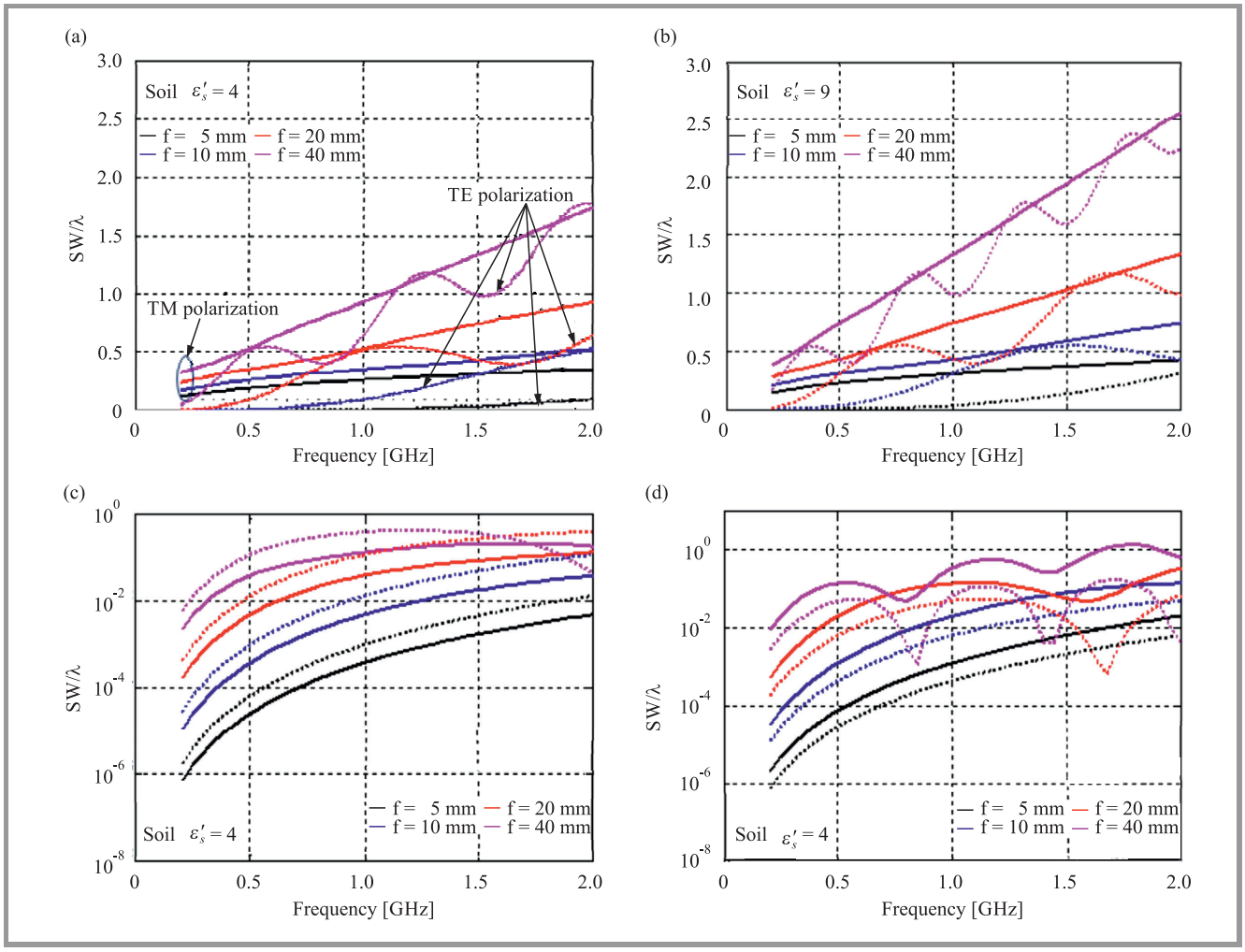


*Fig. 11.* Influence of the pipe radius and the real permittivity on the scattering width (SW) as a function of the frequency in the case of (a, b) a conductive and (c, d) a dielectric air-filled cylinder ($\varepsilon' = 1$ in "c" and $\varepsilon' = 9$ in "d").

where $\beta_0$ and $\beta_d$ are the wavenumbers, associated with the surrounding medium and the dielectric cylinder; they can be complex. $J_n(.)$ is the Bessel function of the first kind of order $n$, $J'_n(.)$ is its derivative, $H_n^{(2)}(.)$ is the Hankel function of the second kind of order $n$, and $H_n^{(2)'}(.)$ is its derivative.

The simplified modeling of the GPR system considers that the antennas, linearly polarized, are closely spaced. This results to a backscattering angle corresponding to $\phi = 180°$. Before analyzing theoretical and experimental B-scans, we have studied the scattered responses SW in a very large frequency band [0.2 ; 2] GHz considering several pipe radii and two dielectric contrasts between the pipe and the surrounding medium. The results collected in Figs. 11a-b, in the case of a conductive cylinder with a radius in the range 5…40 mm, highlight that the TM polarization (electric field parallel to pipe axis) generally leads to a higher backscattering response whatever the value of the real permittivity value ($\varepsilon'_0$ or $\varepsilon''_0 = 0$) of the surrounding medium. We remark that the TE component oscillates under the TM component for a radius higher than 5 mm. In general, the scattering width increases with the pipe radius and when the radius becomes large as compared to the wavelength of the medium; at 2 GHz, $\lambda_0 = 75$ mm for $\varepsilon'_0 = 4$, and $\lambda_0 = 50$ mm for $\varepsilon'_0 = 9$. Consequently, the TM polarization is preferred to detect a conductive pipe independently of its radius and the wavelength of the surrounding medium. Figure 11c-d associated with a dielectric cylinder show that the TE polarization gives a higher SW when the radius value is inferior to the wavelength and when the permittivity of the pipe (here filled with air) is less than the medium permittivity ($\varepsilon'_0 = 4$). When the pipe is more dielectric ($\varepsilon'_0 = 9$) than the medium, we remark that the TM polarization is in general higher than the TE polarization. We also observe that for a radius greater than 10 mm, TE and TM components oscillate and they can meet each other.

### *6.2. In-situ Measurements*

The measurement results presented have been made in the test bed Sense-City (see Fig. 3). To facilitate the subsequent interpretation of vertical profiles with buried pipes, reference measurements were performed apart from the areas

with buried objects to obtain the dielectric characteristics of the multilayered soil. Using the commercial GPR GSSI SIR 3000, a scanning has been acquired to identify the several layers of the sub-surface. Consistently with the direct observations during excavation, the raw radargram at 900 MHz (without time zero correction and clutter removal) shown in Fig. 12 shows a soil made of four layers corresponding to asphalt (layer 1), aggregate cement (layer 2),

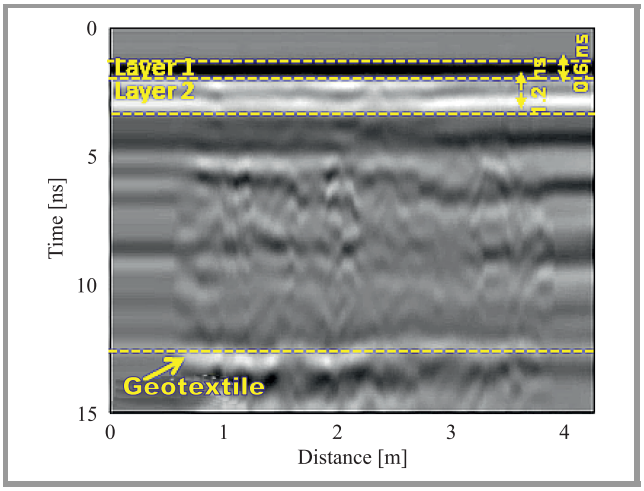


***Fig. 12.*** Experimental radargrams (B-scans) of the subsurface without buried objects measured by the SIR 3000 system (linear gain and low and high pass filters applied) at 900 MHz in the TM polarization.

a natural soil (layer 3), and a wetter natural soil (layer 4) located under the geotextile (a thin discontinuity). A sublayer of layer 3 (layer 3b) of natural soil under the aggregate cement appears visible in this zone of the site and it is attributed to a compacted layer of natural soil. This layer will not be observed in the zone with the trenches because the soil has been excavated. From the radargram at high resolution, we have estimated the real permittivities $\varepsilon'$ since we have an a priori knowledge of the thickness $h$ of each layer from the construction phase. According to Fig. 3a, the real permittivity estimations of the soil layers are the following: asphalt (layer 1) $\varepsilon'_1 = 4.5$ (0.64 ns), aggregate cement (layer 2) $\varepsilon'_2 = 7.7$ (1.4 ns), natural soil (mean of layers 3b and 3) $\varepsilon'_3 = 34$ (8.5 ns). Based on these results, a mean real permittivity of 12.7 is derived (decomposition in volumetric fractions).

Measurements have been made manually using the SFCW georadar system on the pipe zone of the test site whose cross section is presented in Fig. 13. The radargrams are presented in the time domain in both TE and TM polarizations (see Figs. 14a-b) considering a pulse with a peak frequency at 900 MHz. Neither low pass, nor high pass filters and nor time zero correction were applied here. The pipe in T5 was filled with air. A linear time gain [–10 ; 20] dB was applied to the radargram of Fig. 14a in the TE polarization (broadside). We remark in this figure that the air-filled pipe at depth 30 cm in T4 shows a detectable hyperbola signature (contrary to the SIR 3000 results). The signature of trench T1 appears weakly detectable, certainly because the distance step (4 cm) has not been defined here small enough (this will be improved in the future). In the TM polarization (end-fire), such as visualized in Fig. 14b, the measurements were made in two sequences that explains the vertical discontinuity in the radargram. In general, we remark that all the hyperbolas appear strongly attenuated that is consistent with the synthetic radargram obtained from FDTD simulations [22].

## 7. Conclusion

In this work, signal and image processing techniques have been collected with the aim of extracting quantitative information from experimental radargrams containing hyperbola signatures from pipes and strips with lateral dimension less than around ten centimeters. The difficulties met in the analysis of GPR radargrams is the detection of a hyperbola pattern in a noisy background, in a weak image quality, with overlapping between signatures of the clutter and one or multiple targets (particularly buried in a shallow depth), and also the detection of a target with a small lateral dimension and a weak contrast with a perturbed surrounding medium. The main objective was to propose a data processing chain easily implementable to analyze by steps radargrams made of hyperbola signatures associated with relatively small pipes (less than 100 mm). Thus, a semi-automatic data processing has been proposed that is supposed to be adaptable to hyperbola signatures en-

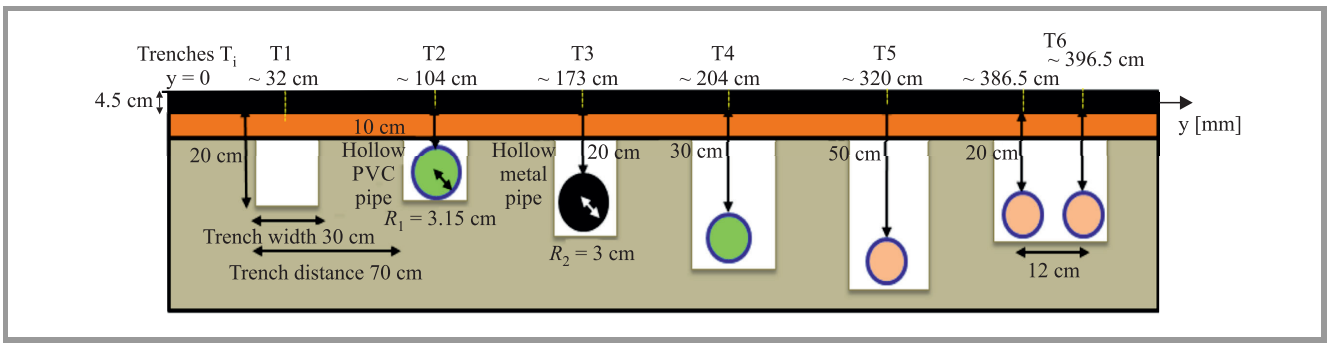


***Fig. 13.*** Cross-section of the pipe zone in the Sense-City test bed.

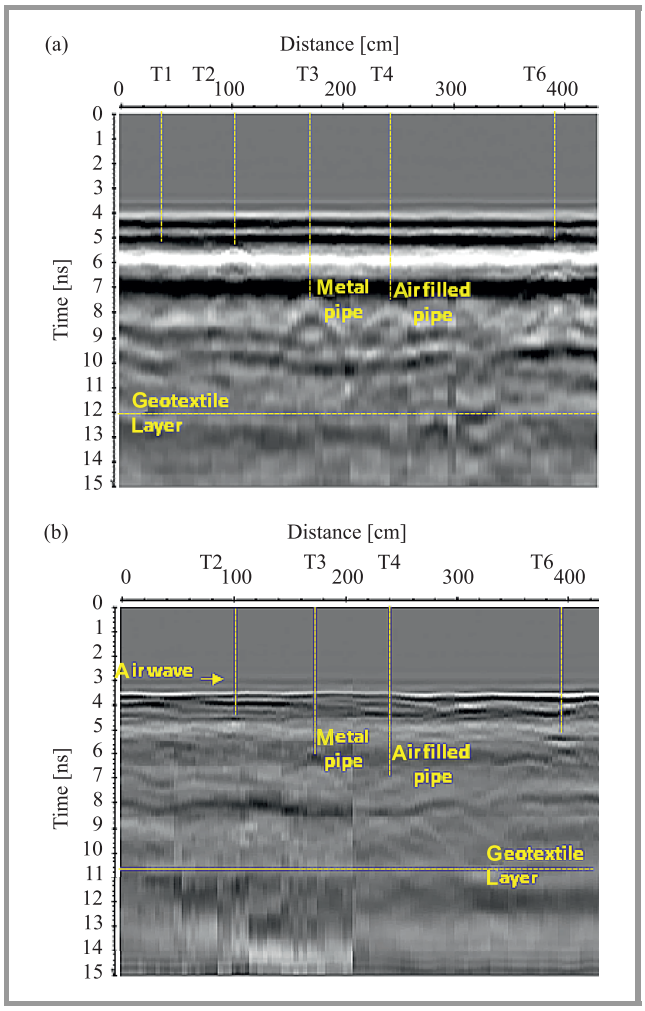


***Fig. 14.*** Experimental radargrams measured by the SFCW GPR system in the: (a) TE (broadside), and (b) TM (end-fire) polarizations.

countered in a generally noisy and heterogeneous environment showing different dielectric contrasts with the targets. It has been observed that to remove the clutter, deep and shallow targets must be distinguished. In the case of a shallow target, which significantly influences the clutter and the interface reflection, the PCA algorithm appears in general more efficient than ICA. In the case of a deep target, ICA appears to be more efficient than PCA. The template matching algorithm has been adapted to the hyperbola detection by means of the definition of a adequate template that represents a hyperbola shape close to the apex. The template has been generated from FDTD simulations. The algorithm has been validated on experimental radargrams, and has been extended to take advantage of data sets that consider the polarization diversity. This additional parameter improves the algorithm robustness. Future researches aim at applying the template matching algorithm on radargrams with different target shapes (pipe and cracks) and dielectric contrasts with the surrounding soil. Improvement of the data processing chain could be made by adding complementary algorithms such as space-frequency time-reversal matrices [24], wavelet transform, or hyperbola detection that accounts for hyperbola misshapedness [25].

## Acknowledgment

The author would like to thank colleagues belonging to several laboratories of IFSTTAR: Vincent Baltazart, Xavier Derobert, Elias Tebchrany, Berengère Lebental and Erick Merliot for their contribution in the different scientific parts to these researches during the past three years.
The author greatly acknowledges the COST Action TU1208 for proposing members to publish their recent research in applied electromagnetics.

## References

[1] Z. Liu and Y. Kleiner, "State of the art review of inspection technologies for condition assessment of water pipes", *Measurement*, vol. 46, no. 1, pp. 1–15, 2013.

[2] H. O. Henriques, M. Z. Fortes, L. Hudson, N. S. V. Silva, and F. O. Teixeira, "Use of radar illegal connections prospecting in buried or embedded cables", *Measurement*, vol. 47, pp. 221–227, 2014.

[3] CI/ASCE38-02, American Society of Civil Engineers, Standard guideline for the collection and depiction of existing subsurface utility data, 2002.

[4] ASTM Designation D 6432-11, Standard Guide for Using the Surface Ground Penetrating Radar Method for Subsurface Investigation, 2011.

[5] Italian Standard CEI-883, Regulations for performing preliminary surveys with ground-probing radar for before laying underground utilities and infrastructures, 2004.

[6] *Proceedings of the First General Meeting of COST Action TU1208*, L. Pajewski, and A. Benedetto, Eds. Rome, Italy, July 2013, Aracne, Rome, Italy, July 2013 [Online]. Available: http://www.cost.eu/domains_actions/tud/Actions/TU1208

[7] F. Sagnard, "Design of a compact ultra-wide band bow-tie slot antenna system for the evaluation of structural changes in civil engineering works", *Progress in Electromag. Res.*, PIER B, vol. 58, pp. 181–191, 2014.

[8] F. Sagnard and E. Tebchrany, "Using polarization diversity in the detection of small discontinuities by an ultra-wide band ground penetrating radar", *Measurement*, vol. 61, pp. 129–141, 2015.

[9] F. Sagnard, C. Norgeot, X. Derobert, V. Baltazart, E. Merliot, F. Derkx, and B. Lebental, "Utility detection and positioning on the urban site Sense-City using Ground Penetrating Radar Systems", *Measurement*, vol. 88, pp. 318–330, 2016.

[10] R. Solimene, A. Cuccaro, A. Dell'Aversano, I. Catapano, and F. Soldovieri, "Ground clutter removal in GPR surveys", *IEEE J. of Selec. Topics in Appl. Earth Observ. and Remote Sensing*, vol. 7, no. 3, pp. 792–798, 2014.

[11] E. Tebchrany, F. Sagnard, V. Baltazart, and J. P. Tarel, "Data processing of ground-penetrating radar signals for the detection of discontinuities using polarization diversity", European Geoscience Union General Assembly 2014, Vienna, Austria, 27 Apr. – 2 May 2014.

[12] G. T. Tesfamariam, D. Mali, and A. M. Zoubir, "Clutter reduction techniques for GPR based buried landmine detection", in *Proc. Int. Conf. on Signal Process., Commun., Comput. and Netw. Technol. ICSCCN 2011*, Thuckalay, India, 2011, pp. 182–186.

[13] I. T. Jolliffe, *Principal Component Analysis*, 2nd ed. Springer, 2002.

[14] A. Hyvärinen, "Independent component analysis: recent advance", *Philos Trans. A Math. Phys. Eng. Sci.*, vol. 371, no. 1984, 2013 (doi: 10.1098/rsta.2011.0534).

[15] A. Hyvärinen and E. Oja, "Independent component analysis: algorithms and applications", *Neural Netw.*, vol. 13, no. 4, pp. 411–430, 2000.

[16] S. J. Radzevicius and J. J. Daniels, "Ground penetrating radar polarization and scattering from cylinders", *J. Applied Geophys*., vol. 45, pp. 111–125, 2000.

[17] H. M. Jol, *Ground Penetrating Radar Theory and Applications*. Elsevier, 2008.

[18] P. K. Verma, A. N. Gaikwad, D. Singh, and M. Nigam, "Analysis of clutter reduction techniques for through wall imaging in UWB range", *Progress in Electromag. Res. B*, vol. 17, pp. 29–48, 2009.

[19] T. Fawcett, "An introduction to ROC analysis", *Pattern Recogn. Lett.*, vol. 27, no. 8, pp. 861–874, 2006.

[20] F. Sagnard and J. P. Tarel "Template-matching based detection of hyperbolas in ground-penetrating radargrams for buried utilities", *J. of Geophys. and Engin.*, vol. 13, no. 4, pp. 491–504, 2016.

[21] S. Shihab and W. Al-Nuamy, "Radius estimation for cylindrical objects detected by ground penetrating radar", *Subsurface Sensing Technol. and Appl*., vol. 6, no. 2, pp. 151–166, 2005.

[22] D. Vernon, *Machine Vision-Automated Visual Inspection and Robot Vision*. Prentice Hall, 1991.

[23] C. A. Balanis, *Advanced Engineering Electromagnetic*. Wiley, 1989.

[24] M. E. Yavuz, A. E. Fouda, and F. L. Teixeira, "GPR signal enhancement using sliding-window space-frequency matrices", *Progress in Electromag. Res.*, vol. 145, pp. 1–10, 2014.

[25] L. Mertens, R. Persico, L. Matera, and S. Lambot, "Automated detection of reflection hyperbolas in complex GPR images with no a priori knowledge on the medium", *IEEE Trans. Geosci. and Remote Sens.*, vol. 54, no. 1, pp. 580–596, 2016.

**Florence Sagnard** received the B.Sc. and the D.E.A. degree in Electronics from Université Pierre et Marie Curie, France, in 1990 and the Ph.D. degree from Université d'Orsay, France, in 1996. In 2005, she was qualified to conduct researches (HDR) from Université de Marne-La-Vallée, France. From 1997 to 2006, she was Assistant Professor at Université de Marne-La-Vallée and worked in the laboratory ESYCOM on the microwave characterization of materials. From 2002 to 2006 she worked as an invited researcher at INSA (Institut National des Sciences Appliquées), Rennes in UWB antennas, and transmission links. In 2007–2009, she joined CEREMA (Centre d'Etudes et d'expertise sur les Risques, l'Environnement, la Mobilité et l'Aménagement), Rouen, and since 2010 she is with IFSTTAR Marne-La-Vallée to develop SFCW GPR systems. Her research interests include data and image processing, FDTD simulations, UWB antennas, soil characterization, and civil engineering.
E-mail: florence.sagnard@ifsttar.fr
Université Lille Nord de France
IFSTTAR
20 rue Elisée Reclus
59650 Villeneuve-d'Ascq, France

Paper

# Search for Chelyabinsk Meteorite Fragments in Chebarkul Lake Bottom (GPR and Magnetic Data)

Vladimir Buzin[1], Dmitry Edemsky[1], Sergey Gudoshnikov[1], Vladimir Kopeikin[1], Pavel Morozov[1], Alexey Popov[1], Igor Prokopovich[1], Vladimir Skomarovsky[1], Nikolay Melnik[2], Andrey Berkut[3], Sergey Merkulov[3], Pavel Vorovsky[3], and Leonid Bogolyubov[3]

[1] *IZMIRAN, Troitsk, Moscow, Russia*
[2] *FIAN, Moscow, Russia*
[3] *JSC "Company VNIISMI", Moscow, Russia*

https://doi.org/10.26636/jtit.2017.120817

**Abstract—The paper summarizes experimental efforts of the Pushkov Institute of Terrestrial Magnetism, Ionosphere and Radio Wave Propagation (IZMIRAN) undertaken in search of the biggest part of Chelyabinsk meteorite in the bottom of lake Chebarkul, South Ural, Russia, and to estimate the ecological effects of its subsequent excavation.**

***Keywords—Chelyabinsk meteorite, Ground Penetrating Radar.***

## 1. Introduction

The Chelyabinsk meteoroid (February 15, 2013) with an estimated initial mass of about 10.000 tons was probably the biggest space object entering the Earth's atmosphere during the last 100 years. It released its kinetic energy, equivalent to a 500,000 tons TNT explosion, into a bright flash at a height of about 25 km (Fig. 1) and a large shock wave causing broken roofs and windows in an about $50 \times 100$ km area of Chelyabinsk region. Happily, no industrial object was touched, and hundreds of people received minor injuries. Many small meteorites produced ice carrots in the snow covering neighboring fields. The biggest part of the meteoroid landed in the western part of Chebarkul Lake

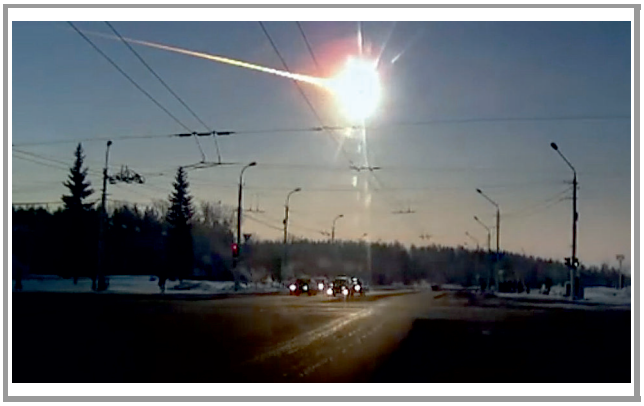

***Fig. 1.*** Chelyabinsk bolide. (See color pictures online at www.nit.eu/publications/journal-jtit)

***Fig. 2.*** Aerial photo of the meteorite ice-hole.

making an oval hole in the ice cover, up to 8 m in diameter (Fig. 2). The meteorite origin of the ice-hole was not commonly believed from the beginning, however Raman scattering analysis of the small chips, lifted from the lake bottom with a powerful magnet, and of micron-seized dust around the breach confirmed their space nature [1].

First divers' attempts to find the meteorite directly under the breach gave no effect (Fig. 3). The lake depth is about 10 m at the impact site, and the operations were hindered by the presence of a thick layer of loose silt, more than two-meter thick, according to their estimates. In order to reduce the search area, Ground Penetrating Radar (GPR) inspection of the lake bottom was performed from the ice surface by means of Loza-N GPR [2], [3]. Along with the information provided by Ural scientists and Czech colleagues [4], [5], the results of the IZMIRAN-VNIISMI GPR and magnetic surveys were used in preparing diving works undertaken later by the Aleut-Special Work Service Company [6] and resulting in the excavation of the biggest fragment of the space guest.

***Fig. 3.*** First diving works from the ice cover.

## 2. GPR Field Works

Loza GPR was designed at Pushkov Institute of Terrestrial Magnetism, Ionosphere and Radio Wave Propagation (IZMIRAN) in relation with a planned space mission [7]. Afterwards its serial production has been undertaken by Joint-Stock Company VNIISMI [8]. The main distinctive feature of Loza GPR is energy accumulation in a single transmitted pulse which is generated by a capacitor rapidly discharging through a high-voltage hydrogen key. Its duration and shape depend on the transmitter antenna parameters. It must be non-resonant in order to avoid spurious "ringing" (generally, it is a resistively loaded dipole following classical Wu-King law). Due to resistive loading, Loza antenna radiation approaches an ideal one-period electromagnetic burst. Its low Q-factor is compensated by the high pulse energy. Serial Loza transmitters have 5 to 20 kV peak voltage, the emitted pulse duration and energy being determined by the dipole length. Widely used in archeology and urban works "high-frequency" Loza-V sets with 0.5 to 1.5 m antennas have pulse central frequency in the range of 100–300 MHz and provide penetration depth of the order of 5–20 m, depending on ground conductivity (Fig. 4).

***Fig. 4.*** Field operation with Loza-V GPR.

In order to radically increase the signal energy and penetration, the pulse spectrum in the low-frequency Loza-N sounder is shifted to the lowest part of the receiver frequency band: 10–50 MHz [9]. A serial Loza-N set contains 3, 6, 10, and 15 meter-long transmitter antennas mounted on a heavy-duty nylon band. Identical antennas are used in the receiver unit recording signals reflected from the subsurface layer interfaces or localized buried objects. The receiver works in a waiting mode, being switched on by the first coming aerial signal. The absence of interconnecting cables eliminates interference and assures high signal-to-noise ratio. Loza central unit registers the waveform of the subsurface return pulse by means of a parallel set of high-rate comparators, with sampling frequency about 1 GHz. By repeating the measurement with input attenuation varying in a quasi-logarithmic scale, we obtain a 256-bit representation of the received signal in a 120 dB dynamic range.

***Fig. 5.*** Loza-N GPR survey around frozen ice-hole in lake Chebarkul.

Along with the aforementioned basic principles, the tight contact of the Loza-N flexible antennas with the ground and natural wave focusing towards electrically denser subsurface medium increase the GPR penetration depth. Compared with domestic and foreign analogs, Loza-N radar potential is increased by four orders of magnitude, allowing operation in highly conductive media, such as loam or wet clay. The sounding depth varies from a few meters to hundreds of meters, depending on the device model and medium properties. Taking into account the environment conditions (lake depth about 10 m and 1 m thickness of the ice/snow cover), low-frequency Loza-N model with 6-meter antennas was selected for GPR survey (Fig. 5). It could provide a sufficient probing depth and minimize interfering resonance effects. During three days of field works, March 12–14, 2013, the IZMIRAN-VNIISMI group (A. V. Popov, V. V. Kopeikin, S. V. Merkulov, V. A. Alek-

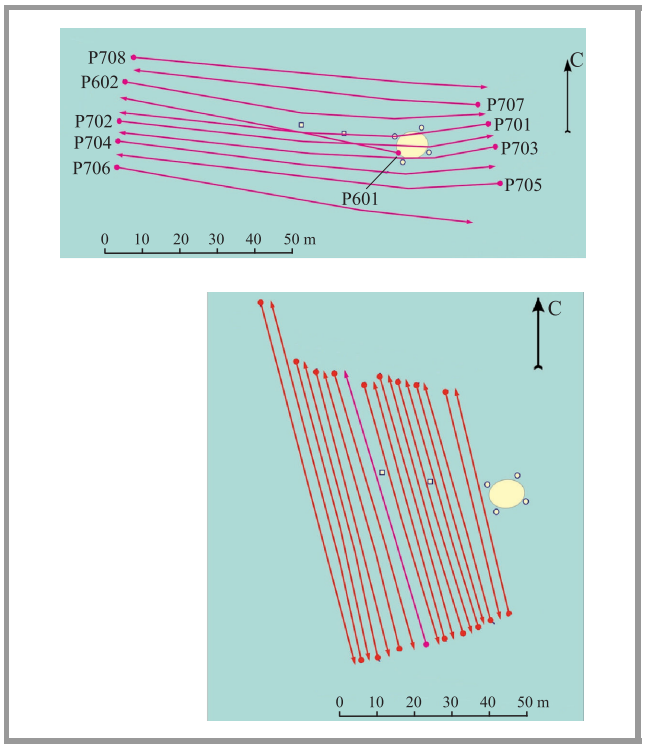


*Fig. 6.* GPR survey paths and ice-hole position.

seev) recorded 36 GPR scans covering a $100 \times 100$ m area around the ice-hole (taking into account the meteorite trajectory, maximum attention was turned to the western neighborhood of the breach) – see Fig. 6.

These data, registered from the ice cover, reveal distinct details of the lake bottom shape indicating probable impact points of big meteorite fragments. Small chips were collected around and under the breach in order to identify possible future findings. The results of magnetic moment measurements of 3-millimeter sized chips [1] are consistent with the reported characteristics of other fragments of Chelyabinsk meteorite.

## 3. Data Analysis

In Fig. 7, an example of raw data recorded by Loza-N GPR and represented by means of Krot-1301 software [8] is given. The right panel displays the waveform of the radar return signal received at a selected point of GPR survey path (A-scan [10]).

In the left panel, the vertical cross-section (B-scan) taken along one of the survey paths is shown. The horizontal axis depicts the distance along the GPR path whereas the vertical axis displays the return signal arrival time in nanoseconds (right scale) and calculated reflector depth (left scale). Peculiar horizontal strips in the upper part of the plot correspond to the direct waves traveling from the transmitter to the receiver antenna with different velocities in the ice layer and pure water beneath the ice cover.

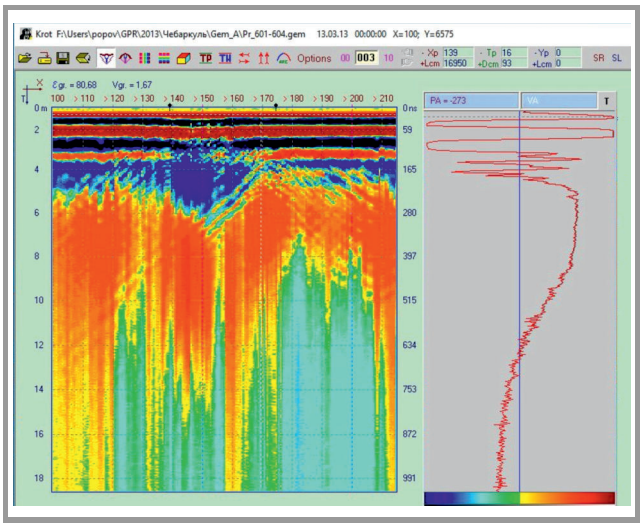

*Fig. 7.* Example of B-scan and selected radar return pulse (A-scan), Chebarkul lake, March 13, 2013.

The extended mono-polar pulses coming from greater depths are due to partial reflection from the gradual transition from pure water to the silt layer. Such a behavior is typical for the low-frequency Loza-N signals, which previously was attributed to the influence of ground conductivity. However, the numerical simulation shows that the main role in this case plays not conductivity but rather partial electromagnetic wave reflections from smooth gradients of the dielectric permittivity arising due to gradual increase of the solid fraction in the thick silt layer. A straightforward approach consists in numerical integration of the one-dimensional (1D) wave equation [11]. A good qualitative agreement with the experimental data has been obtained for a model transition layer between pure water with relative dielectric permittivity $\varepsilon_0 = 81$ and a solid ground with $\varepsilon_1 = 10$–$20$, see the left panel of Fig. 8. Our model also

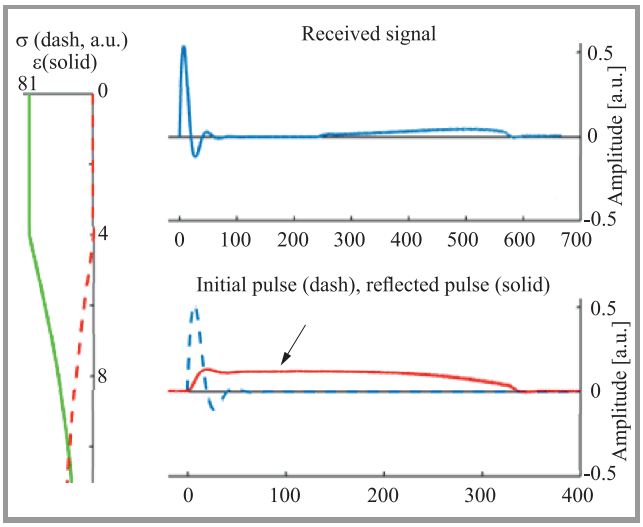


*Fig. 8.* Vertical profile of dielectric permittivity and soil conductivity (left), 1D numerical simulation of GPR return pulse (top), magnified reflected pulse (red, pointed by arrow) versus initial pulse (bottom).

took into account a gradual increase of the medium conductivity from $\sigma_0 = 0$ to $\sigma_1 = 0.001$ S/m. The duration of the model probing pulse is about 25 ns, which is close to the physical Loza-N pulse duration.

The full waveform of the electric field registered by the sensitive GPR receiver placed on the water surface is shown in the upper panel of the figure. Along with the short initial pulse, a weak protracted signal appearing due to partial reflections from the vertical gradients of the dielectric permittivity can be noticed. In order to better visualize the reflected signal on the strong primary pulse background, a minor exponential amplification $e^{\alpha t}$ has been introduced. Its waveform, shown in a magnified scale against the primary GPR pulse in the bottom panel of Fig. 8, is similar to the observed wave forms of low-frequency GPR probing, depicted in Fig. 7 (not taking into account the direct surface waves). In processing raw data with Krot-1301 software package, the characteristic points of the maximum amplitude variations of the reflected signal were interpreted as the interfaces of the non-uniform transition layer between pure water and the solid bottom ground. A qualitative understanding of partial reflections from the vertical permittivity gradients $\varepsilon'(z)$ gives the time-domain version of the coupled Wentzel-Kramers-Brillouin (WKB) approximation [11]:

$$g(s) = -\frac{1}{8}\int_0^{\frac{+}{z}(s)} \left(\frac{\varepsilon'(z)}{\varepsilon^{\frac{3}{2}}(z)}\right)' h\big[s - 2p(z)\big]\mathrm{d}z. \qquad (1)$$

Here, $s = ct$ is normalized propagation time, $g(s)$ – received EM signal, $h(s) = \int f(s)\mathrm{d}s$ is integral of the initial transmitted pulse $f(s)$, and $p(z) = \int_0^z \sqrt{\varepsilon(\xi)}\mathrm{d}\xi$ is optical path from the transmitter to the virtual reflection layer $z$. If the transmitted pulse length is small compared with the characteristic thickness of the transition layer, the integral (1) can be transformed to an explicit analytical expression [9]:

$$g(s) \approx -\frac{I(s)}{8}\left[\varepsilon^{-\frac{1}{2}}\left(\frac{\varepsilon'}{\varepsilon^{\frac{3}{2}}}\right)'\right]_{z=z_m(s)}, \qquad (2)$$

where $I(s) = \frac{1}{2}\int_0^s h(\xi)\mathrm{d}\xi$ and $z_m$ is the depth corresponding to the pulse roundtrip travel time $s \approx 2p(z_m)$.

In this simplified 1D wave propagation model a number of the physical moments have been ignored, i.e. boundary effects at the water surface covered with a thick ice layer, the offset between the transmitter and receiver antennas, wave divergence and radiation pattern of the dipole antenna placed on the interface. Having taken into account these factors in an improved 2D propagation model we reach a good agreement with the experimental radar scans – see Fig. 9a-b, and make our simulation be suitable for the field data analysis.

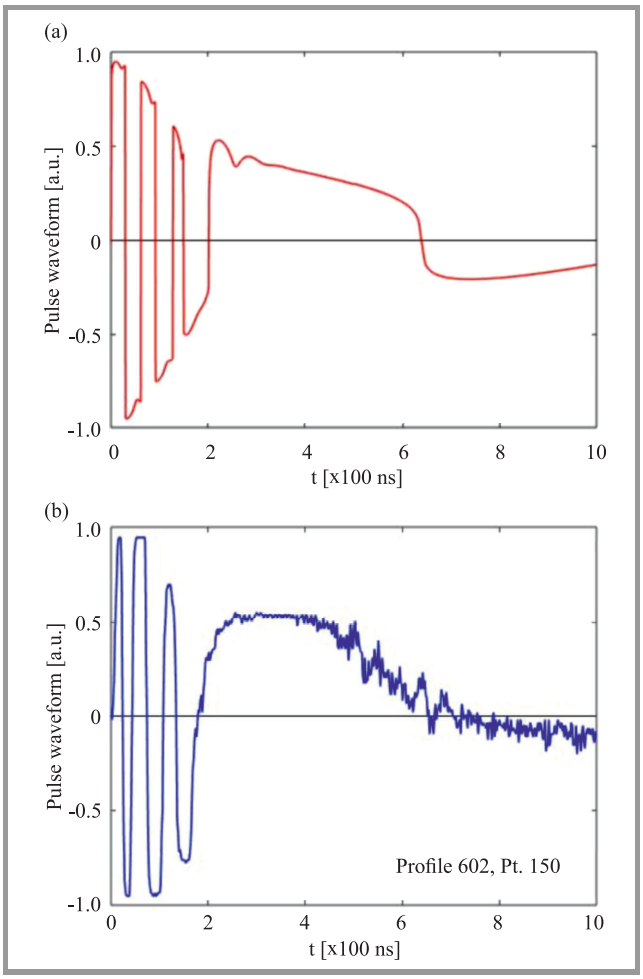


***Fig. 9.*** (a) Numerical simulation using 2D coupled-WKB approximation and (b) experimental A-scan.

## 4. Physical Considerations

A remarkable feature of the GPR B-scan presented in Fig. 7 is a pronounced depression in the bottom curve, accompanied by a local thickening and structure change of the ice cover, in P602 cross-section at its intersection with P603 scan (Fig. 10). We put forward a guess that this anomaly was the result of a meteorite fragment impact onto the lake floor. This hypothesis conforms to the observational facts. The oblique trajectory of meteorite flight with azimuth of 280–290° and small amount of ejected ice suggest that its major portion might be dragged down by the meteorite west of the hole and then float upward disturbing the structure of the ice cover above the impact crater. On the basis of these considerations, the GPR B-scans were analyzed in detail.

A standard frequency windowing procedure implemented in Krot-1301 software package allows one to pick out the characteristic points on the signal plot (e.g. maxima of the derivative) and to bind them into a radio image of the reflecting boundaries. Figure 11 displays an example of such processing distinctly revealing the lake bottom shape and the aforementioned disturbance of the ice cover structure. The interfaces of the transition silt layer between clear wa-

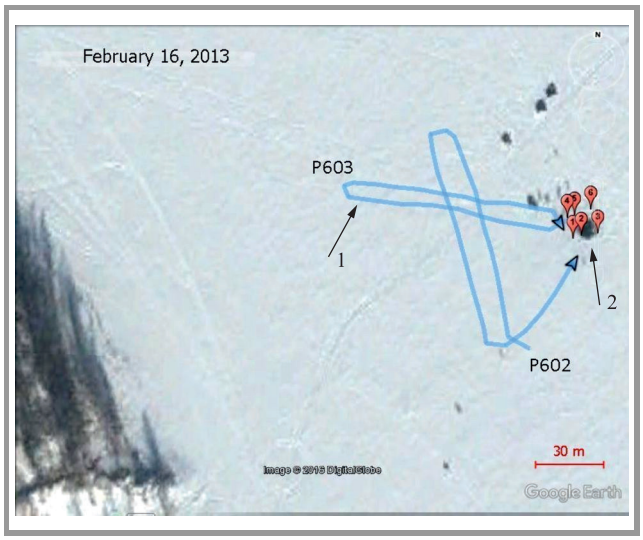


*Fig. 10.* Aerial photograph of the ice-hole. Crossing of P602 and P603 GPR paths (blue – arrow "1") shows probable meteorite fragment position in the lake bottom; red marks (arrow "2") – six stakes around the breach.

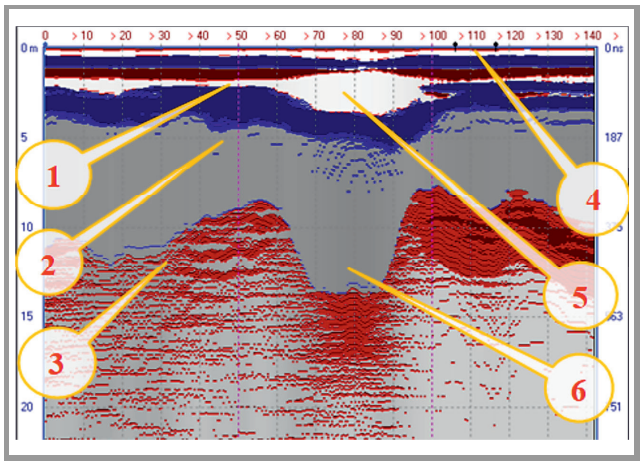


*Fig. 11.* B-scan along P602 track. Interpretation: 1 – ice layer, 2 – pure water and silt layer, 3 – hard bottom, 4 – ice-hole position, 5 – ice anomaly, 6 – meteorite crater.

ter and solid bottom are well seen. The hole produced in the ice cover by the meteorite impact, already frozen during our measurements, is pointed with black markers at the horizontal axis around the value 110 m. The pronounced depression of the bottom curve, which was interpreted as a result of the meteorite collision with the hard lake bed, is observed 30 m to the west (between 70 and 90 m marks). The local violation of the surface wave structure above the dip can be related to the aforementioned thickening of the ice cover due to the ice mass floated upwards from the impact crater.

A similar anomaly is observed at the neighboring GPR paths, resulting in a three-dimensional (3D) reconstruction of the supposed meteorite crater (Fig. 12). The spotted pattern of the reconstructed bottom shape prompts a suggestion that the meteorite, when sinking into the lake water, could break into pieces following a ricochet trajectory [8].

The main crater position relative to the ice-hole, being consistent with the observational trajectory data, allowed us to recommend searching for a big fragment of Chelyabinsk meteorite in the aforementioned region of the Chebarkul lake floor.

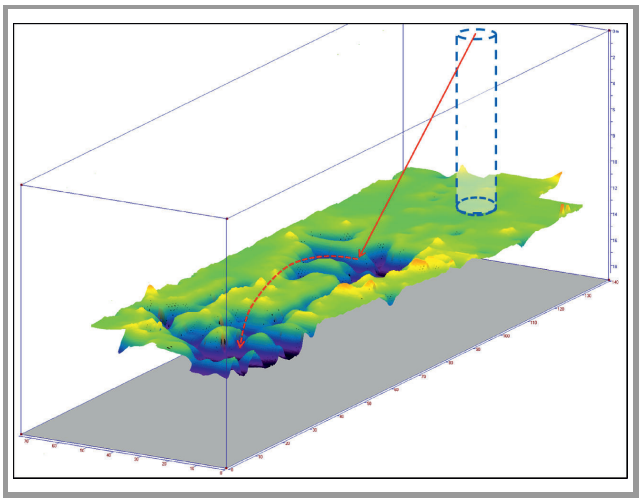

*Fig. 12.* 3D reconstruction of the hard bottom shape; dotted cylinder – ice-hole projection, arrows – possible meteorite fragments trajectories.

## 5. Magnetometry and Meteorite Recovery

Basing on the expected magnetic nature of the Chebarkul meteoroid fragment, several research groups performed magnetometric surveys of the supposed impact site. Just a week after the meteorite fall, February 20–21, 2013, Ovcharenko and Shchapov (Institute of Geophysics, Ural Branch of the Russian Academy of Sciences) performed magnetic mapping of the ice surface around the frozen ice-hole [4]. An overall distribution of the modulus of magnetic induction is presented in Fig. 13.

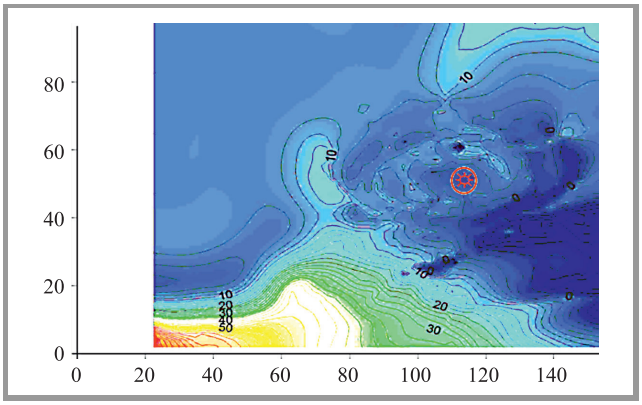


*Fig. 13.* Ural researchers' magnetic data [3].

The authors call the reader's attention to a weak positive horseshue-like anomaly c.a. 5-6 nT about 20 m west of the breach, which might be caused by the main fragments

of the hondrite body. A strong negative linear anomaly of 40–50 nT, south-east of the ice-hole, evidently has no relation with the meteorite body and may have man-caused nature.

Two weeks later, a research group from the Charles University, Prague, led by Kletetschka, made surface magnetic field mapping showing a positive anomaly to the north-west of the breach that was interpreted as a purely geological effect [5]. The subsequent underwater magnetic survey with a submersible fluxgate magnetometer, performed in June 19–22, 2013, revealed two sharp peaks of magnetic induction, south-east of the ice-hole – see Fig. 14. However, these anomalies, centered at the 9 m depth, also might have technogenic origin.

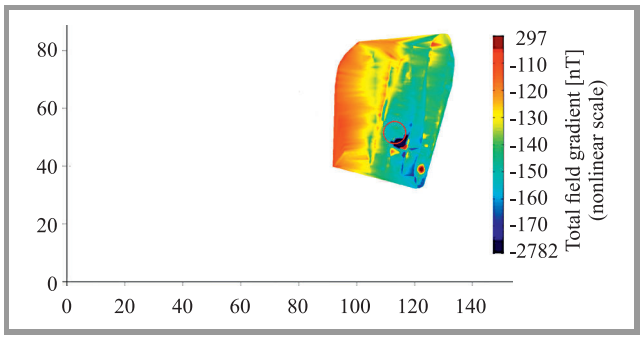


***Fig. 14.*** Czech scientists' magnetic data [5] (submersible magnetometer).

The second IZMIRAN mission (Gudoshnikov, Skomarovskij, Buzin, Alekseev, April 2–5, 2013) performed magnetic survey of a rectangular portion of the ice surface $80 \times 30$ m to the west of the ice-hole. The raw data (Fig. 15) exposed a regular increase of magnetic induction towards the west (coast effect, analogous to Fig. 14).

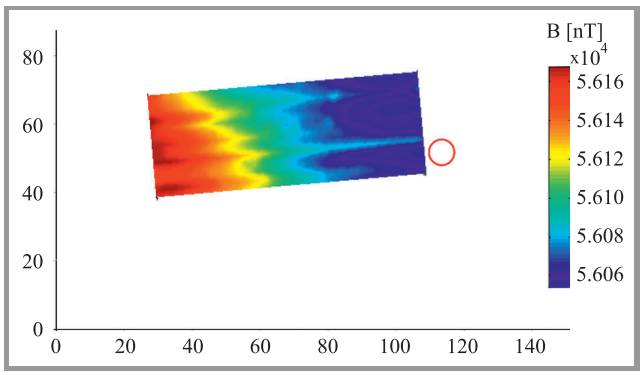


***Fig. 15.*** IZMIRAN team magnetic data.

By subtracting the westward trend we obtain a map of local magnetic anomalies (Fig. 16) having much in common with the pattern of GPR back reflections (cf. Fig. 12). This similarity supports our guess at the meteorite fragments position in the lake bottom ground.

The results of the first IZMIRAN-VNIISMI GPR and magnetic surveys were submitted to the Ministry of Ecology of the Chelyabinsk Region Government having sponsored the

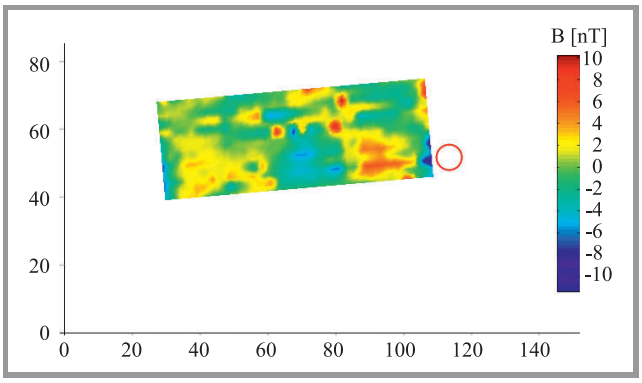


***Fig. 16.*** Magnetic anomaly (coast effect removed).


***Fig. 17.*** Floating platform for diving works.

diving works undertaken during September-October 2013 by the Aleut-Special Work Service Company [6] – Fig. 17. The underwater works ended up in finding and digging up a 654 kg meteorite fragment. These endeavors are vividly depicted in the recently published book [12]. According to the presented data, the biggest piece has been extracted from the depth of about 18 m, some 10 meter south-west of the breach. The main excavated meteorite fragment now is exposed in the Chelyabinsk Lore museum – Fig. 18. Its smaller parts, broken away during the diving works, have

***Fig. 18.*** Chebarkul meteorite fragment in the Chelyabinsk Lore Museum.

been presented to different organizations that took part in the search for the meteorite [13].

Raman scattering analysis of the fragment presented to IZMIRAN – Fig. 19a, performed by Melnik [14], confirmed its mineral composition corresponding to ordinary chondrite LL5 and spectral identity with the small meteorite chips gathered from the ice cover and the bottom of lake Chebarkul immediately after the meteorite fall – Fig. 19b.

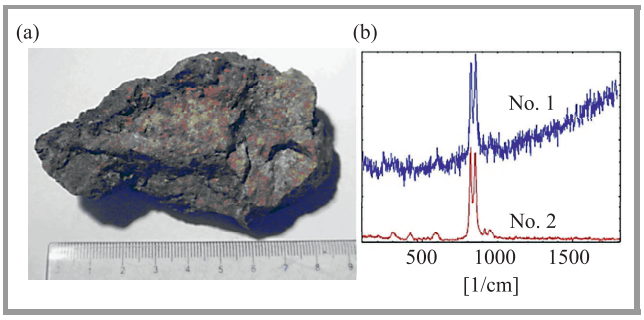


***Fig. 19.*** (a) Fragment presented to IZMIRAN, (b) Olivine manifestation in Raman scattering spectra of IZMIRAN specimen (no. 1) and of a small chip from the ice-hole (no. 2).

The second IZMIRAN-VNIISMI GPR mission (Popov, Prokopovich, Vorovskij, Bogolyubov, December 18–20, 2013) revealed a pronounced dip in the western direction from the ice-hole (see Fig. 20). This anomaly can be identified as a result of Aleut's digging works. The survey was performed with the same 6-meter long Loza-N antennas from the thick ice cover. Its spatial resolution did not allow to resolve finer subsurface features.

Taking into account the continuing interest to the Chelyabinsk event, ecological concerns about lake Chebarkul condition and methodical problems of GPR measurements from the water surface, four years later the third IZMIRAN GPR mission was organized (Edemskij, Popov, Prokopovich, Bogolyubov, June 15–22, 2017). The main goal of the planned survey was to draw the bottom line left after the Aleut diving works and to detect possible subsurface objects. In order to provide better spatial resolution we should use shorter antennas. Basing on our previous experience, we first tried a standard Loza-V GPR transmitter and antenna set (Fig. 4) assuring 10–12 m penetration in a fresh lake water [15]. All the equipment could be placed in a hull of a small rowing boat allowing convenient through-water operation along a chaotic path controlled by GPS.

Unfortunately, the tests performed in the vicinity of the meteorite impact site (west coast of lake Chebarkul) had shown worse penetration, making Loza-V set useless at the depths exceeding 5 m – see Fig. 21.

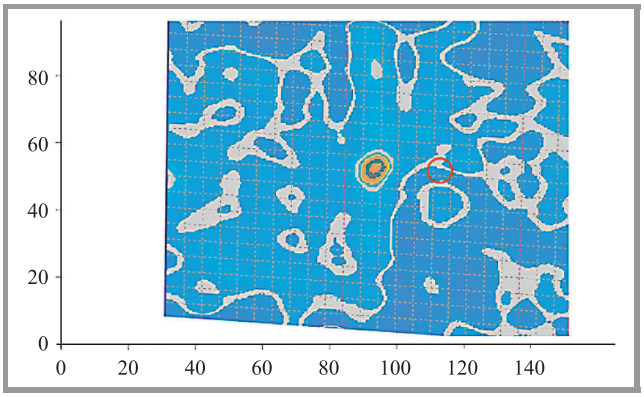


***Fig. 20.*** Lake ground reflectivity according to second IZMIRAN GPR mission.

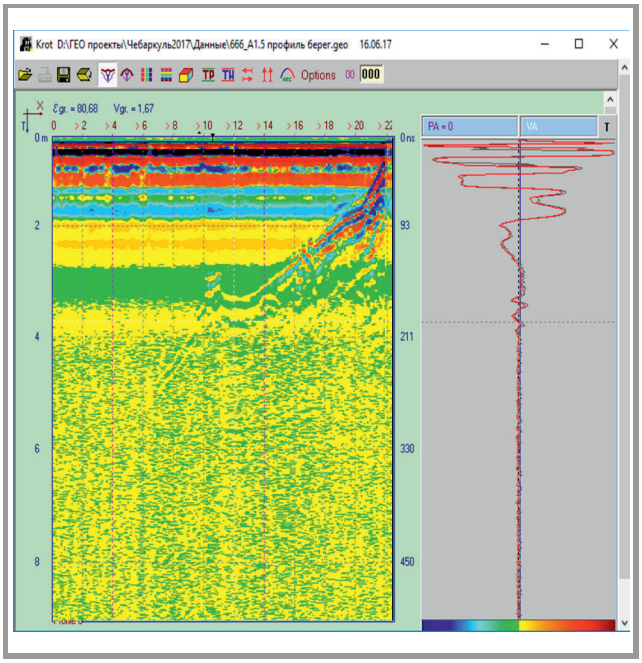


***Fig. 21.*** Lake Chebarkul bottom line, Loza-V GPR (west coast).

***Fig. 22.*** Testing 4-m dipole antennas.

This result allows one to roughly estimate the electrical conductivity of the lake water. The additional linear electromagnetic wave attenuation $1640\frac{\sigma}{\sqrt{\varepsilon_r}}$ dB/m amounts to 120 dB (dynamic range of Loza receiver) on a roundtrip path of 10 meters for $\sigma$: 0.066 S/m, which is in a good agreement with the hydrological data obtained after the meteorite fall [16].

Trying to overcome this limitation, we developed a home-made antenna set of intermediate (4 m) size but heavy rain storms did not allow us to complete the experiment.

## 6. Conclusion

The results of the first IZMIRAN-VNIISMI GPR survey (March 12–14, 2013) and the data of magnetic measurements performed by the next IZMIRAN expedition (April 2–5, 2013) from the ice surface revealed a pronounced anomaly, west of the breach left after Chelyabinsk meteorite fall into lake Chebarkul (February 15, 2013). Along with other research groups' data, they were used in preparing diving works undertaken during September 2013 by the Aleut-Special Work Service Company and sponsored by the Chelyabinsk region government. These works resulted in finding and lifting a big fragment of the meteorite (October 13, 2013). A part of the excavated space body presented to IZMIRAN was put to Raman scattering analysis at Lebedev Physical Institute (FIAN), conforming its mineral composition corresponding to ordinary chondrite (LL5). GPR survey performed by the third IZMIRAN mission (December 18–20, 2013) revealed a sharp dip in the lake bottom, probably a result of the digging operation. An attempt of detailed GPR inspection of the lake bottom undertaken in June 2017 did not give impressive results because of high conductivity of the lake water and bad weather conditions. However, among others, our GPR data and magnetic measurements prompt that a considerable mass of the meteorite matter may still reside in the lake Chebarkul bottom ground.

## Acknowledgment

This publication is dedicated to the memory of Vladimir Alekseev who participated in two IZMIRAN expeditions, collecting small meteorite particles and performing their physical-chemical analysis. The authors are grateful to E. V. Korolkov and Chebarkul city administration for technical support of the field works. This paper is written as a contribution to the Special Issue "Recent Progress in Electromagnetic Theory and its Applications" organized by the COST Action TU1208 "Civil engineering applications of Ground Penetration Radar".

* * *

Regretfully, one of the co-authors – Vladimir Kopeikin passed away during the process of article publication.

## References

[1] V. A. Alekseev, A. I. Berkut, and N. N. Melnik, "Meteorite investigation by CRS method. Chelyabinsk meteorite and Tunguska phenomenon", in *Raman Scattering – 85 Years of Research*, A. N. Vtiurin, Ed. Krasnoyarsk: Institute of Physics, 2013, pp. 162–171.

[2] V. V. Kopeikin *et al*., "Ground penetrating radar investigation of the supposed fall site of a fragment of the Chelyabinsk meteorite in lake Chebarkul", *Geochemistry Int*., vol. 51, no. 7, pp. 575–582, 2013.

[3] V. V. Kopeikin *et al*., "GPR inspection of the Chelyabinsk meteorite impact site at the Chebarkul lake bottom", in *Proc. 15th Int. Conf. on Ground Penetrat. Radar GPR 2014*, Brussels, Belgium, 2014, pp. 1054–1057.

[4] A. V. Ovcharenko and V. A. Shchapov, "Magnetic observations at the Chebarkul fragment of Chelyabinsk meteorite impact site", in *Proc. Scient. Conf. "Chelyabinsk Meteorite, a Year on Earth"*, Chelyabinsk, Russia, 2014, pp. 294–300 (in Russian).

[5] G. Kletetschka, J. Vyhnanek, D. Kawasumiova, L. Nabelek, and V. Petrucha, "Localization of the Chelyabinsk meteorite from magnetic field survey and GPS data", *IEEE Sensors J.*, vol. 15, no. 9, pp. 4875–4881, 2015.

[6] Aleut – Special Work Service [Online]. Available: http://www.aleut.ru

[7] V. V. Kopeikin, D. E. Edemsky, V. A. Garbatsevich, A. V. Popov, A. E. Reznikov, and A. Yu. Schekotov, "Enhanced power ground penetrating radars", in *Proc. 6th Int. Conf. on Ground Penetrat. Radar GPR'96*, pp. 152–154. Sendai, Japan, 1996.

[8] JSC VNIISMI [Online]. Available: www.geo-radar.ru

[9] A. I. Berkut, D. E. Edemsky, V. V. Kopeikin, P. A. Morozov, I. V. Prokopovich, and A. V. Popov, "Deep penetration subsurface radar: hardware, results, interpretation", in *Proc. 9th Int. Symp on Adv. Ground Penetrat. Radar IWAGPR 2017*, PS-2, 3_25, Edinbourgh, United Kingdom, 2017 (doi: 10.1109/IWAGPR.2017.7996052).

[10] D. J. Daniels, *Ground Penetrating Radar*. London: IEE, 2004.

[11] V. A. Vinogradov, V. V. Kopeikin, and A. V. Popov, "An approximate solution of 1D inverse problem", in *Proc. 10th Int. Conf. on Ground Penetrat. Radar GPR 2004*, Delft, Netherlands, 2004, pp. 95–98.

[12] *Search and Excavation of Chelyabinsk Meteorite*. South Ural Publishing House, 2015, ISBN 978-5-7688-1083-2 (in Russian).

[13] A. V. Kocherov and V. A. Tyumentsev, "Fragments of Chelyabinsk meteorite from Lake Chebarkul", in *Proc. Scient. Conf. "Chelyabinsk Meteorite, a Year on Earth"*, Chelyabinsk, Russia, 2014, pp. 348–354 (in Russian).

[14] A. V. Popov and N. N. Melnik, "Notes on the search and characterization of Chelyabinsk meteorite", in *Proc. 2nd Practical Scient. Conf. "Meteorites, Asteroids, Comets"*, Chebarkul, Russia, 2014, pp. 101–106. Theta Publ., Chelyabinsk, 2014 (in Russian).

[15] A. Popov, P. Morozov, D. Edemsky, F. Edemsky, B. Pavlovskij, and S. Zapunidi, "Expedient GPR survey schemes", in *Proc. 11th Int. Radar Symp. IRS 2010*, 8a-3, Inspec Acc. 11474488, Vilnius, Lithuania, 2010.

[16] S. G. Zakharov, *Ecosystem of Lake Chebarkul Before and After Meteorite Fall*. Chelyabinsk: Kraj Ra Publishers, 2014 (in Russian).

**Vladimir Buzin** graduated from Physical Department of Moscow State University in 1969. He is currently working in the Laboratory of Magnetic Cosmic Research, Pushkov Institute of Terrestrial Magnetism, Ionosphere and Radio Wave Propagation, Russian Academy of Sciences. His expertise is magnetic data processing, service and calibration of magnetic measuring installations and devices.
E-mail: buzin.40@mail.ru
IZMIRAN
4 Kaluzhskoye Hwy
Troitsk, Moscow 108840 Russia

**Dmitry Edemsky** received his Ph.D. degree in Technical Sciences from Vinnytsa National Technical University in 1989. He works as Senior Scientist at Pushkov Institute of Terrestrial Magnetism, Ionosphere, and Radio Wave Propagation (IZMIRAN), Russian Academy of Sciences. His research interests include ELF-VLF radio wave propagation, tweak-atmospherics, Earth-ionosphere waveguide, ground penetration radar, deep electromagnetic probing.
E-mail: edemsky@izmiran.ru
IZMIRAN
4 Kaluzhskoye Hwy
Troitsk, Moscow 108840 Russia

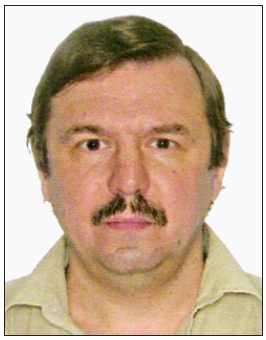

**Sergey Gudoshnikov** received his Ph.D. from Moscow State University, Department of Physics in 1992. Currently, he is a leading researcher in the Institute of Metallurgy, Ecology and Quality at National University of Science and Technology "MISiS". His research interests include: new magnetic materials, high sensitive magnetic sensors, precise magnetic measurements.
E-mail: gudosh@izmiran.ru
Department of Physical Metallurgy of Non-ferrous,
Rare-earth, and Noble Metals
National University of Science and Technology "MISiS"
4 Leninsky Ave
Moscow, 119049 Russia

**Vladimir Kopeikin** received his Ph.D. from the Radiotechnical Faculty of Moscow Power Engineering Institute. Now he is a Senior Researcher of IZMIRAN, Principal Specialist of JSC "Company VNIISMI". Chief designer of Loza GPR series. He is an author and promoter of R&D works on deep penetration radar, underwater marine radar and holographic subsurface radar.
E-mail: kopeikin@izmiran.ru
IZMIRAN
4 Kaluzhskoye Hwy
Troitsk, Moscow 108840 Russia

**Pavel Morozov** is a Senior Researcher of IZMIRAN, Vice Director of JSC "Company VNIISMI". He graduated from Odessa Hydrometeorology Institute, Faculty of Oceanology and Atmospheric Physics, and has Ph.D. in Physics. He is a member of Loza GPR developers' team, author of subsurface radar survey and interpretation methods. He has vast practical experience, teaching and supervision of GPR users.
E-mail: pmoroz5@yandex.ru
IZMIRAN
4 Kaluzhskoye Hwy
Troitsk, Moscow 108840 Russia

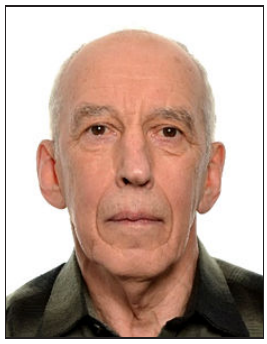

**Alexey Popov** is a D.Sci., Life Member of IEEE and Head of Radiowave Propagation Department, IZMIRAN. He graduated from Moscow Institute of Physics and Technology in 1964. His expertise includes mathematical physics, computational methods, general diffraction theory, radio wave propagation, ground penetrating radar, X-ray and fiber optics.
E-mail: popov@izmiran.ru
IZMIRAN
4 Kaluzhskoye Hwy
Troitsk, Moscow 108840 Russia

**Igor Prokopovich** received his M.Sc. in Applied Mathematics and Physics from Moscow Institute of Physics and Technology in 2012. He did his Ph.D. study at IZMIRAN (2014–2017). His expertise is mathematical physics, computational methods, ground penetrating radar, and subsurface microwave holography.
E-mail: prokop21@mail.ru
IZMIRAN
4 Kaluzhskoye Hwy
Troitsk, Moscow 108840 Russia

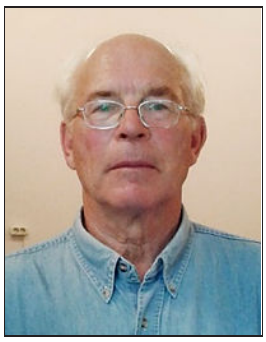

**Vladimir Skomarovsky** received his Ph.D. from Pushkov Institute of Terrestrial Magnetism, Ionosphere, and Radio Wave Propagation, Russian Academy of Sciences in 1980. He is currently Senior Scientist in the Laboratory of quantum and cryogenic magnetometry of IZMIRAN. His research interests include magnetic phenomena, magnetic imaging, magnetometry, and amorphous ferromagnetic microwires.

E-mail: vskom@izmiran.ru
IZMIRAN
4 Kaluzhskoye Hwy
Troitsk, Moscow 108840 Russia

**Sergey Merkulov** is a Chief Specialist of JSC "Company VNIISMI". He graduated from High Military School of air defence pilots and navigators. He is the author and developer of "Krot" software for Loza GPR data processing. GPR profiling and surface survey practical schemes. Teaching and supervision of GPR users.

E-mail: merservit@mail.ru
JSC "Company VNIISMI"
16/1 Olimpijsky Ave
129090 Moscow, Russia

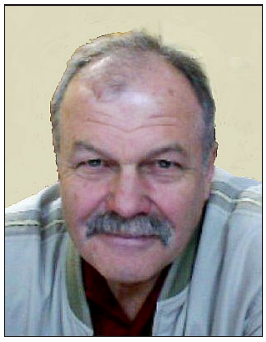

**Nikolay Melnik** is a Ph.D. and Leading Researcher in Laboratory of Physics of Non-uniform Systems, Lebedev Physical Institute. His expertise includes: Raman spectroscopy, micro-Raman, high pressure, low and high temperature, resonance Raman scattering. His scientific interests are: disordered and porous materials, nanocrystals, clusters and quantum dots, carbon materials, nanoparticles, diamond-like films, optical properties of films, multilayer structures, and superlattices.

E-mail: melnik@lebedev.ru
FIAN
53 Leninsky Ave
119991 GSP-1 Moscow, Russia

**Andrey Berkut** is a D.Sci. (Technical Sciences), professor and director general of JSC "Company VNIISMI". He graduated from Moscow Technical University of Communication and Informatics. He is a member of Loza GPR developers' team. Production supervision, marketing, contract activities, development of schemotechnical solutions. GPR application to concrete production in Siberia.

E-mail: lozaberk@yandex.ru
JSC "Company VNIISMI"
16/1 Olimpijsky Ave
129090 Moscow, Russia

**Pavel Vorovsky** is a geologist and Leading Researcher, JSC "Company VNIISMI". He graduated from Russian State Geological Prospecting University. He is an expert in GPR data processing and geological structure characterization, vast practical experience.

E-mail: volga70@inbox.ru
JSC "Company VNIISMI"
16/1 Olimpijsky Ave
129090 Moscow, Russia

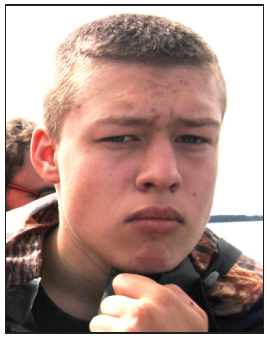

**Leonid Bogolyubov** is a secondary school student (Troitsk Orthodox School, Moscow Institute of Physics and Technology Phys-Math Correspondence School). He is volunteer member of IZMIRAN-VNIISMI field campaigns.

E-mail: l.e.o.n.2002@mail.ru
12/56 Solnechnaya
Troitsk, Moscow, 108840 Russia

Paper

# Multi-Objective Evolutionary Optimization of Aperiodic Symmetrical Linear Arrays

Francesco Napoli[1], Lara Pajewski[2], Roberto Vescovo[3], and Marian Marciniak[4]

[1] *Italian National Agency for New Technologies, Energy and Sustainable Economic Development, Frascati, Italy*
[2] *Department of Information Engineering, Electronics and Telecommunications, Sapienza University of Rome, Rome, Italy*
[3] *Department of Engineering and Architecture, University of Trieste, Trieste, Italy*
[4] *National Institute of Telecommunications, Warsaw, Poland*

https://doi.org/10.26636/jtit.2017.118517

**Abstract—In this paper, a multi-objective approach is applied to the design of aperiodic linear arrays of antennas. The adopted procedure is based on a standard Matlab implementation of the Controlled Elitist Non-Dominated Sorting Genetic Algorithm II. Broadside symmetrical arrays of isotropic radiators are considered with both uniform and non-uniform excitations. The work focuses on whether, and in which design conditions, the aperiodic solutions obtained by the adopted standard multi-objective evolutionary procedure can approximate or outperform the Pareto-optimal front for the uniform-spacing case computable by the Dolph-Chebyshev method.**

***Keywords—antenna array, Dolph-Chebyshev array, genetic algorithms.***

## 1. Introduction

A deeper understanding of evolutionary mechanisms along with an increasing availability of computational resources, allow scientists to simulate natural evolution with computer programs and use it as a new paradigm for problem solving in physics and engineering.

Genetic algorithms (GAs) [1], [2] are robust population-based global-search stochastic iterative methods inspired by the concept of evolution by natural selection. GAs have been successfully applied in many areas to a wide range of engineering problems, and nowadays, they are largely accepted as useful optimization techniques. This is especially true for antenna array design [3], [4].

The typical array design problem consists in finding positions and weight coefficients of the array elements, so that the radiation pattern can satisfy a given set of design specifications [5]. The main design parameters are: gain and directivity, beamwidth (BW) and half-power beamwidth, side-lobe level (SLL), aperture, geometry, robustness, noise sensitivity, bandwidth, dynamic range of current excitations, input and output (radiated) power.

The synthesis techniques for linear arrays can be divided into two main categories: one dealing with uniformly spaced (periodic) arrays and the other with non-uniformly spaced (aperiodic) arrays. The former problem is, at least in some cases, analytically tractable [5], [6]. The latter problem is usually solved by numerical methods [7]–[14].

Aperiodic arrays are very attractive with respect to equally-spaced arrays [10]. A first reason is that the SLL may be improved over the –13.5 dB limit of uniform arrays, while keeping a uniform excitation (provided that a suited number of radiating elements is used and that the average spacing is approximately equal to or less than half wavelength). Second, when dealing with non-uniform excitations it is possible to reduce the amplitude tapering necessary to achieve a required SLL. Third, aperiodic arrays may be realized, in an assigned aperture, by using a reduced number of elements (thinned arrays) with a limited increase of BW and a significant reduction of the array cost. Fourth, by breaking the array periodicity it is possible to improve the bandwidth and reduce the grating lobes in the radiation pattern even if the average spacing is high. Fifth, the mutual coupling between adjacent elements can be reduced thanks to the aperiodicity and to the longer average spacing achievable.

Many numerical methods have been developed to face synthesis problems for aperiodic arrays, including techniques based on mathematical programming, such as constrained [8] and nonlinear [9] programming. Other numerical optimization strategies have also been proposed, based on the synthesis of a density-tapered distribution of uniformly excited elements [7], [12], or of a combined amplitude-density tapered distribution of non-uniformly excited elements [11], approximating a properly chosen continuous source. Stochastic global optimization techniques based on meta-heuristics, such as evolutionary algorithms (GAs, differential evolution), have been successfully applied to the antenna array design problem showing a high flexibility [3], [15]–[27]. In [28], a comparison is presented between different population-based optimization methods applied to the design of scannable circular antenna arrays: genetic algorithms, particle-swarm optimization and the differential evolution method are considered.

In the array design, it is often necessary to simultaneously satisfy two or more conflicting specifications, thus a trade-off between objectives must be found. This is the case where both SLL and BW must be minimized for a given number of array elements. In this case, as it is known,

none of those parameters can be improved without worsening the other: if the radiated power is fixed, in the presence of a more directive main beam, there is also more radiation in undesired directions; smaller side lobes, instead, correspond to a larger main beam. Looking for the best trade-off between SLL and BW is a Multi-Objective Optimization Problem (MOOP). For this class of problems, GA-based methods are well-suited procedures, since they are conceived to handle more solutions at the same time [2]. Despite of their proven effectiveness with MOOPs, few research [17], [19]–[21], [23]–[25], [28], [29] treat the array design as an evolutionary MOOP, whereas the problem is often regarded as a single-objective optimization.

This paper deals with the problem of finding an optimal SLL-BW trade-off, for aperiodic linear arrays, using a GA-based technique. In particular, we aim to investigate whether, by using a standard Multi-Objective GA-based (MOGA) procedure, it is possible to synthesize aperiodic linear arrays with a better SLL-BW trade-off with respect to Dolph-Chebyshev [6] periodic arrays.

In [20], [21] Panduro *et al.* employed a standard MOGA procedure called Non-Dominated Sorting Genetic Algorithm II (NSGA-II) [30], to calculate the SLL-BW trade-off curves for linear arrays with uniform and non-uniform spacing. First, they validated NSGA-II in the uniform spacing case by comparing its non-dominated set against the Pareto front computed by using the Dolph-Chebyshev design method [6]. They observed that NSGA-II yields an effective approximation to the front, regardless of the number of array elements. Subsequently, with reference to the non-uniform spacing case they stated [20] that NSGA-II is able to find a non-dominated front that outperforms the Dolph-Chebyshev front for the same number of array elements. The authors considered both the case of non-uniform excitations [20] and that of uniform excitations [21]. They assumed as a benchmark the results obtained by applying the Dolph-Chebyshev method with a uniform half-wavelength spacing. We believe that a more appropriate benchmark be the optimal front for the periodic case, computed by applying the Dolph-Chebyshev method with optimum spacing, i.e. by using the maximum spacing that allows to prevent grating lobes in the physical domain. Accordingly, we here investigate whether by using a standard MOGA procedure it is possible to approximate or outperform the SLL-BW Pareto-optimal front for the uniform spacing case by means of evolved aperiodic solutions.

The paper is organized as follows. In Section 2 the setup of the MOGA procedure is presented and the adopted method is described in detail. Section 3 presents numerical results. In particular, we first recall the main results from our previous work [31] and analyze them more in depth. Subsequently, we further extend our study by using the adopted MOGA procedure to synthesize aperiodic arrays with uniform excitations. Moreover, the optimization of a third objective is performed: the power radiated by the sidelobes. Section 4 concludes the work.

# 2. The Method

The standard MOGA procedure employed in this work is a Matlab implementation of NSGA-II with Controlled Elitism (CE-NSGA-II). This algorithm shows a better convergence than the original NSGA-II [32]. We use the standard Matlab solver "gamultiobj" with the setup described in [31].

We consider aperiodic linear arrays of isotropic elements symmetrically arranged with respect to the array center, with a real symmetrical distribution of the excitations. Thus, the main beam will be directed to broadside. There are two reasons for this choice. First, symmetrical excitations make the design of the feed network and the compensation of the mutual coupling effects easier. Second, numerical results can be compared with broadside symmetrical Dolph-Chebyshev arrays.

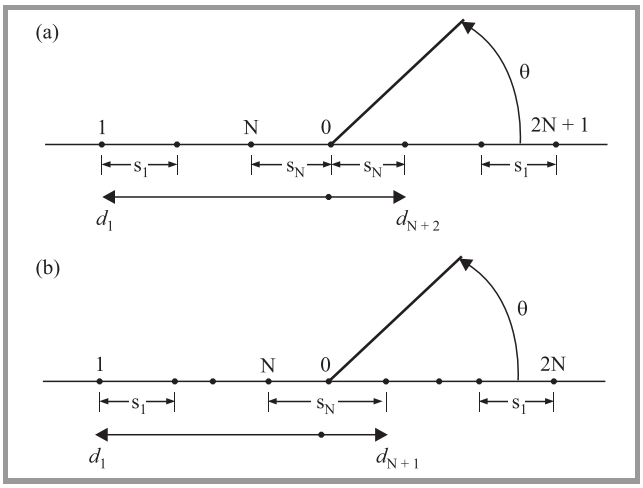


***Fig. 1.*** Array geometry: (a) odd number $M = 2N+1$ of elements, (b) even number $M = 2N$ of elements.

Geometry and notations are described in Fig. 1. When the total number of isotropic elements is $M = 2N+1$ (Fig. 1a) the array factor is given by:

$$F(\theta,\mathbf{I},\mathbf{D}) = \sum_{i=1}^{2N+1} I_i \mathrm{e}^{j\,\mathrm{sign}(i-(N+1))kd_i\cos\theta}, \qquad (1)$$

where $\mathrm{sign}(x) = 1$ if $x > 0$ and $-1$ otherwise, $\theta$ is the angle between the direction of observation and the array axis, $k = \frac{2\pi}{\lambda}$ is the wavenumber ($\lambda$ being the radiation wavelength), $\mathbf{I} = [I_1, I_2, \ldots, I_{2N+1}]$ is the vector of current excitations, and $\mathbf{D} = [d_1, d_2, \ldots, d_{2N+1}]$ is the vector of distances between each array element and the array center. When the total number of isotropic elements is $M = 2N$ (Fig. 1b), the array factor is given by:

$$F(\theta,\mathbf{I},\mathbf{D}) = \sum_{i=1}^{2N} I_i \mathrm{e}^{j\,\mathrm{sign}(i-N)kd_i\cos\theta}, \qquad (2)$$

where $\mathbf{I} = [I_1, I_2, \ldots, I_{2N}]$ is the vector of excitation currents and $\mathbf{D} = [d_1, d_2, \ldots, d_{2N}]$ is the vector of the distances between each array element and the array center.

In the genetic representation, each individual is specified by two vectors: the vector $\mathbf{I}$ of the current excitations and the vector $\mathbf{S} = [s_1, s_2, \ldots, s_{M-1}]$ of the separations between adjacent elements. By exploiting the array symmetry, the length of these two vectors can be roughly halved. More precisely, the two vectors can be re-defined as follows: $\mathbf{I} = [I_1, I_2, \ldots, I_N]$ if $M = 2N$, $\mathbf{I} = [I_1, I_2 \ldots, I_{N+1}]$ if $M = 2N+1$, and $\mathbf{S} = [s_1, s_2, \ldots, s_N]$ in both cases.

The array design problem is modeled as a bound constraint MOOP, namely as a minimization one.

We first deal with two design objectives: SLL and BW. In such a case, for the design of aperiodic non-uniformly excited linear arrays with $M$ isotropic elements, we have the following formal MOOP statement: minimize $(f_1, f_2)$ subject to $\mathbf{I} \in \Delta_1$ and $\mathbf{S} \in \Delta_2$, where the objective fitness functions are $f_1 = \text{SLL}$ and $f_2 = \text{BW}$, $\Delta_1 = [0,1]^L$ and $\Delta_2 = [0.5\lambda, s_{\max}]^L$, where $L = N$ if $M = 2N$ and $L = N+1$ if $M = 2N+1$. The $s_{\max}$ represents the maximum allowed separation between adjacent elements (also called, spacing). For what pertains the amplitude of the current excitations, as the input power is not assigned, only normalized amplitude values are of interest. Hence, we limit them to the dimensionless range $[0, 1]$. Moreover, to neglect mutual coupling effects, we bound the minimum spacing to $0.5\lambda$.

Subsequently, an additional design objective is considered: the power radiated by the sidelobes (SLP) is minimized. The formal MOOP statement in this case becomes: minimize $(f_1, f_2, f_3)$ subject to $\mathbf{I} \in \Delta_1$ and $\mathbf{S} \in \Delta_2$, where the objective fitness functions are $f_1 = \text{SLL}$, $f_2 = \text{BW}$ and $f_3 = \text{SLP}$.

## 3. Results and Discussion

The used benchmark is represented by the trade-off SLL-BW curves obtained by applying the Dolph-Chebyshev method with optimum period (in the following referred to as the Dolph-Chebyshev front).

It is apparent that for a fixed M, according to the Pareto criterion of dominance [2], the Dolph-Chebyshev front dominates the front of solutions adopted in [20], [21] and characterized by a half-wavelength period.

In [31], it was shown that the evolved non-dominated solutions from [20] do not outperform the right benchmark. Except for a bit inaccuracy due to the numerical nature of the method, the MOGA's non-dominated periodic solutions converge to optimum Dolph-Chebyshev solutions. The genetic procedure synthesizes approximations of the Dolph-Chebyshev front not only at objective value levels (SLL and BW) but also at design variable levels (currents and separations).

In [31], we also started the analysis of the non-uniform spacing case. The CE-NSGA-II was used to synthesize aperiodic non-uniformly excited linear arrays, for different values of $M$, in two test cases: separations belonging to the interval $[0.5\lambda, \lambda]$, as in [20], [21], and separations belonging to $[0.5\lambda, 5\lambda]$. The latter case was considered because aperiodic arrays can control the grating lobes in the radiation pattern, even if the average spacing is large. As a result, it was shown that the evolved non-dominated solutions can outperform Dolph-Chebyshev solutions when separations belong to $[0.5\lambda, 5\lambda]$, i.e. when the MOGA procedure can fully exploit the aperiodicity to control the grating lobes. Unfortunately, this happens only when SLL $> -13$ dB. It was also observed that, in the outperforming region, evolved fronts cross Pareto-optimal fronts with a higher number of elements. This behavior is known in the literature as array thinning [10], [33]. With an aperiodic array it is possible to obtain almost the same SLL-BW trade-off as a periodic array involving a higher number of elements.

Let us now study more in depth the non-uniform spacing case.

Figure 2 shows the evolved front obtained for aperiodic non-uniformly excited arrays, with $M = 12$ and separations belonging to the interval $[0.5\lambda, 5\lambda]$ (dotted line with circles). In the same figure, the Pareto-optimal front is reported (solid line, Dolph-Chebyshev). The evolved trade-off curve between SLL and BW was computed over data collected in 5 consecutive runs of the CE-NSGA-II. It can be appreciated that evolved solutions outperform Dolph-Chebyshev solutions when SLL is higher than nearly –13 dB as mentioned before, and that for lower SLL values the evolved front follows the Dolph-Chebyshev front (a worse approximation is observed for SLL lower than nearly –22 dB).

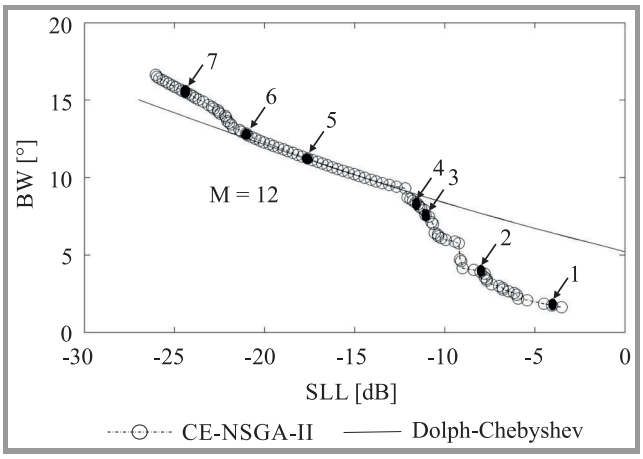


***Fig. 2.*** SLL-BW trade-off curves computed over data collected in 5 consecutive runs of the CE-NSGA-II, with separations in $[0.5\lambda, 5\lambda]$ against the Dolph-Chebyshev front computed by means of the Dolph-Chebyshev method with optimum period.

For seven solutions of the evolved front, Fig. 3 shows array factors, excitation amplitudes, and spacing distributions. Each row refers to a different solution, identified by the relevant sampling number. The first column reports array factors, with angles in radians and amplitudes normalized to the peak value. The second column shows array current distributions, with amplitudes normalized to the maximum current. The third column shows array spacing distributions (normalized to $\lambda$). A horizontal solid line indicates a separation of one wavelength.

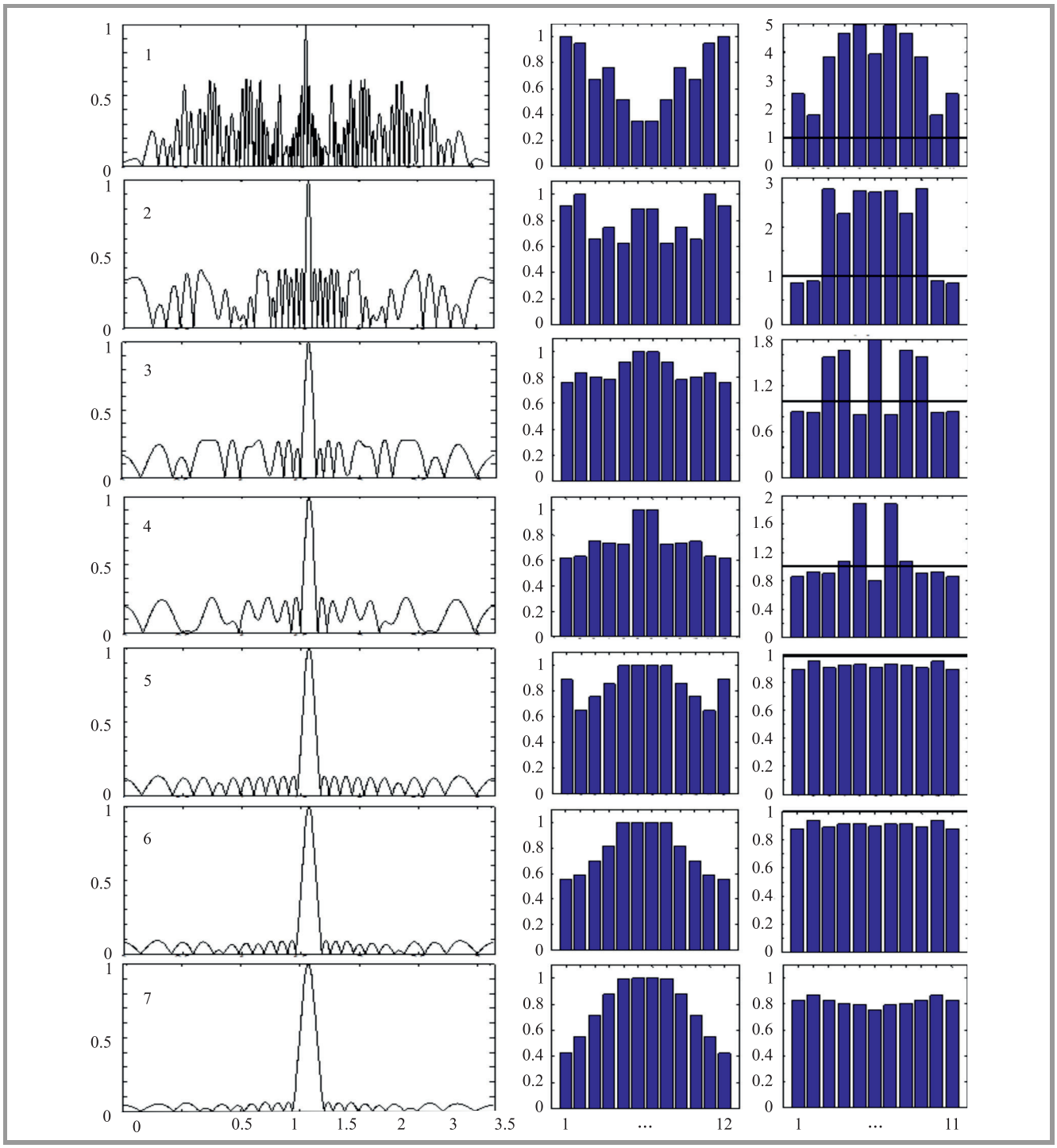


***Fig. 3.*** Study of seven non-dominated solutions, sampled over the evolved front of Fig. 2. Each row refers to one of those solutions. The first column illustrates array factors (amplitudes, normalized to the peak value, as a function of angle in radians). The second column shows array current distributions, with amplitudes normalized to the maximum current. The third column shows array spacing distributions (normalized to $\lambda$). A horizontal solid line indicates a separation of one wavelength.

Observing rows 1 to 5 in Fig. 3, a transition can be noted from solutions with an aperture wider than the corresponding Dolph-Chebyshev solutions, to solutions with a comparable aperture. Solution 1 has all separations greater than one wavelength, and a number of zeros in the visible space much greater than the 22 zeros placed in the visible space by the Dolph-Chebyshev method. This result highlights the capability of aperiodic arrays of controlling the grating lobes in the visible space at the expense of an SLL value, which is only –4.23 dB. From row 1 to 4 a lowering of the side-lobes is observed as well as an increase of the beam width. Furthermore, a reduction of the number of zeros in the visible space occurs.

Solution 5 is an aperiodic approximation of a Dolph-Chebyshev array. The number of zeros in the visible space is 22, the side-lobe pattern is almost uniform, all separations are smaller than one wavelength, and the mean spacing is very close to the optimum period. From row 5 to 6 a transition occurs toward tapered current distributions, thus achieving lower SLL values.

Finally, the Solution 7 witnesses the deviation of the evolved front from the Dolph-Chebyshev one. The sidelobe pattern becomes more irregular, losing two zeros in visible space. The aperture gets smaller than the corresponding Dolph-Chebyshev solution, with an average separation shorter than the optimal period. The current distribution is still tapered to match the low SLLs. Thus, in this low SLLs region the adopted MOGA procedure reveals to be not able to efficiently exploit the array aperture, by putting all zeros in visible space to shrink the beam width.

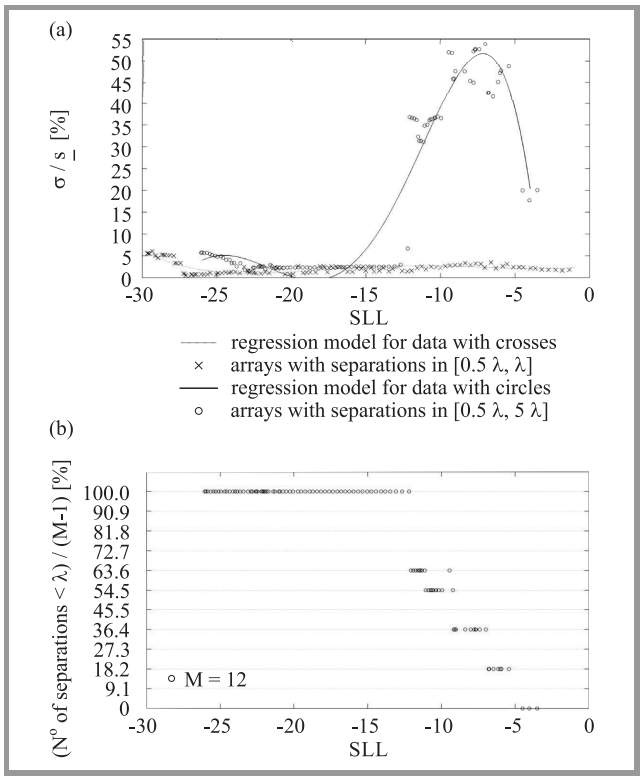


***Fig. 4.*** Analysis of the distribution of separations obtained in the evolved solutions with $M = 12$ non-uniformly excited elements: (a) ratio between standard deviation and average spacing for each evolved solution as a function of SLL, (b) number of separations shorter than $\lambda$ vs. SLL for evolved solutions with separations in $[0.5\lambda, 5\lambda]$.

The spacing distributions of the presented evolved non-dominated aperiodic solutions are further studied in Fig. 4. In Fig. 4a, the ratio $\frac{\sigma}{\overline{s}}$ between the standard deviation $\sigma$ and the average separation $\overline{s}$ is plotted as a function of SLL for each evolved solution. Circles and crosses represent solutions with separations in $[0.5\lambda, 5\lambda]$ and $[0.5\lambda, \lambda]$, respectively. The corresponding regression models are in solid and dash-dotted line, respectively. This figure shows that the MOGA procedure fully exploits the aperiodicity of evolved arrays only in the region where the evolved front outperforms the Dolph-Chebyshev front. In Fig. 4b, the number of separations shorter than $\lambda$ is plotted as a function of SLL, for evolved solutions with separations in $[0.5\lambda, 5\lambda]$. It can be argued that the outperforming occurs in a region of the SLL-BW plane where the MOGA procedure synthesizes a larger array aperture to shrink the BW, with separations longer than one wavelength. In fact, going towards SLLs smaller than –13 dB, we notice a transition of evolved solutions from arrays with all (or most) separations longer than one wavelength (right side of Fig. 4b) towards arrays with all separations shorter than one wavelength (left side of Fig. 4b). When SLL $<$ –13 dB, it is not possible to find aperiodic radiating configurations with apertures significantly larger than the corresponding Dolph-Chebyshev solutions, taking simultaneously under control the entrance of grating lobes in visible space.

Here a special case of symmetrical excitations is considered, which can highly simplify the design and realization of the feed network – the uniform current distribution. The CE-NSGA-II is used to synthesize aperiodic uniformly excited linear arrays for different values of $M$. The setup of the algorithm is the same as that of the previous experiment, except for the vector of current excitations, that now is $\mathbf{I} = [1]^L$ with $L$ as in Section 2. The objectives are, once

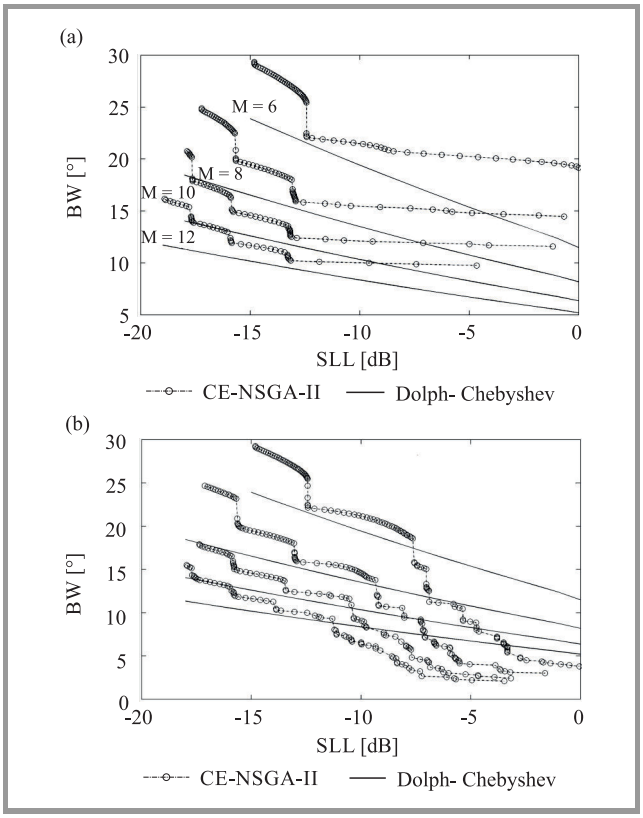


***Fig. 5.*** SLL-BW trade-off curves, computed over data collected in 5 consecutive runs of CE-NSGA-II with separations in: (a) $[0.5\lambda, \lambda]$, (b) $[0.5\lambda, 5\lambda]$, against the Pareto-optimal fronts computed with the Dolph-Chebyshev method with optimum period.

again, SLL and BW. We distinguish two test cases: in the first case the separations belong to the interval $[0.5\lambda, \lambda]$, in the second one they belong to $[0.5\lambda, 5\lambda]$.

In Figs. 5a-b the numerical results obtained in the first and second test case are shown, respectively. In particular, in Fig. 5a the SLL-BW trade-off curves are plotted, computed over data collected in 5 consecutive runs of CE-NSGA-II (dash-dotted line) with separations in $[0.5\lambda, \lambda]$. The Pareto-optimal fronts computed with the Dolph-Chebyshev method with optimum period are also plotted (solid line). Figure 5b refers to the case where the separations are in the $[0.5\lambda, 5\lambda]$ interval.

As in the previous experiment, Fig. 5 shows that the presented evolved non-dominated solutions can outperform Dolph-Chebyshev solutions only when the separations belong to $[0.5\lambda, 5\lambda]$. Again, this happens in a region of the SLL-BW plane characterized by SLL $>$ –13 dB. In both cases it is possible to observe an interesting partial overlapping of an evolved front with the Dolph-Chebyshev front relevant to solutions with slightly fewer elements.

This result is of practical interest, since it can be exploited to achieve the same array performances as non-uniformly excited arrays with a slightly greater number of radiating elements, but with uniform excitations. Moreover, when separations belong to $[0.5\lambda, 5\lambda]$, it can be noted an array-thinning effect in crossing points between evolved fronts and the Dolph-Chebyshev fronts with a higher number of elements (see Fig. 5b).

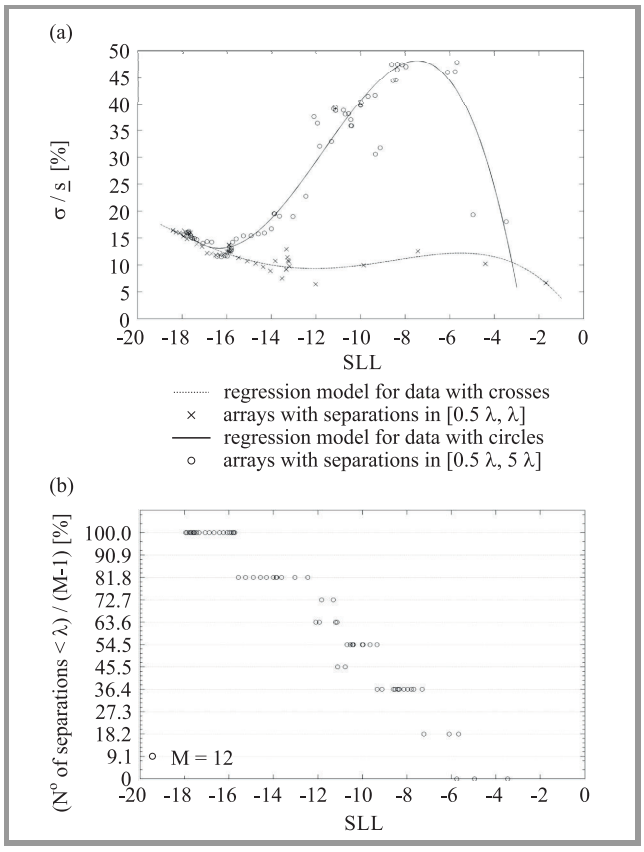


***Fig. 6.*** Same as in Fig. 4 but with uniform excitations.

It is interesting to analyze the spacing distributions of presented evolved solutions. In Fig. 6, the same as in Fig. 4 is reported, but with uniform array excitations. It can be observed that the MOGA procedure yields solutions with a higher exploitation of aperiodicity with respect to the case studied in Fig. 4, with an enhancement of this behavior in the region where the evolved front outperforms the Dolph-Chebyshev fronts. Again, this happens for a selection of arrays with greater array apertures with respect to the corresponding Dolph-Chebyshev solutions.

Finally, we use CE-NSGA-II to synthesize aperiodic non-uniformly excited linear arrays with minimal radiated power in unwanted directions. For this purpose, the power radiated in sidelobes normalized to the power radiated in the main lobe is considered:

$$SLP = \frac{P_{SL}}{P_{ML}}, \tag{3}$$

where $P_{SL}$ is the radiated power in side-lobes and $P_{ML}$ is the radiated power in the main lobe. Therefore, the objectives to be minimized are now three: SLL, BW and SLP.

In Fig. 7a, non-dominated solutions with $M = 12$ are shown, computed over data collected in 5 consecutive runs of CE-NSGA-II with 3 objectives (circles). Some representative solutions obtained by the Dolph-Chebyshev method with optimum period are also reported (black triangles) for SLL = –5, –10, –15, –20, –25 and –30 dB. Figure 7b shows a comparison between the SLL-BW trade-off curves computed by CE-NSGA-II with 2 (dash-dotted line with black dots) and 3 (dash-dotted line with circles) objectives. The latter curve is the result of the application of the Pareto dominance criterion over data obtained from a projection of the tridimensional front (shown in Fig. 7a) on over the SLL-BW plane. For comparison, the Dolph-Chebyshev front is also reported (solid line).

It is apparent that the introduction of the third objective helps the MOGA procedure to converge towards fronts with a better spread [27]. In fact, the fronts are calculated over a wider range of SLLs. This is due to the synergy of the third objective (SLP) with the first one (SLL) for solutions approaching the Dolph-Chebyshev front, i.e. having almost the same BW.

In Fig. 8, a comparison is presented between the array factor of one evolved solution, sampled very close to the Dolph-Chebyshev front, and the array factor of the corresponding solution on the Dolph-Chebyshev front. The sidelobe radiation pattern of the evolved solution appears irregular and tapered to keep minimized the SLP. The evolved array considered in Fig. 8 has about the 33% of the SLP corresponding to a uniform sidelobe pattern.

Examining the current distributions, similar tapering strategies as in the Dolph-Chebyshev solutions are observed when SLL $<$ –13 dB. In Fig. 9 the same as in Fig. 4 is reported, but with three objectives, and separations in the $[0.5\lambda, 5\lambda]$ interval. In the outperforming region, there is a greater exploitation of aperiodicity with respect to the solutions computed with two objectives (and with separations in $[0.5\lambda, 5\lambda]$). The higher aperiodicity in this SLL

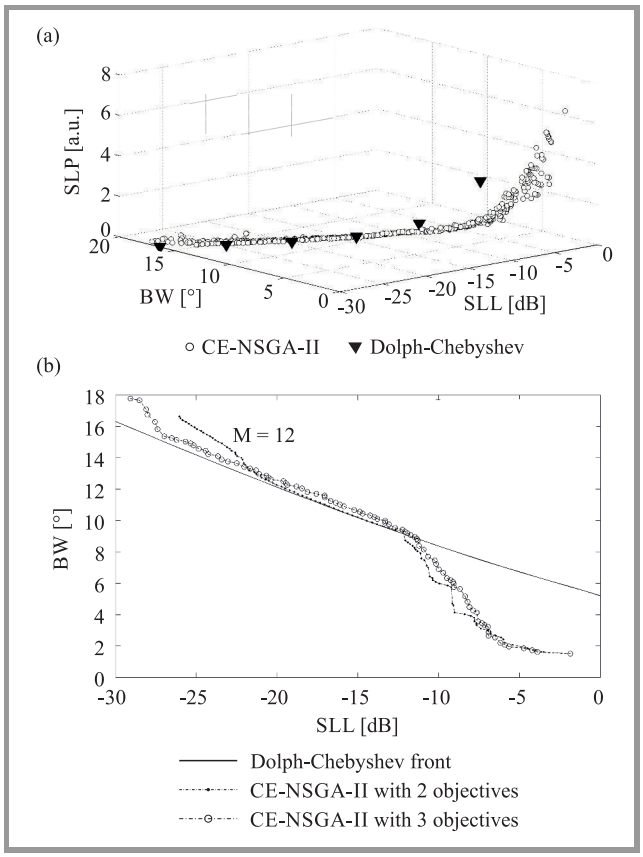


***Fig. 7.*** Numerical result for: (a) non-dominated solutions with $M = 12$ computed over data collected in 5 consecutive runs of CE-NSGA-II with 3 objectives, (b) comparison of the SLL-BW trade-off curves computed by CE-NSGA-II with 2 and 3 objectives. The Dolph-Chebyshev front for $M = 12$ is also reported.

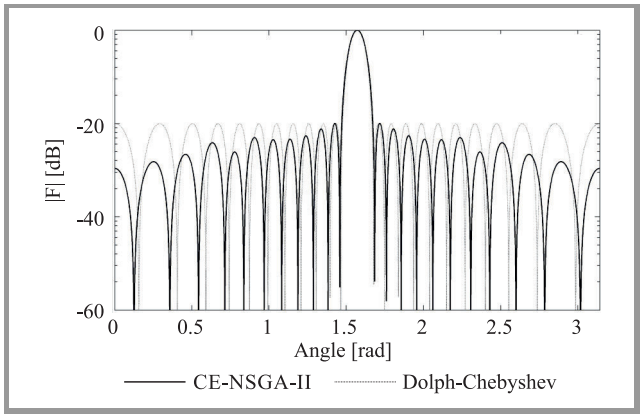


***Fig. 8.*** Array factors for $M = 12$ and SLL = –20 dB of one evolved solution obtained by means of CE-NSGA-II working with three objectives (solid line) and of the corresponding Dolph-Chebyshev solution (dashdot line).

region is exploited by the MOGA procedure to minimize the radiated power in the reduced grating lobes, that are visible due to the larger array aperture.

These results confirm that now we can approximate the Dolph-Chebyshev front with aperiodic arrays of different nature, and precisely aperiodic linear arrays with optimal SLL-BW-SLP trade-off. It is worth to note that, as shown

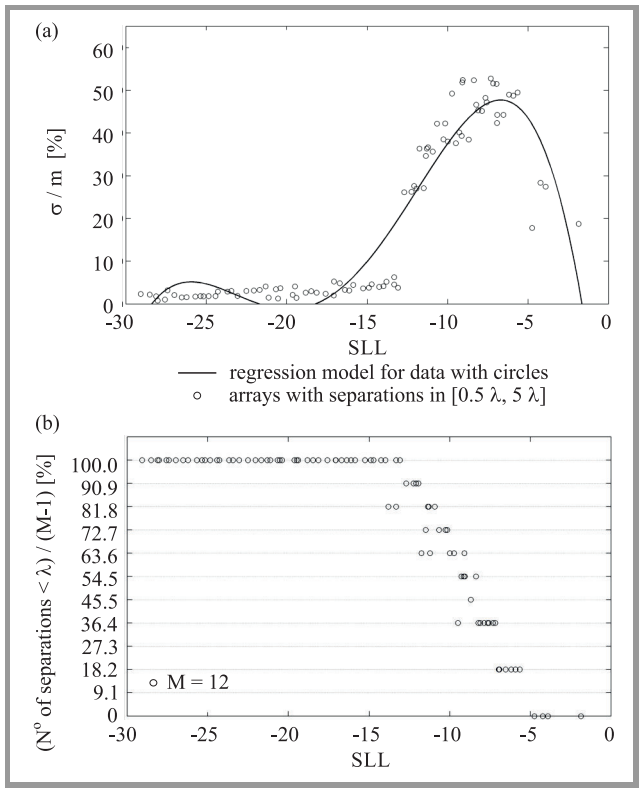


***Fig. 9.*** Same as in Fig. 6 when the objectives are three and separations are in the $[0.5\lambda, 5\lambda]$ interval.

in Fig. 8a, the advantage over Dolph-Chebyshev solutions in the reduction of radiated power in unwanted directions gets smaller when SLL increases.

# 4. Conclusions

The main purpose of this work was to experimentally verify the capability of a standard Multi-Objective GA-based (MOGA) procedure to synthesize aperiodic linear arrays of antennas with a better trade-off between side-lobe level (SLL) and main beam width (BW) with respect to Dolph-Chebyshev arrays with optimum period. To this aim, we considered symmetrical broadside arrays with isotropic radiators, focusing on the problem of optimizing SLL and BW simultaneously.

The adopted procedure is based on a standard Matlab implementation of the so-called Controlled Elitist Non-Dominated Sorting Genetic Algorithm II (CE-NSGA-II).

First, we recalled numerical results obtained in [31] for aperiodic non-uniformly excited linear arrays. Those results furnish a better interpretation of CE-NSGA-II behavior, compared to results obtained by other authors in previous works, where Dolph-Chebyshev solutions with half-wavelength period were inappropriately utilized as a benchmark. We adopted as a benchmark the SLL-BW trade-off curves obtained by applying the Dolph-Chebyshev method with an optimum period, here defined as the Dolph-Chebyshev front. In the present paper, we demonstrated that the evolved aperiodic solutions obtained by the adopted MOGA procedure, as well as the aperiodic ones

from [20], [21], cannot outperform Dolph-Chebyshev solutions. They only yield an aperiodic approximation of the Dolph-Chebyshev front, as long as the separations belong to the $[0.5\lambda, \lambda]$ interval.

As a further step, we allowed the MOGA procedure to fully exploit the capability of aperiodic arrays to take under control grating lobes in the visible space by considering a wider range of separations, i.e. the $[0.5\lambda, 5\lambda]$ interval. In this case, SLL-BW trade-off curves of evolved non-dominated solutions outperform the Dolph-Chebyshev front in a narrow region of the SLL-BW plane characterized by SLL $>$ –13 dB. We also analyzed results with respect to the spacing distribution: a higher exploitation of the aperiodicity was observed by the adopted MOGA procedure in the region where the Dolph-Chebyshev front is outperformed. In other regions, as long as the evolved front follows the Dolph-Chebyshev front, the MOGA procedure provides aperiodic approximations of Dolph-Chebyshev solutions. The obtained results suggest that the evolved arrays can outperform the Dolph-Chebyshev front thanks to a greater aperture, which they exploit – by using a higher aperiodicity – to take the grating lobes under control. An extrapolation of the data set constituted by the first non-outperforming points of the evolved fronts with respect to the corresponding Dolph-Chebyshev fronts for each number of radiating elements considered in our previous experiments [31] (shown in Fig. 10 of the present paper) suggests that, by further increasing the number of radiating elements, this behavior can be exploited only until a SLL limit of about –13.2 dB.

Subsequently, we studied the attractive case of aperiodic arrays with uniform excitations. As in the previous experiment, the evolved non-dominated solutions outperform Dolph-Chebyshev solutions only when separations are longer than one wavelength, i.e. only when the adopted MOGA procedure can synthesize aperiodic arrays with a higher aperture and, thanks to a higher aperiodicity, achieve a better control of the grating lobes. Again, this happens in a region of the SLL-BW plane characterized by SLL $>$ –13 dB. In all other cases, the evolved non-dominated solutions belong to discontinuous fronts. We also observed an interesting overlapping of evolved fronts with Dolph-Chebyshev fronts with slightly fewer radiating elements, which could be interesting for practical applications. By analyzing the spacing distributions of the evolved non-dominated solutions, we noticed that the adopted MOGA procedure provides solutions with a higher level of aperiodicity with respect to the previous experiment, with an enhancement of such behavior in the region where evolved fronts outperform Dolph-Chebyshev fronts. This was to be expected because, by assuming a uniform current distribution, we have reduced the degrees of freedom of the problem, so that the optimizing procedure can exploit only the spacing distribution.

In the last part of the paper, we extended the presented multi-objective approach and introduced a third objective: the minimization of the side-lobe power (SLP). We compared the obtained results with the previous ones, calculated with only two objectives (SLL and BW). The introduction of the third objective helps the MOGA procedure to converge to fronts with a better spread and to find new interesting solutions with irregular sidelobes, when SLL $<$ –13 dB, with radiation patterns different from those of Dolph-Chebyshev solutions, but very close to them in the SLL-BW plane.

In conclusion, the numerical results reported in this paper shed light on whether and in which design conditions, it is possible to synthesize, by using a standard MOGA procedure, aperiodic broadside symmetrical linear arrays with a SLL-BW trade-off competitive with optimal periodic Dolph-Chebyshev solutions.

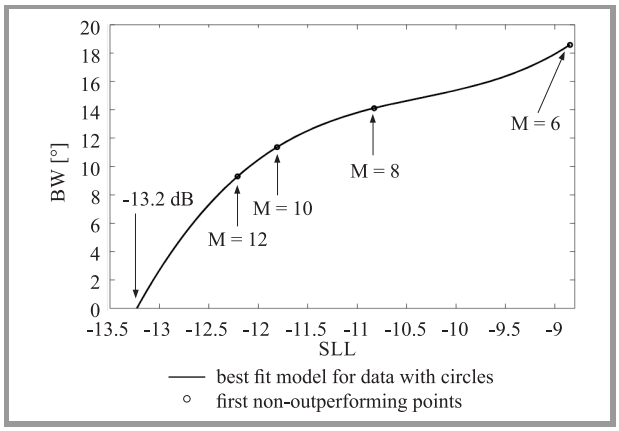


***Fig. 10.*** Extrapolation analysis of the first non-outperforming points for different numbers of radiating elements. The data set is obtained by the evolutionary synthesis of aperiodic arrays with non-uniform excitations and with separations in the $[0.5\lambda, 5\lambda]$ interval. The figure shows (with circles) the first non-outperforming points for aperiodic arrays with $M = 6$, 8, 10, 12 radiating elements and (with a solid line) the extrapolation polynomial obtained by interpolation of the collected data.

## Acknowledgements

This work benefited from the networking activities carried out in the COST (European Cooperation in Science and Technology) Actions MP0702 “Towards Functional Sub-Wavelength Photonic Structures” (cost-mp0702.nit.eu) and TU1208 “Civil engineering applications of Ground Penetrating Radar” (www.GPRadar.eu). The authors are grateful to COST (www.cost.eu) for funding and supporting the Actions MP0702 and TU1208.

## References

[1] J. H. Holland, *Adaptation in Natural and Artificial Systems: An Introductory Analysis with Applications to Biology, Control, and Artificial Intelligence*. Michigan: University of Michigan Press, 1975.

[2] A. E. Eiben and J. E. Smith, *Introduction to Evolutionary Computing*, Natural Computing Series. Heidelberg, Germany: Springer, 2003.

[3] R. Haupt, “Thinned arrays using genetic algorithms”, *IEEE Trans. on Antenn. and Propag.*, vol. 2, no. 7, pp. 712–715, 1994 (doi: 10.1109/8.299602).

[4] J. M. Johnson and Y. Rahmat-Samii, “Genetic algorithms in engineering electromagnetics”, *IEEE Antenn. and Propag. Mag.*, vol. 39, no. 4, pp. 7–21, 1997.

[5] C. Balanis, *Antenna Theory: Analysis and Design*, 3rd ed. Hoboken, New Jersey: Wiley, 2005.
[6] C. L. Dolph, "A current distribution for broadside arrays which optimizes the relationship between beam width and side-lobe level", *Proc. of the IRE*, vol. 34, no. 6, pp. 335–348, 1946 (doi: 10.1109/JRPROC.1946.225956).
[7] W. Doyle, "On approximating linear array factors", RAND Corporation Research Memoranda, Article ID RM-3530-PR, 1963.
[8] M. H. Er, S. L. Sim, and S. N. Koh, "Application of constrained optimization techniques to array pattern synthesis", *Sig. Process.*, vol. 34, no. 3, pp. 323–334, 1993.
[9] Y. C. Jiao, W. Y. Wei, L. W. Huang, and H. S. Wu, "A new low-side-lobe pattern synthesis technique for conformal arrays", *IEEE Trans. on Antenn. and Propag.*, vol. 41, no. 6, pp. 824–830, 1993.
[10] G. Toso, C. Mangenot, and A. G. Roederer, "Sparse and thinned arrays for multiple beam satellite applications", in *Proc. 29th ESA Antenna Worksh.*, Noordwijk, The Netherlands, 2007.
[11] P. Angeletti and G. Toso, "Aperiodic arrays for space applications: A combined amplitude/density synthesis approach", in *Proc. 3rd Eur. Conf. on Antenn. and Propag. EuCAP 2009*, Berlin, Germany, 2009.
[12] O. M. Bucci, M. D'Urso, T. Isernia, P. Angeletti, and G. Toso, "Deterministic synthesis of uniform amplitude sparse arrays via new density taper techniques", *IEEE Trans. on Antenn. and Propag.*, vol. 58, no. 6., pp. 1949–1958, 2010.
[13] G. Olivieri, M. Donelli, and A. Massa, "Linear array thinning exploiting almost difference sets", *IEEE Trans. on Antenn. and Propag.*, vol. 57, no. 12, pp. 3800–3812, 2009.
[14] G. Olivieri, P. Rocca, and A. Massa, "Analytic techniques for the design of non-regular arrays", in *Proc. IEEE Int. Symp. on Phased Array Syst. and Technol.*, Waltham, MA, USA, 2010 (doi: 10.1109/ARRAY.2010.5613281).
[15] K. K. Yan and Y. Lu, "Side lobe reduction in array-pattern synthesis using genetic algorithm", *IEEE Trans. on Antenn. and Propag.*, vol. 45. no. 7, pp. 1117–1122, 1997.
[16] F. J. Ares-Pena, J. A. Rodriguez-Gonzalez, E. Villanueva-Lopez, and S. R. Rengarajan, "Genetic algorithms in the design and optimization of antenna array patterns", *IEEE Trans. on Antenn. and Propag.*, vol. 47, no. 3, pp. 506–510, 1999.
[17] D. Ansell and E. J. Hughes, "Use of multi-objective genetic algorithms to optimize the excitation and subarray division of multifunction radar antennas", in *Proc. IEE Multifunc. Radar and Sonar Sensor Manag. Techniq.*, London, UK, 2001, vol. 8, pp. 1–4 (doi: 10.1049/ic:20010185).
[18] M. G. Bray, D. H. Werner, D. W. Boeringer, and D. W. Machuga, "Optimization of thinned aperiodic linear phased arrays using genetic algorithms to reduce grating lobes during scanning", *IEEE Trans. on Antenn. and Propag.*, vol. 50, no. 12, pp. 1732–1742. 2002.
[19] D. Ansell and E. J. Hughes, "Using multi-objective genetic algorithms to optimise the subarray partitions of conformal array antennas", *IEEE Trans. on Antenn. and Propag.*, vol. 52, pp. 151–155, 2004.
[20] M. A. Panduro, C. A. Brizuela, D. H. Covarrubias, and C. Lopez, "A multi-objective approach in the linear antenna array design", *Int. J. of Electron. and Commun.*, vol. 59, no. 4, pp. 205–212, 2004.
[21] M. A. Panduro, D. H. Covarrubias, C. A. Brizuela, and F. R. Marante, "A trade-off curve computation for linear antenna arrays using an evolutionary multi-objective approach", *Soft Comput.*, vol. 10, no. 2, pp. 125–131, 2005.
[22] K. Cheng, X. Yun, Z. He, and C. Han, "Synthesis of sparse planar arrays using a modified real genetic algorithm", *IEEE Trans. on Antenn. and Propag.*, vol. 55, no. 4, pp. 1067–1073, 2007.
[23] M. A. Panduro, C. A. Brizuela, and D. H. Covarrubias, "Design of electronically steerable linear arrays with evolutionary algorithms", *Appl. Soft Comput.*, vol. 8, no. 1, pp. 46–54, 2008 (doi: 10.1016/j.asoc.2006.10.011).
[24] M. A. Panduro, D. H. Covarrubias, and A. L. Mendez, "Design of phased antenna arrays using evolutionary optimization techniques", in *Advances in Evolutionary Algorithms*, W. Kosinski, Ed. Vienna, Austria: I-Tech Education and Publishing, 2008, pp. 361–376.
[25] F. Tokan and F. Gunes, "The multi-objective optimization of non-uniform linear phased arrays using the genetic algorithm", *Progr. in Electromag. Res. B*, vol. 17, pp. 135–151, 2009.
[26] S. Pal, B. Y. Qu, S. Das, and P. N. Suganthan, "Optimal synthesis of linear antenna arrays with multi-objective differential evolution", *Progr. in Electromag. Res. B*, vol. 21, pp. 87–111, 2010.
[27] S. Pal, S. Das, and A. Basak, "Design of time-modulated linear arrays with a multi-objective optimization approach", *Progr. in Electromag. Res. B*, vol. 23, pp. 83–107, 2010.
[28] M. A. Panduro, C. A. Brizuela, L. I. Balderas, and D. A. Acosta, "A comparison of genetic algorithms, particle swarm optimization and the differential evolution method for the design of scannable circular antenna arrays", *Progr. in Electromag. Res. B*, vol. 13, pp. 171–186, 2009.
[29] M. A. Panduro, C. A. Brizuela, and S. Jesus Garza, "A comparison of NSGA-II, DEMO, and EM-MOPSO for the multi-objective design of concentric rings antenna arrays", *J. of Electromag. Waves and Appl.*, vol. 27, no. 9, pp. 1110–1113, 2013.
[30] K. Deb, S. Agrawal, A. Pratap, and T. Meyarivan, "A fast and elitist multiobjective genetic algorithm: NSGA-II", *IEEE Trans. on Evol. Comput.*, vol. 6, no. 2, pp. 182–197, 2002.
[31] F. Napoli, L. Pajewski, G. Schettini, and R. Vescovo, "On a multi-objective approach in the non-uniform symmetrical linear antenna array design", in *Proc. 5th Eur. Conf. on Antennas and Propag. EuCap 2011*, Rome, Italy, 2011.
[32] K. Deb and T. Goel, "Controlled elitist non-dominated sorting genetic algorithm for better convergence", in *Evolutionary Multi-Criterion Optimization*, A. Gaspar-Cunha, C. Henggeler Antunes, C. A. Coello Coello, Eds. *LNCS*, vol. 1993, pp. 67–81. Springer, 2001.
[33] X. Chen, Z. Luo, X. He, and L. Zhu, "Thinning and weighting of planar arrays by modified teaching-learning-based optimization algorithm", *J. of Electromag. Waves and Appl.*, vol. 28, no. 15, pp. 1924–1934, 2014.

**Francesco Napoli** holds the Ph.D. in Electromagnetics and a M.Sc. in Electronic Engineering, both from Roma Tre University, Italy. Since 2006 he is involved in the study of evolutionary algorithms and in their applications to electronic design automation. Since 2009 he is collaborating with the Department of Engineering of Roma Tre University and with the ENEA Research Center of Frascati for the RF heating of magnetically confined hot plasmas relevant for nuclear fusion. His current research interests include multi-objective evolutionary techniques applied to the design of electromagnetic devices, aperiodic arrays, traveling wave tubes, computational electromagnetics, mathematical modeling, machine learning, symbolic regression, complex system theory, plasma physics, and nonlinear plasma interactions of microwaves with artificial hot plasmas.
E-mail: ganimede55@hotmail.com
Italian National Agency for New Technologies, Energy and Sustainable Economic Development (ENEA)
Via Enrico Fermi 45
00044 Frascati (RM), Italy

**Lara Pajewski**, **Roberto Vescovo** – for biographies, see this issue, p. 29.

**Marian Marciniak** – for biography, see this issue, p. 35.

Paper

# Reconfigurable Antenna Arrays with Phase-only Control in the Presence of Near-field Nulls

Giulia Buttazzoni and Roberto Vescovo

*Department of Engineering and Architecture, University of Trieste, Trieste, Italy*

https://doi.org/10.26636/jtit.2017.118817

**Abstract—In this paper an effective iterative method is presented for the power synthesis of reconfigurable antenna arrays. The algorithm is suitable for arrays of arbitrary geometry, including the case where a large number of elements is involved. The reconfigurability is achieved by phase-only control, so that the excitation amplitude of each array element remains constant during the reconfiguration process. Such amplitudes may be different from one array element to the others, and they are not assigned *a priori*, but are optimized. Furthermore, the electric field is imposed to vanish in a number of prescribed points of the near-field region, so that a strong field reduction is obtained in a neighborhood of them.**

***Keywords—antenna arrays, near-field nulls, phase-only control, power synthesis, reconfigurability.***

## 1. Introduction

Nowadays, antenna arrays consisting of many elements are very common structures in several applications, such as radars [1], [2], satellites [3], [4] and wireless communications [5], [6]. One of their attracting features is the reconfigurability, that is, the capability of generating different radiation patterns by suitably modifying parameters, such as for example the position and/or the excitation of the radiating elements, so that many patterns can be radiated by a single antenna. The position-control, also known as *mechanical steering*, requires a mechanical driving system and is not very well suited in some applications such as automotive and aeronautical ones. This makes fully electronically steerable structures more interesting. Modifying both the amplitude and phase of the excitations yields many degrees of freedom, but may require the use of expensive feeding networks. Usually, the reconfigurability from one pattern to another is achieved by modifying only the phase of the excitations. This allows the use of simpler feeding networks. Many techniques have been proposed for the power pattern synthesis of reconfigurable antenna arrays with phase-only control [1], [7]–[13]. In [7], [8] a pre-assigned amplitude distribution is assumed and only the optimum values for the phase are calculated. This transforms an inherently coupled problem into a number of (simpler) independent synthesis problems (one for each pattern), but provides a non-optimal solution because the pre-assigned amplitude distribution is not the optimal one. A research of a common amplitude distribution, in conjunction with the combination of a suitable phase distribution, is more convenient [1], [9]–[13].
Besides, antenna arrays are often mounted in complex environments, such as for example ships, aircrafts and satellites, thus involving obstacles which can interfere with the far-field patterns. It is important to take into account the effects of the environment on the radiation patterns. This can be done in two ways. The first one consists in including the environment in which the antenna is operating into the synthesis procedure [14], [15]. This approach, however, requires a detailed material and geometrical description of the operating environment, as well as a significant modification of the numerical code for the pattern evaluation, necessary to evaluate the electromagnetic coupling. The second approach consists in reducing the radiated field in the zone where the obstacle is located, in order to isolate it. The obstacle isolation can be realized by minimizing the power radiated into the near-field region that includes the obstacle [16]–[19]], or by imposing an upper bound on the electric-field amplitude in the region of interest [20]–[24], or finally by imposing that the near-field vanishes in suitably chosen points [25]–[27], thus reducing the field in a neighborhood of such points. It has been demonstrated [16] that both these two approaches give satisfactory results. However, the second one (i.e., reducing the radiated field in a given zone) is much simpler. But although the near-field constraint has an increasing relevance in practical applications involving arrays, only [19]–[21], [23] propose synthesis techniques for reconfigurable arrays involving near-field constraints, and following the above second approach.
The algorithm proposed in this paper allows to synthesize a number of desired patterns for phase-only reconfigurable antenna arrays of arbitrary geometry, in such a way that the near-fields corresponding to all of the synthesized patterns vanish at a prescribed number of points close to the antenna. This results in a reduction of the near-field amplitude also in a neighborhood of these points.

## 2. The Problem Formulation and the Solving Procedure

With reference to a Cartesian system $O(x,y,z)$, let us consider an antenna array of arbitrary geometry consisting of

$N$ arbitrary radiating elements. We want to find $S$ (complex) excitation vectors $\mathbf{i}_s = [i_{1s}, \ldots, i_{Ns}]^T$ such that the $S$ corresponding radiation patterns $F(\mathbf{i}_s; \varphi)$, where $\varphi$ is the azimuth angle of the generic direction of the $xy$-plane, have a desired shape. This requirement is obtained by imposing that the $s$-th pattern belong to a suitable mask $K_s = \left\{ f_s(\varphi) : K_s^1(\varphi) \leq |f_s(\varphi)| \leq K_s^2(\varphi), -\pi \leq \varphi \leq \pi \right\}$, where $K_s^1(\varphi)$ and $K_s^2(\varphi)$ are the lower and the upper bound of the mask, respectively. Furthermore, we require that each of the $S$ array patterns can be transformed into any of the others by keeping constant the excitation amplitude of each array element (phase-only control). Finally, we impose that the electric field radiated by the array in correspondence of $\mathbf{i}_s$, $\overline{\mathbf{E}}(\mathbf{i}_s; \overline{\mathbf{r}})$, be zero in $M$ suitable points $\overline{\mathbf{r}}_m$ located in the near-field region, with $M < \frac{N}{3}$. If such points are close to each other, then the field reduction is achieved in a neighborhood of them.

This problem can be formalized as follows: find $\mathbf{i}_s = [i_{1s}, \ldots, i_{Ns}]^T$, $s = 1, \ldots, S$, in such a way as to satisfy the following constraints:

$$F(\mathbf{i}_s; \varphi) \in K_s,\ s = 1, \ldots, S, \tag{1}$$

$$|i_{n1}| = \cdots = |i_{nS}|,\ n = 1, \ldots, N, \tag{2}$$

$$\overline{\mathbf{E}}(\mathbf{i}_s; \overline{\mathbf{r}}_m) = 0,\ s = 1, \ldots, S, m = 1, \ldots, M\ . \tag{3}$$

We want to specify that the problem and the synthesis procedure are here formulated and described in the $xy$-plane for simplicity. However, the extension to the $(\vartheta, \varphi)$-space is straightforward. The array pattern $F(\mathbf{i}_s; \varphi)$ is given by:

$$F(\mathbf{i}_s; \varphi) = \sum_{n=1}^{N} i_{ns} F_n(\varphi)\,, \tag{4}$$

where $F_n(\varphi)$ is the array pattern corresponding to the excitation vector $\mathbf{e}_n = [0, \ldots, 1, \ldots, 0]^T$ having the unity in the $n$-th position (active element pattern). The electric field $\overline{\mathbf{E}}(\mathbf{i}_s; \overline{\mathbf{r}})$ is given by:

$$\overline{\mathbf{E}}(\mathbf{i}_s; \overline{\mathbf{r}}) = \sum_{n=1}^{N} i_{ns} \overline{\mathbf{E}}_n(\overline{\mathbf{r}})\,, \tag{5}$$

where $\overline{\mathbf{E}}_n(\overline{\mathbf{r}})$ is the electric field radiated by the array in correspondence of the excitation vector $\mathbf{e}_n$. The constraint (1) imposes the mask requirements, with the aim of generating $S$ patterns, each having a desired shape. Constraint (2) imposes the phase-only control. Condition (3) imposes that the electric field vanishes at $M$ prescribed points $\overline{\mathbf{r}}_m$ located in the near-field region. If such points are close to each other, the electric field amplitude will exhibit a strong reduction in a neighborhood of them, as will be shown by the numerical example. The reason for the requirement $M < \frac{N}{3}$ will be explained below.

The method of solution that we are presenting is an evolution of that proposed in [27], and is based on the alternating projections method. We first formulate the problem as an intersection finding problem. To do so, we introduce the set $\mathscr{H} = \{\hat{\mathbf{h}} = (g_1(\varphi), \ldots, g_S(\varphi), \mathbf{h}_1, \ldots, \mathbf{h}_S)\}$ where each $g_s(\varphi)$ is an arbitrary complex scalar function defined in the interval $[-\pi, \pi]$ with square integrable modulus, and $\mathbf{h}_s = [h_{1s}, \ldots, h_{Ns}]^T$ is a column vector with $N$ arbitrary complex components. We define the scalar product between two elements $\hat{\mathbf{h}}, \hat{\mathbf{h}}' \in \mathscr{H}$ as:

$$<\hat{\mathbf{h}}, \hat{\mathbf{h}}'>_{\mathscr{H}} = \sum_{s=1}^{S} <g_s(\varphi), g'_s(\varphi)> + \sum_{s=1}^{S} \mathbf{h}_s'^{\mathbf{H}} \mathbf{h}_\mathbf{s}\,, \tag{6}$$

where the superscript indicates the components of the column vector $\hat{\mathbf{h}}'$, $<g_s(\varphi), g'_s(\varphi)> = \int_{-\pi}^{\pi} g_s(\varphi)\, g'^{*}_s(\varphi)\, \mathrm{d}\varphi$, the asterisk denotes the complex conjugate and the superscript $H$ denotes transpose conjugate. The scalar product in Eq. (6) yields the norm $\|\hat{\mathbf{h}}\|_{\mathscr{H}} = \sqrt{<\hat{\mathbf{h}}, \hat{\mathbf{h}}>_{\mathscr{H}}}$ and the distance $\rho(\hat{\mathbf{h}}, \hat{\mathbf{h}}') = \|\hat{\mathbf{h}} - \hat{\mathbf{h}}'\|_{\mathscr{H}}$, which becomes

$$\begin{aligned} \rho^2(\hat{\mathbf{h}}, \hat{\mathbf{h}}') &= \sum_{s=1}^{S} \int_{-\pi}^{\pi} |(g_s(\varphi) - g'_s(\varphi)|^2 \mathrm{d}\varphi + \\ &+ \sum_{s=1}^{S} \sum_{n=1}^{N} |h_{ns} - h'_{ns}|^2. \end{aligned} \tag{7}$$

In $\mathscr{H}$ we now introduce the sets:

$$\begin{aligned} K = \{\hat{\mathbf{k}} = (f_1(\varphi), \ldots, f_s(\varphi), \mathbf{k}_1, \ldots, \mathbf{k}_s) :\\ f_s(\varphi) \in K_s, \text{ and } |k_{n1}| = \cdots = |k_{nS}|,\\ s = 1, \ldots, S, n = 1, \ldots, N\}, \end{aligned} \tag{8}$$

$$W = \{\hat{\mathbf{w}} = (F(\mathbf{w}_1; \varphi), \ldots, F(\mathbf{w}_S; \varphi), \mathbf{w}_1, \ldots, \mathbf{w}_S)\} \tag{9}$$

and

$$\begin{aligned} Z = \{\hat{\mathbf{z}} = (F(\mathbf{z}_1; \varphi), \ldots, F(\mathbf{z}_S; \varphi), \mathbf{z}_1, \ldots, \mathbf{z}_S) :\\ \overline{\mathbf{E}}(\mathbf{z}_s; \overline{\mathbf{r}}_\mathbf{m}) = 0, s = 1, \ldots, S,\ m = 1, \ldots, M\}. \end{aligned} \tag{10}$$

Note that the elements of $K$ consist of $S$ arbitrary scalar complex functions and of $S$ arbitrary complex vectors satisfying (1) and (2), respectively, but the functions $f_s(\varphi)$ are not array patterns. Instead, the elements of $W$ consist of $S$ array patterns and of $S$ excitation vectors that produce such patterns, but such elements do not satisfy constraints (1) and (2). The set $Z$ consists of those elements of $W$ whose electric field vectors satisfy condition (3). It becomes now evident that each element belonging to the intersection $K \cap Z$ is a solution to our problem. Since such an intersection may be empty, we consider as a solution an element of $K$ minimizing the distance from $Z$. Such solution can be sought with the alternating projections method as described below.

Starting from a suitable point $\hat{\mathbf{k}}_0 \in K$, we follow the iteration scheme:

$$\hat{\mathbf{k}}_{n+1} = T_K T_Z[\hat{\mathbf{k}}_n], \qquad n = 0, 1, 2, \ldots\,, \tag{11}$$

where $T_K$ and $T_Z$ are the projection operators onto the sets $K$ and $Z$, respectively. By definition of distance, and due to $T_K$ and $T_Z$ being two projectors, it results: $\rho_n \geq \rho_{n+1}$ [12], where $\rho_n$ is the distance from $\hat{\mathbf{k}}_n$ to the set $Z$. In other words, the non-negative sequence $\{\rho_n\}$ is non-increasing, and therefore is convergent. The

iteration (11) generates a sequence of points $\hat{\mathbf{k}}_n$ of $K$, which are closer and closer to $Z$. We stop the procedure at a point $\hat{\mathbf{k}}_n^o = \left(f_1^o(\varphi),\ldots,f_S^o(\varphi),\mathbf{k}_1^o,\ldots,\mathbf{k}_S^o\right)$ such that:

$$\rho_n < \varepsilon \qquad \text{or} \qquad \frac{(\rho_{n-1}-\rho_n)}{\rho_n} < \delta \tag{12}$$

with $\varepsilon$ and $\delta$ two suitable thresholds. As the optimal excitation vectors we consider the $S$ vector components $\mathbf{k}_s^o$ of $\hat{\mathbf{k}}_n^o$ which (being $\hat{\mathbf{k}}_n^o \in K$) satisfy (2) rigorously, so that phase-only control is guaranteed. The optimal radiation patterns and the radiated fields are calculated replacing $\mathbf{i}_s$ with $\mathbf{k}_s^o$ in (4) and (5), respectively. With this choice, constraints (1) and (3) are satisfied only approximately. However, the accuracy is very good, as will be shown by the numerical example.

# 3. The Projector Operators

In this section, formulas to implement the above projectors are derived. We recall that the projector $T_C$ onto the closed set $C \subset \mathscr{H}$ is the operator that associates with each point $\hat{\mathbf{h}} \in \mathscr{H}$ the point $\hat{\mathbf{c}} \in C$ closest to $\hat{\mathbf{h}}$, that is

$$T_C : \hat{\mathbf{h}} \in \mathscr{H} \mapsto T_C[\hat{\mathbf{h}}] = \hat{\mathbf{c}} \in C : \rho(\hat{\mathbf{c}},\hat{\mathbf{h}}) = \min_{\hat{\mathbf{y}}\in C}\left\{\rho(\hat{\mathbf{y}},\hat{\mathbf{h}})\right\}. \tag{13}$$

### 3.1. The Projector $T_K$

It is easy to show [12] that $\hat{\mathbf{k}} = (f_1(\varphi),\ldots,f_S(\varphi),\mathbf{k}_1,\ldots,\mathbf{k}_S)$ is the projection of $\hat{\mathbf{h}} = (g_1(\varphi),\ldots,g_S(\varphi),\mathbf{h}_1,\ldots,\mathbf{h}_S)$ onto the set $K$ if for each $s = 1,\ldots,S$, it results:

$$f_s(\varphi) = \begin{cases} g_s(\varphi) & \text{if} \quad K_s^1(\varphi) \le |g_s(\varphi)| \le K_s^2(\varphi) \\ K_s^1(\varphi)\dfrac{g_s(\varphi)}{|g_s(\varphi)|} & \text{if} \quad |g_s(\varphi)| < K_s^1(\varphi) \\ K_s^2(\varphi)\dfrac{g_s(\varphi)}{|g_s(\varphi)|} & \text{if} \quad |g_s(\varphi)| > K_s^2(\varphi) \end{cases} \tag{14}$$

and $\mathbf{k}_s = [k_1 e^{j\varphi_{1s}},\ldots,k_N e^{j\varphi_{Ns}}]^T$, where for $n = 1,\ldots,N$, $k_n = \dfrac{1}{S}\sum_{s=1}^{S}|h_{ns}|$ is the amplitude of the $n$-th array element and $\varphi_{ns} = \arg\{h_{ns}\}$ is the phase of the $n$-th element necessary to radiate the $s$-th pattern.

### 3.2. The Projector $T_W$

Let us note [27] that $T_Z[\hat{\mathbf{h}}] = T_Z[T_W[\hat{\mathbf{h}}]]$, so before expressing $T_Z$ we express $T_W$. The projection of $\hat{\mathbf{h}} = \left(g_1(\varphi),\ldots,g_S(\varphi),\mathbf{h}_1,\ldots,\mathbf{h}_S\right)$ onto the set $W$ is the point $T_W[\hat{\mathbf{h}}] = \hat{\mathbf{w}} = (y_1(\varphi),\ldots y_S(\varphi),\mathbf{w}_1,\ldots,\mathbf{w}_S)$, which minimizes the distance $\rho_W(\mathbf{w}_1,\ldots,\mathbf{w}_S) = \rho(\hat{\mathbf{w}},\hat{\mathbf{h}})$. From the definition of scalar product and distance in $\mathscr{H}$ (see Section 2 and Eqs. (6) and (7)), it results:

$$\rho_W^2(\mathbf{w}_1,\ldots,\mathbf{w}_S) = \sum_{s=1}^{S} <y_s(\varphi)-g_s(\varphi), y_s(\varphi)-g_s(\varphi)> + \\ + \sum_{s=1}^{S}(\mathbf{w}_s-\mathbf{h}_s)^H(\mathbf{w}_s-\mathbf{h}_s). \tag{15}$$

By definition (9) of $W$, after some manipulations we find:

$$\rho_W^2(\mathbf{w}_1,\ldots,\mathbf{w}_S) = \sum_{s=1}^{S}\left\{\mathbf{w}_s^H\mathbf{F}\mathbf{w}_s - \mathbf{w}_s^H\mathbf{g}_s - \mathbf{g}_s^H\mathbf{w}_s + \mathbf{g}_s^H\mathbf{g}_s\right\} + \\ + \sum_{s=1}^{S}\left\{\mathbf{w}_s^H\mathbf{w}_s - \mathbf{w}_s^H\mathbf{h}_s\right\} - \sum_{s=1}^{S}\left\{\mathbf{h}_s^H\mathbf{w}_s - \mathbf{h}_s^H\mathbf{h}_s\right\}, \tag{16}$$

where $\mathbf{F} = [F_{mn}]$, with $F_{mn} = \int_{-\pi}^{\pi} F_n(\varphi)\,F_m^*(\varphi)\,d\varphi$ and $\mathbf{g}_s$ is the $s$-th column of the $[N \times S]$ matrix $\mathbf{G} = [g_{ms}]$ with $g_{ms} = \int_{-\pi}^{\pi} g_s(\varphi)\,F_m^*(\varphi)\,d\varphi$. Imposing the condition $\frac{\partial \rho_W^2}{\partial w_{ps}^*} = 0$, $p = 1,\ldots,N$, $s = 1,\ldots,S$, yields the $S$ matrix equations:

$$\mathbf{J}\mathbf{w}_s = \mathbf{m}_s, \tag{17}$$

or equivalently the matrix equation:

$$\mathbf{J}\mathbf{W} = \mathbf{M}, \tag{18}$$

where $\mathbf{J} = \mathbf{F} + \mathbf{I}_N$, $\mathbf{M} = \mathbf{G} + \mathbf{H}$, being $\mathbf{I}_N$ the identity matrix of rank $N$, $\mathbf{W}$ and $\mathbf{H}$ the $[N \times S]$ matrices whose $s$-th columns are, respectively, $\mathbf{w}_s$ and $\mathbf{h}_s$. The solution to (18) is

$$\mathbf{W} = \mathbf{J}^{\dagger}\mathbf{M}, \tag{19}$$

where $\mathbf{J}^{\dagger}$ is the pseudo-inverse matrix of $\mathbf{J}$ (which coincides with the inverse matrix $\mathbf{J}^{-1}$ if $\mathbf{J}$ is non-singular [28]). Once we have the vectors $\mathbf{w}_s$, with the definition (9) of $W$ we can calculate the functions $y_s(\varphi) = \sum_{n=1}^{N} w_{ns}F_n(\varphi)$, hence the projection $\hat{\mathbf{w}} = (y_1(\varphi),\ldots,y_S(\varphi),\mathbf{w}_1,\ldots,\mathbf{w}_S) = T_W[\hat{\mathbf{h}}]$.

### 3.3. The Projector $T_Z$

Now, in order to implement the projector $T_Z$, we have to minimize the quantity $\rho_Z(\mathbf{z}_1,\ldots,\mathbf{z}_S) = \rho(\hat{\mathbf{z}},\hat{\mathbf{h}})$ or, equivalently, $\rho(\hat{\mathbf{z}},T_W[\hat{\mathbf{h}}]) = \rho(\hat{\mathbf{z}},\hat{\mathbf{w}}_0)$, where $\hat{\mathbf{w}}_0 = T_W[\hat{\mathbf{h}}]$. By definition (10) of $Z$, after some manipulations we have:

$$\rho_Z^2(\hat{\mathbf{z}},\hat{\mathbf{w}}_0) = \sum_{s=1}^{S}(\mathbf{z}_s-\mathbf{w}_{0_s})^H\mathbf{J}(\mathbf{z}_s-\mathbf{w}_{0_s}), \tag{20}$$

where $\mathbf{w}_{0_s}$ is the $s$-th excitation vector of $\hat{\mathbf{w}}_0$. Note that, by (17),

$$\mathbf{w}_{0_s} = \mathbf{J}^{\dagger}\mathbf{m}_s, \tag{21}$$

Since $\mathbf{F}$ and $\mathbf{I}_N$ are Hermitian, also $\mathbf{J} = \mathbf{F} + \mathbf{I}_N$ is Hermitian and hence all eigenvalues of $\mathbf{J}$ are real and $\mathbf{J}$ is unitarily diagonalizable [28]. Therefore $\mathbf{J} = \mathbf{U}^H\Lambda\mathbf{U}$, where $\Lambda$ is the diagonal matrix of the eigenvalues of $\mathbf{J}$, the columns of $\mathbf{U}^H$ are the corresponding eigenvectors, and $\mathbf{U}^H$ is unitary. Replacing $\mathbf{J}$ with $\mathbf{U}^H\Lambda\mathbf{U}$ yields:

$$\rho_Z^2(\hat{\mathbf{z}},\hat{\mathbf{w}}_0) = \sum_{s=1}^{S}(\mathbf{z}_s-\mathbf{w}_{0_s})^H\mathbf{U}^H\Lambda\mathbf{U}(\mathbf{z}_s-\mathbf{w}_{0_s}), \tag{22}$$

which can be written as:

$$\rho^2(\hat{\mathbf{z}},\hat{\mathbf{w}}_0) = \sum_{s=1}^{S}(\mathbf{v}_s-\mathbf{v}_{0_s})^H(\mathbf{v}_s-\mathbf{v}_{0_s}) = \sum_{s=1}^{S}\|\mathbf{v}_s-\mathbf{v}_{0_s}\|_E^2, \tag{23}$$

where we set

$$\mathbf{v}_s = \Lambda^{\frac{1}{2}}\mathbf{U}\mathbf{z}_s \quad \text{and} \quad \mathbf{v}_{0_s} = \Lambda^{\frac{1}{2}}\mathbf{U}\mathbf{w}_{0_s}. \tag{24}$$

So, projecting $\hat{\mathbf{h}}$ onto $Z$ reduces to minimize the quantity (23) subject to the constraint (3). Now, constraint (3) can be formulated due the matrix equations

$$\mathbf{E}\mathbf{z}_s = \mathbf{E}\mathbf{U}^{-1}\Lambda^{-\frac{1}{2}}\mathbf{v}_s = \mathbf{S}\mathbf{v}_s = 0, \tag{25}$$

where $\mathbf{E}$ denotes the $3M \times N$ matrix defined as follows:

$$\mathbf{E} = \begin{bmatrix} \mathbf{E}_x \\ \mathbf{E}_y \\ \mathbf{E}_z \end{bmatrix}, \tag{26}$$

with $\mathbf{E}_x, \mathbf{E}_y, \mathbf{E}_z$ being the three $M \times N$ matrices whose entries are $E_{x_{mn}} = E_{x_n}(\overline{\mathbf{r}}_m)$, $E_{y_{mn}} = E_{y_n}(\overline{\mathbf{r}}_m)$, $E_{z_{mn}} = E_{z_n}(\overline{\mathbf{r}}_m)$, respectively, with $E_{\xi_n}(\overline{\mathbf{r}}_m)$ denoting the $\xi-$component ($\xi = x, y, z$) of the electric field produced at the point $\overline{\mathbf{r}}_m$ by the array with excitation vector $\mathbf{e}_n$. The matrix $\mathbf{S} = \mathbf{E}\mathbf{U}^{-1}\Lambda^{-\frac{1}{2}}$ has $3M$ rows and $N$ columns, thus Eq. (25), expressing the near-field constraints, has a solution if $M < \frac{N}{3}$. The vectors $\mathbf{v}_s$ minimizing (23) and satisfying (25) are:

$$\mathbf{v}_s = (\mathbf{I}_N - \mathbf{S}^{\dagger}\mathbf{S})\,\mathbf{v}_{0_s}. \tag{27}$$

Therefore, recalling Eq. (24) yields:

$$\mathbf{z}_s = \mathbf{P}\mathbf{w}_{0_s}, \quad s = 1, \ldots, S, \tag{28}$$

where $\mathbf{P} = \mathbf{U}^{-1}\Lambda^{-\frac{1}{2}}(\mathbf{I}_N - \mathbf{S}^{\dagger}\mathbf{S})\Lambda^{\frac{1}{2}}\mathbf{U}$ and $\mathbf{w}_{0_s}$ is given by Eq. (21), which solves Eq. (17). With the vectors $\mathbf{z}_s$ and the definition (10) of $Z$, we can calculate the functions $F(\mathbf{z_s}, \varphi) = \sum_{n=1}^{N} z_{ns} F_n(\varphi)$, hence the projection $\hat{\mathbf{z}} = (F(\mathbf{z}_1, \varphi), \ldots, F(\mathbf{z}_S, \varphi), \mathbf{z}_1, \ldots, \mathbf{z}_S) = T_Z[\hat{\mathbf{h}}]$.

## 4. Numerical Example

We considered the array shown in Fig. 1, consisting of $N = 429$ elementary vertical dipoles with length $l = \frac{\lambda}{50}$.

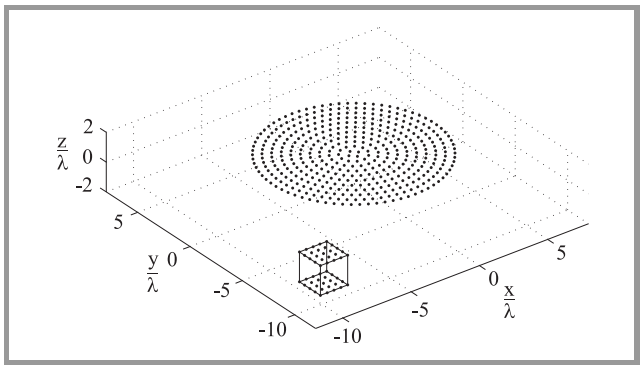


***Fig. 1.*** Array geometry and near-field region for the proposed example. The null points lie on the top and bottom faces of the cube.

The elements are equally spaced on 11 circular rings (as it is described in Table 1), with each ring having the center at the origin of the Cartesian system $O(x, y, z)$ and lying on the $xy$-plane. In the near-field region, on the planes $z = \pm\lambda$, two meshes were defined, consisting of 25 equally spaced points (see Fig. 1), with $-10.5\lambda \leq x, y \leq -8.5\lambda$, resulting in $M = 50$ points $\overline{\mathbf{r}}_m$ with a minimum distance between adjacent points of $\frac{\lambda}{2}$. Note also that $M = 50 < 143 = \frac{N}{3}$. The array was required to synthesize by phase-only control the $S = 4$ patterns of Fig. 2.

Table 1
Array geometry details: normalized radius $\frac{R_i}{\lambda}$ and number of elements $N_i$ of each ring

| $i$ | $\frac{R_i}{\lambda}$ | $N_i$ | $i$ | $\frac{R_i}{\lambda}$ | $N_i$ | $i$ | $\frac{R_i}{\lambda}$ | $N_i$ |
|---|---|---|---|---|---|---|---|---|
| 1 | 0.35 | 4 | 5 | 2.55 | 32 | 9 | 4.77 | 60 |
| 2 | 0.88 | 11 | 6 | 3.11 | 39 | 10 | 5.33 | 67 |
| 3 | 1.44 | 18 | 7 | 3.66 | 46 | 11 | 5.8 | 74 |
| 4 | 1.99 | 25 | 8 | 4.22 | 53 | | | |

First, the synthesis was performed without imposing the near-field nulls, that is, in the absence of condition (3). This was realized by replacing the projector $T_Z$ in Eq. (11) with $T_W$. In the following it will be referred to as the "reduced" problem. Then constraint (3) was taken into account and the "complete" problem was solved.

Both the reduced and the complete problem gave very good results in a satisfactory computer time. In fact, the former required only 1.78 s (corresponding to 104 iterations) and the latter required 30.19 s (1761 iterations). As it was expected, constraint (2) was satisfied exactly. Condition (1) was very well approximated. In fact, the synthesized patterns exceeded the mask limits at most of 0.18 dB (reduced problem) and 0.03 dB (complete problem), and in particular, the maximum side lobe levels in the worst case were –34.82 dB (reduced problem) and –34.97 dB (complete problem). Figure 2 shows the radiation patterns obtained solving the complete problem. Figure 3 shows a contour plot of the near-field amplitude in both the reduced and the complete problem. Constraint (3) was approximated quite satisfactorily, as the maximum near-field amplitude on the constraint points in the complete problem exhibited a 50.03 dB reduction with respect to that of the reduced problem. Finally, the field amplitudes were evaluated on a mesh of $\frac{\lambda}{8}$ spaced points in the cube of Fig. 1 for both the reduced and the com-

Table 2
Near-field amplitude comparison

| | |
|---|---|
| Reduction of the maximum amplitude | 48.25 dB |
| Reduction of the mean amplitude | 43.06 dB |
| Maximum reduction | 58.62 dB |
| Minimum reduction | 15.86 dB |
| Mean reduction | 39.42 dB |

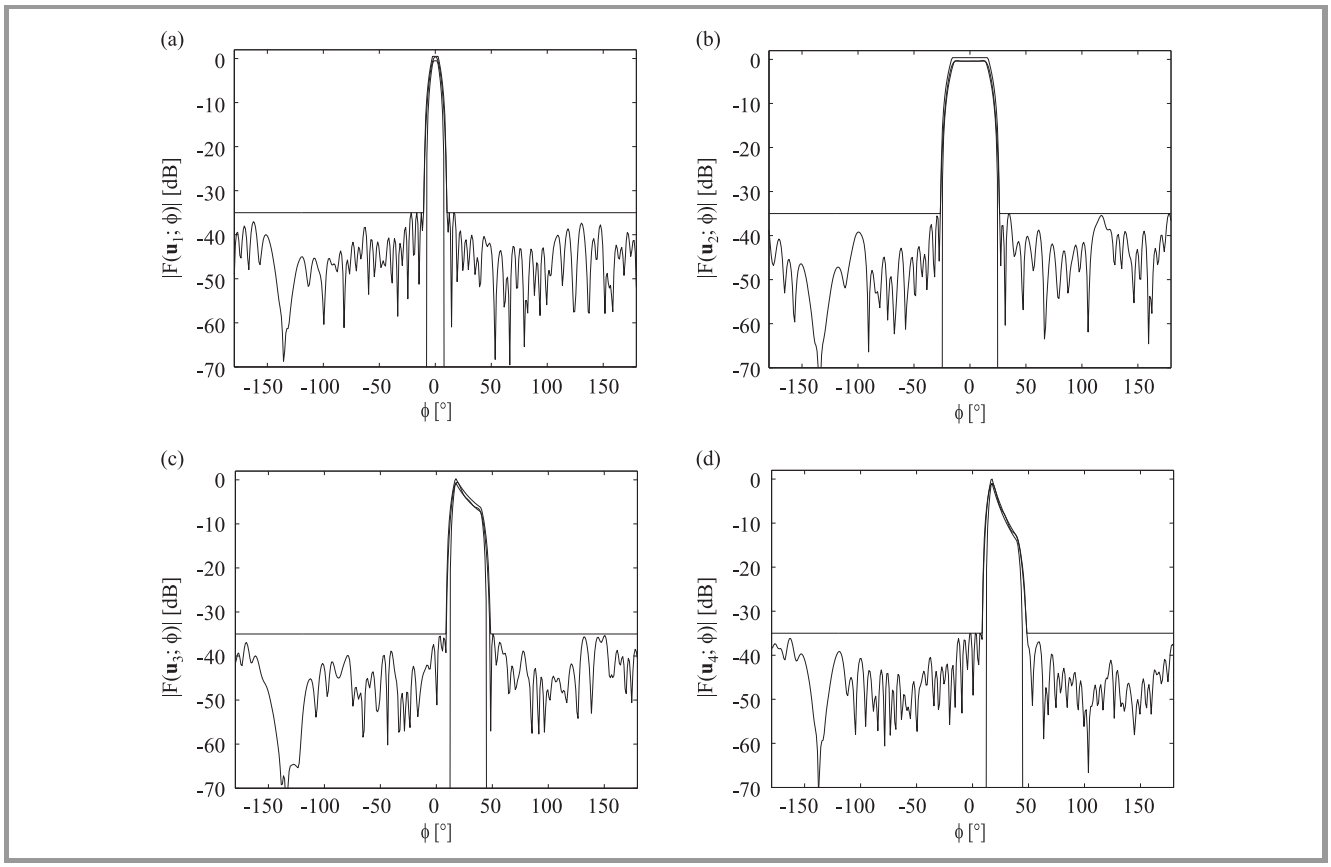


***Fig. 2.*** The assigned masks and the synthesized patterns for the complete problem: (a) a pencil beam, (b) a flat top beam), (c) a cosecant, (d) a squared cosecant.

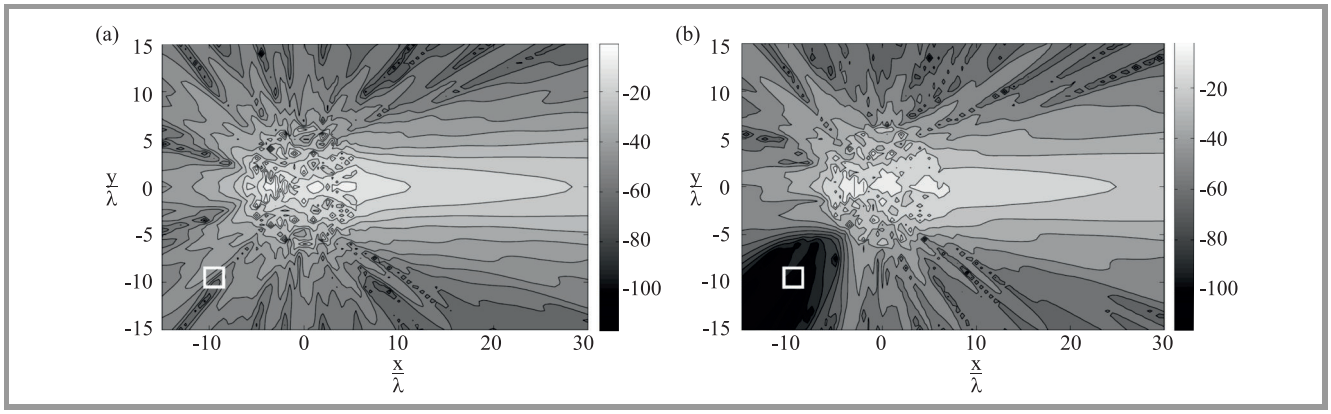


***Fig. 3.*** Contour plot of the near-field amplitude (in dB) on a portion of the *xy*-plane, obtained in the reduced (a) and complete (b) problem.

plete problem. The results are summarized in Table 2 and show that imposing near-field nulls on a number of suitably located points allows to obtain a very strong reduction of the electric field amplitude in the whole region of interest.

## 5. Conclusions

The algorithm presented in this paper allows us to synthesize reconfigurable antenna arrays with phase-only control, simultaneously reducing the near-field amplitude in a region close to the antenna. The near-field reduction is obtained by imposing that the field vanishes at a prescribed number of suitably located points. In such a way, strong reductions can be obtained without increasing the dimensions of the problem and so keeping low the required computational time. This represents one of the main advantages of the presented algorithm with respect to those presented in [20], [21], which allow to control the near-field reduction, but with a higher computational time.

## Acknowledgements

We thank the Guest Editors Lara Pajewski, Hovik Baghdasaryan, and Marian Marciniak for inviting us to participate in the JTIT Special Issue "Recent Progress in Electromagnetic Theory and its Applications" organized by the COST Action TU1208 "Civil engineering applications of Ground Penetrating Radar".

## References

[1] G. Buttazzoni and R. Vescovo, "Deterministic and stochastic approach to the synthesis of conformal arrays for SAR applications", in *Proc. 2013 Int. Conf. on Electromag. in Adv. Appl. ICEAA 2013*, Torino, Italy, 2013, pp. 520–523.

[2] R. K. Singh, A. Basu, and S. K. Koul, "Efficient null broadening and steering using slot antenna array for radar applications", in *Proc. 2016 Asia-Pacific Microwave Conf. APMC 2016*, New Delhi, India, 2016, pp. 1–4.

[3] G. Buttazzoni, M. Comisso, A. Cuttin, M. Fragiacomo, R. Vescovo, and R. Vincenti Gatti, "Reconfigurable phased antenna array for extending cubesat operations to Ka-band: Design and feasibility", *Acta Astronautica*, vol. 137, pp. 114–121, 2017.

[4] J. Huang, F. Qiu, W. Lin, Z. Tang, D. Lei, M. Yao, Q. X. Chu, and Y. J. Guo, "A new compact and high gain circularly-polarized slot antenna array for Ku-band mobile satellite TV reception", *IEEE Access*, vol. 5, pp. 6707–6714, 2017.

[5] Q. U. A. Nadeem, A. Kammoun, M. Debbah, and M. S. Alouini, "Performance analysis of compact FD-MIMO antenna arrays in a correlated environment", *IEEE Access*, vol. 5, pp. 4163–4178, 2017.

[6] O. M. Haraz, A. Elboushi, S. A. Alshebeili, and A. R. Sebak, "Dense dielectric patch array antenna with improved radiation characteristics using EBG Ground structure and dielectric superstrate for future 5G cellular networks", *IEEE Access*, vol. 2, pp. 909–913, 2014.

[7] L. I. Vaskelainen, "Phase synthesis of conformal array antennas", *IEEE Trans. Antennas Propag.*, vol. 48, no. 6, pp. 987–991, 2000.

[8] M. Durr, A. Trastoy, and F. Ares, "Multiple-pattern linear antenna arrays with single prefixed amplitude distributions: modified Woodward-Lawson synthesis", *Electron. Lett.*, vol. 36, no. 16, pp. 1345–1346, 2000.

[9] O. M. Bucci, G. Mazzarella, and G. Panariello, "Reconfigurable arrays by phase-only control", *IEEE Trans. Antennas Propag.*, vol. 39, no. 7, pp. 919–925, 1991.

[10] O. M. Bucci and G. D'Elia, "Power synthesis of reconfigurable conformal arrays with phase-only control", *IEE Proc. Microw. Antennas Propag.*, vol. 145, no. 1, pp. 131–136, 1998.

[11] G. K. Mahanti and A. Chakraborty, "Phase-only and amplitude-phase synthesis of dual-pattern linear antenna arrays using floating-point genetic algorithms", *Progress in Electromag. Res.*, PIER 68, pp. 247–259, 2007.

[12] R. Vescovo, "Reconfigurability and beam-scanning with phase-only control for antenna arrays", *IEEE Trans. Antennas Propag.*, vol. 56, no. 6, pp. 1555–1565, 2008.

[13] G. Buttazzoni and R. Vescovo, "Synthesis of co-polar and cross-polar patterns with dynamic range ratio reduction for phase-only reconfigurable arrays", in *Proc. 6th Eur. Conf. on Antenn. and Propag. EUCAP 2012*, Prague, Czech Republic, 2012, pp. 2623–2627.

[14] F. Obelleiro, L. Landesa, J. L. Rodriguez, A. G. Pino, and M. R. Pino, "Directivity optimisation of an array antenna with obstacles within its near field region", *Electron. Lett.*, vol. 33, no. 25, pp. 2087–2088, 1997.

[15] L. Landesa and F. Obelleiro, "Maximising directivity of array antennas mounted over complex environments with near-field null constraints", *Electron. Lett.*, vol. 37, no. 2, pp. 74–76, 2001.

[16] L. Landesa, F. Obelleiro, J. L. Rodriguez, J. A. Rodriguez, F. Ares, and A. G. Pino, "Pattern synthesis of array antennas with additional isolation of near field arbitrary objects", *Electron. Lett.*, vol. 34, no. 16, pp. 1540–1542, 1998.

[17] R. Vescovo, "Pattern synthesis with assigned field reduction in near-field for circular arrays", in *Proc. IEEE Antenn. and Propag. Soc. Int. Symp.*, San Antonio, TX, USA, 2002, vol. 1, pp. 540–543.

[18] M. Comisso and R. Vescovo, "Fast power pattern synthesis with near-field control for antenna arrays", in *Proc. EEE Antenn. and Propag. Soc. Int. Symp.*, Charleston, SC, USA, 2009, pp. 1–4.

[19] M. Comisso, G. Buttazzoni, and R. Vescovo, "Reconfigurable antenna arrays with multiple requirements: A versatile 3D approach", *Int. J. of Antenn. and Propag.*, vol. 2017, Article ID 6752108, 2017 (doi: 10.1155/2017/6752108).

[20] O. M. Bucci, A. Capozzoli, and G. D'Elia, "Power pattern synthesis of reconfigurable conformal arrays with near-field constraints", *IEEE Trans. Antennas Propag.*, vol. 52, no. 1, pp. 132–141, 2004.

[21] G. Buttazzoni and R. Vescovo, "Reconfigurable array synthesis with constraints on near field, far field and dynamic range ratio", in *Proc. Int. Conf. on Electromag. in Advanced Appl. ICEAA '09*, Torino, Italy, 2009, pp. 257–260.

[22] G. Buttazzoni and R. Vescovo, "Phase-controlled beam-scanning with near-field and DRR reduction for arbitrary antenna arrays", in *2010 IEEE Antenn. and Propag. Soc. Int. Symp.*, Toronto, ON, Canada, 2010, pp. 1–4.

[23] G. Buttazzoni and R. Vescovo, "An efficient and versatile technique for the synthesis of 3D copolar and crosspolar patterns of phase-only reconfigurable conformal arrays with DRR and near-field control", *IEEE Transactions on Antennas and Propagation*, vol. 62, no. 4, pp. 1640–1651, 2014.

[24] G. Buttazzoni and R. Vescovo, "A deterministic approach to the synthesis of sparse arrays with far-field and near-field constraints", in *Proc. 2015 IEEE-APS Topical Conf. on Antenn. and Propag. in Wireless Commun. APWC 2015*, orino, Italy, 2015, pp. 161–164.

[25] H. Steyskal, "Synthesis of antenna patterns with imposed near-field nulls", *Electron. Lett.*, vol. 30, no. 24, pp. 2000–2001, 1994.

[26] O. M. Bucci, F. D'Agostino, C. Gennarelli, G. Riccio, and C. Savarese, "Array pattern synthesis with null field constraints in the near-field region", in *IEEE Antenn. and Propag. Soc. Int. Symp.*, vol. 3, Boston, MA, USA, 2001, pp. 716–719.

[27] R. Vescovo, "Power pattern synthesis for antenna arrays with null constraints in the near-field region", *Microw. Opt. Technol. Lett.*, vol. 44, no. 6, pp. 542–545, 2005.

[28] R. A. Horn and C.R. Johnson, *Matrix Analysis*. New York: Cambridge University Press, 1992.

**Giulia Buttazzoni** received the Laurea degree (summa cum laude) in Telecommunication Engineering and the Ph.D. degree in Information Engineering from the University of Trieste (Italy), in 2008 and 2013, respectively. She is currently a researcher at the Department of Engineering and Architecture of the University of Trieste. Her research interests involve antenna array synthesis and numerical methods for electromagnetic fields.
E-mail: gbuttazzoni@units.it
Department of Engineering and Architecture
University of Trieste
Piazzale Europa 1
34127 Trieste, Italy

**Roberto Vescovo** – for biography, see this issue, p. 29.

Paper

# The Optimum-efficiency Beam Multiplier for an Arbitrary Number of Output Beams and Power Distribution

Fabrizio Frezza[1], Marian Marciniak[2], and Lara Pajewski[1]

[1] *Department of Information Engineering, Electronics and Telecommunications, Sapienza University of Rome, Rome, Italy*
[2] *National Institute of Telecommunications, Warsaw, Poland*

https://doi.org/10.26636/jtit.2017.118617

**Abstract—This paper deals with phase gratings working in the paraxial domain. The profile of the optimum-efficiency beam multiplier with an arbitrary number of output diffraction orders is derived in an analytic form by exploiting methods from the calculus of variation. The output beams may be equi-intense or with arbitrary distribution of power. Numerical examples are given for different values of the number of output beams.**

***Keywords—beam multipliers, diffractive optical elements, gratings, periodic structures.***

## 1. Introduction

Diffractive Optical Elements (DOEs) [1] that split a laser beam into multiple output beams are used in many industrial and scientific applications, i.e. in optical signal processing, laser manufacturing, interferometry, read-write magneto-optic data-storage systems, and optical networks. In several cases, the so-called polarizing beam splitters are used [2], which divide an incoming beam into output beams with different polarization states. More often, beam multipliers are employed to replicate an incoming beam into a set of output beams with identical polarization state. The output beams may be equi-intense or show a suitable distribution of power. To realize a beam multiplier, binary Dammann structures are primarily used [3], [4]. Continuous-phase gratings are also sometimes realized [5]–[7].

The diffraction efficiency of a beam multiplier is the fraction of the incident beam power that is converted into the power of the desired output beams. Maximization of this parameter is a fundamental target in designing beam multipliers. Usually, in the evaluation of the diffraction efficiency, absorption and reflection losses are not considered. The former is negligible and the latter can be reduced by using suitable antireflection coatings.

Another important goal to be pursued in the design of beam multipliers is the uniformity of the output beams (or the achievement of the desired power distribution).

The upper bound of the diffraction efficiency of beam multipliers was derived and studied in [10]–[12], for diffractive phase gratings working in the scalar domain. Obviously, the maximum diffraction efficiency of real devices is generally lower than the upper bound. It is worth citing that, by exploiting the further degree of freedom offered by the polarization, in some cases it is possible to overcome the efficiency upper bound and achieve 100% efficiency [13].

In this paper, we focus on phase gratings working in the paraxial domain. We exploit mathematical methods from the calculus of variations for solving the problem of finding optimal profiles for diffractive beam multipliers and we calculate their diffraction efficiency. The problem of optimizing a phase profile is usually faced by using numerical techniques [8], [9], whereas here the optimal profiles in an analytic form are derived.

The present work is the continuation of previous studies, where our research team concentrated on beam multipliers with three [5], [14] and four [6] equi-intense output beams. In particular, in [5], the profile of a DOE producing three equi-intense diffraction orders with the maximum efficiency was derived in an analytic form. In [14], a full-wave electromagnetic analysis of this beam multiplier was performed. In [6], the profile of a DOE producing four equi-intense diffraction orders with the maximum efficiency was derived and its full-wave electromagnetic analysis was presented. It is worth mentioning that in [15] the optimum triplicator proposed in [5] was realized, experimentally tested, and compared to binary gratings of Dammann type. Here, we generalize the procedure proposed in [5], [6] and prove that an optimum-efficiency beam multiplier with an arbitrary number of equi-intense diffraction orders exists. We derive its phase transmittance in an analytic form. This phase transmittance can also be used to design the optimum-efficiency beam multiplier with a fixed power distribution.

The paper is organized as follows. In Section 2 the analytical derivation of the phase transmittance of the optimum-efficiency beam multiplier is presented. In Section 3 numerical examples for different values of the number of output beams are presented. For each considered number of output beams, we give the profile of the optimum beam-multiplier and calculate its diffraction efficiency. Conclusions and ideas for future work are given in Section 4.

## 2. Theory

As is well known, in the paraxial domain the vectorial nature of light can be neglected and the influence of a diffractive element on the illuminating wavefront can be described by its transmission function [16]. Here the transmission function of a phase grating producing an arbitrary number of replicas of an incident field is obtained, with an arbitrary power distribution and with the maximum diffraction efficiency (see Fig. 1).

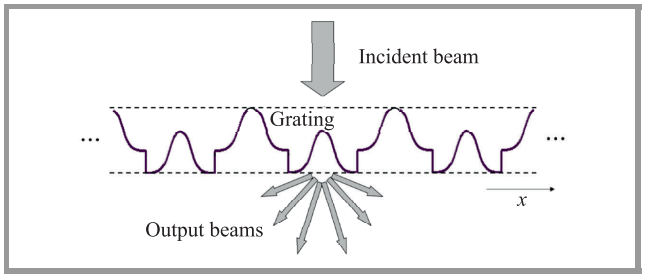


***Fig. 1.*** Scheme illustrating the operation of a phase grating acting as a beam multiplier.

Let us consider a grating having the transmission function $\tau(x) = \mathrm{e}^{i\Phi(x)}$, where $\Phi(x)$ denotes the phase profile. Without loss of generality, in the following formulas we assume a unitary value (in suitable units) of the grating period $d$. Due to the periodicity of the structure, the following Fourier series expansion holds:

$$\tau(x) = \sum_{\mathrm{m}=-\infty}^{\infty} \tau_{\mathrm{m}} \mathrm{e}^{i2\pi \mathrm{m}x}, \tag{1}$$

where $\tau_{\mathrm{m}}$ is the Fourier coefficient corresponding to the diffracted order of index m having the following expression:

$$\tau_{\mathrm{m}} = \int_{-\frac{1}{2}}^{\frac{1}{2}} \mathrm{e}^{i[\Phi(x)-2\pi \mathrm{m}x]} \mathrm{d}x. \tag{2}$$

We define $M$ as the set of indices corresponding to the desired diffracted orders. Generalizing the approach proposed in [5], [6], we consider the functional:

$$\mathscr{I} = \sum_{\mathrm{m}\in \mathrm{M}} \beta_{\mathrm{m}} |\tau_{\mathrm{m}}|^2, \tag{3}$$

where $\beta_{\mathrm{m}}$ are suitable positive multipliers and the sum includes the desired output diffracted orders. The first variation of $\mathscr{I}$ is

$$\delta\mathscr{I} = \sum_{\mathrm{m}\in \mathrm{M}} \beta_{\mathrm{m}} \delta |\tau_{\mathrm{m}}|^2 \tag{4}$$

and the first variation of the Fourier-coefficient square magnitude is:

$$\delta|\tau_{\mathrm{m}}|^2 = \\ = i \int \varepsilon(x) \left\{ \tau_{\mathrm{m}}^* \mathrm{e}^{i[\Phi(x)-2\pi \mathrm{m}x]} - \tau_{\mathrm{m}} \mathrm{e}^{-i[\Phi(x)-2\pi \mathrm{m}x]} \right\} \mathrm{d}x, \tag{5}$$

where the difference between a typical phase profile and the optimum one has been denoted by $\varepsilon(x)$. On imposing that the first variation of $\mathscr{I}$ vanishes, we have:

$$\sum_{\mathrm{m}\in \mathrm{M}} \beta_{\mathrm{m}} |\tau_{\mathrm{m}}| \sin(\alpha_{\mathrm{m}} - \Phi(x) + 2\pi \mathrm{m}x) = 0, \tag{6}$$

being $\alpha_{\mathrm{m}}$ the argument of $\tau_m$. From Eq. (6) it follows that

$$\cos\Phi \sum_{\mathrm{m}\in \mathrm{M}} \beta_{\mathrm{m}} |\tau_{\mathrm{m}}| \sin(\alpha_{\mathrm{m}} + 2\pi \mathrm{m}x) = \\ = \sin\Phi \sum_{\mathrm{m}\in \mathrm{M}} \beta_{\mathrm{m}} |\tau_{\mathrm{m}}| \cos(\alpha_{\mathrm{m}} + 2\pi \mathrm{m}x). \tag{7}$$

Assuming that

$$R(x) = \sum_{\mathrm{m}\in \mathrm{M}} \beta_{\mathrm{m}} |\tau_{\mathrm{m}}| \cos(\alpha_{\mathrm{m}} + 2\pi \mathrm{m}x) \tag{8}$$

and

$$\Gamma(x) = \sum_{\mathrm{m}\in \mathrm{M}} \beta_{\mathrm{m}} |\tau_{\mathrm{m}}| \sin(\alpha_{\mathrm{m}} + 2\pi \mathrm{m}x), \tag{9}$$

Eq. (6) can be satisfied if $\Phi(x)$ satisfies

$$\cos[\Phi(x)] = g(x)R(x) \tag{10}$$

and

$$\sin[\Phi(x)] = g(x)\Gamma(x), \tag{11}$$

being $g(x)$ a real arbitrary function. Therefore, the phase distribution $\Phi_{opt}(x)$ maximizing the functional $\mathscr{I}$ assumes the form:

$$\Phi_{opt}(x) = \arctan\left[\frac{\Gamma(x)}{R(x)}\right] + \pi \mathrm{step}[\mathrm{R(x)}], \tag{12}$$

where step$(\cdot)$ denotes the Heaviside step function, i.e., for $x \geq 0$: step$(x) = 1$, for $x < 0$: step$(x) = 0$. The parameters $\alpha_{\mathrm{m}}$ and $\beta_{\mathrm{m}}$ have to be chosen in such a way that all the Fourier coefficients $|\tau_m|$ have the same magnitude, or else they respect a fixed distribution. In this case, a maximum of $\mathscr{I}$ is also a maximum of transmission efficiency and Eq. (12) gives the profile of the optimum-efficiency beam multiplier.

## 3. Numerical Results

Although the expression in Eq. (12) seems to be quite complicated, the optimum profile assumes, eventually apart from discontinuities, a simple and regular shape.

In Figs. 2 and 3, two different solutions for the four-beam multiplier are reported. The phase distribution $\Phi(x)$ is plotted as a function of $\frac{x}{d}$.

The first solution works on the diffracted orders $m = \pm 1$ and $\pm 3$. In this case, for symmetry reasons $\alpha_1 = \alpha_{-1}$, $\beta_1 = \beta_{-1}$, $\alpha_3 = \alpha_{-3}$, $\beta_3 = \beta_{-3}$, it is possible to choose $\alpha_1 = 0$ and $\beta_1 = 1$. The following optimum values for the other two parameters are found: $\beta_3 = 1.046$ and $\alpha_3 = 1.845$. The achieved diffraction efficiency is $\eta = 91.9025\%$. This result is consistent with [6].

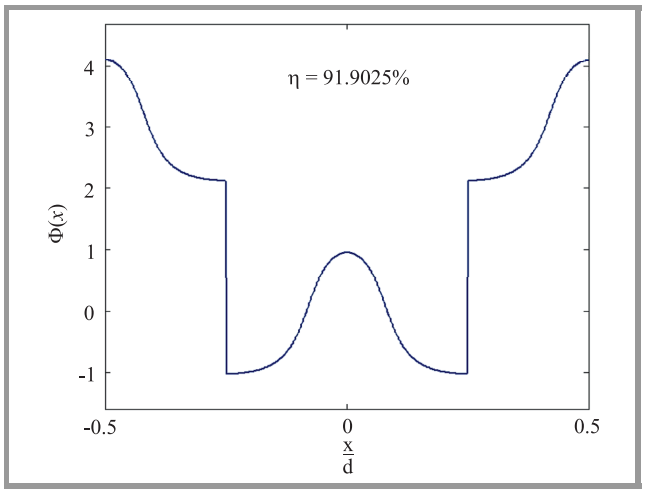


***Fig. 2.*** Profile of the optimum 4-beam multiplier, working on the diffracted orders $m = \pm 1$ and $\pm 3$.

The second solution works on the diffracted orders $m = \pm 1$ and $\pm 2$. For symmetry reasons $\alpha_1 = \alpha_{-1}$, $\beta_1 = \beta_{-1}$, $\alpha_2 = \alpha_{-2}$, $\beta_2 = \beta_{-2}$, it is possible to choose $\alpha_1 = 0$ and $\beta_1 = 1$. The following optimum values for the other two parameters are found: $\beta_2 = 1.05$ and $\alpha_2 = 1.5883$. The diffraction efficiency turns out to be $\eta = 94.1306\%$.

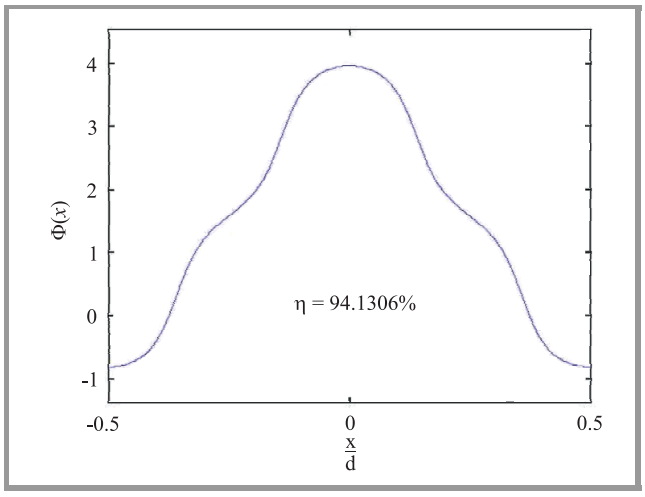


***Fig. 3.*** Profile of the optimum 4-beam multiplier, working on the diffracted orders $m = \pm 1$ and $\pm 2$.

These examples show that, for a given number of output beams, different solutions are possible if there are no specifications on the diffracted orders to be used. The second solution presents an efficiency higher than the first. However, in the first solution the output beams are equally spaced. Both the presented solutions are even-phase gratings. It is also possible to work on different diffracted orders obtaining a four-beam multiplier with asymmetric phase distribution. If the angular directions of the output beams are not specified, then as part of the optimization problem it is necessary to determine which diffracted orders have to be chosen to achieve the maximum transmission efficiency.

It is observed that the first solution presents a discontinuity in $x = \pm 0.25d$, whereas the second solution is continuous. Note that, if a beam is splitted into an even number of odd diffracted orders, the optimal phase distribution will always have discontinuities.

In Fig. 4, a further example is presented. The profile of the optimum-efficiency five-beam multiplier is plotted as a function of $\frac{x}{d}$. This grating works on the diffracted orders $m = 0, \pm 1$ and $\pm 2$. For symmetry reasons $\alpha_1 = \alpha_{-1}$, $\beta_1 = \beta_{-1}$, $\alpha_2 = \alpha_{-2}$, $\beta_2 = \beta_{-2}$, it is possible to choose $\alpha_0 = 0$ and $\beta_0 = 1$. The following optimum values for the other parameters are found: $\beta_1 = 0.459$, $\alpha_1 = -1.5708$, $\beta_2 = 0.899$, $\alpha_2 = 3.1416$. The diffraction efficiency turns out to be $\eta = 92.1\%$.

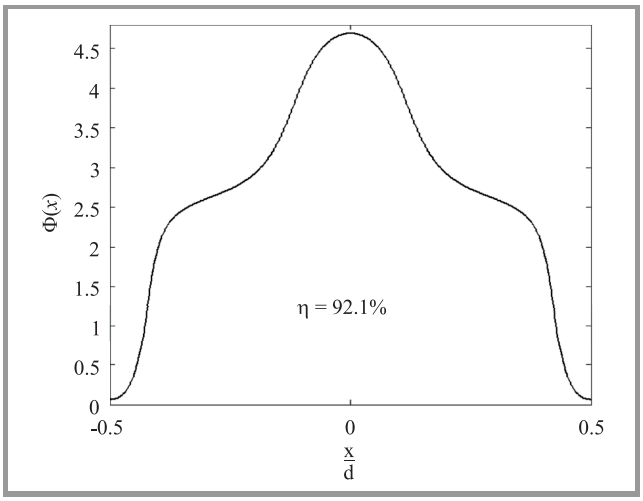


***Fig. 4.*** Profile of the optimum 5-beam multiplier.

For each beam multiplier, the parameters $\alpha_m$ and $\beta_m$ maximizing the transmission efficiency have been found by imposing a beam uniformity equal to 0.001 and by performing a simple optimization search over a multi-dimensional grid of possible values for the parameters. For sure, there are better and faster ways of solving this optimization problem, but our aim was giving some numerical examples to highlight theoretical work. For high values of the number of output beams, this kind of optimization search becomes computationally difficult and more sophisticated techniques have to be applied to find the parameters $\alpha_m$ and $\beta_m$.

As already mentioned, we derived the profile of the optimum-efficiency beam multiplier in the paraxial domain. In the resonance domain, when grating-profile features have transverse dimensions comparable with the wavelength of the impinging radiation, the scalar diffraction theory fails. To study the properties of a DOE rigorously, a full-wave application of the electromagnetic theory is necessary. A rigorous treatment of the problem allows, for example, to understand the operational limits of a diffractive beam multiplier and study its angular response, as in [6] and [14]. The theory of propagation of electromagnetic waves in periodic media is well developed [17]–[21]. An efficient and versatile electromagnetic spectral-domain technique

that we suggest to apply for the full-wave investigation of DOEs is the Fourier Modal Method. This approach was originally developed for the characterization of two-dimensional diffraction gratings, but nowadays is employed also for the modeling of two-dimensional photonic crystals [22]–[25], crossed gratings and three-dimensional photonic crystals [26], as well as electromagnetic band-gap materials working in the microwave region of the frequency spectrum [27]–[33].

## 4. Conclusions

This paper focuses on the problem of splitting a beam into a set of equi-intense output beams, or in beams respecting a fixed power distribution. The profile of the optimum-efficiency beam multiplier, with an arbitrary number of output diffraction orders, is derived in an analytic form; methods from the calculus of variation are exploited. Numerical examples are given, for different values of the number of equi-intense output beams. For a given number of output beams, solutions with different angular directions of the output beams are compared.
Ideas for future research activities include:

- checking the performances of the optimum beam multiplier when a high number of output beams is required,
- performing a detailed comparison between the optimum beam multiplier and Dammann gratings,
- designing suitable antireflection coatings for the optimum beam multiplier and studying their effect on the performance of the grating,
- carrying out a full-wave study of the optimum beam multiplier by using a rigorous electromagnetic technique, such as the Fourier Modal Method,
- fabricating and measuring some prototypes.

## Acknowledgements

The authors would like to thank Franco Gori for his useful suggestions and ideas, which were essential for the development of this work. This work benefited from the networking activities carried out in COST (European Cooperation in Science and Technology) Actions MP0702 "Towards Functional Sub-Wavelength Photonic Structures" (http://cost-mp0702.nit.eu) and TU1208 "Civil engineering applications of Ground Penetrating Radar" (www.GPRadar.eu). The paper was finalized during the TU1208 STSM no. 37998, carried out by Lara Pajewski at the National Institute of Telecommunications of Poland from 5 to 24 June 2017. The authors are grateful to COST for funding and supporting the Actions MP0702 and TU1208.

## References

[1] G. J. Swanson, "Binary optics technology: the theory and design of multi-level diffractive optical elements", Tech. Rep. no. TR-854, Massachusetts Institute of Technology, Lexington Lincoln Lab., pp. 1–47, 1989 [Online]. Available: www.dtic.mil/dtic/tr/fulltext/u2/a213404.pdf

[2] L. Pajewski, R. Borghi, G. Schettini, F. Frezza, and M. Santarsiero, "Design of a binary grating with subwavelength features that acts as a polarizing beam splitter", *Appl. Optics*, vol. 40, no. 32, pp. 5898–5905, 2001.

[3] G. H. Dammann and K. Görtler, "High efficiency in-line multiple imaging by means of multiple phase holograms", *Optics Commun.*, vol. 3, no. 5, pp. 312–315, 1971.

[4] H. Dammann and E. Klotz, "Coherent optical generation and inspection of two-dimensional periodic structures", *Opt. Acta*, vol. 24, no. 4, pp. 505–515, 1977.

[5] F. Gori *et al.*, "Analytical derivation of the optimum triplicator", *Optics Commun.*, vol. 157, no. 1–6, pp. 13–16, 2008.

[6] R. Borghi, F. Frezza, L. Pajewski, M. Santarsiero, and G. Schettini, "Optimum even-phase four-beam multiplier", *Optical Engin.*, vol. 41, no. 11, pp. 2736–2742, 2002.

[7] J. Song, Y. Li, X. Zhou, and X. Li, "Planar grating multiplexers using silicon nanowire technology: numerical simulations and fabrications", *Progress in Electromag. Res.*, vol. 123, pp. 509–526, 2012.

[8] J. L. Jiang, H. Wu, L. Y. Jiang, and X. Y. Li, "Genetic optimization of double subwavelength metal slits sorrounded by surface dielectric gratings for directional beaming manipulation", *Optics Commun.*, vol. 285, no. 8, pp. 2201–2206, 2012.

[9] G. Bloom *et al.*, "Design and optimization of a high-efficiency array generator in the mid-IR with binary subwavelength grooves", *Appl. Optics*, vol. 50, no. 5, pp. 701–709, 2011.

[10] F. Wyrowski, "Upper bound of the diffractive efficiency of diffractive phase elements", *Opt. Letters*, vol. 16, no. 24, pp. 1915–1917, 1991.

[11] U. Krackhardt, J. N. Mait, and N. Streibl, "Upper bound on the diffraction efficiency of phase-only fan out elements", *Appl. Optics*, vol. 31, no. 1, pp. 27–37, 1992.

[12] F. Wyrowski, "Design theory of diffractive elements in the paraxial domain", *J. Opt. Soc. of America A*, vol. 10, no. 7, pp. 1553–1561, 1993.

[13] J. Tervo and J. Turunen, "Paraxial-domain diffractive elements with 100% efficiency based on polarization gratings", *Opt. Lett.*, vol. 25, pp. 785–786, 2000.

[14] R. Borghi, F. Frezza, L. Pajewski, M. Santarsiero, and G. Schettini, "Full-wave analysis of the optimum triplicator", *J. Electromag. Waves Appl.*, vol. 15, no. 6, pp. 689–708, 2001.

[15] F. Aroca and I. Moreno, "Comparison and experimental realization of different phase only grating designs and optimal triplicators", *Optica Pura y Aplicada*, vol. 49, no. 3, pp. 155–166, 2016.

[16] M. Born and E. Wolf, *Principles of Optics*, 7th ed. Cambridge University Press, 1999.

[17] F. Frezza, L. Pajewski, and G. Schettini, "Characterization and design of two-dimensional electromagnetic band-gap structures by use of a full-wave method for diffraction gratings", *IEEE Trans. Microwave Theory Techniq.*, vol. 51, no. 3, pp. 941–951, 2003.

[18] G. Zheng *et al.*, "Analysis of finite periodic dielectric gratings by the finite-difference frequency-domain method with the sub-entire-domain basis functions and wavelets", *Progress in Electromag. Res.*, vol. 99, pp. 453–463, 2009.

[19] J.-J. Liau *et al.*, "A new look at numerical analysis of uniform fiber Bragg gratings using coupled mode theory", *Progress in Electromag. Res.*, vol. 93, pp. 385–401, 2009.

[20] N.-H. Sun *et al.*, "Numerical analysis of apodized fiber Bragg gratings using coupled mode theory", *Progress in Electromag. Res.*, vol. 99, pp. 289–306, 2009.

[21] J. Frances, C. Neipp, A. Marquez Ruiz, A. Belendez, and I. Pascual, "Analysis of reflection gratings by means of a matrix method approach", *Progress in Electromag. Res.*, vol. 118, pp. 167–183, 2011.

[22] F. Frezza, L. Pajewski, and G. Schettini, "Fast and accurate modeling of finite-thickness 2D-EBG structures made by circular-section rods", *Microwave and Optical Technol. Lett.*, vol. 39, no. 6, 433–437, 2003.

[23] F. Frezza, L. Pajewski, and G. Schettini, "Periodic defects in 2D-PBG materials: Full-wave analysis and design", *IEEE Trans. Nanotechnol.*, vol. 2, no. 3, pp. 126–134, 2003.

[24] F. Frezza, L. Pajewski, and G. Schettini, "Fractal two-dimensional electromagnetic band-gap structures", *IEEE Trans. Microwave Theory Techniq.*, vol. 52, no. 1, pp. 220–227, 2004.

[25] F. Frezza, L. Pajewski, and G. Schettini, "Numerical investigation on the filtering behavior of 2D-PBGs with multiple periodic defects", *IEEE Trans. Nanotechnol.*, vol. 4, no. 6, pp. 730–739, 2005.

[26] F. Frezza, L. Pajewski, and G. Schettini, "Full-wave Characterization of three-dimensional photonic bandgap structures", *IEEE Trans. Nanotechnol.*, vol. 5, no. 5, pp. 545–553, 2006.

[27] F. Frezza, L. Pajewski, E. Piuzzi, C. Ponti, and G. Schettini, "Design and fabrication of a 3D-EBG superstrate for patch antennas", in *Proc. 39th Eur. Microwave Conf. EuMC 2009*, Rome, Italy, 2009, pp. 1496–1499.

[28] F. Frezza, L. Pajewski, E. Piuzzi, C. Ponti, and G. Schettini, "Analysis and experimental characterization of an alumina woodpile-covered planar antenna", in *Proc. 40th Eur. Microwave Conf. EuMC 2010*, Paris, France, 2010, pp. 200–203.

[29] F. Frezza, L. Pajewski, E. Piuzzi, C. Ponti, and G. Schettini, "Advances in EBG-resonator antenna research", in *Proc. Int. Symp. on Antennas and Propagation ISAP 2012*, Nagoya, Japan, 2012, pp. 1301–1304.

[30] S. Ceccuzzi, L. Pajewski, C. Ponti, and G. Schettini, "Directive propagation in two EBG structures: a comparison", *2013 IEEE MTT-S Int. Microwave Symp. Digest IMS 2013*, Seattle, WA, USA, 2013, (doi: 0.1109/MWSYM.2013.6697579).

[31] S. Ceccuzzi, L. Pajewski, C. Ponti, and G. Schettini, "Comparison between two methods for directivity enhancement of antennas through 2-D EBGs", in *Proc. 2013 Progress in Electromag. Res. Symp. PIERS 2013*, Stockholm, Sweden, 2013, pp. 557–561.

[32] F. Frezza, L. Pajewski, E. Piuzzi, C Ponti, and G. Schettini, "Radiation-enhancement properties of an X-band woodpile EBG and its application to a planar antenna", *Int. J. on Antennas and Propag.*, vol. 2014, Article ID 729187, 2014 (doi: 10.1155/2014/729187).

[33] S. Ceccuzzi, L. Pajewski, C. Ponti, and G. Schettini, "Directive EBG antennas: a comparison between two different radiating mechanisms", *IEEE Trans. on Antennas and Propag.*, vol. 62, no. 10, pp. 5420–5424, 2014 (doi: 10.1109/TAP.2014.2346174).

---

**Fabrizio Frezza** – for biography, see this issue, p. 23.

**Lara Pajewski** – for biography, see this issue, p. 29.

**Marian Marciniak** – for biography, see this issue, p. 35.

Paper

# Influence of Chirped DBR Reflector on the Absorption Efficiency of Multi-nanolayer Photovoltaic Structures: Wavelength-scale Analysis by the Method of Single Expression

Hovik Baghdasaryan[1], Tamara Knyazyan[1], Tamara Hovhannisyan[1], Gurgen Mardoyan[2], Marian Marciniak[3], and Trevor Benson[4]

[1] *National Polytechnic University of Armenia, Yerevan, Armenia*
[2] *National Instruments AM LLC, Yerevan, Armenia*
[3] *National Institute of Telecommunications, Warsaw, Poland*
[4] *George Green Institute for Electromagnetics Research, Faculty of Engineering, University of Nottingham, Nottingham, UK*

https://doi.org/10.26636/jtit.2017.120117

**Abstract—An electromagnetic wavelength-scale analysis of the optical characteristics of multi-nanolayer photovoltaic (PV) structures: without an antireflection coating, with an antireflection coating on the top of the structure, and with both the antireflection coating on the top and a broadband non-periodic (chirped) distributed Bragg reflector (DBR) on the bottom of the structure is performed. All the PV structures studied are based on a Si p-i-n type absorber supported by a metallic layer (Cu) and $SiO_2$ substrate. The top-to-bottom electromagnetic analysis is performed numerically by the method of single expression (MSE). Absorbing and reflecting characteristics of the multi-nanolayer PV structures are obtained. The influence of the thicknesses and permittivities of the layers of the PV structures on the absorbing characteristics of the structures is analyzed to reveal favourable configurations for enhancement of their absorption efficiency. The localizations of the electric component of the optical field and the power flow distribution within all the PV structures considered are obtained to confirm an enhancement of the absorption efficiency in the favorable configuration. The results of the electromagnetic wavelength-scale analysis undertaken will have scientific and practical importance for optimizing the operation of thin-film multi-nanolayer PV structures incorporating a chirped DBR reflector with regards to enhancing their efficiency.**

***Keywords—antireflection coating, chirped distributed Bragg reflector, electromagnetic modeling, method of single expression, multi-nanolayer photovoltaic structure, photovoltaics.***

## 1. Introduction

Today's photovoltaic (PV) technology is one of the most attractive, scalable and mature renewable energy sources. PV technology has gained great scientific and practical interest since the end of the 19-th century and now is proven as the cleanest and safest of all energy technologies. Due to growing demand for renewable energy sources, the manufacturing of solar cells and photovoltaic arrays has advanced considerably in recent years [1]–[5].

Photovoltaics are based on the photovoltaic effect by which solar energy is converted directly into electrical energy by photovoltaic or solar cells. The conversion efficiency of a PV cell depends on the probability of absorption of an incident photon, generating an electron-hole pair, which can contribute to the external electric current.

Though today's PVs technology is well developed, and has been extensively exploited for household and industrial applications, there is still a need to enhance the PV efficiency over a wider spectral range, whilst using a cheap material base and a low cost technology for the mass production of durable PV devices.

Materials used for the first generation of PV cells included monocrystalline and polycrystalline silicon, for the second generation of PV cells cadmium telluride, copper indium gallium selenide/sulfide, and thin films from amorphous silicon were used. The third generation of PV cells uses different organic polymers, perovskite crystals, monocrystalline and polycrystalline graphene, quantum dots, and multilayers of different semiconductor materials.

Nowadays PV cells are thin-film cells with absorbing layer thicknesses that are of the same order or smaller than the operating wavelength [5], [6]. Thin films essentially reduce the amount of semiconductor material required for each PV cell compared to bulk PV cells and hence lower the cost of production [2], [7]. The probability of photon absorption increases with an increased thickness of the absorbing layer [8]. However, enhancement of the recombination probability decreases the probability of conversion of absorbed photons into electrical current as the

active layer thickness increases. For better light harvesting in PV cells different multilayer optical structures are used. Generally, they consist of an absorbing layer covered from top and bottom, correspondingly by transparent and reflecting metal electrodes. Some structures have an antireflection coating above the top transparent electrode to reduce reflection losses in the PV cell [9], [10]. Antireflection coatings can improve the absorption efficiency when the thickness of an absorbing layer much greater than the operating wavelength. When the thickness of the absorbing layer is comparable to or smaller than the operating wavelength high-reflectivity dielectric mirrors are used to enhance the absorption over a narrow spectral and angular range. The dielectric mirrors are usually high reflectivity distributed Bragg reflectors (DBRs) [11]–[13]. DBRs should exhibit a high reflectivity in the spectral range where the absorption of the PV cell is weak to enhance absorption, and a low reflectivity where the absorption of the PV cell is strong. DBRs made as non-periodic dielectric stacks, where the thicknesses of bilayers are monotonously changed by some linear, quadratic, exponential or other law, are called chirped DBRs. Absorption in thin-film PV cells using chirped DBR mirrors can be enhanced over a wider spectral range by providing higher efficiency in comparison with those using conventional reflectors [7], [14]–[16]. By tailoring the law of chirp, and the number and thickness of bilayers in chirped DBRs, the efficiency of such PV cells can essentially be enhanced.

It is important to note that for the analysis of a PV cell's efficiency enhancement there is a need to apply two different methodologies: the first is optical (electromagnetic) modeling directed to light-matter interaction analysis and the second is an analysis of the physics of semiconductors and semiconductor junctions. The optical analysis is the less investigated topic for thin-film nano-scale PV structures. Semiconductor junction physics has been intensively analyzed and is a well-established area. There is a need for detailed optical simulations to understand and further optimize the beneficial effects of the PV cells [15].

The present paper is devoted to the wavelength-scale numerical analysis, by the method of single expression (MSE) [13], [17]–[21], of the optical characteristics of multi-nanolayer PV structures:

- without an antireflection coating,
- with an antireflection coating on the top of the structure,
- with both an antireflection coating on the top and chirped DBRs on the bottom of the structure.

The influence of layer thicknesses and permittivities on the optical characteristics of multi-nanolayer PV cells is analyzed by observing the localization of the electric component of the optical field and the power flow density distribution within the structures. The numerical modeling reveals an optimal PV structure for efficient light absorption.

## 2. Modeling Method

The modeling has been performed by the method of single expression (MSE) which is a convenient and correct tool for wavelength-scale analysis of multilayer and modulated structures comprising dielectric, semiconductor or metallic layers in the presence of loss, gain or (Kerr-type) nonlinearity [13], [17]–[21].

Here the backbone of the MSE for wave normal incidence on a non-magnetic multilayer structure is presented. From Maxwell's equations in 1D case the following Helmholtz equation can be obtained for linearly polarized complex electric field component $\dot{E}_x(z)$:

$$\frac{d^2\dot{E}_x(z)}{dz^2} + k_0^2\dot{\varepsilon}(z)\dot{E}_x(z) = 0\,, \tag{1}$$

where $k_0 = \frac{\omega}{c}$ is the free space propagation constant, $\dot{\varepsilon}(z) = \varepsilon'(z) + i\varepsilon''(z)$ is the complex relative permittivity of a medium. The essence of the MSE is the presentation of a general solution of Helmholtz equation for the electric field component $\dot{E}_x(z)$ in the special form of a single expression:

$$\dot{E}_x(z) = U(z)\cdot \mathrm{e}^{-iS(z)} \tag{2}$$

instead of the traditional presentation as a sum of counter-propagating waves. Here $U(z)$ and $S(z)$ are real quantities describing the resulting electric field amplitude and phase, respectively. A time dependence of $\mathrm{e}^{i\omega t}$ is assumed, but suppressed, throughout the analysis. A solution in the form (2) prevails upon the traditional approach of counter-propagating waves and is more general because it does not rely on the superposition principle. This form of solution describes all possible distributions in space of electric field amplitude, corresponding to propagating, standing or evanescent waves. It means that no preliminary assumptions concerning the solution of the Helmholtz equation in different media are needed in the MSE. This gives advantages in allowing investigation of the interaction of a wave with any longitudinally non-uniform linear and intensity dependent non-linear media with the same ease and exactness.

Based on expression (2) the Helmholtz equation (1) is reformulated to the set of first order differential equations regarding the electric field amplitude $U(z)$, its spatial derivative $Y(z)$ and a quantity $P(z)$ proportional to the power flow density (Poynting vector) in a medium:

$$\begin{cases} \dfrac{dU(z)}{d(k_0z)} = Y(z) \\ \dfrac{dY(z)}{d(k_0z)} = \dfrac{P^2(z)}{U^3(z)} - \varepsilon'(z)\cdot U(z) \\ \dfrac{dP(z)}{d(k_0z)} = \varepsilon''(z)\cdot U^2(z) \end{cases}, \tag{3}$$

where $P(z) = U^2(z)\frac{dS(z)}{d(k_0z)}$. An actual value of Poynting vector can be obtained by multiplication of $P(z)$ by $\frac{1}{2}\sqrt{\frac{\varepsilon_0}{\mu_0}}$, where $\varepsilon_0$ and $\mu_0$ are free space permittivity and permeability, respectively. Hereafter this multiplier is suppressed.

The sign of $\varepsilon'(z)$ can be taken either positive or negative describing relevant electromagnetic features of dielectric or metal (plasma), correspondingly. The sign of $\varepsilon''(z)$ indicates loss or gain in a medium.

The set of differential equations (3) is integrated numerically starting from the non-illuminated side of a multilayer structure, where only one outgoing traveling wave is supposed. Initial values for the integration are obtained from the boundary conditions of electrodynamics at the non-illuminated side of the structure (at $z = L$): $U(L) = E_{tr}$, $Y(L) = 0$ and $P(L) = \sqrt{\varepsilon_r} E_{tr}^2 = P_{tr}$, where $P_{tr}$ is proportional to the Poynting vector in the medium beyond the structure (at $z > L$) of relative permittivity $\varepsilon_r$, and $E_{tr}$ is the amplitude of the transmitted wave.

Numerical integration of the set (3) goes step by step towards the illuminated side of the structure taking into account the actual value of the structure's relative permittivity for the given coordinate at each step of the integration. In the process of integration it is possible to record any variable of the set (3) in order to have full information regarding distributions of electric field amplitude, its derivative and power flow density inside and outside of a structure. At the borders between the layers constituting a multilayer structure, the ordinary boundary conditions of electrodynamics bring continuity of $U(z)$, $Y(z)$ and $P(z)$. From the boundary conditions of electrodynamics at the illuminated side of the structure the amplitude of incident wave $E_{inc}$

$$E_{inc} = \left| \frac{U^2(0) \cdot \sqrt{\varepsilon_l} + P(0) + iU(0) \cdot Y(0)}{2U(0) \cdot \sqrt{\varepsilon_l}} \right|, \qquad (4)$$

and the power reflection coefficient $R$

$$R = \left| \frac{E_{ref}}{E_{inc}} \right|^2 = \left| \frac{U^2(0) \cdot \sqrt{\varepsilon_l} - P(0) - iU(0) \cdot Y(0)}{U^2(0) \cdot \sqrt{\varepsilon_l} + P(0) + iU(0) \cdot Y(0)} \right|^2, \qquad (5)$$

are restored at the end of the calculation. Here $U(0)$ is the resultant amplitude of the electromagnetic wave, $Y(0)$ is its derivative and $P(0)$ is proportional to the power flow density at the illuminated interface of the structure at $z = 0$, $E_{ref}$ is the amplitude of the reflected wave, $\varepsilon_l$ is the relative permittivity of the medium in front of the structure, at $z < 0$, and in the considered case is air $\varepsilon_l = 1$. In accordance with the energy conservation law $P(0) = P_{inc} - P_{ref}$, where $P_{inc} = \sqrt{\varepsilon_l} \cdot E_{inc}^2$ is proportional to the incident power flow density and $P_{ref} = \sqrt{\varepsilon_l} \cdot E_{ref}^2$ is proportional to the reflected power flow density. The power transmission coefficient $T = \frac{P_{tr}}{P_{inc}} = \frac{\sqrt{\varepsilon_r} E_{tr}^2}{\sqrt{\varepsilon_l} E_{inc}^2}$ is defined as the ratio of the transmitted power flow density $P_{tr}$ to the incident one $P_{inc}$.

## 3. Numerical Analysis of Multi-Nanolayer Photovoltaic Structures

In the current paper the PV structures of the following configurations: a) without antireflection coating, b) with an antireflection coating on the top of the PV structure, and c) both the antireflection coating on the top and a broadband non-periodic (chirped) distributed Bragg reflector (DBR) on the bottom of the PV structure, are considered. All PV structures are based on a Si p-i-n type absorber and supported by a metallic mirror (Cu) and $SiO_2$ substrate.

The results of a preliminary analysis of the thin-film multi-nanolayer PV structure with chirped DBR on the top of the structure was presented at ICTON 2016 [22].

Chirped DBR mirrors should possess broadband reflective features in the range of 350–750 nm in the vicinity of the central wavelength of 550 nm of the sun's maximal radiation.

The consideration and analysis of the PV structures is aiming to reveal an optimal structure for efficient absorption of incident light in the specific region of the PV structure, namely in the "i" region of the p-i-n junction, where generation of electron-hole pairs is favorable.

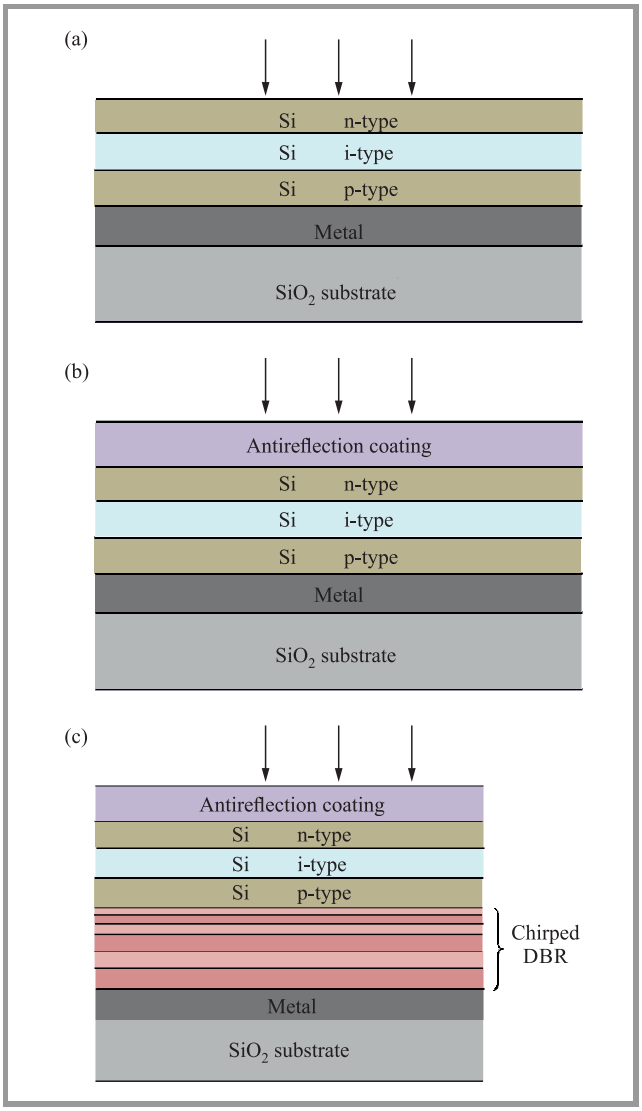


***Fig. 1.*** Schematic representations of the PV structures: (a) without antireflection coating, (b) with an antireflection coating on the top of the PV structure, and (c) with both the antireflection coating on the top and a chirped DBR on the bottom of the PV structure.

The schematic representations of the considered PV structures are shown in Figs. 1a–1c, respectively.

In the structures considered the thickness of the substrate of relative permittivity $\varepsilon_{SiO_2} = 2.1313$ is taken to be $L_{SiO_2} = 100\ \mu$m. The thickness of the metallic layer, of relative permittivity $\varepsilon_m = \varepsilon'_m - \varepsilon''_m = -6.12 - i4.48$ at the central wavelength of $\lambda_0 = 550$ nm, is taken as $L_m = 0.6\ \mu$m. Dispersive properties of Cu in the range of wavelengths 350–750 nm are taken into account [23]. Dispersion of other materials of the structure are not taken into account.

The p-i-n absorbing region made of silicon (Si) has the following parameters: *p*-type and *n*-type layers of relative permittivity $\varepsilon_n = \varepsilon_p = 15$ have thicknesses $L_p = 1.45$ *mu*m and $L_n = 0.255\ \mu$m, respectively. The *i*-type layer of relative permittivity $\varepsilon_i = \varepsilon'_i - i\varepsilon''_i = 15.5 - i0.3$ has a thickness of $L_i = 1\ \mu$m.

The antireflection coating made of $TiO_2$ of relative permittivity $\varepsilon_{coat} = 5$ has the thickness $L_{coat} = 61.5$ nm.

Chirped DBRs made of $TiO_2$ are composed of 7 bilayers of slightly different high $\varepsilon_{H-TiO_2} = 5$ and low $\varepsilon_{L-TiO_2} = 3.5$ relative permittivities. The permittivity of a material can be lowered by introducing porosity, provided that the pore sizes are much smaller than the electromagnetic wavelengths of interest [24]. The thicknesses of the layers of high and low permittivities decrease gradually towards the illuminated side of the structure to provide a chirp law for the DBR. The thicknesses of the layers of low permittivity are as follows (starting from the bottom of the structure): $L_{L1-TiO_2} = 108$ nm, $L_{L2-TiO_2} = 1038$ nm, $L_{L3-TiO_2} = 97$ nm, $L_{L4-TiO_2} = 91$ nm, $L_{L5-TiO_2} = 85$ nm, $L_{L6-TiO_2} = 79$ nm, $L_{L7-TiO_2} = 73$ nm.

The thicknesses of the layers of high permittivity are as follows (starting from the bottom of the structure): $L_{H1-TiO_2} = 91$ nm, $L_{H2-TiO_2} = 86$ nm, $L_{H3-TiO_2} = 81$ nm, $L_{H4-TiO_2} = 76$ nm, $L_{H5-TiO_2} = 71$ nm, $L_{H6-TiO_2} = 66$ nm, $L_{H7-TiO_2} = 61$ nm.

The results of modeling of the PV structures considered are presented below successively in following subsections.

### *3.1. The Modeling of the PV Structure without an Antireflection Coating*

The reflection spectrum of the PV structure without an antireflection coating (Fig. 1a) with the above-mentioned parameters is presented in Fig. 2 for the range of the incident wavelengths $\lambda_0$ = 350–750 nm.

As it follows from Fig. 2 the reflection spectrum of the PV structure without antireflection coating has an oscillating character with maxima and minima at specific wavelengths. The oscillations of the reflectance in the considered frequency range are stipulated by an optical wave resonant interaction with the wavelength-scaled multilayer dielectric-semiconductor-metal structure.

In order to understand which part of the incident light is absorbed in the i absorbing layer of p-i-n region contributing to the PV effect it is useful to analyse the distributions

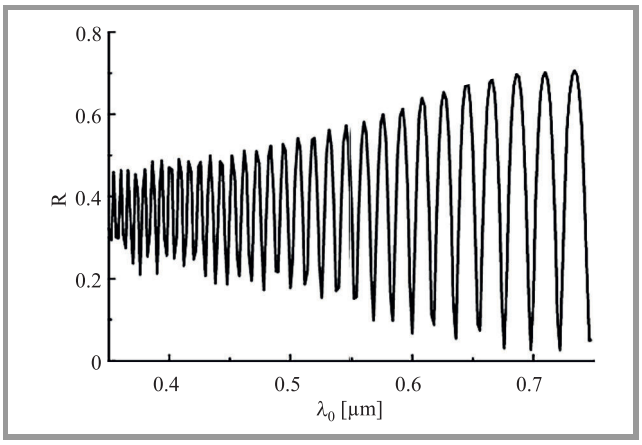


***Fig. 2.*** The reflection spectrum of the PV structure without antireflection coating (presented in Fig. 1a).

of the electric component of optical field and the power flow density within and outside of the structure. The permittivity profile of the PV structure without antireflection coating and the distributions of the electric component of the optical field and the power flow density within and outside of the structure at the central wavelength $\lambda_0$ = 550 nm, corresponding to the sun's maximal radiation, are presented in Fig. 3.

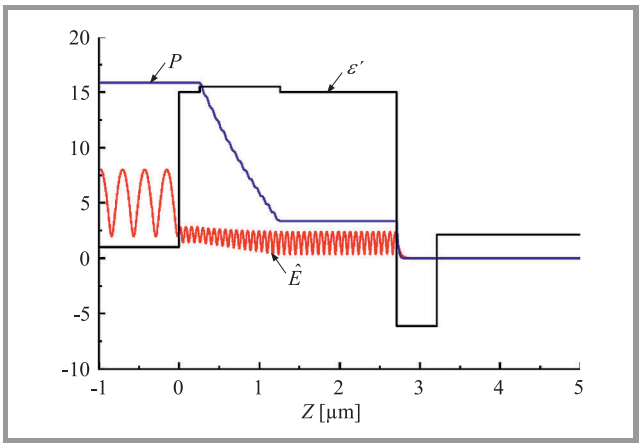


***Fig. 3.*** The relative permittivity profile $\varepsilon'$ of the PV structure without antireflection coating (presented in Fig. 1a) and the distributions of electric field amplitude $\hat{E}$ and power flow density $P$ within and outside of the structure at the wavelength $\lambda_0$ = 550 nm, $P_{inc} = 25$ a.u., the reflectance $R = 0.366$.

As can be seen from Fig. 3, electric field amplitude has an oscillating character in the p-i-n region and forms a standing wave pattern in the front of the structure (at $z < 0$) due to some reflection from it. A decrease of power flow density in the *i* absorbing layer of $\Delta P_{p-i-n} = 12.5135$ a.u. is observed, indicating an absorption rate $\frac{\Delta P_{p-i-n}}{P_{inc}} \approx 0.5$ (about 50%) of the incident light ($P_{inc} = 25$ a.u.) contributing to the PV effect. Outside of the absorbing region the power flow density is constant except for some decay within the metallic layer ($\Delta P_m = 3.3485$ a.u.). The absorption rate $\frac{\Delta P_m}{P_{mc}} \approx 0.134$ in the metal is about 13.4%. Thus,

essential absorption of the incident energy takes place in the "i" absorbing layer of the structure. The rest of the incident energy, 36.6%, relates to the reflectance from the structure.

### 3.2. The Modeling of the PV Structure with an Antireflection Coating on the Top of the Structure

The reflection spectrum of the PV structure with the antireflection coating on the top of the structure (Fig. 1b) with above-mentioned parameters is presented in Fig. 4 for the range of incident wavelengths $\lambda_0$ = 350–750 nm.

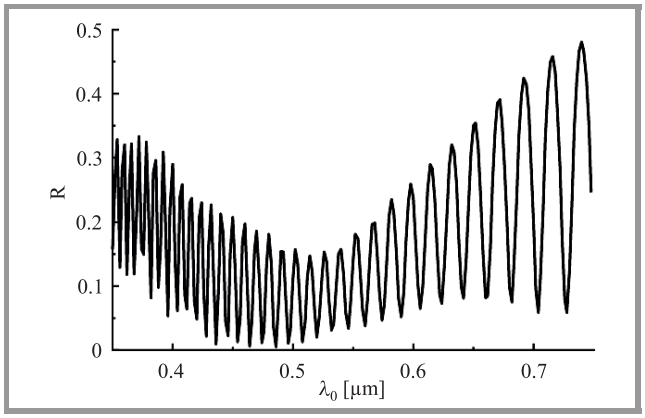


*Fig. 4.* The reflection spectrum of the PV structure with the antireflection coating on the top of the structure (presented in Fig. 1b).

It follows from Fig. 4 that the reflection spectrum of the PV structure with the antireflection coating also has an oscillating character, however the average value of the reflectance oscillations has a minimum around $\lambda_0 = 500$ nm.

As with the previous structure it is useful to analyse the distributions of the electric component of the optical field and the power flow density within the considered structure. The permittivity profile of the PV structure with the antireflection coating on the top of the structure and the distributions of electric component of optical field and power flow density within the structure at the central wavelength $\lambda_0 = 550$ nm of the sun's maximal radiation are presented in Fig. 5.

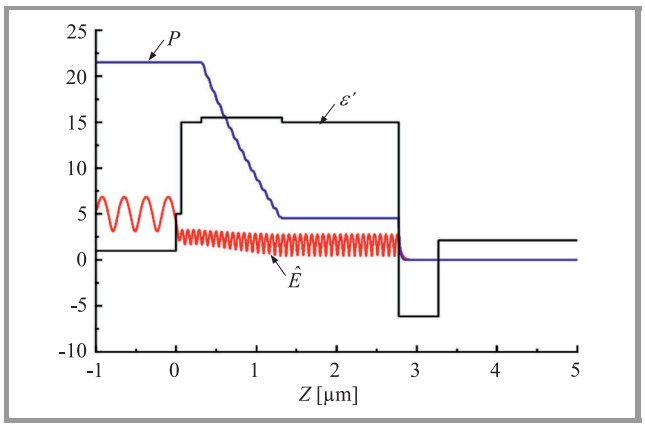


*Fig. 5.* The relative permittivity profile $\varepsilon'$ of the PV structure with antireflection coating on the top of the structure (presented in Fig. 1b) and the distributions of electric field amplitude $\hat{E}$ and power flow density $P$ within the structure at the wavelength $\lambda_0$ = 550 nm, $P_{inc} = 25$ a.u., the reflectance $R = 0.14$.

As can be seen from Fig. 5, the electric field amplitude has an oscillating character in the p-i-n region and forms a standing wave pattern in front of the structure (at $z < 0$) due to some reflection from the structure. A decrease of power flow density in the "i" absorbing layer $\Delta P_{p-i-n} = 16.97$ a.u. is observed, indicating an absorption rate $\frac{\Delta P_{p-i-n}}{P_{inc}} \approx 0.679$ (about 68%) of the incident light ($P_{inc} =$ 25 a.u.) contributing to the PV effect. Outside of this region the power flow density is constant except for some decay within the metallic layer ($\Delta P_m = 4.541$ a.u.). The absorption rate $\frac{\Delta P_m}{P_{inc}} \approx 0.182$ nm in the metal is about 18%. Thus, essential absorption of incident energy takes place in the "i" absorbing layer of the structure. The rest of the incident energy, 14%, relates to the reflectance from the structure.

### 3.3. The Modeling of the PV Structure with an Antireflection Coating on the Top and a Chirped DBR on the Bottom of the Structure

The reflectance of the PV structure with the antireflection coating on the top and the chirped DBR on the bottom of the PV structure (Fig. 1c) with above-mentioned parameters is presented in Fig. 6 for the range of incident wavelengths $\lambda_0$ = 350–750 nm.

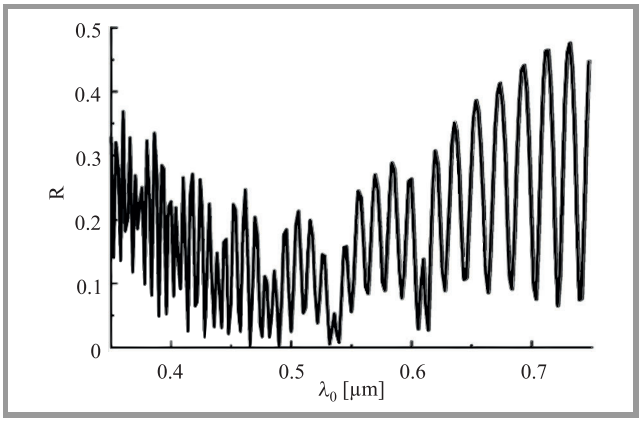


*Fig. 6.* The reflection spectrum of the PV structure with the antireflection coating on the top and the chirped DBR on the bottom of the structure (presented in Fig. 1c).

It follows from Fig. 6 that the reflection spectrum of the PV structure with the antireflection coating on the top and the chirped DBR on the bottom of the structure also has an oscillating character with maxima and minima at specific wavelengths. However, the average value of the reflectance oscillations has a minimum around $\lambda_0 = 550$ nm.

As with the previous structures it is useful to analyse the distributions of the electric component of the optical field and the power flow density within and outside of the struc-

ture considered. The relative permittivity profile of the PV structure with the antireflection coating on the top and the chirped DBR on the bottom of the structure, and the distributions of the electric component of the optical field and the power flow density within the structure, are presented in Fig. 7 for the central wavelength $\lambda_0 = 550$ nm of the sun's maximal radiation.

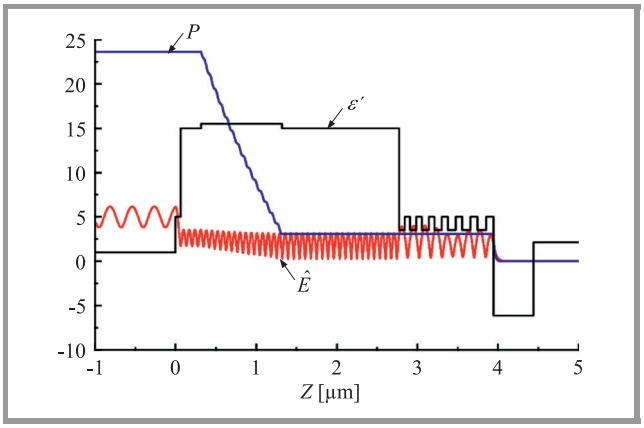


***Fig. 7.*** The relative permittivity profile $\varepsilon'$ of the PV structure with the antireflection coating on the top and the chirped DBR on the bottom of the structure (presented in Fig. 1c) and the distributions of electric field amplitude $\hat{E}$ and power flow density $P$ within the structure at the wavelength $\lambda_0 = 550$ nm, $P_{inc} = 25$ a.u., the reflectance $R = 0.056$.

As can be seen from Fig. 7, the electric field amplitude has an oscillating character in the p-i-n region and forms a standing wave pattern in front of the structure (at $z < 0$) due to some reflection from the structure. A strong decrease of power flow density in the "i" absorbing layer $\Delta P_{p-i-n} = 20.52$ a.u. is observed, indicating an absorption rate $\frac{\Delta P_{p-i-n}}{P_{inc}} \approx 0.8208$ (about 82.1%) of incident light ($P_{inc} = 25$ a.u.) contributing to the PV effect. Outside of this region the power flow density is constant except for the small decay within the metallic layer ($\Delta P_m = 3.08$ a.u.). The absorption rate $\frac{\Delta P_m}{P_{inc}} \approx 0.1232$ in the metal is about 12.3%. Thus, essential absorption of incident energy takes place in the $i$ absorbing layer of the structure. The rest of the incident energy, 5.6%, relates to the reflectance from the structure as can be seen from Fig. 6.

The results of comparative analysis of the considered PV structures are summarized and presented in Table 1.

Table 1
Example results of the new metric

| Structure described in | $R = \frac{P_{ref}}{P_{inc}}$ | $\frac{\Delta P_{p-i-n}}{P_{inc}}$ | $\frac{\Delta P_m}{P_{inc}}$ |
|---|---|---|---|
| 3.1 | $\approx 0.366$ | $\approx 0.5$ | $\approx 0.134$ |
| 3.2 | $\approx 0.14$ | $\approx 0.679$ | $\approx 0.181$ |
| 3.3 | $\approx 0.056$ | $\approx 0.821$ | $\approx 0.123$ |

It is evident that the structure with the antireflection coating on the top and the broadband non-periodic (chirped) DBR reflector on the bottom of the PV structure is favorable for light absorption in the $i$ region of the p-i-n structure.

## 4. Conclusions

An electromagnetic wavelength-scale numerical analysis of the optical characteristics of thin-film multi-nanolayer PV structures has been performed by the MSE. The following configurations of the PV structures are considered: without an antireflection coating, with an antireflection coating on the top of the structure, and with both the antireflection coating on the top and a broadband non-periodic (chirped) distributed Bragg reflector (DBR) on the bottom of the structure. All PV structures are based on a Si p-i-n type absorber supported by a metallic layer (Cu) and $SiO_2$ substrate.

The reflection spectra of all structures have an oscillating character in the whole spectral range of $\lambda_0$ = 350–750 nm nm with maxima and minima at specific wavelengths. The oscillations in the frequency range considered are stipulated by an optical wave resonant interaction with the wavelength-scaled multilayer dielectric-semiconductor-metal structures. At the fixed wavelength $\lambda_0 = 550$ nm (the wavelength of the sun's maximal radiation and the central part of the spectrum considered) the distributions of electric field amplitude and power flow density within and outside of the structures are obtained. For all structures high absorption of incident light is observed in the i-layer of the p-i-n junction. The highest absorption of incident light takes place in the $i$-layer of the p-i-n junction of the structure with the antireflection coating on the top and the broadband non-periodic (chirped) DBR reflector on the bottom of the PV structure while the lowest absorption in the metallic layer is observed. Thus, this structure is favorable for strong absorption of the incident light that will contribute to the PV effect.

Though the current analysis is performed for a plane wave normal incidence on the PV structures, the MSE permits the case of an oblique incidence of a plane wave to be considered as well [25].

## Acknowledgement

This work was supported by the RA MES State Committee of Science, in the frame of the research project no. 15T-2J372.

## References

[1] G. K. Singh, "Solar power generation by PV (photovoltaic) technology: A review", *Energy*, vol. 53, pp. 1–13, 2013.

[2] B. Parida, S. Iniyan, and R. Goic, "A review of solar photovoltaic technologies", *Renewable and Sustain. Energy Rev.*, vol. 15, no. 3, pp. 1625–1636, 2011.

[3] M. A. Green, K. Emery, Y. Hishikawa, W. Warta, and E. D. Dunlop, "Solar cell efficiency tables (Version 45)", *Progr. in Photovolt: Res. and Appl.*, vol. 23, no. 1, pp. 1–9, 2015 (doi: 10.1002/pip.2573).

[4] R. W. Miles, K. M. Hynes, and I. Forbes, "Photovoltaic solar cells: An overview of state-of-the-art cell development and environmental issues", *Progr. in Crystal Growth and Charact. of Mater.*, vol. 51, no. 1–3, pp. 1–42, 2005.

[5] Y. Hamakawa, Ed., *Thin-Film Solar Cells: Next Generation Photovoltaics and Its Applications*. Springer, 2004.

[6] A. G. Aberle, "Thin-film solar cells", *Thin Solid Films*, vol. 517, no. 17, pp. 4706–4710, 2009.

[7] I. J. Kuzma-Filipek, F. Duerinckx, E. Van Kerschaver, K. Van Nieuwenhuysen, G. Beaucarne, and J. Poortmans, "Chirped porous silicon reflectors for thin-film epitaxial silicon solar cells", *J. of Appl. Phys.*, vol. 104, no. 7, pp. 073529-1–073529-8, 2008 (doi: 10.1063/1.2993753).

[8] T. Tiedje, E. Yablonovitch, G. D. Cody, and B. G. Brooks, "Limiting efficiency of silicon solar cells", *IEEE Trans. Electron Devices*, vol. ED-31, no. 5, pp. 711–716, 1984.

[9] J. Zhao and M. A. Green, "Optimized antireflection coatings for high-efficiency silicon solar cells", *IEEE Trans. Electron Devices*, vol. 38, no. 8, pp. 1925–1934, 1991.

[10] J. K. Selj, D. Young, and S. Grover, "Optimization of the antireflection coating of thin epitaxial crystalline silicon solar cells", *Energy Procedia*, vol. 77, pp. 248–252, 2015.

[11] P. Yeh, *Optical Waves in Layered Media*. N.Y.: Willey, 1988.

[12] D. I. Babic and S. W. Corzine, "Analytic expressions for the reflection delay, penetration depth, and absorptance of quarter-wave dielectric mirrors", *IEEE J. Quantum Elect.*, vol. 28, pp. 514–524, 1992.

[13] H. V. Baghdasaryan, T. M. Knyazyan, T. H. Baghdasaryan, B. Witzigmann, and F. Roemer, "Absorption loss influence on optical characteristics of multilayer distributed Bragg reflector: wavelength-scale analysis by the method of single expression", *Opto-Electron. Rev.*, vol. 18, no. 4, pp. 438–445, 2010 (doi: 10.2478/s11772-010-0049-0).

[14] M. Agrawal and P. Peumans, "Broadband optical absorption enhancement through coherent light trapping in thin-film photovoltaic cells", *Optics Express*, vol. 16, no. 8, pp. 5385–5396, 2008 (doi: 10.1364/OE.16.005385).

[15] F. Duerinckx *et al.*, "Simulation and implementation of a porous silicon reflector for epitaxial silicon solar cells", *Progr. in Photovolt: Res. and Appl.*, vol. 16, pp. 399–407, 2008.

[16] J. Zheng, R. A. Barton, and D. Englund, "Broadband coherent absorption in chirped-planar-dielectric cavities for 2D-material-based photovoltaics and photodetectors", *ACS Photonics*, vol. 1, no. 9, pp. 768–774, 2014 (doi: 10.1021/ph500107b).

[17] H. V. Baghdasaryan, "Method of backward calculation", in *Photonic Devices for Telecommunications: How to Model and Measure*, G. Guekos, Ed. Springer, 1999, pp. 56–65.

[18] H. V. Baghdasaryan and T. M. Knyazyan, "Problem of plane EM wave self-action in multilayer structure: An exact solution", *Optical and Quant. Electron.*, vol. 31, no. 9, pp. 1059–1072, 1999 (doi: 10.1023/A:1007024312874).

[19] H. V. Baghdasaryan and T. M. Knyazyan, "Modelling of strongly nonlinear sinusoidal Bragg gratings by the Method of Single Expression", *Optical and Quant. Electron.*, vol. 32, no. 6-8, pp. 869–883, 2000.

[20] H. V. Baghdasaryan, T. M. Knyazyan, T. H. Baghdasaryan, B. Witzigmann, and F. Roemer, "Absorption loss influence on optical characteristics of multilayer distributed Bragg reflector: wavelength-scale analysis by the method of single expression", *Opto-Electron. Rev.*, vol.18, pp. 438–445, 2010.

[21] H. V. Baghdasaryan, *Basics of the Method of Single Expression: New Approach for Solving Boundary Problems in Classical Electrodynamics*. Yerevan: Chartaraget, 2013.

[22] H. V. Baghdasaryan, T. M. Knyazyan, T. T. Hovhannisyan, G. R. Mardoyan, and M. Marciniak, "Wavelength-scale analysis of influence of chirped DBRs on optical characteristics of multi-nanolayer Photovoltaic Cells", in *Proc. of 18th In. Conf. on Transp. Opt. Netw. ICTON 2016*, Trento, Italy, 2016, We.P.33, 5 pages.

[23] E. D. Palik, Ed., *Handbook of Optical Constants of Solids.* Academic Press, 1998.

[24] A. Vincent, S. Babu, E. Brinley, A. Karakoti, S. Deshpande, and S. Seal, "Role of catalyst on refractive index tenability of porous silica antireflective coatings by sol-gel technique", *J. Phys. Chem. C*, vol. 111, no. 23, pp. 8291–8298, 2007.

[25] H. V. Baghdasaryan, T. M. Knyazyan, T. H. Baghdasaryan, and G. G. Eyramjyan, "Development of the Method of Single Expression (MSE) for analysis of plane wave oblique incidence on multilayer structures having complex permittivity and permeability", in *Proc. of 10th Int. Conf. on Transp. Opt. Netw. ICTON 2008*, Athens, Greece, 2008, Th.A1.4, pp. 250–254.

**Gurgen R. Mardoyan** graduated in Radio-engineering from the State Engineering University of Armenia (now National Polytechnic University of Armenia, NPUA) in 2010. He received M.Sc. degree in Radio-engineering and Communications in 2012 and the Ph.D. degree in Wireless Communications in 2015 from National Polytechnic University of Armenia. His postgraduate research dealt with problems of spectrum efficiency in MIMO communication systems, while multiple channels in both transmitters and receivers were not fully phase-coherent. Since 2010 he works at National Instruments as a Systems Engineer prototyping RF systems for wireless/cellular test, RF component test, radio-navigation, Radars and next generation wireless communications. Since 2016 he focuses on Advanced Driver Assistance Systems (ADAS), particularly on 77 GHz automotive radar test applications. Collaborating with R&D department of National Instruments he is working on software development for automotive radar test systems and actively participating in engagements with end-users worldwide.

E-mail: gurgen.mardoyan@gmail.com
National Instruments AM LLC
123 Hovsep-Emin St
EIF Entrance, 0051 Yerevan, Armenia

**Trevor M. Benson** received a First Class honours degree in Physics and the Clark Prize in Experimental Physics from the University of Sheffield in 1979, a Ph.D. in Electronic and Electrical Engineering from the same University in 1982 and the D.Sc. degree from the University of Nottingham in 2005.

After spending over six years as a Lecturer at University College Cardiff, he moved to The University of Nottingham in 1989. He was promoted to a Chair in Optoelectronics in 1996, having previously been Senior Lecturer (1989) and Reader (1994). Professor Benson's research interests include experimental and numerical studies of electromagnetic fields and waves with particular emphasis on the theory, modeling and simulation of optical waveguides, lasers and amplifiers, nano-scale photonic circuits and sensors, and electromagnetic compatibility. He is a Fellow of the Institute of Engineering Technology (FIET) and the Institute of Physics (FInst.P). He was elected a Fellow of the Royal Academy of Engineering in 2005 for his achievements in the development of versatile design software used to analyze propagation in optoelectronic waveguides and photonic integrated circuits.

E-mail: trevor.benson@nottingham.ac.uk
George Green Institute for Electromagnetics Research
Faculty of Engineering
University of Nottingham
University Park
Nottingham NG7 2RD, UK

**Hovik V. Baghdasaryan** – for biography, see this issue, p. 34.

**Marian Marciniak, Tamara M. Knyazyan, Tamara T. Hovhannisyan** – for biographies, see this issue, p. 35.

Paper

# A Photonic-Crystal Selective Filter

Lara Pajewski[1] and Giuseppe Schettini[2]

[1] *Department of Information Engineering, Electronics and Telecommunications, Sapienza University of Rome, Rome, Italy*
[2] *Roma Tre University, Rome, Italy*

https://doi.org/10.26636/jtit.2017.119817

**Abstract—A highly selective filter is designed, working at 1.55 $\mu$m and having a 3-dB bandwidth narrower than 0.4 nm, as is required in Dense Wavelength Division Multiplexed systems. Different solutions are proposed, involving photonic crystals made rectangular- or circular-section dielectric rods, or else of holes drilled in a dielectric bulk. The polarization and frequency selective properties are achieved by introducing a defect in the periodic structure. The device is studied by using in-house codes implementing the full-wave Fourier Modal Method. Practical guidelines about advantages and limits of the investigated solutions are given.**

***Keywords—filter, Fourier Modal Method, periodic structures, photonic bandgap materials, photonic crystals.***

## 1. Introduction

Photonic crystals are artificial media, constituted by periodic implants of a material with a specific dielectric permittivity embedded in a homogeneous background of different permittivity [1], [2]. The main feature of a photonic crystal is the presence of frequency bands within which the waves are highly attenuated and do not propagate (bandgaps or stopbands). This property is exploited in a lot of applications, in the microwave region, as well as in the infrared and optical range; new ideas are under continuous research and novel components are designed [3]–[17].

The study of photonic crystals with defects is a topic of great interest. Defects may obviously be present in a structure due to fabrication errors [18], [19]. Very often, though, defects are on purpose introduced in photonic crystals to design resonant cavities, filters or switches [20]–[24]. In fact, the occurrence of a sharp transmission peak inside a bandgap may result from defect creation. By suitably choosing the configuration of the structure, it is possible to shape its transmission properties in a versatile way [25], [26].

In this work, we focus on the design of a photonic-crystal filter for fiber optic applications. The design specifications are that radiation at 1.55 $\mu$m has to be transmitted, with a 3-dB selectivity smaller than 0.4 nm, as is required in Dense Wavelength Division Multiplexed (DWDM) systems. The required filtering properties are obtained by using a dielectric photonic crystal and by properly interrupting its periodicity. In particular, some implants are removed in the middle of the synthesized structure, so that a homogeneous layer of anomalous thickness is present between two adjacent layers of rods.

The proposed device is studied by using in-house codes implementing the Fourier Modal Method (FMM) [27], as briefly resumed in Section 2. The FMM is a fast, accurate and versatile spectral-domain technique for the solution of plane-wave scattering problems by dielectric diffractive optical elements and photonic crystals.

Numerical results for the synthesized filter are presented in Section 3. Different solutions are proposed and compared, with photonic crystals made of rectangular- or circular-section dielectric rods, or else of holes drilled in a dielectric bulk. The transmission properties of the proposed components are investigated as a function of the polarization and the wavelength of the incident radiation.

Practical comments about advantages and limits of the different investigated solutions are given in Section 4, where conclusions are drawn.

## 2. FMM Modeling of Photonic Crystals

The structures proposed in this paper are designed and characterized by using an in-house code implementing the Fourier Modal Method (FMM), a full-wave spectral-domain technique that solves the monochromatic plane-wave diffraction problem by dielectric photonic crystals. The formulation of the method proposed in [27] is adopted. This approach was originally developed for the characterization of two-dimensional diffraction gratings [28]–[30]. Subsequently, it was demonstrated that the FMM can be successfully employed for the accurate modeling of two-dimensional photonic crystals [27], [31], [32]. More recently, the method has been extended and applied to the characterization of three-dimensional photonic crystals and crossed gratings [7], [8], [33].

The photonic crystal is considered as a finite stack of periodic grids of implants in a hosting medium (e.g., dielectric rods arranged in the air, or air holes drilled in a dielectric bulk). Adjacent grids may be separated by homogeneous layers. The general approach for exactly solving the electromagnetic problem associated to this kind of structure involves the solution of Maxwell's equations inside each periodic layer of the crystal, in the homogeneous regions

between different periodic layers and outside the crystal. Boundary conditions have to be imposed between different regions.

A fundamental step in the FMM is the expansion in a Fourier series of the dielectric permittivity of each layer constituting the photonic crystal. Plane-wave expansions of the electromagnetic field are used (Rayleigh expansions outside the crystal, modal expansions in the crystal layers). This approach leads to a set of eigenvalue problems, which have to be solved. Then, the tangential electric and magnetic field components are matched at all the boundary surfaces. The resulting linear equation system is solved for the reflected and transmitted field amplitudes, so that the reflection and transmission efficiencies of the photonic crystal can be determined.

The total transmission efficiency of a photonic crystal is defined as the sum of the efficiencies of all the transmitted diffracted orders. The efficiency of the $n$-th transmitted order is equal to the Poynting-vector component, along the transmission direction, of the $n$-th order transmitted wave, divided by the Poynting-vector component, along the same direction, of the incident wave.

The FMM treatment of photonic crystals is accurate and versatile, it allows studying structures with arbitrary-shape implants forming whatever kind of lattice. The effects of interruptions in the photonic-crystal periodicity can be investigated by this method [25], [26].

## 3. Numerical Results

### *3.1. Rectangular-Section Rods*

The first solution that we propose uses a two-dimensional photonic crystal with rectangular-section silicon rods arranged in a rectangular lattice. The host material is the air. The geometry of the filter is sketched in Fig. 1. The refractive index of rods is assumed to be $n_d = 3.4$ in the considered frequency range, the lattice periods along the two orthogonal periodicity directions are $d_1$ and $d_2$, and the size of the cross-section of the rods is $b_1 d_1 \times b_2 d_2$. The required frequency-selective behavior of the structure is obtained by suitably interrupting its periodicity. In particular, the introduced defect consists of some rods missing in the middle of the structure: an air gap with length $L$ is present between the two central layers of rods. $ND$ is the number of rod layers located on each side of the defect. The structure can also be viewed as a Fabry-Perot resonator, with two mirrors consisting of identical photonic crystals separated by an air region.

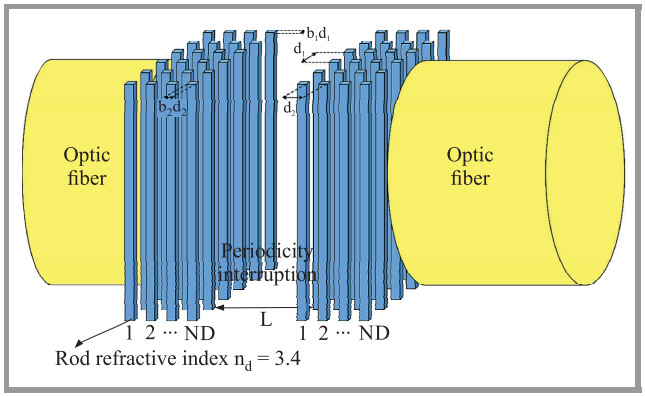


*Fig. 1.* Geometry of the photonic-crystal filter made of square-section rods.

Calculation results for this filtering structure are presented in Fig. 2, for different values of $ND$. It is chosen to design a square-lattice ($d_1 = d_2 = d$) square-section rod ($b_1 = b_2 = b$) structure, because it is easier and cheaper to fabricate with respect to a rectangular-lattice rectangular-section solution. The electromagnetic behavior of the synthesized filter is illustrated by plotting its total transmission efficiency as a function of the free-space wavelength $\lambda$ normalized to $d$. Curves for both the fundamental TE (full line) and TM (dashed line) polarization states are reported. In TE polarization, the electric field propagating through the filter is parallel to the photonic-crystal rods. In TM polarization, instead, the electric field is orthogonal to the rods. With $b = 0.4$ and $L = 1.6d$, a TE transmission peak centered on $\frac{\lambda}{d} \cong 2.75$ is present while propagation is prohibited for TM polarization.

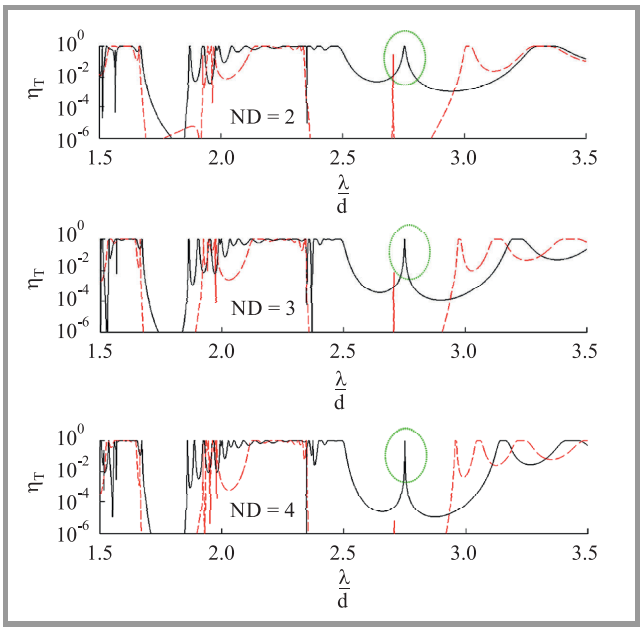


*Fig. 2.* FMM results for the photonic-crystal filter made of square-section rods.

It can be appreciated that the selectivity of the structure becomes higher as $ND$ increases. In particular, if $ND = 2$ the transmission peak is centered on $\frac{\lambda}{d} = 2.758$: with a period $d = 0.562\ \mu$m, transmission of radiation at $\lambda = 1.55\ \mu$m occurs and the 3-dB width of the transmission peak turns out to be 4.5 nm. If $ND = 3$ the peak is centered on $\frac{\lambda}{d} = 2.753$: with $d = 0.563\ \mu$m, radiation at $\lambda = 1.55\ \mu$m is transmitted and the 3-dB width of the peak is 1.1 nm. Finally, if $ND = 4$ the peak is centered on $\frac{\lambda}{d} = 2.748$: with $d = 0.564\ \mu$m, the transmission of radiation at $\lambda = 1.55\ \mu$m

is obtained and the 3-dB width of the peak is 0.28 nm (less than 0.4 nm, that is the design specification).

### 3.2. Rectangular-Section Holes

The second structure that we consider is a two-dimensional photonic crystal with rectangular-section holes arranged in a rectangular lattice and drilled in a dielectric bulk, as sketched in Fig. 3. The geometrical parameters are denoted as for the first structure, the refractive index of the dielectric material is again $n_d = 3.4$.

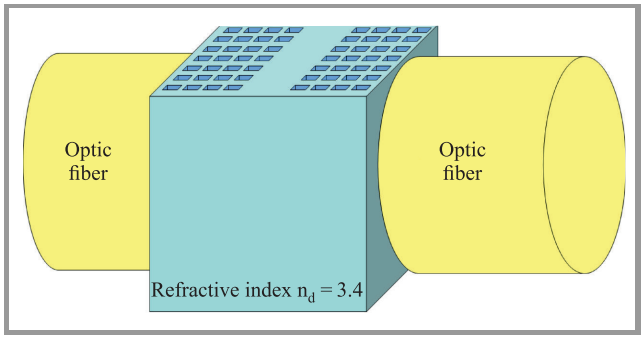


*Fig. 3.* Geometry of the photonic-crystal filter made of square-section holes drilled in a dielectric bulk.

Numerical results are given in Fig. 4 for different values of $ND$, being $d_1 = d_2 = d$, $b_1 = b_2 = 0.75$ and $L = 1.25d$; the full-line curves correspond to TE polarization and the dashed-line curves correspond to TM polarization.

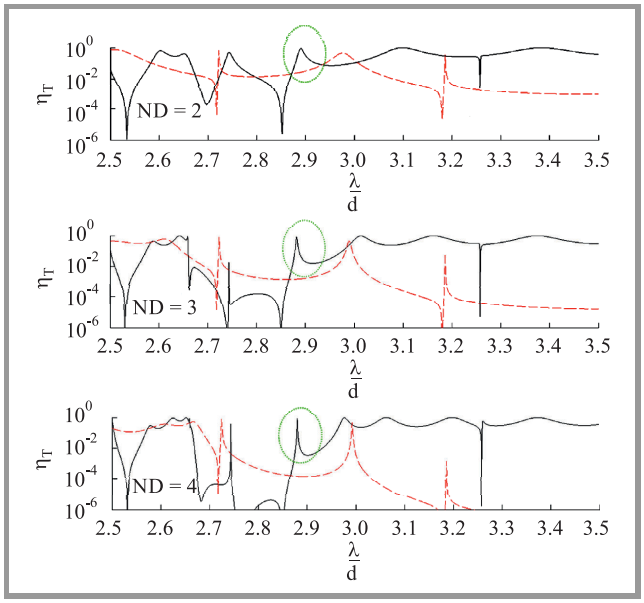


*Fig. 4.* FMM results for the photonic-crystal filter made of square-section holes drilled in a dielectric bulk.

If $ND = 2$, a TE transmission peak in $\frac{\lambda}{d} = 2.892$ is obtained: with a period $d = 0.536$ $\mu$m this peak is centered on $\lambda = 1.55$ $\mu$m and its 3-dB width is 6.4 nm. If $ND = 3$, the TE transmission peak is in $\frac{\lambda}{d} = 2.881$. If a period $d = 0.538$ $\mu$m is chosen, this peak is centered on $\lambda = 1.55$ $\mu$m and its 3-dB width is 1.4 nm. Moreover, if $ND = 4$, the TE transmission peak is in $\frac{\lambda}{d} = 2.876$. With a period $d = 0.539$ $\mu$m this peak is centered on $\lambda = 1.55$ $\mu$m and its 3-dB width is 0.47 nm.

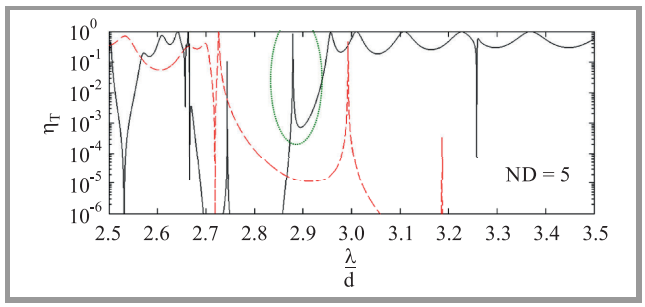


*Fig. 5.* FMM results for the photonic-crystal filter made of square-section holes drilled in a dielectric bulk: $ND = 5$.

This filter is easier to fabricate but slightly less selective than the solution with square-section rods proposed in the previous subsection, if the same number of inclusions $ND$ is considered. It is necessary to drill $ND = 5$ rows of holes in the dielectric bulk, to satisfy the design specification. Relevant centered results are reported in Fig. 5. In this case, the transmission peak is centered on $\frac{\lambda}{d} = 2.870$. By choosing a period $d = 0.540$ $\mu$m, the transmission of radiation having wavelength $\lambda = 1.55$ $\mu$m is achieved, and the 3-dB width of the transmission peak turns out to be 0.16 nm.

### 3.3. Circular-Section Rods

The third structure that we propose is shown in Fig. 6. It uses a two-dimensional photonic crystal with circular-section rods arranged in a rectangular lattice, with periods $d_1$ and $d_2$. The radius of the rod section is called $R$ and the refractive index of the dielectric material is again $n_d = 3.4$. The length of the periodicity interruption (the central air gap) is called $L$.

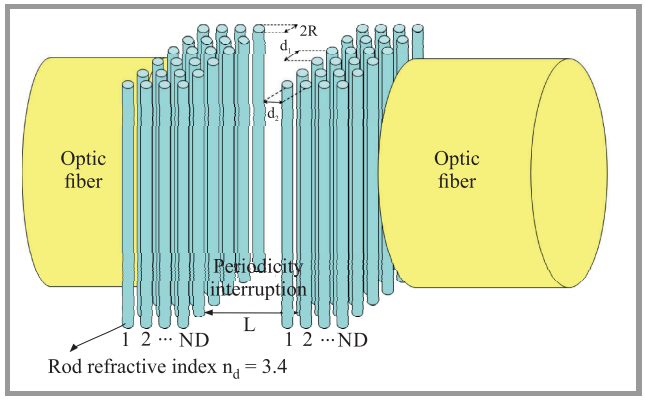


*Fig. 6.* Geometry of the photonic-crystal filter made of circular-section rods.

The results presented in Fig. 7 are obtained for a structure with $d_1 = d_2 = d$, $R = 0.226d$, $L = 1.55d$ and $ND = 5$. The total transmission efficiency of the filter is plotted

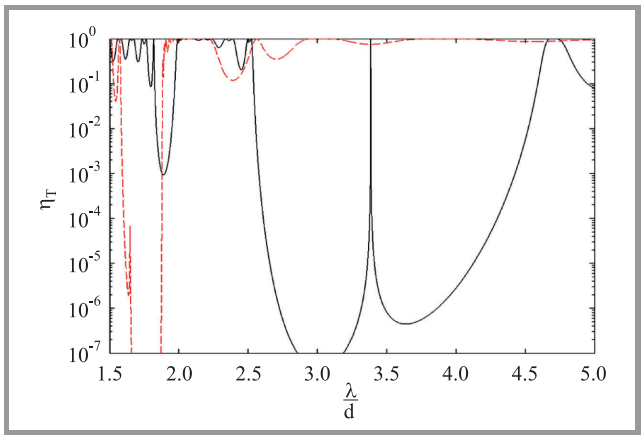


***Fig. 7.*** FMM results for the photonic-crystal filter made of circular-section rods.

as a function of the normalized wavelength $\frac{\lambda}{d}$. The presence of a sharp TE transmission peak is observed, centered on $\frac{\lambda}{d} = 3.385$. By choosing a period $d = 0.458$ $\mu$m, the transmission of waves propagating at $\lambda = 1.55$ $\mu$m is achieved; the 3-dB width of the transmission peak turns out to be 0.14 nm.

### *3.4. Circular-Section Holes*

The fourth structure that we consider is sketched in Fig. 8. It consists of a two-dimensional photonic crystal with

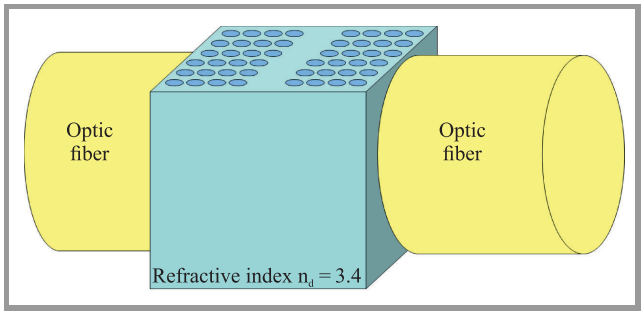


***Fig. 8.*** Geometry of the photonic-crystal filter made of circular-section holes drilled in a dielectric bulk.

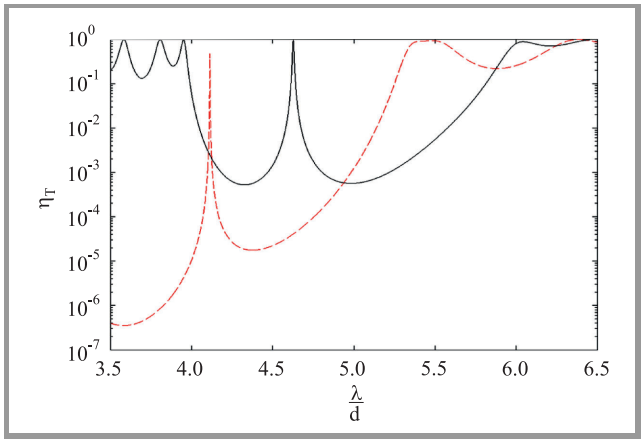


***Fig. 9.*** FMM results for the photonic-crystal filter made of circular-section holes drilled in a dielectric bulk.

circular-section holes arranged in a rectangular lattice and drilled in a dielectric bulk. The geometrical parameters are denoted as for the third structure and the refractive index of the dielectric material is $n_d = 3.4$.

In Fig. 9 results obtained with $d_1 = d_2 = d$, $R = 0.432d$, $L = 1.136d$ and $ND = 5$ are presented. Even in this case, a transmission peak for TE polarization is present. This peak is centered on $\frac{\lambda}{d} = 4.627$. With a period $d = 0.335$ $\mu$m, the transmission of $\lambda = 1.55$ $\mu$m is guaranteed and the 3-dB width of the peak is 3 nm.

## 4. Conclusions

In this work, the design of a photonic-crystal filter is presented. The filter transmits radiation at 1.55 $\mu$m, with a 3-dB selectivity smaller than 0.4 nm. Four different solutions are proposed and examined, involving photonic crystals made of square or circular cross-section dielectric rods, or holes drilled in a dielectric bulk. The required selective behavior is obtained by suitably introducing a defect in the adopted photonic crystal. The structures are simulated by using in-house codes implementing the rigorous Fourier Modal Method.

Solutions with holes are easier to fabricate, with respect to solutions involving rods, moreover they are less fragile; however, they are less selective than solutions involving rods, thus requiring a slightly higher number of periodic layers to satisfy the 0.4 nm specification. Thus, a filter made of holes turns out to be larger than a filter made of rods and stronger scattering losses occur during the propagation of the radiation through the filter. An advantage of the filter made of rods, is that its transmission peak can be easily tuned to 1.55 $\mu$m by adjusting the defect length $L$. To deal with imperfections and non-idealities in the fabricated photonic-crystal structure, which may be present and influence the optical properties of the filter.

The calculation results show that strong and narrow dips are present in the transmission-efficiency curves (e.g., in Fig. 2 at $\frac{\lambda}{d} \cong 2.4$ and in Fig. 4 at $\frac{\lambda}{d} \cong 3,27$). This suggests that the studied structures may be designed and sized to act as highly-reflective narrow-band filters, which also are of interest in fiber optics communication.

## Acknowledgements

The authors thank Gabriella Cincotti for the interesting discussions. The first author is grateful to COST (European Cooperation in Science and Technology, www.cost.eu) for funding and supporting the Actions MP0702 "Towards Functional Sub-Wavelength Photonic Structures" (cost-mp0702.nit.eu) and TU1208 "Civil engineering applications of Ground Penetrating Radar" (www.GPRadar.eu). This work is a contribution to the TU1208 Special Issue "Recent Progress in Electromagnetic Theory and its Applications".

# References


[1] J. D. Joannopoulos, S. G. Johnson, J. N. Winn, and R. D. Meade, *Photonic Crystals: Molding the Flow of Light*. Princeton: Princeton Univ. Press, 2008.

[2] K. Yasumoto, Ed., *Electromagnetic Theory and Applications for Photonic Crystals*, New York: CRC Press, Taylor & Francis, 2005.

[3] E. Ozbay, B. Temelkuran, and M. Bayindir, "Microwave applications of photonic crystals", *Progress in Electromag. Res.*, vol. 41, pp. 185–209, 2003.

[4] H.-H. Xie, Y.-C. Jiao, K. Song, and Z. Zhang, "A novel multi-band electromagnetic band-gap structure", *Progress in Electromag. Res. Lett.*, vol. 9, pp. 67–74, 2009.

[5] F. Yang and Y. Rahmat-Samii, *Electromagnetic Band Gap Structures in Antenna Engineering*. New York: Cambridge University Press, 2009.

[6] H. Li and X. Yang, "Larger absolute band gaps in two-dimensional photonic crystals fabricated by a three-order-effect method", *Progress in Electromagn. Res.*, vol. 108, pp. 385–400, 2010.

[7] F. Frezza, L. Pajewski, E. Piuzzi, C. Ponti, and G. Schettini, "Design and fabrication of a 3D-EBG superstrate for patch antennas", in *Proc. 39th Eur. Microwave Conf. EuMC 2009*, Rome, Italy, 2009, pp. 1496–1499.

[8] F. Frezza, L. Pajewski, E. Piuzzi, C. Ponti, and G. Schettini, "Analysis and experimental characterization of an alumina woodpile-covered planar antenna", in *Proc. 40th Eur. Microwave Conf. EuMC 2010*, Paris, France, 2010, pp. 200–203.

[9] V. Jandieri, K. Yasumoto, and Y.-K. Cho, "Rigorous analysis of electromagnetic scattering by cylindrical EBG structures", *Progress in Electromag. Res.*, vol. 121, pp. 317–342, 2011.

[10] J.-Y. Chen, E. Li, and L.-W. Chen, "Optical absorption enhancement in solar cells via 3D photonic crystal structures", *Progress in Electromag. Res. M*, vol. 17, pp. 1–11, 2011.

[11] F. Guller, M. E. Inchaussandague, and R. A. Depine, "Dispersion relation and band gaps of 3D photonic crystals made of spheres", *Progress in Electromag. Res. M*, vol. 19, pp. 1–12, 2011.

[12] D. M. Nashaat Elsheakh, H. A. Elsadek, E. A.-F. Abdallah, H. M. El-Henawy, and M. F. Iskander, "Ultra-wide bandwidth microstrip monopole antenna by using electromagnetic band-gap structures", *Progress in Electromag. Res. Lett.*, vol. 23, pp. 109–118, 2011.

[13] F. Frezza, L. Pajewski, E. Piuzzi, C. Ponti, and G. Schettini, "Advances in EBG-resonator antenna research", *Proc. Int. Symp. on Antennas and Propag. ISAP 2012*, Nagoya, Japan, 2012, pp. 1301–1304.

[14] S. Ceccuzzi, L. Pajewski, C. Ponti, and G. Schettini, "Directive propagation in two EBG structures: a comparison", in *IEEE MTT-S Int. Microwave Symp. Digest IMS 2013*, Seattle, WA, USA, 2013, pp. 1–4 (doi: 0.1109/MWSYM.2013.6697579).

[15] S. Ceccuzzi, L. Pajewski, C. Ponti, and G. Schettini, "Comparison between two methods for directivity enhancement of antennas through 2-D EBGs", in *Proc. 34th Progress in Electromag. Res. Symp. PIERS 2013*, Stockholm, Sweden, 2013, pp. 557–561.

[16] F. Frezza, L. Pajewski, E. Piuzzi, C. Ponti, and G. Schettini, "Radiation-enhancement properties of an X-band woodpile EBG and its application to a planar antenna", *Int. J. on Antenn. and Propag.*, vol. 2014, article ID 729187, pp. 1–15, 2014 (doi: 10.1155/2014/72918).

[17] S. Ceccuzzi, L. Pajewski, C. Ponti, and G. Schettini, "Directive EBG antennas: a comparison between two different radiating mechanisms", *IEEE Trans. on Antenn. and Propag.*, vol. 62, no. 10, pp. 5420–5424, 2014 (doi: 10.1109/TAP.2014.2346174).

[18] A. O. Silva, R. Bertholdo, M. G. Schiavetto, B.-H. V. Borges, S. J. L. Ribeiro, Y. Messaddeq, and M. A. Romero, "Comparative analysis between experimental characterization results and numerical FDTD modeling of self-assembled photonic crystals", *Progress in Electromag. Res. B*, vol. 23, pp. 329–342, 2010.

[19] V. A. Tolmachev, V. Baldycheva, K. Berwick, and T. S. Perova, "Influence of fluctuations of the geometrical parameters on the photonic band gaps in one-dimensional photonic crystals", *Progress in Electromag. Res.*, vol. 126, pp. 285–302, 2012.

[20] H.-T. Hsu, M.-H. Lee, T.-J. Yang, Y.-C. Wang, and C.-J. Wu, "A multichanneled filter in a photonic crystal containing coupled defects", *Progress in Electromag. Res.*, vol. 117, pp. 379–392, 2011.

[21] H. Butt, Q. Dai, T. D. Wilkinson, and G. A. J. Amaratunga, "Photonic crystals and metamaterial filters based on 2D arrays of silicon nanopillars", *Progress in Electromag. Res.*, vol. 113, pp. 179–194, 2011.

[22] C.-J. Wu and Z.-H. Wang, "Properties of defect modes in one-dimensional photonic crystals", *Progress in Electromag. Res.*, vol. 103, pp. 169–184, 2010.

[23] A. Gharaati and H. Azarshab, "Characterization of defect modes in one-dimensional ternary metallo-dielectric nanolayered photonic crystal", *Progress in Electromag. Res. B*, vol. 37, pp. 125–141, 2012.

[24] K. R. Khan, S. Bidnyk, and T. J. Hall, "Tunable all optical switch implemented in a liquid crystal filled dual-core photonic crystal fiber", *Progress in Electromag. Res. M*, vol. 22, pp. 179–189, 2012.

[25] F. Frezza, L. Pajewski, and G. Schettini, "Periodic defects in 2D-PBG materials: full-wave analysis and design", *IEEE Trans. on Nanotechnol.*, vol. 2, no. 3, pp. 126–134, 2003.

[26] F. Frezza, L. Pajewski, and G. Schettini, "Numerical investigation on the filtering behavior of 2D-PBGs with multiple periodic defects", *IEEE Trans. on Nanotechnol.*, vol. 4, no. 6, pp. 730–739, 2005.

[27] F. Frezza, L. Pajewski, and G. Schettini, "Characterization and design of two-dimensional electromagnetic band-gap structures by use of a full-wave method for diffraction gratings", *IEEE Trans. on Microw. Theory and Techniq.*, vol. 51, no. 3, pp. 941–951, 2003.

[28] L. Pajewski, R. Borghi, G. Schettini, F. Frezza, and M. Santarsiero, "Design of a binary grating with subwavelength features that acts as a polarizing beam splitter", *Applied Optics*, vol. 40, no. 32, pp. 5898–5905, 2001.

[29] R. Borghi, F. Frezza, L. Pajewski, M. Santarsiero, and G. Schettini, "Full-wave analysis of the optimum triplicator", *J. of Electromag. Waves and Appl.*, vol. 15, no. 6, pp. 689–708, 2001.

[30] R. Borghi, F. Frezza, L. Pajewski, M. Santarsiero, and G. Schettini, "Optimum even-phase four-beam multiplier", *Optical Engin.*, vol. 41, no. 11, pp. 2736–2742, 2002.

[31] F. Frezza, L. Pajewski, and G. Schettini, "Fast and accurate modeling of finite-thickness 2D-EBG structures made by circular-section rods", *Microw. and Optical Technol. Lett.*, vol. 39, no. 6, pp. 433–437, 2003.

[32] F. Frezza, L. Pajewski, and G. Schettini, "Fractal two-dimensional electromagnetic band-gap structures", *IEEE Trans. on Microw. Theory and Techniq.*, vol. 52, no. 1, pp. 220–227, 2004.

[33] F. Frezza, L. Pajewski, and G. Schettini, "Full-wave characterization of three-dimensional photonic bandgap structures", *IEEE Trans. on Nanotechnol.*, vol. 5, no. 5, pp. 545–553, 2006.

[34] M. Veysi and M. Shafaee, "EBG frequency response tuning using an adjustable air-gap", *Progress in Electromag. Res. Lett.*, vol. 19, pp. 31–39, 2010.


**Giuseppe Schettini** received the Laurea (cum laude) degree in Electronic Engineering, the Ph.D. degree in Applied Electromagnetics, and the Laurea (cum laude) degree in Physics from the La Sapienza University of Rome, Rome, Italy, in 1986, 1991, and 1995, respectively. He joined the Italian Energy and Environment Agency,

where he was initially involved in free electron generators of millimeter waves and then in microwave components and antennas for the heating of thermonuclear plasmas. In 1992, he joined the La Sapienza University of Rome as a Researcher of Electromagnetics. In 1998, he joined the Applied Electronics Department, now Department of Engineering, of Roma Tre University, Rome, where he was an Associate Professor, from 1998 to 2005, and has been a Full Professor of Electromagnetic Fields and Antennas, since 2005. His current research interests include structures for guiding and radiation of electromagnetic fields for microwave and millimeter waves applications, scattering, diffractive optics, plasma heating and current drive, artificial electromagnetic bandgap media, and anisotropic media.

E-mail: giuseppe.schettini@uniroma3.it
Roma Tre University
Via Vito Volterra 60-62
00146 Rome, Italy

**Lara Pajewski** – for biography, see this issue, p. 29.

Paper

# Experimental Analysis of a Directive Antenna with a 3D-EBG Superstrate

Lara Pajewski[1], Fabrizio Frezza[1], Marian Marciniak[2], Emanuele Piuzzi[1], and Giorgia V. Rossi[3]

[1] *Department of Information Engineering, Electronics and Telecommunications, Sapienza University of Rome, Rome, Italy*
[2] *National Institute of Telecommunications, Warsaw, Poland*
[3] *Imperial College London, London, United Kingdom*

https://doi.org/10.26636/jtit.2017.120017

**Abstract—A three-dimensional electromagnetic crystal is employed as a directivity-enhancing superstrate for planar antennas. The crystal is a woodpile made of alumina rods. In a shielded anechoic chamber, the performance of a patch antenna covered with the woodpile is measured. The superstrate is positioned at different distances from the antenna and its orientation is varied in the 8–12 GHz frequency range. The return loss, gain and radiation pattern in the E- and H-planes are measured. The electromagnetic behavior of Fabry-Perot cavities with woodpile mirrors, equivalent to the compound radiator, is also studied. The main effect of the crystal on the antenna performance is an enhancement of about 10 dB in maximum gain. A rather complete series of experiments is presented, highlighting the role of the periodic structure in the directivity enhancement and allowing a deeper understanding of the electromagnetic phenomena involved in EBG resonator antennas. Benefits and disadvantages of this kind of antennas are discussed and ideas for future research are given.**

***Keywords—directivity enhancement, electromagnetic bandgap materials, Fabry-Perot cavities, periodic structures, woodpile.***

## 1. Introduction

Electromagnetic band gap (EBG) materials [1] can be successfully employed to improve the performance of antennas [2], [3]. When used as planar reflectors [4], substrates [5], or high-impedance ground-planes [6], are able to eliminate the drawbacks of conducting ground-planes, to prevent the propagation of surface waves also allowing a lowering of the antenna profile, and to improve the radiation efficiency. In EBG resonator antennas [7]–[11], an electromagnetic crystal is employed as a superstrate on a primary radiator, backed with a ground plane, and its main effect is a considerable increase in the directivity. Else, it is possible to obtain a highly-directive antenna by embedding a source in an EBG working near its band gap [12], thanks to the limited angular propagation allowed within the crystal. Recently, these two different methods for antenna-directivity enhancement were compared, with reference to several optimized two-dimensional configurations based on either square or triangular lattices of dielectric rods [13].

Several research teams have been studying the EBG resonator antenna as a possible solution to be adopted when a directive beam is needed. This is an interesting alternative to aperture antennas and antenna arrays, free of some problems inherent to the usual directive systems, such as the size of the focal structures and the limitations/complications induced by the feeding circuit of arrays.

In EBG resonator antennas, the periodic cover is placed at a distance equal to an integer multiple of half a wavelength from the source. Forward radiation can be remarkably enhanced by means of in-phase multiple reflections. A single feed is usually employed, allowing the gain to be increased with low complexity. In some cases [14], arrays of patches or horns were used as sources. Systems operating at different frequencies, ranging from the microwave region to millimeter waves, can be designed and realized. Electromagnetic crystals with one, two or three periodicity directions can be employed as superstrates.

In [15], the characteristics of directivity enhancement using EBGs, frequency-selective surfaces and left-handed metamaterials were compared. A Fabry-Perot cavity can be used as a cover, in spite of a single EBG superstrate [14]. Usually, the cover is a planar structure. In [16], a dipole source embedded in a cylindrical EBG was studied, by using a rigorous semi-analytical method, and the performances of the compound antenna were numerically investigated for three different EBG configurations as well as varying the dipole position inside the periodic structure.

In this paper, we use a woodpile cover to increase the gain of a microstrip-patch antenna. The woodpile is a three-dimensional (3D) EBG with a rather simple geometry, that may present complete 3D stop-bands [17], [18]. It consists of a stack of dielectric rods with alternating orthogonal orientations. The cross-section of the rods may be rectangular or circular, or else air cylindrical holes may be drilled in a dielectric sample. A woodpile with square-section rods is often preferred, because easier to fabricate.

The aim of our paper is to complement the work published in [11], by presenting several new experimental results. These results highlight the role of the periodic superstrate in the directivity enhancement and we believe that they al-

low researchers interested in EBG resonator antennas to achieve a deeper understanding of the electromagnetic phenomena involved in this kind of structures. It is worth noting that experimental works at microwave frequencies, regarding the use of EBGs in antenna engineering, are not so frequent. In most of the published papers numerical results of simulations are reported.

In Section 2, proposed EBG resonator antenna is described. We designed a woodpile, with a complete band gap centered on $f = 12$ GHz and extending over almost 4 GHz [19]. The design was carried out by using an in-house code that implements the Fourier Modal Method (FMM) [20]. Woodpile samples were fabricated, by means of alumina rods with square cross-section [11]. A rectangular patch antenna was realized, resonating at 10.3 GHz. A supporting structure was specifically designed and realized, to hold the antenna together with its woodpile cover during experimental investigations.

Section 3 is devoted to numerical results. In a shielded anechoic chamber, in the 8–12 GHz frequency range, the return loss, gain, and radiation pattern were measured in the E- and H-planes, of the compound antenna. The superstrate was positioned at different distances from the patch and its orientation was varied. The electromagnetic behavior of woodpile Fabry-Perot cavities, equivalent to the EBG resonator antenna, was also measured.

Conclusions are drawn in Section 4, where benefits and disadvantages of the EBG resonator antenna are also discussed, new applications of these radiators are suggested and ideas for future research are given.

## 2. The EBG Resonator Antenna

A woodpile crystal was synthesized, by using an in-house code implementing the FMM, a full-wave approach that solves the monochromatic plane-wave scattering problem by dielectric finite-thickness crossed gratings, as proposed in [20]. The design is described in [19] and resumed in [11], where the electromagnetic behavior of the proposed woodpile is also analyzed.

The crystal consists of four periodic layers of alumina rods, with square section having side length $w = 3.18$ mm. The relative dielectric constant of the rods is $\varepsilon_{r,al} = 9.8$. The spacing of each layer is $d = 8$ mm. Rods belonging to consecutive layers are orthogonal. In the third and fourth layers, the rods have the same orientation as in the first and second ones, respectively, but they are in offset by half of the horizontal spacing (see Fig. 1). We used the above-mentioned FMM code to simulate a monochromatic plane-wave with electric/magnetic field parallel to the rods impinging normally on this crystal. Results show that there is a band gap centered on $f = 12$ GHz, extending over almost 4 GHz. By studying the off-plane behavior of the woodpile, we found that the band gap is scarcely sensitive to variations of the electromagnetic-field incidence and polarization. Only a slight reduction in depth and width of the band gap occurs, when these parameters are changed.

Two identical woodpile samples were realized. The rod length is 20 cm, that is almost seven wavelengths at 10 GHz, and is equal to $25d$. This ensures that the sample behavior is close to that of an electromagnetic crystal with rods of infinite length and with an infinite number of periods in both the directions of the rod axes. The diameter tolerance of the rods is $\pm 3\%$, their straightness is represented by a camber/length parameter $\leq 0.003$, and the maximum twist is $2^{o}$ per 30.48 cm. For more details about the woodpile fabrication see [11].

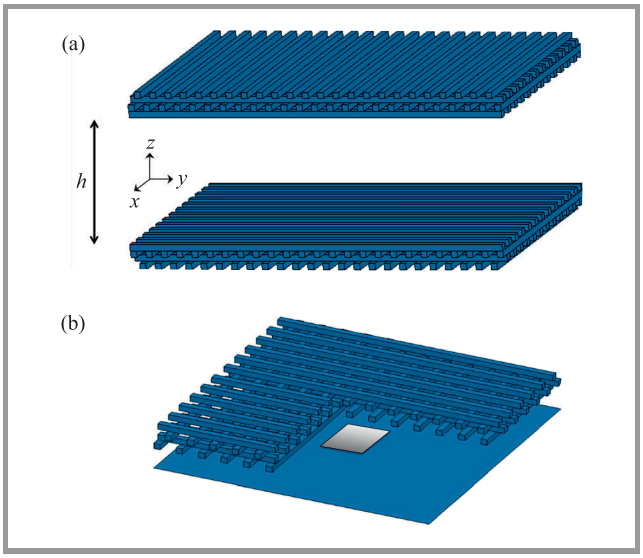


***Fig. 1.*** Woodpile cavity (a), woodpile-covered antenna (b).

We realized a microstrip antenna, from a 0.76 mm thick Rogers/RT Duroid 5870 laminate (relative permittivity 2.33), printed on both sides with 36-$\mu$m thick copper. With a PC-controlled milling table, on one side of the layer a $8 \times 8.4$ mm rectangular patch was cut. The antenna is fed from below by a coaxial probe (SMA connector). The feed point, where the probe is attached to the patch, is centered with respect to the shorter side of the patch, and it is 1.2 mm away from the centre of the longer side.

A PVC table and a teflon-PVC support were designed and realized, to hold the couple of woodpile samples, or the antenna and a woodpile, during experimental investigations.

## 3. Experimental Results

All the experiments were performed in a $3.20 \times 3.20 \times 2.70$ m shielded anechoic chamber, by using a HP 8530 vector network analyzer. We analyze the electromagnetic behavior of Fabry-Perot cavities with woodpile mirrors, changing the cavity length and the field polarization (Subsection 3.1). We subsequently study the performances of the woodpile-covered patch, changing the distance between the antenna and the EBG cover, and the field polarization (Subsections 3.2–3.4). As many results are reported, it is possible to appreciate the consistence of the experimental

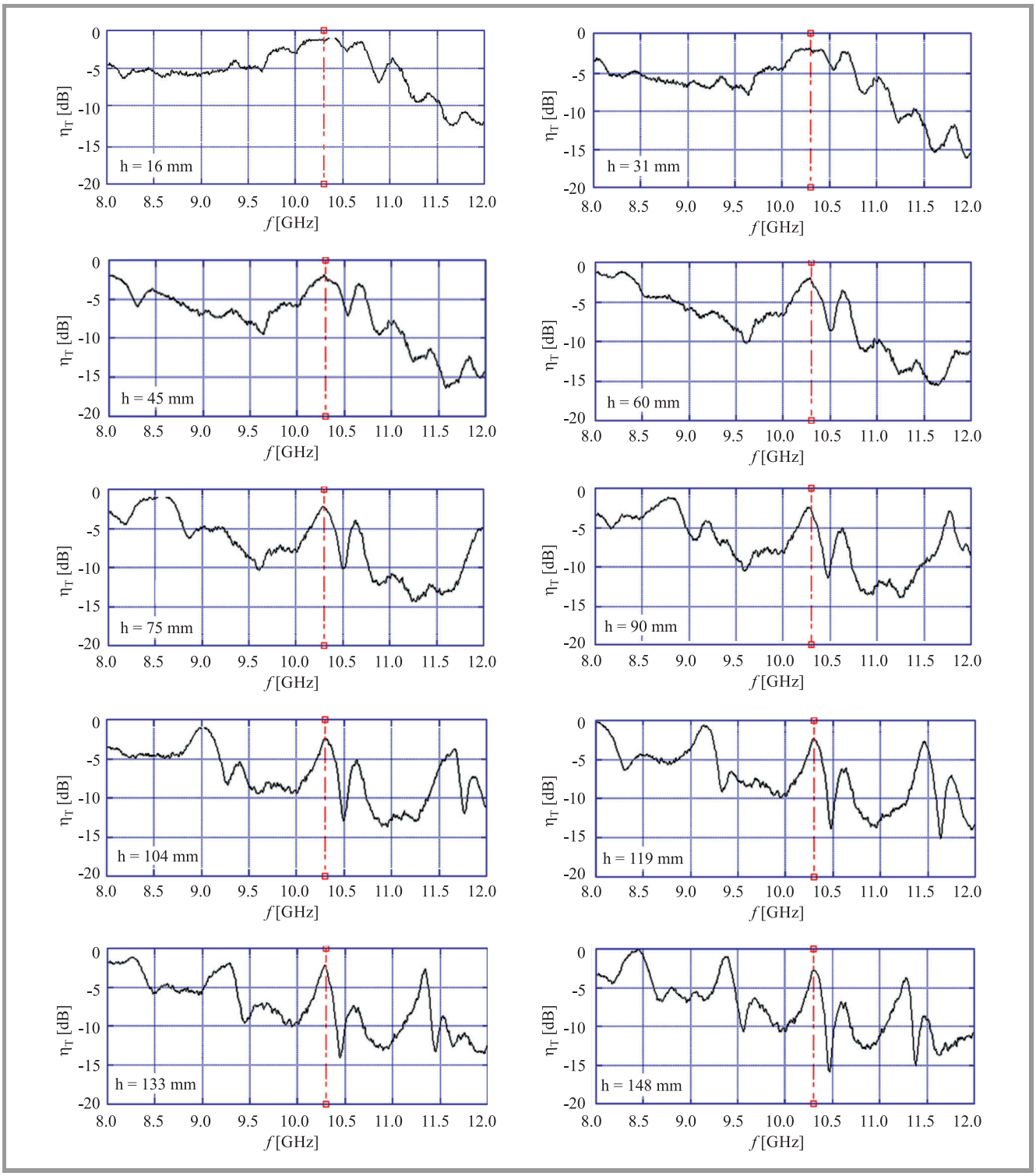


***Fig. 2.*** Transmission efficiency of the cavity, $\eta_T$, as a function of frequency, for ten different cavities resonating at 10.3 GHz; the electric field is parallel to the internal rods of the woodpile cavity.

data we collected. Moreover, one may achieve a general understanding of the electromagnetic behavior of the considered devices. The effects of the cavity length and of the field polarization on the overall performance of the EBG resonator antenna are clearly pointed our. A sketch of both the Fabry-Perot cavity and the woodpile-patch is reported in Fig. 1.

As a preliminary experiment, we measured the reflection parameter, the gain, and the radiation diagram in the E- and H-planes, of the patch antenna introduced in Section 2. This antenna resonates at 10.3 GHz. At this frequency, the magnitude of its return loss is $|S_{11}| = -11.69$ dB. By using, as a standard transmitter, a horn antenna with a maximum gain equal to 16 dB and a standing-wave ratio (SWR) equal

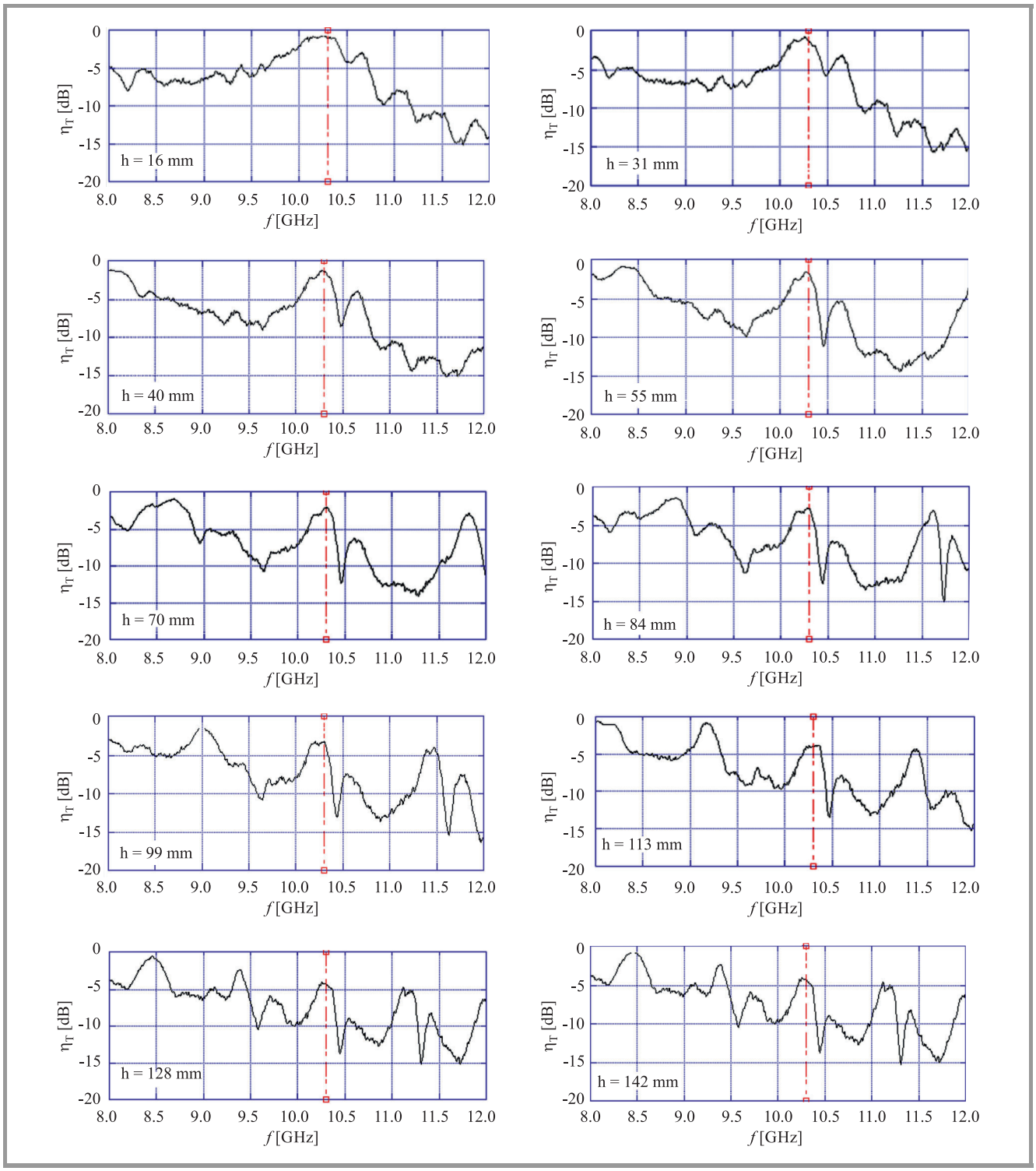


***Fig. 3.*** Transmission efficiency of the cavity, $\eta_T$, as a function of frequency, for ten different cavities resonating at 10.3 GHz; the electric field is orthogonal to the internal rods of the woodpile cavity.

to 1.25, we found that the maximum gain of our patch antenna is $G_\mathrm{p} = 6.18$ dB.

### *3.1. Fabry-Perot Cavity with Woodpile Mirrors*

We performed a series of measurements on a Fabry-Perot cavity with woodpile mirrors. The adopted setup consisted of a couple of X-band precision pyramidal horn antennas, placed one in front of the other, with both the woodpile samples in the middle. The samples were placed at a distance $h$ from each other and held by the PVC/Teflon support.

This structure resonates when its equivalent length $L_\mathrm{eq}$ is an integer multiple of $\frac{\lambda}{2}$, where $\lambda$ is the wavelength of the

electromagnetic field in air. The cavity may also be considered as an EBG with a break of its periodicity, in which some periodic layers are replaced by a homogeneous air-region with thickness $h$: the main effect of creating a defect in a band-gap structure, is the occurrence of transmission peaks inside the prohibited bands [21], [22].

We identified a set of cavities with different lengths and showing a transmission peak at 10.3 GHz (resonance frequency of proposed patch antenna). We considered different polarization states of the electromagnetic field (electric field parallel or orthogonal to the most internal rods of the cavity).

In order to comply with the frequency band of the horn antennas, measurements were performed in the 8–12 GHz range. The distance between the horns was chosen after a series of preliminary experiments aimed at ensuring a good compromise between the planarity of the wavefront impinging on the woodpile and the diffraction effects due to the finite extension of the samples.

The cavity transmission properties were determined from the measured $S_{21}$ scattering parameter. Its magnitude is equal to the transmission efficiency of the cavity.

A preliminary reference calibration was performed with no sample placed between the two horns. Upon completion of each experimental session a further measurement was performed removing again the woodpile samples, to check that the drift in the measurement system was within acceptable levels.

In Fig. 2, the measured transmission efficiency $\eta_T$ is plotted as a function of frequency, for ten different cavities resonating at 10.3 GHz. In all those measurements, the electric field was parallel to the rods of the woodpile layers nearest to the air region inside the cavity. It is noted that in longer cavities a higher number of transmission peaks occurs within the considered frequency range, as expected. Accordingly, the peak centered in 10.3 GHz has a higher quality factor when the cavity is longer. It is also noted that, in all the studied cases (i.e. for all values of the cavity length), the transmission peaks occurring at lower frequencies show a higher efficiency. This is an expected phenomenon and is due to the fact that, when the wavelength of the electromagnetic field is longer, the thickness of the woodpile mirrors is electrically smaller, hence the propagation through the mirrors causes smaller losses.

In Fig. 3, the same as in Fig. 2 is shown, for ten different cavities with electric field orthogonal to the most internal rods of the cavity. Similar comments apply. It can be appreciated that the equivalent length of a woodpile cavity is highly dependent on the electromagnetic field polarization with respect to the EBG orientation. In this regard, please also see [11], where we presented simulation results showing that the periodic arrangement of bars perpendicular to the electric field has a negligible effect on the transmission efficiency through the whole structure.

### *3.2. Return Loss of the Woodpile-covered Patch Antenna*

According to the image theory, a configuration equivalent to the Fabry-Perot woodpile cavity is obtained, if the cavity is halved, with respect to its symmetry plane, by means of a perfectly conducting surface. If the ground plane of a patch antenna is employed instead of a perfectly conducting surface, an EBG resonator antenna is built (see Fig. 1b).

The measurements we performed on the woodpile-covered patch antenna include return loss, gain, and radiation patterns in the E- and H- planes. In this Subsection, return-loss results are reported.

For return-loss measurements, an Agilent E8363B performance network analyzer was used, which was preliminarily calibrated at the port by means of a short-open-load procedure, employing the 85052B mechanical calibration kit.

The superstrate was positioned at various distances $\frac{h}{2}$ from the patch, corresponding to half length of the cavities resonating at 10.3 GHz. We verified that achieving a good parallelism between the ground-plane and the woodpile is very important to maximize the performances of the compound antenna. Moreover, we observed that a woodpile shift, parallel to the ground plane, does not affect the behavior of the radiator. The orientation of the superstrate, instead, is very important, as in woodpile cavities.

In Figs. 4 and 5, the return loss of the woodpile-covered patch antenna is presented. In particular, in Fig. 4 ten different values of $\frac{h}{2}$ are considered and the woodpile rods nearest to the ground plane are parallel to the electric field radiated by the patch. Figure 5 is analogous to Fig. 4, but now the rods nearest to the ground plane are orthogonal to the electric field. For the return loss of the patch alone, see Fig. 15 in [11].

In all the examined cases, we observed that the EBG superstrate does not significantly affect the antenna matching. However, we found that when the equivalent distance between the woodpile and the patch is roughly equal to an integer multiple of $\frac{\lambda}{2}$ (as in the right-column plots of Figs. 4 and 5), the effect of the EBG over the $|S_{11}|$ frequency trend is stronger than it is when the above-mentioned equivalent distance is an odd integer multiple of $\frac{\lambda}{4}$ (as in the left-column plots of Figs. 4 and 5). This happens because in the former case (right-column plots) the multiple reflections between the antenna and the superstrate are summed in phase. Hence their overall effect on the return loss is more pronounced, whereas in the latter case (left-column plots) the multiple reflections are in phase opposition to each other and their overall effect on the return loss is totally negligible.

### *3.3. Gain of the Woodpile-covered Patch Antenna*

Gain and radiation pattern measurements were performed with a setup similar to the one described for cavity characterization. In particular, the receiving horn antenna was replaced by the patch antenna, which was positioned on a remotely controlled turntable. The distance between the two antennas was chosen to be 1 m, in order to be in the

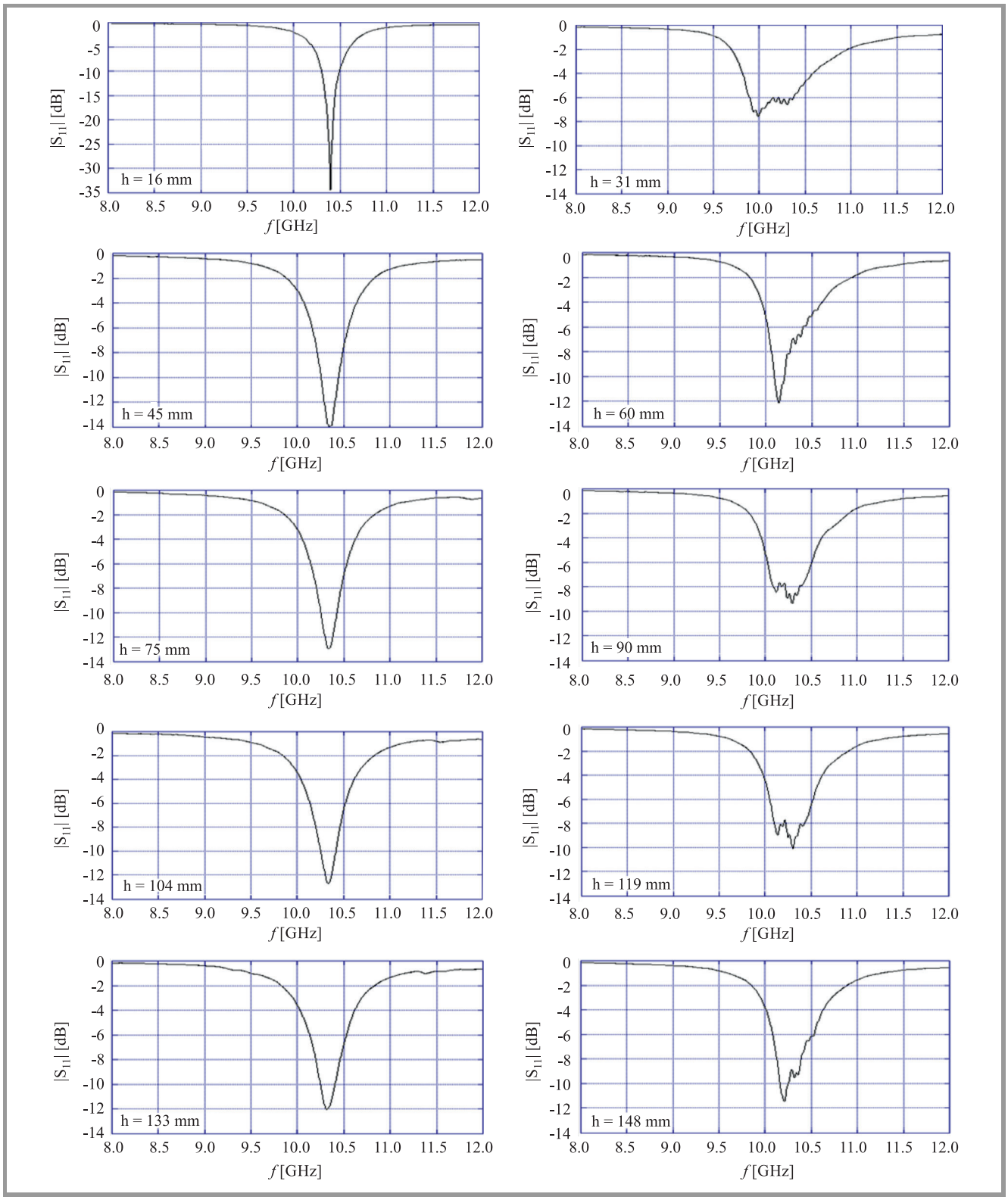


***Fig. 4.*** Return loss of the woodpile-covered patch antenna, vs. frequency. Ten different values of the distance $\frac{h}{2}$ between patch and woodpile are considered. The woodpile rods nearest to the ground plane are parallel to the electric field radiated by the patch.

far field of the radiators. The setup was preliminarily subjected to a reference calibration with the microstrip antenna replaced by the second standard gain horn. In this Subsection, gain results are presented.

In Fig. 6, the maximum gain of the woodpile-covered patch antenna, $G_{\mathrm{pw}}$, normalized to the maximum gain of the patch alone, $G_{\mathrm{p}}$, is plotted as a function of frequency, for the same woodpile orientation and $\frac{h}{2}$ distances studied

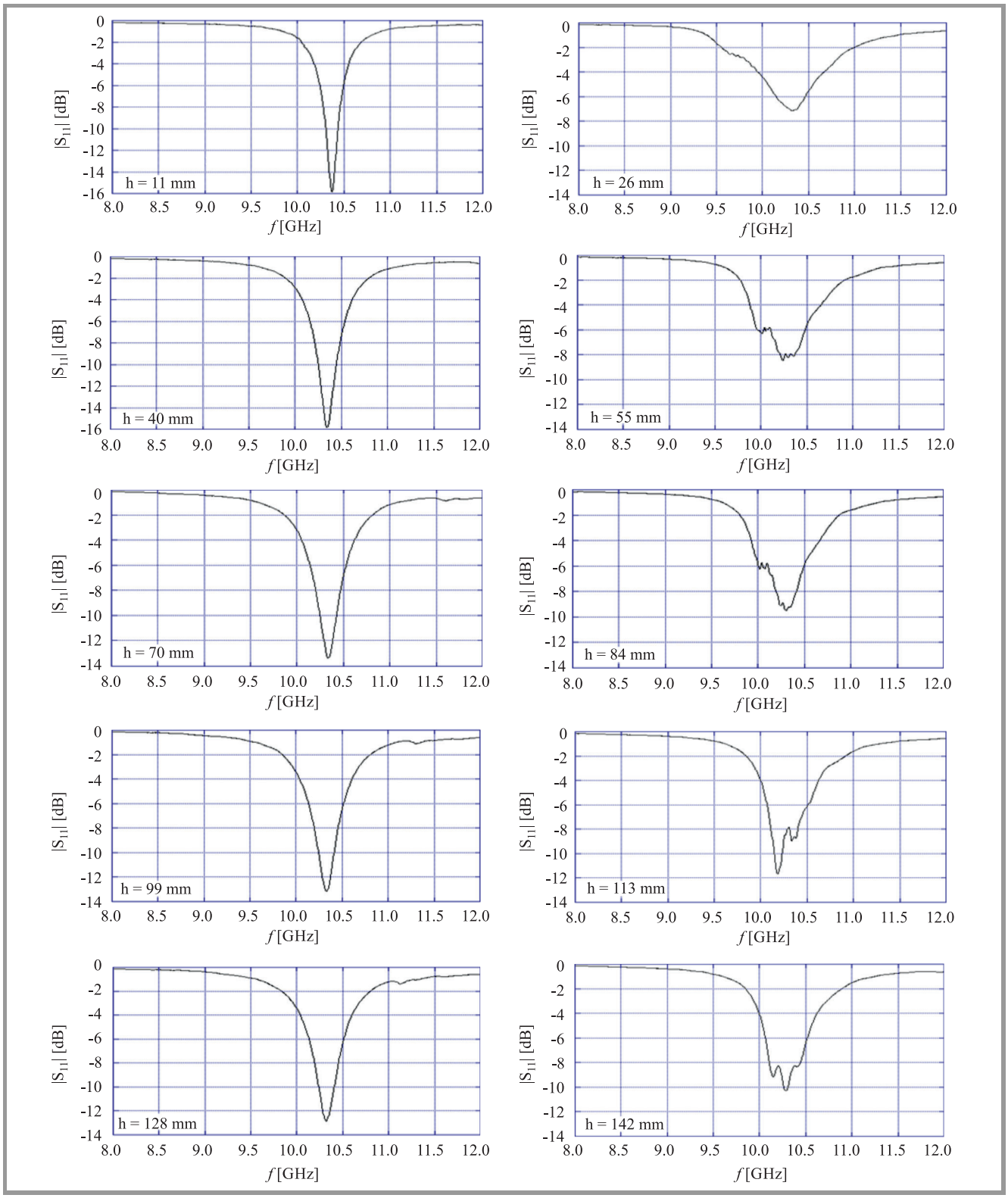


***Fig. 5.*** Return loss of the woodpile-covered patch antenna, vs. frequency. Ten different values of the distance $\frac{h}{2}$ between patch and woodpile are considered. The woodpile rods nearest to the ground plane are orthogonal to the electric field radiated by the patch.

in Fig. 4. When the equivalent distance between the woodpile and the patch is roughly equal to an integer multiple of $\frac{\lambda}{2}$, as in the right column of the figure, the maximum gain enhancement due to the woodpile occurs at 10.3 GHz. The multiple reflections are present between the antenna and the superstrate, and they are summed in phase at the interface between air and woodpile. Instead, when the above-mentioned equivalent distance is an odd integer multiple

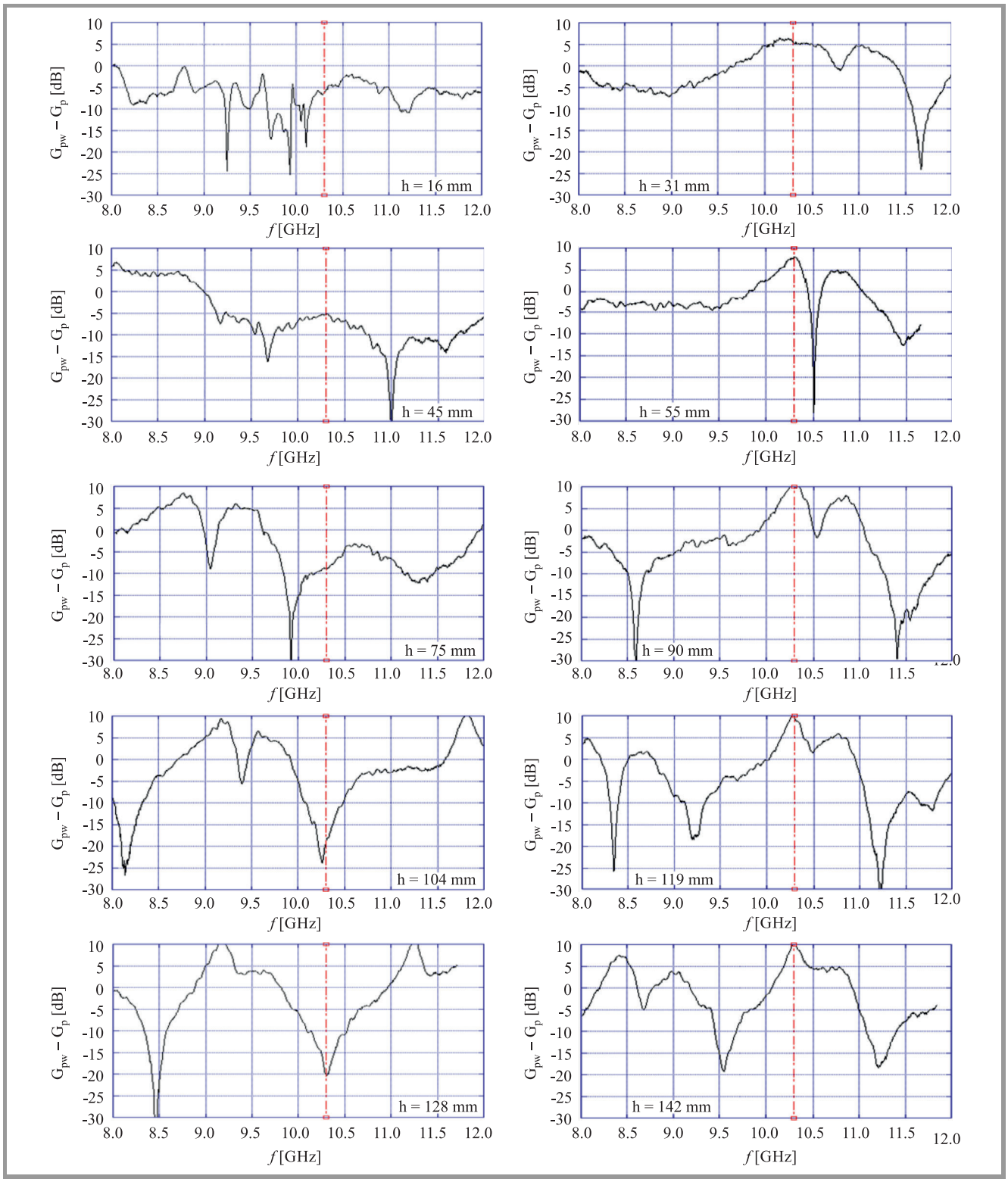


***Fig. 6.*** Maximum gain of the woodpile-covered patch antenna, $G_{pw}$, normalized to the maximum gain of the patch alone, $G_p$, in decibels, vs. frequency; the distance $\frac{h}{2}$ assumes ten different values, the woodpile bars nearest to the ground plane are parallel to the electric field radiated by the patch.

of $\frac{\lambda}{4}$, as in the left column of the figure, at 10.3 GHz the effect of the woodpile is a strong reduction of the gain. The multiple reflections arrive at the woodpile in phase opposition to each other.

Similar results were collected for the configurations with the bars nearest to the ground plane parallel or orthogonal to the electric field, as can be appreciated by comparing Fig. 6 with Fig. 7.

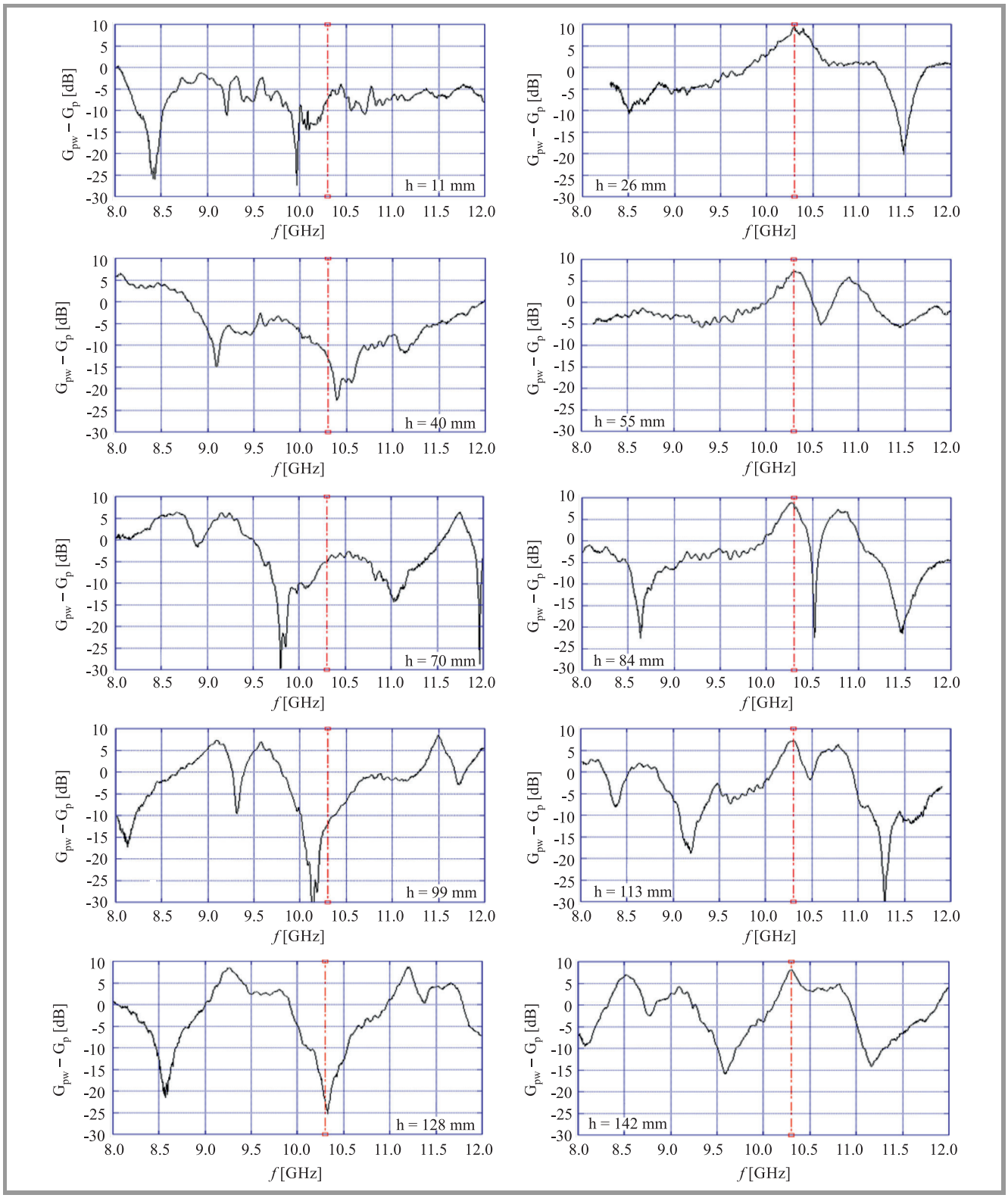


***Fig. 7.*** Maximum gain of the woodpile-covered patch antenna, $G_{pw}$, normalized to the maximum gain of the patch alone, $G_p$, in decibels, vs. frequency; the distance $\frac{h}{2}$ assumes ten different values, the woodpile bars nearest to the ground plane are orthogonal to the electric field radiated by the patch.

The gain enhancement at 10.3 GHz turns out to be equal to about 10 dB, regardless of the distance between patch and woodpile. Note that, in some cases, we measured a smaller gain enhancement. This is due to the fact that achieving a good parallelism between the ground plane and the woodpile is extremely important for maximizing the per-

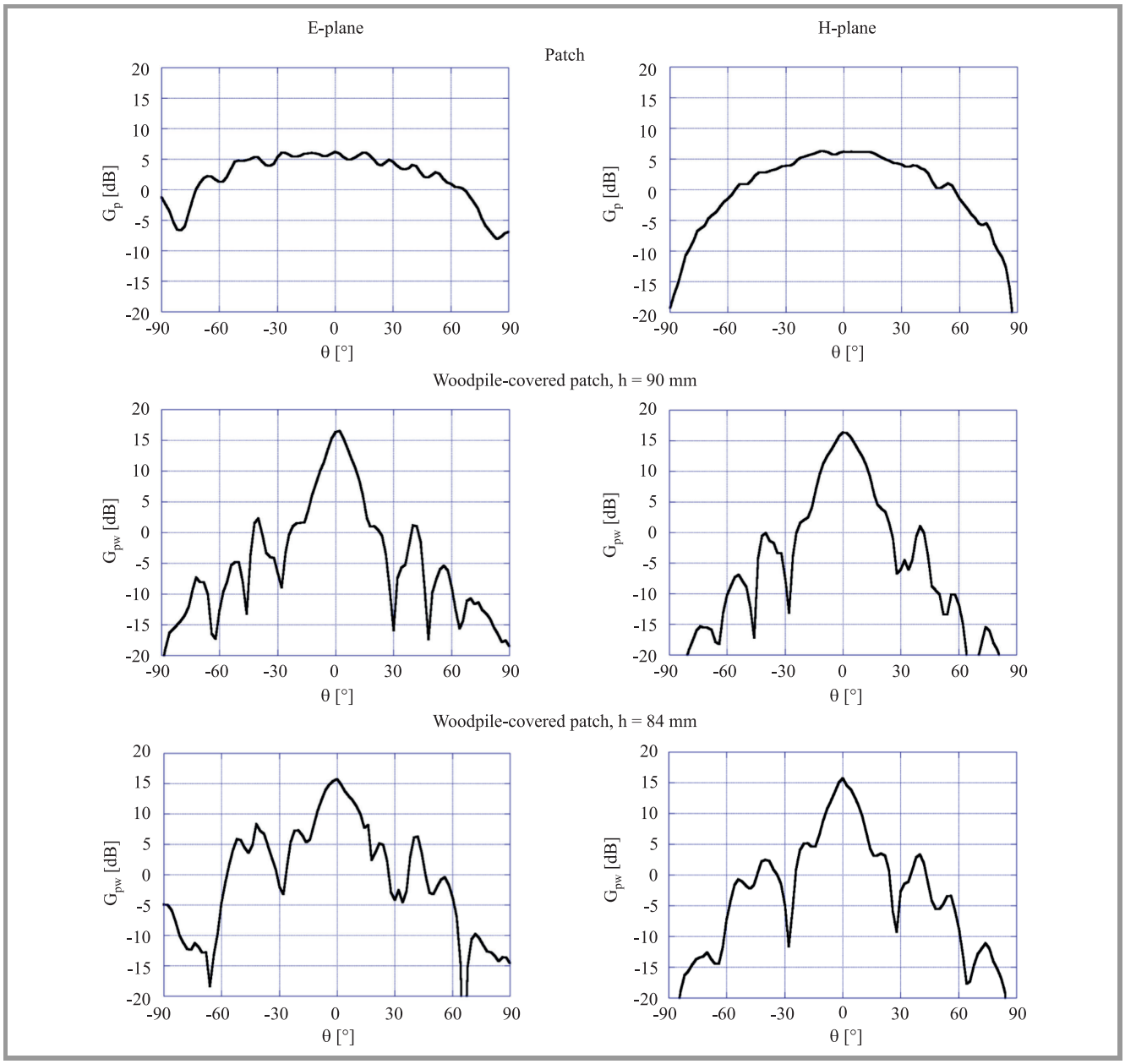


***Fig. 8.*** E- and H-plane radiation pattern for the patch alone, for the woodpile-covered patch with $h = 90$ mm (configuration studied in Fig. 6), and for the woodpile-covered patch with $h = 84$ mm (configuration studied in Fig. 7), at 10.3 GHz.

formance of the compound antenna, but unfortunately we do not have the necessary experimental means for checking and optimizing the parallelism.

### *3.4. Radiation Pattern of the Woodpile-covered Patch Antenna*

We finally measured the E- and H-plane radiation patterns of the woodpile-covered patch antenna at 10.3 GHz. In Fig. 8, a couple of examples are reported. In particular, we present results for the patch alone, for the woodpile-covered patch with $h = 90$ mm (configuration studied in Fig. 6), and for the woodpile-covered patch with $h = 84$ mm (configuration studied in Fig. 7). Data were recorded every 2°. The directivity enhancement due to the presence of the EBG cover can be easily appreciated.

## 4. Conclusions

This work dealt with EBG resonator antennas. A woodpile was used for directivity-enhancing of a linearly-polarized rectangular-patch antenna. The compound radiating system was experimentally characterized in the 8–12 GHz frequency range, in a shielded anechoic chamber, by using a vector network analyzer.

The EBG superstrate was designed by using an in-house code implementing the Fourier Modal Method. Two wood-

pile samples were fabricated, by means of alumina rods with square cross-section. Moreover, a rectangular patch antenna was realized.

First, the transmission properties of Fabry-Perot resonators with woodpile mirrors were measured. The cavity length and the orientation of the mirrors were varied. In particular, we looked for configurations resonating at 10.3 GHz, i.e. at the resonance frequency of the patch antenna.

Subsequently, the return loss, the gain, and the radiation pattern in the E- and H-planes were measured, for the patch antenna covered with the woodpile. The superstrate was positioned at different distances from the antenna and its orientation was varied. In order to obtain a directivity enhancement the equivalent distance between the woodpile and the antenna had to be an integer multiple of $\frac{\lambda}{2}$. With such setup, the presence of the EBG superstrate above the patch determined an enlargement of the source equivalent-aperture area, resulting in highly directive radiation. The gain of the woodpile-covered patch turned out to be about 10 dB higher than the gain of the patch alone. Similar results were obtained for configurations with the bars nearest to the patch parallel or orthogonal to the electric field. In all the examined cased, the periodic superstrate did not significantly affect the antenna matching.

An interesting feature of this kind of radiating systems is that they are more compact than classical highly-directive antennas. Moreover, they can be excited by a single feeding device. Note that achieving a high directivity by means of an array of sources is more expensive. Also that typically an array has a highly resonant matching.

From our results it is evident that, once the distance between ground-plane and woodpile is fixed, there are different resonance frequencies at which the gain enhancement occurs. This suggests that a number of primary radiators, working at appropriate frequencies, may benefit from the same superstrate to increase their directivity.

We also observed that the resonance frequency of the compound antenna strongly depends on the source polarization, and rods orthogonal to the electric-field direction have a very little influence on the antenna performances. Hence, orthogonal radiators might exploit different layers of the same EBG cover. This means that it is possible to design a device generating or receiving two orthogonal uncoupled linear polarization states, with high directivity, or else, a device allowing an easy control of the polarization of the emitted or received field.

Further ideas for future work include: the design and realisation of EBG resonator antennas with low-thickness superstrates, in order to reduce the radiating-system size or, with monolithic superstrates, easier to implement with respect to a woodpile and less fragile; else, with low-permittivity and low-cost superstrates, to be fabricated with common 3D printers. With respect to the latter, we plan to investigate the possibility to realise heterogeneous superstrates, in which different permittivity values can be achieved from a single material. Our idea is to create small (compared to the wavelength) air inclusions in the material, so that – by varying the size and periodicity of the small voids – the local permittivity of the superstrate can be controlled.
The authors are keen to develop these innovative applications in the near future.

## Acknowledgements

This study was carried out in the framework of the PRIN (National Interest Research Programs) Project "Development of design procedures and strategies for frequency selective structures," funded by the Italian Government.
This work strongly benefited from the networking activities carried out in the COST (European Cooperation in Science and Technology) Actions MP0702 "Towards Functional Sub-Wavelength Photonic Structures" (cost-mp0702.nit.eu) and TU1208 "Civil engineering applications of Ground Penetrating Radar" (www.GPRadar.eu). The authors are deeply grateful to COST (www.cost.eu) for funding and supporting the Actions MP0702 and TU1208. This paper is a contribution to the JTIT Special Issue "Recent Progress in Electromagnetic Theory and its Applications" organized by the COST Action TU1208.

## References

[1] J. D. Joannopoulos *et al.*, *Photonic Crystals: Molding the Flow of Light*, 2nd ed. Princeton: Princeton University Press, 2008.

[2] F. Yang and Y. Rahmat-Samii, *Electromagnetic Band Gap Structures in Antenna Engineering.* New York: Cambridge University Press, 2009.

[3] M. Shahidul Alam, N. Misran, B. Yatim, and M. Tariqul Isla, "Development of electromagnetic band gap structures in the perspective of microstrip antenna design", *Int. J. on Antenn. and Propag.*, vol. 2013, Article ID 507158, pp. 1–22, 2013.

[4] M. Thevenot *et al.*, "Directive photonic band-gap antennas", *IEEE Trans. on Microwave Theory and Techniq.*, vol. 47, no. 11, pp. 2115–2122, 1999.

[5] R. Gonzalo *et al.*, "Enhanced Patch antenna performance by suppressing surface waves using photonic band-gap structures", *IEEE Trans. on Microwave Theory and Techniq.*, vol. 47, no. 11, pp. 2131–2138, 1999.

[6] D. Sievenpiper *et al.*, "Antennas on high-impedance ground planes", in *IEEE MTT-S Int. Microwave Symp. Digest*, Anaheim, CA, USA, 1999, vol. 3, pp. 1245–1248.

[7] A. R. Weily, L. Horvath, K. P. Esselle, B. C. Sanders, and T. S. Bird, "A planar resonator antenna based on a woodpile EBG material", *IEEE Trans. on Antenn. and Propag.*, vol. 53, no. 1, pp. 216–223, 2005.

[8] R. Chantalat, L. Moustafa, M. Thevenot, T. Monediere, and B. Jecko, "Low profile EBG resonator antennas", *Int. J. on Antenn. and Propag.*, vol. 2009, Article ID 394801, 2009.

[9] Z. Liu *et al.*, "Research progress on Fabry-Perot resonator antenna", *J. of Zhejiang Univ. Sci. A*, vol. 10(8), 583-588, 2009.

[10] J. Gomez, A. Tayebi, J. R. Almagro, I. Gonzalez, and F. Catedra, "Design and optimization of an EBG antenna with an efficient electromagnetic solver", *Int. J. on Antenn. and Propag.*, vol. 2012, Article ID 427178, 8 pages, 2012.

[11] F. Frezza, L. Pajewski, E. Piuzzi, C. Ponti, and G. Schettini, "Radiation-enhancement properties of an X-band woodpile EBG and its application to a planar antenna", *Int. J. on Antenn. and Propag.*, vol. 2014, Article ID 729187, 15 pages, 2014.

[12] L. Pajewski, L. Rinaldi, and G. Schettini, "Enhancement of directivity using 2D-electromagnetic crystals near the band-gap edge: a full-wave approach", *Progress in Electromag. Res.*, vol. 80, pp. 179–196, 2008.

[13] S. Ceccuzzi, L. Pajewski, C. Ponti, and G. Schettini, "Directive EBG antennas: a comparison between two different radiating mechanisms", *IEEE Trans. on Antenn. and Propag.*, vol. 62, no. 10, pp. 5420–5424, 2014.

[14] Y. Lee, X. Lu, Y. Hao, S. Yang, J. R. G. Evans, and C. G. Parini, "Low-Profile Directive Millimeter-Wave Antennas Using Free-Formed Three-Dimensional (3-D) Electromagnetic Bandgap Structures", *IEEE Trans. on Antenn. and Propag.*, vol. 57, no. 10, pp. 2893–2903, 2009.

[15] H. Liu, S. Lei, X. Shi, and L. Li, "Study of antenna superstrates using metamaterials for directivity enhancement based on Fabry-Perot Resonant cavity", *Int. J. on Antenn. and Propag.*, vol. 2013, Article ID 209741, 10 pages, 2013.

[16] V. Jandieri, K. Yasumoto, and Y. Liu, "Directivity of Radiation of a dipole source coupled to cylindrical electromagnetic bandgap structures", *J. Opt. Soc. of America B*, vol. 29, no. 9, pp. 2622–2629, 2012.

[17] K. M. Ho, C. T. Chan, C. M. Soukoulis, R. Biswas, and M. Sigalas, "Photonic band gaps in three dimensions: new layer-by-layer periodic structures", *Solid State Commun*., vol. 89, no. 5, pp. 413–416, 1994.

[18] H. S. Sözüer and J. P. Dowling, "Photonic band calculations for woodpile structures", *J. of Modern Optics*, vol. 41, no. 2, pp. 231–239, 1994.

[19] F. Frezza, L. Pajewski, E. Piuzzi, C. Ponti, and G. Schettini "Design and fabrication of a 3D-EBG superstrate for patch antennas", in *Proc. 39th Eur. Microwave Conf. EuMC 2009*, Rome, Italy, 2009, pp. 1496–1499.

[20] F. Frezza, L. Pajewski, and G. Schettini, "Full wave characterization of three-dimensional electromagnetic band-gap structures", *IEEE Trans. on Nanotechnol.*, vol. 5, no. 5, pp. 545–553, 2006.

[21] F. Frezza, L. Pajewski, and G. Schettini, "Periodic defects in 2D-PBG materials: full-wave analysis and design", *IEEE Trans. on Nanotechnol*., vol. 2, no. 3, pp. 126–134, 2003.

[22] F. Frezza, L. Pajewski, and G. Schettini, "Numerical investigation on the filtering behaviour of 2D-PBGs with multiple periodic defects", *IEEE Trans. on Nanotechnol.*, vol. 4, no. 6, pp. 730–739, 2005.

**Emanuele Piuzzi** received the M.Sc. (cum laude) and Ph.D. degrees in Electronics Engineering from the Sapienza University of Rome, Rome, Italy, in 1997 and 2001, respectively. He is currently an Associate Professor of Electrical and Electronic Measurements with the Department of Information Engineering, Electronics and Telecommunications, Sapienza University of Rome. He has co-authored over 100 publications. His current research interests include the measurement of complex permittivity of materials, time domain reflectometry applications, biomedical instrumentation design, and evaluation of human exposure to electromagnetic fields. Dr. Piuzzi is a member of the Italian Group of Electrical and Electronic Measurements, and the Italian Electrotechnical Committee.

E-mail: emanuele.piuzzi@uniroma1.it
La Sapienza University of Rome
Department of Information Engineering, Electronics and Telecommunications
via Eudossiana 18
00184 Rome, Italy

**Giorgia V. Rossi** received her Ph.D. in Electrical and Electronic Engineering from Imperial College London, United Kingdom, in 2017. During her Ph.D., as part of the Communications and Signal Processing group, her research focused on improving the performance of current vehicle-to-vehicle communication standards, to enable applications in road safety and hybrid networking. This research was funded by the Defence Science and Technology Laboratory (DSTL) and further involved a collaboration with Toshiba Research Europe Limited (TREL), in the form of a research placement in 2016. Previously, she received an M.Sc. in Electronic Engineering for Telecommunications from Roma Tre University, Italy. Her final M.Sc. thesis focused on the design of vehicular ad hoc networks and was carried out in cooperation with the Imperial College London. She is currently working at Cisco Systems.

E-mail: giorgia.rossi12@imperial.ac.uk
Imperial College London
South Kensington Campus
London SW7 2AZ, United Kingdom

**Lara Pajewski** – for biography, see this issue, p. 29.

**Fabrizio Frezza** – for biography, see this issue, p. 23.

**Marian Marciniak** – for biography, see this issue, p. 35.

# *Information for Authors*

***Journal of Telecommunications and Information Technology*** **(JTIT)** is published quarterly. It comprises original contributions, dealing with a wide range of topics related to telecommunications and information technology. **All papers are subject to peer review**. Topics presented in the JTIT report primary and/or experimental research results, which advance the base of scientific and technological knowledge about telecommunications and information technology.

JTIT is dedicated to publishing research results which advance the level of current research or add to the understanding of problems related to modulation and signal design, wireless communications, optical communications and photonic systems, voice communications devices, image and signal processing, transmission systems, network architecture, coding and communication theory, as well as information technology.

Suitable research-related papers should hold the potential to advance the technological base of telecommunications and information technology. Tutorial and review papers are published only by invitation.

**Manuscript.** TEX and LATEX are preferable, standard Microsoft Word format (.doc) is acceptable. The authors JTIT LATEX style file is available:
http://www.nit.eu/for-authors

Papers published should contain up to 10 printed pages in LATEX authors style (Word processor one printed page corresponds approximately to 6000 characters).

The manuscript should include an abstract about 150200 words long and the relevant keywords. The abstract should contain statement of the problem, assumptions and methodology, results and conclusion or discussion on the importance of the results. Abstracts must not include mathematical expressions or bibliographic references.

Keywords should not repeat the title of the manuscript. About four keywords or phrases in alphabetical order should be used, separated by commas.

The original files accompanied with pdf file should be submitted by e-mail: redakcja@itl.waw.pl

**Figures, tables and photographs.** Original figures should be submitted. Drawings in Corel Draw and PostScript formats are preferred. Figure captions should be placed below the figures and can not be included as a part of the figure. Each figure should be submitted as a separated graphic file, in .cdr, .eps, .ps, .png or .tif format. Tables and figures should be numbered consecutively with Arabic numerals.

Each photograph with minimum 300 dpi resolution should be delivered in electronic formats (TIFF, JPG or PNG) as a separated file.

**References.** All references should be marked in the text by Arabic numerals in square brackets and listed at the end of the paper in order of their appearance in the text, including exclusively publications cited inside. Samples of correct formats for various types of references are presented below:


[1] Y. Namihira, Relationship between nonlinear effective area and mode field diameter for dispersion shifted fibres, *Electron. Lett*., vol. 30, no. 3, pp. 262264, 1994.

[2] C. Kittel, *Introduction to Solid State Physics*. New York: Wiley, 1986.

[3] S. Demri and E. Orłowska, Informational representability: Abstract models versus concrete models, in *Fuzzy Sets, Logics and Knowledge-Based Reasoning*, D. Dubois and H. Prade, Eds. Dordrecht: Kluwer, 1999, pp. 301314.


**Biographies and photographs of authors.** A brief professional authors biography of up to 200 words and a photo of each author should be included with the manuscript.

**Galley proofs.** Authors should return proofs as a list of corrections as soon as possible. In other cases, the article will be proof-read against manuscript by the editor and printed without the author's corrections. Remarks to the errata should be provided within one week after receiving the offprint.



A copy of the JTIT is provided to each author of paper published.

---


*Journal of Telecommunications and Information Technology* has entered into an electronic licencing relationship with EBSCO Publishing, the worlds most prolific aggregator of full text journals, magazines and other sources. The text of *Journal of Telecommunications and Information Technology* can be found on EBSCO Publishings databases. For more information on EBSCO Publishing, please visit www.epnet.com.

(*Contents Continued from Front Cover*)



INSTYTUT ŁĄCZNOŚCI
PAŃSTWOWY INSTYTUT BADAWCZY

Editorial Office

National Institute
of Telecommunications
Szachowa st 1
04-894 Warsaw, Poland

tel. +48 22 512 81 83
fax: +48 22 512 84 00
e-mail: redakcja@itl.waw.pl
http://www.nit.eu

JOURNAL OF TELECOMMUNICATIONS AND INFORMATION TECHNOLOGY 3/2017